HAL
open science

Applications of the Josephson mixer : ultrastrong coupling, quantum node and injection locking in conversion

Danijela Marković

To cite this version:

Danijela Marković. Applications of the Josephson mixer : ultrastrong coupling, quantum node and injection locking in conversion. Mathematical Physics [math-ph]. Université Paris sciences et lettres, 2017. English. NNT : 2017PSLEE025 . tel-01774258

HAL Id: tel-01774258

https://theses.hal.science/tel-01774258

Submitted on 23 Apr 2018

HAL is a multi-disciplinary open access archive for the deposit and dissemination of scientific research documents, whether they are published or not. The documents may come from teaching and research institutions in France or abroad, or from public or private research centers.

L'archive ouverte pluridisciplinaire **HAL**, est destinée au dépôt et à la diffusion de documents scientifiques de niveau recherche, publiés ou non, émanant des établissements d'enseignement et de recherche français ou étrangers, des laboratoires publics ou privés.

THÈSE DE DOCTORAT

de l'Université de recherche Paris Sciences et Lettres
PSL Research University

Préparée à l'Ecole Normale Supérieure

Applications of the Josephson mixer

Ultrastrong coupling, quantum node and injection locking in conversion

Ecole doctorale n°564
Physique en Île-de-France

Spécialité Physique Quantique

Soutenue par
Danijela **MARKOVIĆ**
le 14 Décembre 2017

Dirigée par Benjamin **HUARD**

COMPOSITION DU JURY :

M. HOFHEINZ Max
Université de Sherbrooke, Rapporteur

M. STEELE Gary
TU Delft, Rapporteur

M. BUISSON Olivier
Institut Néel, CNRS, Membre du jury

M. CIUTI Cristiano
Université Paris Diderot, CNRS,
Président du jury

M. ESTEVE Daniel
CEA Saclay, Membre du jury

Mme. GUICHARD Wiebke
Institut Néel, CNRS, Membre du jury

M. HUARD Benjamin
ENS Lyon, Directeur de thèse

Za taju

ACKNOWLEDGMENTS

"On est bien ici". C'est ce que je me suis dit lors de ma première journée dans cette petite salle où on était deux permanents, un post-doc, trois thésards, deux cryostats et deux bruits de tubes pulsés. Parce que c'était l'ambiance Qelec, chaleureuse, amicale et partage-tout et elle l'est tout d'abord grâce à Benjamin Huard.

Je tiens à te remercier Ben, pour tout le temps que tu as consacré à la relecture de ce manuscrit et que tu as réussi à trouver malgré le déménagement à Lyon et tous les projets que tu arrives à mener simultanément. J'ai beaucoup appris de toi, sur la physique, la recherche et la gestion d'un laboratoire. Merci François Mallet, pour tout ce que tu m'as appris sur les techniques expérimentales lors de ma première année de thèse. Merci Emmanuel Flurin, Philippe Campagne et Landry Bretheau d'avoir fait en sorte que j'ai l'impression d'appartenir à l'équipe dès le premier jour devant le tableau et la première soirée à la Montagne.

Merci Nathanael Cottet, Quentin Ficheux, Théau Perronin, Raphael Lescanne et Sébastien Jézouin, avec qui on a pris la relève du groupe Qelec, qui savait aussi bien échanger ses idées sur la physique quantique et débuguer les mesures micro-ondes, que fêter l'arrivée de la nouvelle imprimante au Mayflower.

Merci Zaki Leghtas de nous avoir adopté dès ton arrivé dans l'équipe et pour toute l'énergie que tu as investi pour comprendre et expliquer toutes les questions qu'on a pu se poser. Merci Takis Kontos pour ton éternel enthousiasme, pour les discussions autour d'un café et pour les très bons baklavas grecs - qui restent malgré tout moins bons que les serbes. Merci tous les Takis boys, Lauriane Contamin, Matthieu Dartail, Matthieu Desjardins, Laure Bruhat, Tino Cubaynes, Jeremy Viennot et tous les thésards du LPA, Arthur Margueritte, Sarah Houver...

Merci Sergueï Fedortschenko et Simone Felicetti pour notre collaboration très agréable et fructueuse sur le couplage ultrafort et merci à Jean-Damien Pillet pour nos discussions sur l'oscillation paramétrique.

Merci Sukhdeep Dhillon d'avoir été un parrain investi et rassurant, toujours disponible à donner un bon conseil même au coin de l'escalier. Merci Michael Rosticher d'être resté faire des lithos jusque tard des vendredis, tout en racontant des blagues et sans (trop) se plaindre.

Merci Pascal Morfin pour les heures qu'on a passées à dessiner des cavités toujours plus compliquées et à Mathieu Sardin, Jules Silembo, Saysavanh Souramasing et toute l'équipe de l'atelier mécanique sans qui ces cavités n'auraient jamais connu la troisième dimension et merci pour votre fameux : "Tu en as besoin pour quand? Hier?"

Je tiens à remercier Wiebke Guichard, Gary Steele, Olivier Buisson, Christiano Ciuti, Daniel Estève et Max Hofheinz d'avoir fait partie du jury.

Merci à mes colocataires et mes amis qui sont ma famille en France. Et enfin merci à ma famille qui m'inonde d'amour et de soutien depuis la Serbie, l'Autriche et la Suisse : mama, tata, Saška, Mako, Dragi, Vlado, bako, deko, Leco, hvala!

CONTENTS

1 INTRODUCTION 1
1.1 Josephson Mixer 2
1.2 Simulating the ultrastrong coupling 3
1.3 Node for a microwave quantum network 6
1.4 Injection locking in conversion 8

i ULTRASTRONG COUPLING 13

2 SIMULATING ULTRASTRONG COUPLING 15
2.1 State of the art 15
2.1.1 Light Matter Coupling 15
2.1.2 Quantum Rabi Model 17
2.1.2.1 Quantum Simulators 19
2.1.3 USC of two bosonic modes 21
2.2 Constructing an effective ultrastrong coupling Hamiltonian 24
2.2.1 Josephson Mixer 25
2.2.2 Amplification mode 29
2.2.3 Off-resonant pumping 35
2.2.3.1 Input - Output Theory 37
2.2.4 Off-resonant amplification 40
2.2.5 Two tone pumping 43
2.2.5.1 Kerr effect 45
2.2.5.2 Input-Output Theory with Kerr terms 46
2.3 Ground state in USC 47
2.3.1 Two mode squeezing 47
2.3.2 Single mode squeezing 49
2.3.3 Revealing the ground state correlations 50
2.4 Conclusion 53

3 EXPERIMENTALLY EVIDENCING SIGNATURES OF THE ULTRASTRONG COUPLING 55
3.1 Spectral evidence of mode hybridization 55
3.2 Characterization of entanglement and squeezing 58
3.2.1 Homodyne detection 59
3.2.2 Heterodyne detection 60

3.2.3 ON-OFF measurements 63
3.2.4 Calibration of the quadrature measurements 63
3.2.5 EPR state 66
3.2.6 Pulsed measurement of the USC ground state 71
3.2.7 Emission radiation of the USC ground state 72
3.2.7.1 Single mode squeezing 73
3.2.7.2 Two-mode squeezing 77
3.3 Quadrature resolved spectroscopy 79
3.4 Conclusion 80

ii QUANTUM NODE 81

4 QUANTUM NODE FOR QUANTUM INFORMATION PROCESSING 83
4.1 Microwave quantum nodes: state of the art 84
4.1.1 Spin ensemble memories 86
4.1.2 Ferromagnetic magnons memories 86
4.1.3 Hybrid Optomechanical Quantum Node 87
4.1.4 Microwave cavities 89
4.2 Microwave resonators 90
4.2.1 Planar microwave resonators 90
4.2.2 Rectangular waveguide microwave resonators 92
4.2.3 Equivalent LC resonator 93
4.3 Coupling a qubit to a cavity 94
4.3.1 Transmon qubit 94
4.3.2 3D transmon 96
4.4 Transmon coupled to a cavity 97
4.4.1 Jaynes-Cummings method in the strong dispersive coupling limit 97
4.4.2 Black Box Quantization (BBQ) 99
4.4.3 Arbitrary quantum state preparation with a coupled cavity-qubit system 100
4.5 Quantum Node based on Josephson Parametric Converter 102
4.6 Conclusion 105

5 BUILDING A QUANTUM NODE 107
5.1 Microwave quantum memory 107
5.1.1 Experimental design 107
5.1.2 Conversion to the memory mode 111

5.1.3 Mode identification using Kerr shift 112
5.2 Adding a transmon qubit to the memory 113
5.2.1 Aluminum cavity with qubit 114
5.2.2 Lead plated copper cavity with qubit 117
5.3 Quantum memory 121
5.4 Characterizing the qubit 123
5.4.1 Transmission through frequency conversion 123
5.4.2 DDROP cooling protocol 127
5.5 Qubit as an ancilla for the quantum node 128
5.5.1 Dressed qubit spectroscopy 129
5.5.2 Fock state occupation probabilities for a coherent state 130
5.6 Limiting factors of the hybrid 2D/3D quantum node 133
5.7 Conclusion 135
6 QUANTUM NODE ARCHITECTURES 137
6.1 Fully 3D waveguide architecture 137
6.1.1 Separate photon storage and qubit readout modes 137
6.1.2 Fully 3D design 138
6.1.3 Waveguide filtering 142
6.1.4 Lumped buffer resonator 143
6.1.5 Vanishing Kerr shift 146
6.1.6 Asymmetric coupling to the memory mode 149
6.1.7 Conversion pump 150
6.1.8 Conclusion on the full 3D geometry 152
6.2 2D coplanar waveguide architecture 152
6.2.1 Circuit design 153
6.3 Conclusion 155

iii PARAMETRIC OSCILLATION 157
7 PARAMETRIC OSCILLATION 159
7.1 Parametric instability 160
7.2 Injection Locking 164
7.2.1 Injection locking theory 164
7.2.2 Standard injection locking of a Josephson mixer 166
7.2.3 Injection locking in conversion 169
7.3 Conclusion 171

iv EXPERIMENTAL TECHNIQUES 173
8 DEVICE FABRICATION 175
8.1 Nanofabrication 175
8.2 Lead plating the cavity 180
9 LOW TEMPERATURE MEASUREMENTS 183
9.1 Cryogenics and wiring 183
9.2 Room temperature measurements and waveguide filtering 184
10 ELECTROMAGNETIC SIMULATIONS 189
10.1 HFSS 189
10.1.1 Single mode Jaynes-Cummings method 189
10.1.2 Full 3D device design 191
10.2 qucs 192
11 SUMMARY AND CONCLUSIONS 195

v BIBLIOGRAPHY 197

BIBLIOGRAPHY 199

1 INTRODUCTION

> "I start writing when I overcome my disgust with literature."
>
> *Danilo Kiš*

During the last decade, few technologies have qualified as quantum information processing platforms. Universal quantum computing requires numbers of qubits that are not yet available, but well controlled quantum systems exist, that offer a variety of controlled interactions that can be used to build Hamiltonians by design. In 2017, arguably the most advanced technologies are trapped ions and superconducting circuits. Trapped ions currently offer long coherence times and high fidelity quantum gates. However, the scalability of these processors presents an outstanding challenge that seems difficult to overcome. In contrast, superconducting circuits offer more freedom in their implementation and a wide range of reachable coupling strengths.

A key element in the superconducting circuit toolbox is the Josephson mixer. It is a superconducting device that performs three-wave mixing at microwave frequencies [1]. Though it has been conceived with a primary focus on quantum limited parametric amplification, it has subsequently been demonstrated to perform entanglement generation [2], efficient coherent frequency conversion [3], directional amplification [4], circulation [5] and quantum state storage [6].

All of these operations constitute the elementary building blocks for many quantum information protocols. They can be combined in order to tailor a desired Hamiltonian, which opens a way towards analog quantum simulation. Hamiltonian of a system of interest can be decomposed into pieces that can be mapped onto different operating regimes of the Josephson mixer. An example of such a Hamiltonian, that is hard to realize experimentally, is that of two ultrastrongly coupled bosonic modes. In the first part of this thesis, we have explored

a scheme that permits mapping an ultrastrongly coupled system onto a doubly pumped Josephson mixer.

Besides, the ability to create and distribute entanglement and store and release on demand arbitrary quantum states, qualifies Josephson mixer for a quantum node of a modular quantum network [7]. Microwave resonators coupled by the JRM can straightforwardly be coupled to superconducting qubits, which further increases their controllability. In the second part of this thesis, we have investigated few different architectures for a quantum node based on a Josephson mixer.

However, all of these well understood operations, that result from the parametric interaction provided by the JRM, emerge in the regime of linear response of the resonators. In the third part of this thesis, we go a step further and explore the regime of the saturated non-linearity in which parametric self-oscillation emerges.

1.1 JOSEPHSON MIXER

The Josephson parametric converter (JPC) was first built at Yale in 2010, as a first phase-preserving amplifier operating near the quantum limit in the microwave frequency range [8, 9]. It is based on a Josephson Ring Modulator (JRM), which is a nonlinear element consisting of four Josephson junctions in a Wheatstone bridge configuration. Its tunable upgrade, called the Josephson mixer, was subsequently built in our group in 2012 by shunting the Josephson ring with inductances.

The Josephson mixer consists of three spatially and spectrally separated modes a, b and p, that interact through a three-wave mixing interaction Hamiltonian

$$\hat{H} = \hbar\omega_a \hat{a}^\dagger \hat{a} + \hbar\omega_b \hat{b}^\dagger \hat{b} + \hbar\chi(p + p^*)(\hat{a} + \hat{a}^\dagger)(\hat{b} + \hat{b}^\dagger), \tag{1}$$

where $\hat{a}$ and $\hat{b}$ are annihilation operators for the fundamental modes of two microwave resonators coupled by a Josephson ring, and $|p|$ is the amplitude of the classical pump tone that is applied far off-resonance on the common mode of the Josephson mixer. It is the frequency of this pump tone that distinguishes particular operating modes of the Josephson mixer.

When the pump is applied at a frequency that is the sum of the resonance frequencies of the modes a and b, $\omega_p = \omega_B = \omega_a + \omega_b$, in

the rotating wave approximation the three-wave mixing interaction simplifies to the parametric down conversion

$$\hat{H}_{amp} = \hbar g_B(\hat{a}\hat{b} + \hat{a}^\dagger\hat{b}^\dagger), \tag{2}$$

where $g_B = \chi|p_B|$ is the coupling rate of the amplification pump that we refer to as "blue". In this regime, when a signal is sent to one of the input ports of modes a or b, the Josephson mixer acts as a quantum-limited amplifier. When additionally modes a and b are driven by vacuum fluctuations only, the two output fields are in an *Einstein-Podolsky-Rosen* (EPR) state, as illustrated in Fig. 1a.

On the other hand, when the pump tone is applied at the difference frequency $\omega_p = \omega_R = \omega_a - \omega_b$, the interaction becomes that of the parametric frequency conversion

$$\hat{H}_{conv} = \hbar g_R(\hat{a}\hat{b}^\dagger + \hat{a}^\dagger\hat{b}). \tag{3}$$

where $g_R = \chi|p_R|$ is the coupling rate of the "red" conversion pump. Interestingly, using these two well-controllable operating modes, the Josephson mixer can be mapped onto a complex quantum problem, such as the ultrastrongly coupled bosonic modes, in order to mimic its dynamics.

1.2 SIMULATING THE ULTRASTRONG COUPLING

Coupled light and matter modes have been relentlessly providing questions for physicists. Depending on the coupling strength, different phenomena of interest emerge. Whereas the weak coupling has enabled to spy on a quantum system without destroying its quantum nature, in the strong coupling regime, the two systems form hybridized excited states that are a precious resource for quantum information applications.

Strong light-matter coupling corresponds to the situation where the coupling rate between the light and matter modes is larger then the dissipation rates of each of the interacting parts. In this regime, excitations can be coherently exchanged between the interacting systems before they decay. Nowadays, this type of coupling can be systematically reached in various physical systems [10, 11, 12, 13]. Nevertheless, making the coupling rate as strong as the oscillation rates of the

modes is still a challenging task. This regime, first introduced by Ciuti in 2004 [14], is commonly referred to as the ultrastrong coupling.

There, owing to the breakdown of the rotating wave approximation, that is commonly used to describe behavior of strongly coupled systems, new quantum phenomena, such as generation of non classical radiation and entanglement in the ground state, are expected to develop. This fact has motivated experimental realizations of such ultrastrong interaction in various physical systems, ranging from cavity polaritons [15], superconducting circuits [16] and cavity magnons [17]. Most of these works are focused on coupling a two-level system to a harmonic oscillator. Conversely, ultrastrong coupling of two harmonic oscillators was realized by coupling a collective cyclotron resonance in a 2DEG to a THz cavity mode in Houston [18] and to a THz light mode of a split ring resonator in Zurich [19].

All of these experimental realizations demonstrated spectroscopic signatures of the ultrastrong coupling, but insight into the ground state properties and its dynamics are still out of reach in genuine experiments. Nevertheless they can be reached using quantum simulation. In the case of a two-level system coupled to a harmonic oscillator, both analog [20] and digital [21] quantum simulation were recently performed.

In Chapter 2, we propose a scheme that uses the Josephson mixer to perform an analog simulation of two ultrastrongly coupled harmonic oscillators. Experimental evidence of the signatures of the highly non-classical ground state is presented in Chapter 3. The simulation scheme is based on the application of two transversal microwave drive tones used to engineer the desired effective Hamiltonian. Indeed, two interacting bosonic modes a and b are described by the Hamiltonian

$$\hat{H} = \hbar\omega_a \hat{a}^\dagger \hat{a} + \hbar\omega_b \hat{b}^\dagger \hat{b} + g(\hat{a} + \hat{a}^\dagger)(\hat{b} + \hat{b}^\dagger). \tag{4}$$

They are in the ultrastrong coupling regime if the coupling rate g is not only larger than the dissipation rates κ_a and κ_b but is also comparable to the resonance frequencies of the interacting systems $g > 0.1\omega_{a,b}$.

As it is not straightforward to increase the coupling rate, we realize an effective ultrastrong coupling by choosing a rotating frame in which the effective mode frequencies are smaller then the coupling rate g. This is done by simultaneously applying the amplification and

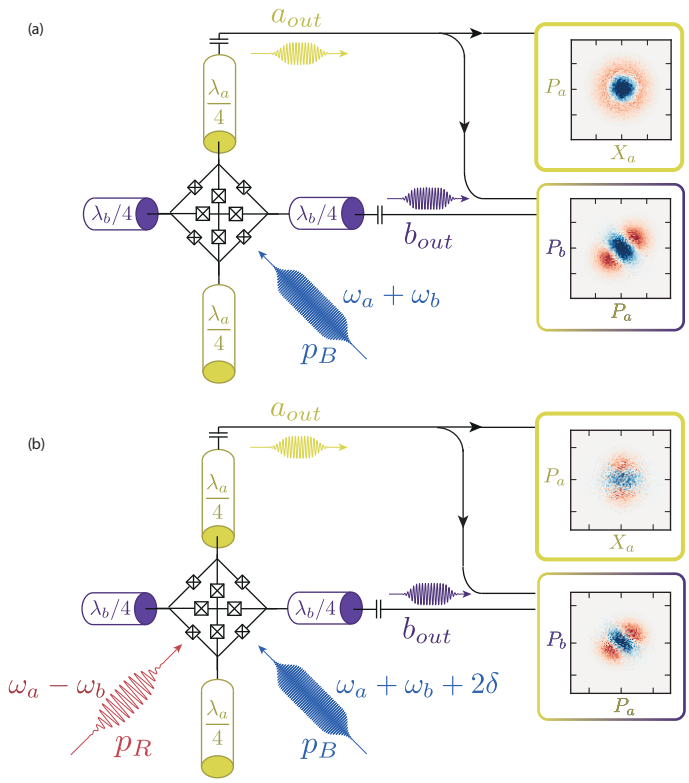

Figure 1: (a) Schematic representation of the Josephson mixer pumped only with the blue amplification pump. Measured quadrature statistics reveal signature of a two-mode squeezed EPR state. (b) Josephson mixer pumped simultaneously with "blue" amplification and "red" conversion pumps. Measured quadrature statistics reveal both single mode and two mode squeezing, which is a signature of effective ultrastrong coupling.

the conversion pump on the Josephson mixer. The full interaction Hamiltonian is then

$$\hat{H}_{int} = \hat{H}_{amp} + \hat{H}_{conv} = g_B(\hat{a}\hat{b} + \hat{a}^\dagger\hat{b}^\dagger) + g_R(\hat{a}\hat{b}^\dagger + \hat{a}^\dagger\hat{b}). \tag{5}$$

For equal coupling rates of the two pump tones, $g_B = g_R = g$, the interaction Hamiltonian is

$$\hat{H}_{int} = g(\hat{a} + \hat{a}^\dagger)(\hat{b} + \hat{b}^\dagger). \tag{6}$$

We have shown that detuning the amplification pump by 2δ, gives the effective frequencies $-\delta$ to the effective modes. For $\delta < g$, we

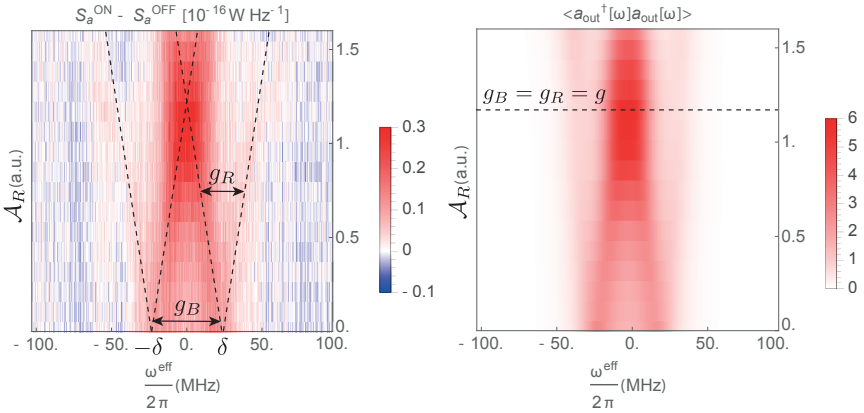

(a) (b)

Figure 2: Spectroscopic evidence of the ultrastrong coupling. (a) Measured power spectral density of the ground state radiation. (b) Expected average number of photons in the outgoing mode. Each of the two resonances exhibits Rabi splitting proportional to the coupling rate g.

have thus constructed an effective system of two ultrastrongly coupled harmonic oscillators.

We have experimentally evidenced a few signatures of ultrastrong coupling. First, as shown in Fig. 1b, radiation emitted from the ground state presents both single mode and two mode squeezing. Second, spectroscopic evidence of the Rabi splitting is shown in Fig. 2a. The expected spectra calculated in the quantum Langevin equation formalism are shown in Fig. 2b.

1.3 NODE FOR A MICROWAVE QUANTUM NETWORK

The idea of a modular quantum network, consisting of nodes formed by clusters of trapped atoms or ions connected by photonic quantum channels, has been present since the 90s [22]. Recent improvements in performance of superconducting qubits have put forward the prospect of local microwave quantum processors based on superconducting circuits, equipped with microwave to optical photon transducers, possibly built on optomechanical systems, that enable long distance connections through optical photons. Transposing the modular architec-

ture of a quantum network to that of a microwave quantum processor [7] even emerges as an alternative approach to the surface code [23].

In a quantum network or a quantum processor of modules, the nodes contain at least one logical memory qubit and one communication qubit that enables information exchange with other modules. As a single harmonic oscillator offers as many states as a full qubit register [24], implementation of a protected logical qubit as a microwave resonator appears as an interesting solution to reduce the system complexity.

(a)

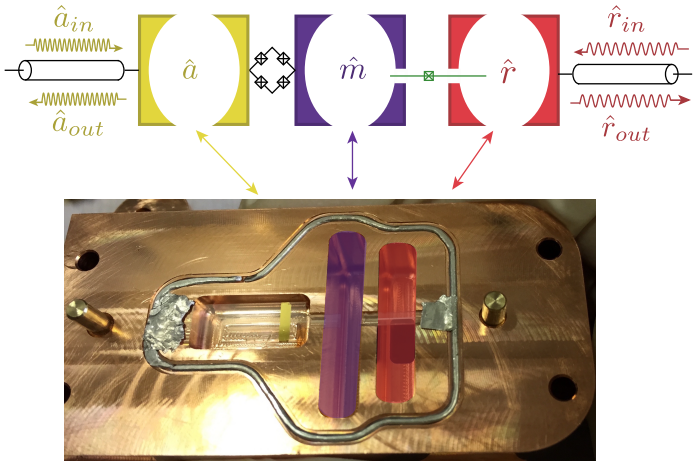

(b)

Figure 3: (a) Schematic of a quantum node based on a Josephson mixer. It consists of a communication buffer resonator a and a memory resonator m coupled through a Josephson ring. Transmon qubit is integrated into the memory mode. (b) Schematic of a device with a qubit readout mode r separate from the photon storage mode m and a photograph of the bottom half of the fully 3D device.

In the second part of this thesis, we show that the Josephson mixer fulfils all the requirements for a quantum node of a modular quantum network. During my PhD, we have designed and tested three different

architectures of the quantum node. The first architecture, schematically represented in Fig. 3a, is based on the quantum memory realized by Flurin *et al.* [6] and consists of a Josephson ring coupling a 2D low Q resonator a that acts as a communication device, and a 3D high Q resonator m that plays the role of the memory. We have integrated a transmon qubit to the memory mode to enable efficient cavity readout and gain controllability over the system state. Indeed, preparation of non-Gaussian states such as Schrödinger cat states requires introducing a nonlinearity to the harmonic oscillator.

As we have found that the lifetime of the memory mode was lower than expected, we pursued an exhaustive study of dissipation sources in 3D structures. This led us to the conclusion that losses are dominated by the 2D/3D interfaces, that necessarily involve holes in the 3D cavity walls, wire bonds for the planar resonators and non-convex 3D cavities. In order to improve this first architecture and in particular the memory lifetime, we have made a few changes in the design. First, we have implemented a qubit readout resonator separately from the photon storage mode, as shown in Fig. 3b. Second, we have realized in parallel a fully 3D design and a fully 2D design, in order to bypass the transitions between the two different architectures. Preliminary results for both of these architectures are exposed in Chapter 6, although this project is still ongoing in our group.

1.4 INJECTION LOCKING IN CONVERSION

Injection locking is a commonly used technique for narrowing the emission linewidth [25] and improving coherence of a laser [26]. It relies on the injection of a tone that stimulates the emission of the system at the input frequency. It has recently been demonstrated in various systems ranging from a semiconductor double-quantum-dot micromaser [27], an ac Josephson junction laser [28] and a trapped ion phonon laser [29]. In the part iii of this thesis, we apply this technique in a specific operating regime of a Josephson mixer, that is the parametric self-oscillation.

Indeed, in the first two parts of this thesis, we have made use of the Josephson mixer as an amplifier and frequency converter. Both of these operating regimes can be described in the context of linear

resonator response to the perturbation by the pump tone. For large pump powers though, behavior of this rich device radically changes.

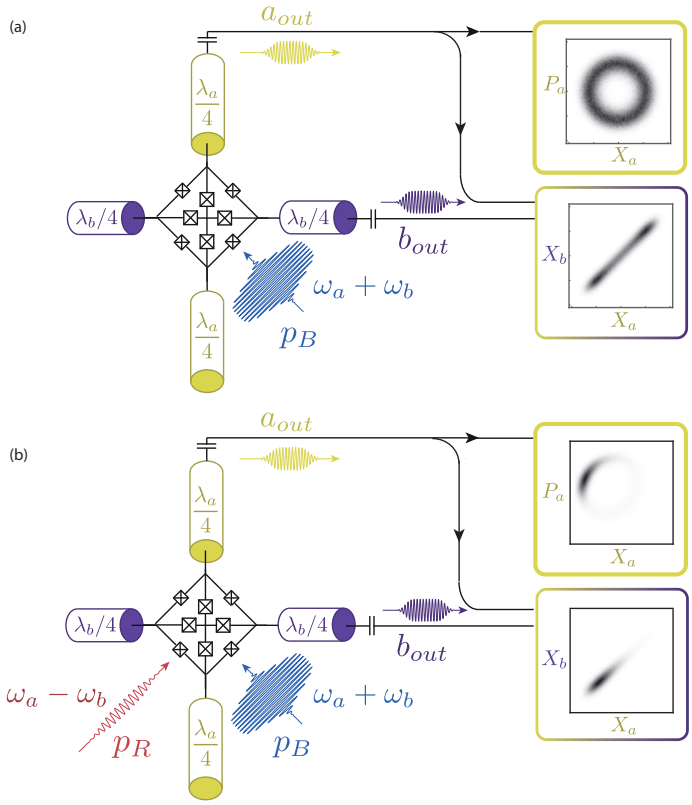

Figure 4: (a) Schematic representation of the Josephson mixer pumped only with the strong amplification pump at frequency $\omega_a + \omega_b$ above the parametric instability threshold. Measured quadrature statistics reveal unlocked self-oscillating state. (b) An additionnal small tone is injected on a conversion pump frequency $\omega_a - \omega_b$. Measured quadrature statistics reveal phase locked coherent state.

For low amplifying pump powers, the resonators dissipate the excitations created by amplification of the vacuum fluctuations at a rate that is larger than their creation rate. The device acts as a linear amplifier and the cavity hosts amplified version of vacuum fluctuations.

Beyond an instability threshold, that corresponds to the total dissipation rate that equals the insertion rate of the photons in the cavity, the intracavity field acquires a finite amplitude corresponding to the square root of the mean photon number in the resonator. The phase

of this field however presents a continuous degeneracy, as can be seen in Fig. 4a. This behavior is referred to as self-oscillation.

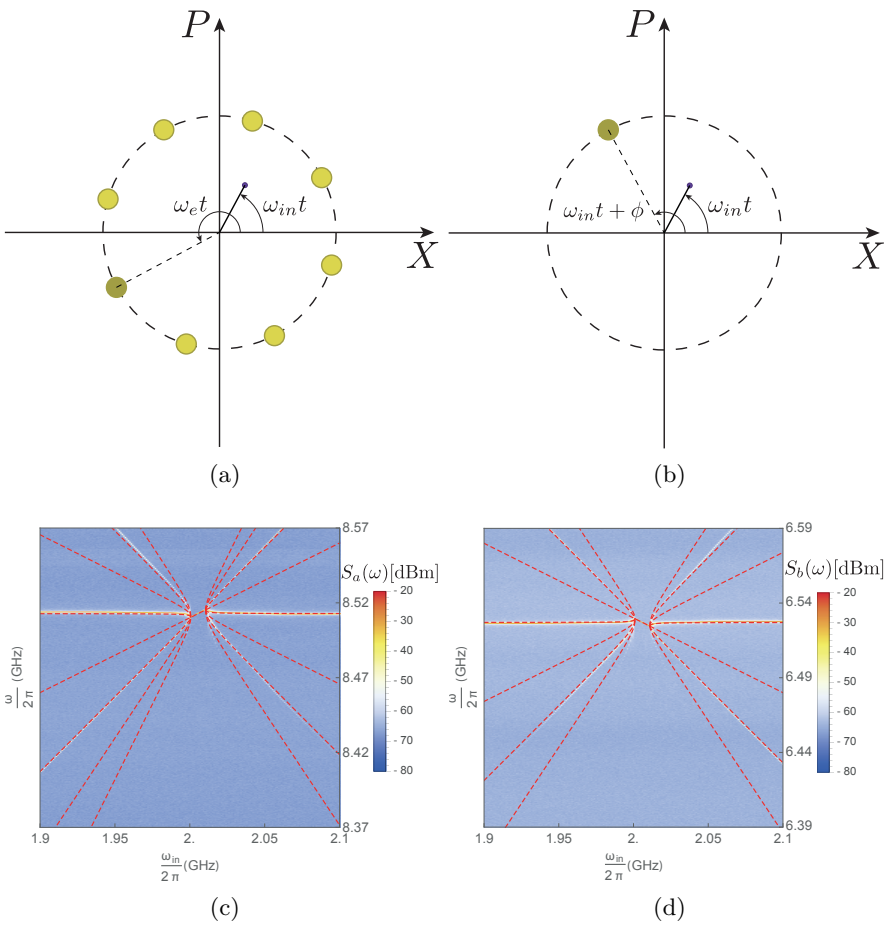

Figure 5: Phase of the natural emission field at frequency ω_e compared to the phase of the field injected at frequency ω_{in} (a) in the unlocked regime and (b) in the injection locked regime. (c) and (d) Emitted radiation spectra of the modes a and b, locked by the conversion pump tone.

We have first studied the onset of parametric oscillation as a function of the detuning of the amplification pump tone and the stability of the empty cavity state. It gave us insight into bistability regions, where both the empty cavity and self-oscillating solution simultaneously exist. This results from the competition of the two stabilizing mechanisms that are the Kerr effect and pump depletion.

We then studied the phase dynamics in the self-oscillation regime. Inspired by the injection locking technique used with optical lasers, we show that field emitted at frequency ω_e from both non-degenerate modes a and b of the Josephson mixer can be locked by a signal injected at frequency ω_{in} on one of the two modes, as illustrated in Fig. 5a and Fig. 5b. Interestingly, owing to the four-wave-mixing interaction of the Kerr effect, the emission field can be locked in a non standard way using the conversion pump.

Emitted radiation spectra, shown in Fig. 5c for the mode a and Fig. 5d for the mode b reveal injection locking for the input frequencies in the proximity of the parametric conversion frequency. These spectra, including sideband positions, can be understood and reproduced using the standard Adler theory for lasers and an effective locking frequency produced in a Kerr four-wave interaction, show in a red dashed line.

Finally, we conclude this thesis with the part iv, where some of the main experimental techniques used for all the presented experiments are described.

Part I

ULTRASTRONG COUPLING

2 SIMULATING ULTRASTRONG COUPLING

"Without a revolutionary theory there cannot be a revolutionary movement."

Vladimir Ilyich Lenin

2.1 STATE OF THE ART

2.1.1 *Light Matter Coupling*

The role of quantum mechanics in the description of the interaction between light and matter was acknowledged since the early days of the quantum theory and is known as quantum electrodynamics. In its simplest modeling, both light and matter modes have a resonance frequency ω that characterizes their internal dynamics and a dissipation rate κ that quantifies their interaction with the environment. The interaction between the modes can be quantified by defining a coupling rate g that corresponds to the exchange rate of excitation quanta between modes. The ratio of the coupling and dissipation rates defines the weak coupling regime where $g < \kappa$ and the strong coupling regime where $g > \kappa$. Then at resonance the collective light-matter excitations have an energy separation of $2g$ called the vacuum Rabi splitting.

The realization of the strong coupling regime represents an important milestone in physics as it has given rise to the field of cavity quantum electrodynamics (CQED). It began with Rydberg atoms in cavity [30, 31, 32] but is now reached in a broad range of systems such as trapped ions [33, 34], NV centers [35, 36], mechanical oscillators [37], silicon donors, spin qubits, quantum dots [38] etc. In 2004, the strong coupling was demonstrated between a superconducting qubit

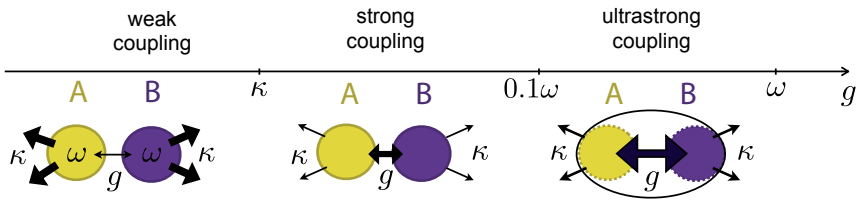

Figure 6: Light-matter coupling regimes parametrized by the dissipation rate κ, coupling rate g and resonance frequency ω.

and a cavity by Wallraff *et al.* [11], which started the field of circuit quantum electrodynamics (cQED).

When strongly coupled, the two interacting systems can coherently exchange an excitation faster than they dissipate, which results in entangled excited hybrid states of light and matter. By consequence, light and matter cannot be considered as separate entities any more and the energy spectrum of the coupled system is split into two separated resonances, which correspond to collective excitations of the coupled light-matter system, called the upper and lower polaritons. Furthermore, if the coupling is still increased and becomes of the order of the frequencies of the interacting systems themselves, a different and much less explored regime is reached: the ultrastrong coupling (USC). In this regime, the standard rotating wave approximation, that is used to model the system's dynamics, breaks down, which means that the number of excitations is not conserved anymore and even the ground state effectively appears as populated and hybridized with the other mode.

Ultrastrong coupling has been predicted in 2004 for polaritons [14], where it has first been experimentally demonstrated as well [15], thanks to the giant dipole moments of intersubband transitions in quantum wells that give rise to large coupling constants. Recently, few experiments have been realized with superconducting circuits, that have exploited the extraordinarily large magnetic moments of particular artificial atoms based on Josephson junctions, called flux

qubits. All of these experiments can be described by the quantum Rabi model.

2.1.2 *Quantum Rabi Model*

The quantum Rabi model (QRM) considers a two-level system, or a qubit, coupled to a single quantized electromagnetic mode. It applies for a variety of physical systems, including cavity QED, the interaction between light and trapped ions or quantum dots, and the interaction between microwaves and superconducting qubits in circuit QED. The general Hamiltonian of the QRM is

$$\frac{1}{\hbar}\hat{H}_{QRM} = \omega_q \frac{\hat{\sigma}_z}{2} + \omega_a \hat{a}^\dagger \hat{a} + g\hat{\sigma}_x(\hat{a}^\dagger + \hat{a}), \tag{7}$$

where $\hat{a}^\dagger$ and $\hat{a}$ are creation and annihilation operators for the electromagnetic (cavity) mode and $\hat{\sigma}_x = \hat{\sigma}_+ + \hat{\sigma}_-$ and $\hat{\sigma}_z$ are Pauli operators for the two-level system

$$\sigma_z = \begin{pmatrix} 1 & 0 \\ 0 & -1 \end{pmatrix}, \quad \sigma_- = \begin{pmatrix} 0 & 0 \\ 1 & 0 \end{pmatrix}, \quad \sigma_+ = \begin{pmatrix} 1 & 0 \\ 0 & 0 \end{pmatrix}. \tag{8}$$

The first term in Eq. (7) corresponds to the free Hamiltonian of the qubit with frequency ω_q and the second to the field at the cavity resonance frequency ω_a. The last term represents the transverse coupling between the qubit and the resonator field with coupling strength g. It is useful to expand the Hamiltonian Eq.(7) as

$$\frac{1}{\hbar}\hat{H}_{QRM} = \omega_q \frac{\hat{\sigma}_z}{2} + \omega_a \hat{a}^\dagger \hat{a} + g(\hat{\sigma}_- \hat{a}^\dagger + \hat{\sigma}_+ \hat{a} + \hat{\sigma}_+ \hat{a}^\dagger + \hat{\sigma}_- \hat{a}). \tag{9}$$

For coupling rate $g \ll \omega$, this model can be simplified by going from Schrödinger to interaction picture, where the last two interaction terms in Eq. (9) that simultaneously excite or de-excite both the atom and the cavity can be neglected by making the rotating wave approximation (RWA). We then obtain the Jaynes-Cummings (JC) Hamiltonian

$$\frac{1}{\hbar}\hat{H}_{JC} = \omega_q \frac{\hat{\sigma}_z}{2} + \omega_a \hat{a}^\dagger \hat{a} + g(\hat{\sigma}_- \hat{a}^\dagger + \hat{\sigma}_+ \hat{a}). \tag{10}$$

Although it accurately predicts a wide range of experiments in weak and strong coupling regimes, its validity breaks down for the ultrastrong coupling, where the full QRM Hamiltonian has to be taken into

account. However, exactly solving the quantum Rabi model is a difficult problem as its state space is infinite-dimensional. Even though the model has been known for over 70 years, an analytical solution to it, given in the form of transcendental functions, has only been calculated in 2011 [39]. However, its spectrum and eigenfunctions can be more easily found by numerical diagonalization in a truncated, finite-dimensional Hilbert space. Using this method, we compare the numerical solutions for eigenstates of the JC and full QRM Hamiltonian as shown in Fig. 7.

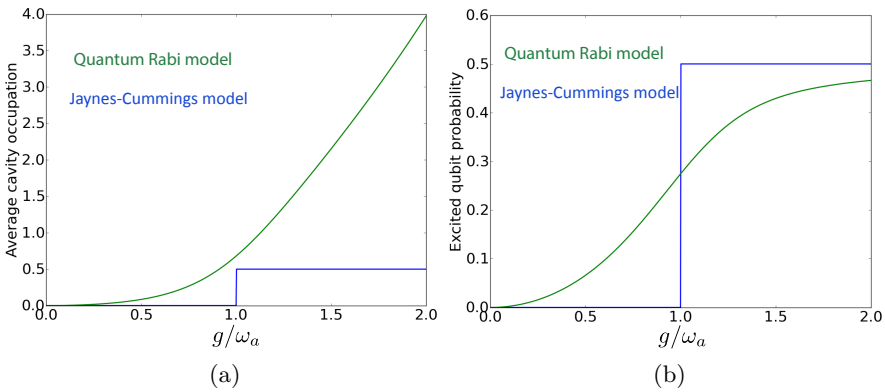

Figure 7: (a) Mean number of photons in the cavity in the ground state $\langle \hat{a}^\dagger \hat{a} \rangle$ and (b) occupation probability of the excited state of the qubit $\frac{\langle \hat{\sigma}_z \rangle}{2}$ are plotted as a function of coupling rate g for the Jaynes-Cummings Hamiltonian using RWA and for the full Quantum Rabi model Hamiltonian. In this simulation, cavity and qubit are on resonance.

For small couplings $g/\omega_{a,q} \ll 1$, the cavity occupation in the ground state is low, $\langle \hat{a}^\dagger \hat{a} \rangle \ll 1$, such that it can be well approximated by the Jaynes-Cummings Hamiltonian, whose ground state is vacuum. However, for coupling $g/\omega_{a,q} \lesssim 1$, the difference between the two models in Fig. 7 indicates that the counter-propagating terms cannot be neglected anymore. Indeed, for $g/\omega_{a,q} > 1$, the eigenmodes of the Jaynes-Cummings Hamiltonian are $\frac{|e0\rangle \pm |g1\rangle}{2}$, so that the mean occupation number for both qubit and cavity is 0.5. In the QRM however, more excitations can be created in the cavity and the average number of photons is higher. For large enough coupling, its ground

state is not the standard vacuum but a maximally entangled state of the photon field and the atom.

The validity of the quantum Rabi model is remarkably large. Even tough it describes the simple case of a two-level system interacting with a single bosonic mode, its predictions apply for the couplings $g/\omega_{a,q} \gg 1$ where the multilevel structure of the interacting atom has to be taken into account [40].

The ultrastrong coupling regime has recently raised a lot of interest as it gives rise to a variety of new and unexplored quantum processes. As number of excitations is not conserved, multiphoton Rabi oscillations become possible, where multiple photons excite the qubit and a single photon can excite multiple qubits [41]. Furthermore, frequency conversion of photons can be realized if a single qubit is coupled ultrastrongly to two resonator modes [42]. Finally, USC has several potential applications in quantum computing, such as ultra fast quantum gates [43], protected quantum computation with multiple resonators [44] and quantum memories [45].

All of these perspectives have motivated experimental efforts to realize genuine ultrastrongly coupled systems. Some of them are summarized in Table 1.

Quantum Rabi model in the ultrastrong coupling regime has been experimentally realized in several types of systems that include semiconductor quantum wells [15, 48, 47], organic molecules [46], YIG sphere in a magnetic-field-focusing resonator with photon-magnon and magnon-magnon couplings [17] and superconducting circuits [49, 16, 50, 51]. All of these experiments have demonstrated spectroscopic signatures of mode hybridization, yet, demonstrating the ground-state entanglement and large ground-state photon numbers that can arise in the QRM is an open challenge in USC research. An alternative approach has thus been adopted with superconducting circuits, which is to perform quantum simulations of the dynamics of an USC system.

2.1.2.1 *Quantum Simulators*

The idea behind the quantum simulation, originally proposed by Feynman in 1982 [52], is to map a well-controllable artificial quantum system onto a complex quantum problem of interest in order to mimic

system	experiment	$\omega_r/2\pi$	g/ω_r
superconducting circuits [16]	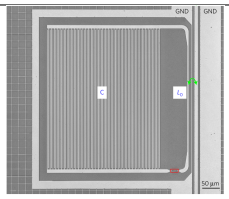	5.7 GHz	1.34
organic molecules [46]	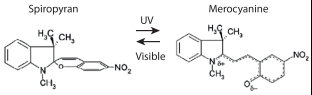	530 THz	0.32
semiconductor polaritons [47]	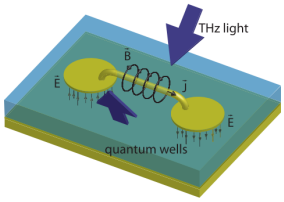	670 GHz	0.27
CQED magnons [17]	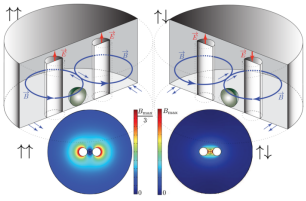	20 GHz	0.1

Table 1: Exemples of experimental realizations of the quantum Rabi model in different systems with the resonance frequency ω_r and the relative coupling g/ω_r.

its dynamics. Since both systems are described by the same equations of motion, the solution of the studied quantum problem is deduced by observing the time evolution of the artificially built model system, thus exploiting its intrinsic quantumness. This procedure is referred to as analog quantum simulation.

In the particular case where the complex quantum problem of interest is a system of two ultrastrongly coupled modes, the analog quantum simulation relies on properly driving strongly interacting systems so that they effectively behave as ultrastrongly coupled modes and exhibit the corresponding characteristic features. The use of an analog simulator is thus restricted to a particular problem, or class of prob-

lems, because there has to be a direct mapping between the state and the dynamics of the simulated system and those of the simulator.

Different approach is adopted in digital quantum simulators, where any complex Hamiltonian of interest can be simulated by decomposing it onto sequences of discrete interaction components, from which the evolution of the artificial Hamiltonian can be synthesized. A universal set of quantum operations or gates can be performed, which enables an execution of a stroboscopic sequence of quantum gates, that approximate the dynamics of the simulated system. This procedure allows access to more exotic dynamics than the simulator can realize naturally.

Quantum simulators, both analog [20] and digital [21], have recently been used to probe the dynamics of the QRM and the exotic properties of its ground state. They have enabled the first detection of a time domain signature of the USC as well as of the entanglement in the ground state. The quantum hardware used in both experiments were superconducting circuits.

2.1.3 *USC of two bosonic modes*

What happens if, instead of an atom in the cavity, we consider two cavities that are ultrastrongly coupled? The electromagnetic field of each cavity can be decomposed into field modes, to each of which a quantum harmonic oscillator is associated. The Hamiltonian of two coupled modes is

$$\frac{1}{\hbar}\hat{H} = \omega_a \hat{a}^\dagger \hat{a} + \omega_b \hat{b}^\dagger \hat{b} + g(\hat{a}^\dagger + \hat{a})(\hat{b}^\dagger + \hat{b}), \tag{11}$$

where $\hat{a}$ and $\hat{b}$ are bosonic operators that annihilate one excitation at frequency ω_a or ω_b in the corresponding bosonic mode. These modes can be compared to mechanical oscillators such as two springs with masses attached to their ends and coupled through a third spring as schematically represented in Fig. 8.

The classical Hamiltonian of this mechanical system is

$$H = \frac{1}{2}kx_a^2 + \frac{p_a^2}{2m} + \frac{1}{2}kx_b^2 + \frac{p_b^2}{2m} + \frac{1}{2}k_m(x_a - x_b)^2, \tag{12}$$

where the $x_{a,b}$ and $p_{a,b}$ are positions and momenta of resonators a and b with equal spring stiffnesses $k_a = k_b = k$ and equal masses

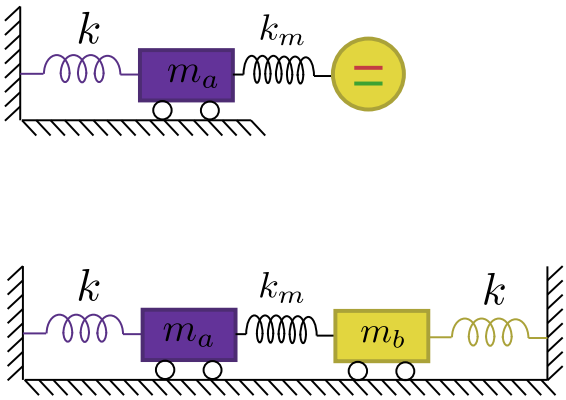

Figure 8: Mechanical oscillator coupled to a two level system as in the quantum Rabi model and two coupled mechanical oscillators analogous to two coupled bosonic modes. Note that the stiffness k_m of the middle spring is larger than stiffness k of each of the springs of the two oscillators. The resonance frequencies are given by $\omega_{a,b} = \sqrt{\frac{k}{m_{a,b}}}$.

$m_a = m_b = m$ connected through a spring of stiffness k_m. Due to the interaction term, the effective spring stiffnesses are modified and the Hamiltonian reads

$$H = \frac{1}{2}(k + k_m)x_a^2 + \frac{p_a^2}{2m} + \frac{1}{2}(k + k_m)x_b^2 + \frac{p_b^2}{2m} - k_m x_a x_b. \quad (13)$$

For the quantum mechanical resonators, the positions and momenta can be mapped on operators that we can be quantified, so that the interaction term becomes

$$\hat{H}_{int} = -k_m \hat{x}_a \hat{x}_b = -k_m x_a^{ZPF} x_b^{ZPF} (\hat{a} + \hat{a}^\dagger)(\hat{b} + \hat{b}^\dagger), \quad (14)$$

where $x_a^{ZPF} = x_b^{ZPF} = x^{ZPF} = \sqrt{\frac{\hbar}{2m\omega_r}} = \sqrt{\frac{\hbar}{2m}\sqrt{\frac{m}{k+k_m}}}$ are the zero point fluctuations. This interaction is equivalent to that of two bosonic modes a and b coupled at a rate g such that

$$\hbar g = -k_m x_{ZPF}^2 = -k_m \frac{\hbar}{2m}\sqrt{\frac{m}{k + k_m}}, \quad (15)$$

for two oscillators of resonance frequencies

$$\omega_r = \sqrt{\frac{k + k_m}{m}}. \quad (16)$$

In order to test the validity of this model, it is interesting to notice that the situation where the coupling rate reaches half of the resonance frequency

$$\frac{g}{\frac{\omega_r}{2}} = 1 = \frac{\frac{k_m}{2}\frac{1}{\sqrt{m(k+k_m)}}}{\frac{1}{2}\sqrt{\frac{k+k_m}{m}}} = \frac{k_m}{k+k_m}, \tag{17}$$

is equivalent to $k_m \to \infty$, which corresponds to the ultrastrong coupling. Furthermore, a coupling stronger than this limit is equivalent to a negative stiffness k as

$$g > \frac{\omega_r}{2} \quad \Leftrightarrow \quad k_m > k + k_m, \tag{18}$$

or $k < 0$, which doesn't not correspond to a physical situation. A natural limit thus emerges for a maximum reachable coupling as the model breaks down for $g > \frac{\omega_r}{2}$. An equivalent theoretical coupling limit has been demonstrated for the quantum Rabi model as well [53], where $2g \lesssim \sqrt{\omega_a \omega_q}$ for a two-level system of resonance frequency ω_q coupled to an oscillator of resonance frequency ω_a.

Indeed, for a coupling rate g comparable to the resonance frequencies $\omega_{a,b}$, all the terms in the interaction Hamiltonian need to be taken into account, so that

$$\frac{1}{\hbar}\hat{H}_{int} = g(\hat{a}\hat{b}^\dagger + \hat{a}^\dagger\hat{b} + \hat{a}\hat{b} + \hat{a}^\dagger\hat{b}^\dagger). \tag{19}$$

Due to the last two terms in this development, the number of excitations in the system $\langle \hat{N} \rangle = \langle \hat{a}^\dagger\hat{a} + \hat{b}^\dagger\hat{b} \rangle$ is not a conserved quantity because $[\hat{N}, \hat{H}] \neq 0$. By consequence, the ground state is populated with virtual photons that exhibit quantum correlations or entanglement [54].

This Hamiltonian has been experimentally realized by coupling a collective cyclotron resonance in a 2DEG to THz photons in a photonic crystal cavity [18]. Counter propagating terms in Hamiltonian had to be kept in order to reproduce the observed anticrossing of polariton branches, which constitutes a convincing spectroscopic proof of the USC with the coupling $g/\omega \sim 0.12$. Stronger coupling rates, $g/\omega \sim 0.87$, were reached by replacing the cavity by a split-ring resonator [19], whereas shaping the vacuum mode enabled reaching the record value of $g/\omega \sim 1.43$ [55].

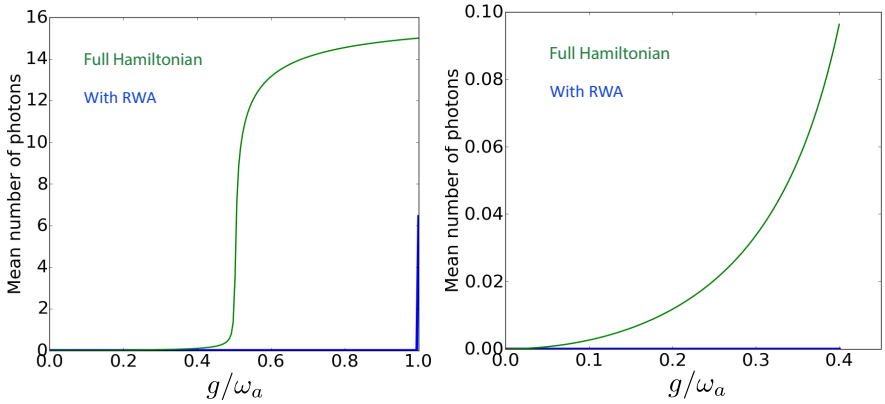

(a) (b)

Figure 9: (a) Average number of photons in the ground state of each of the two coupled bosonic modes as a function of the coupling rate g. In this simulation, the two modes are degenerate, so that the mean occupation is the same for both of them. With RWA, the number of excitations is expected to be conserved and the mean number of photons is zero. However, taking the full Hamiltonian into account, we see that the ground state is populated when the coupling is increased. (b) Zoom into smaller couplings. The photon population become non negligeable already for $g/\omega_a \simeq 0.1$.

In order to go beyond the spectroscopic signature of mode hybridization in USC and demonstrate the quantum correlations in the ground state, we have realized an analog quantum simulation of two ultrastrongly coupled bosonic modes. The coupling in simulation being tunable, it allows us to study the transition from strong to ultrastrong coupling. More importantly, it gives us access to the field radiated from the ground state which allows up to probe its highly non classical nature.

2.2 CONSTRUCTING AN EFFECTIVE ULTRASTRONG COUPLING HAMILTONIAN

In this section we propose a simulation scheme to engineer an effective ultrastrong coupling Hamiltonian. It is based on the application of two microwave drive tones and can be used as a tool to demonstrate the squeezing properties of the system in its ground state. The

quantum hardware of the simulator used for the physical implementation is a cQED setup embedding a superconducting circuit called the Josephson Mixer.

2.2.1 *Josephson Mixer*

Parametric amplifiers based on Josephson junctions have first been introduced by Yurke and collaborators in 1980s [56] and following their work, several designs have been developed [57, 58]. They can be categorized into phase-preserving and phase-sensitive amplifiers. Those belonging to the first group amplify both quadratures of the signal while adding the minimum amount of noise allowed by quantum mechanics. Phase-sensitive amplifiers though can amplify one quadrature without adding any noise to it, while attenuating the conjugate quadrature. They thus create squeezed electromagnetic field. The Josephson Mixer [1] is a tunable upgrade of the Josephson Parametric Converter, first built at Yale in 2010 [8, 9] as a phase-preserving microwave parametric amplifier operating at the quantum limit of added noise. Since then it has been vastly studied and demonstrated to be used as entanglement generator [2], frequency converter [3], directional amplifier [4], circulator [5] and quantum memory [6]. It consists of two superconducting $\lambda/2$ microwave resonators coupled through the Josephson Ring Modulator (JRM), that is through a loop of four identical Josephson junctions, threaded by an applied magnetic flux. The JRM realizes a three-wave-mixing parametric interaction between the resonator modes.

Josephson junctions are superconducting tunnel junctions that behave as pure nonlinear inductors with inductance $L_J = \frac{\varphi_0}{I_0 \cos\delta}$, where $\varphi_0 = \frac{\hbar}{2e}$ is the reduced flux quantum, I_0 is the critical current of the junctions and δ is the phase difference between the two superconducting electrodes of the junction.

In order to increase the frequency tunability and extend the stability range of the JRM by avoiding the phase-slips [59], the ring is shunted with four large and thus very weakly nonlinear Josephson junctions, acting as inductors.

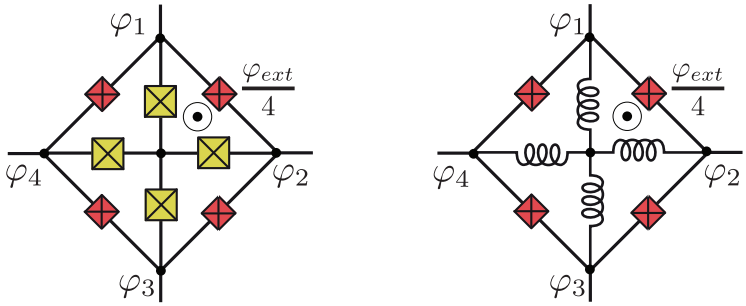

Figure 10: Shunted Josephson Ring Modulator is a ring of four Josephson junctions (red), that provide nonlinearity for the parametric interaction. It is shunted with four larger and less inductive Josephson junctions (yellow) that behave like pure linear inductors. The whole loop is threaded by an externally applied magnetic flux φ_{ext}.

The Hamiltonian of such shunted Josephson ring is

$$\begin{aligned}\hat{H}_{JRM} = &- 4E_J \cos\frac{\varphi_a}{2}\cos\frac{\varphi_b}{2}\cos\varphi_c\cos\frac{\varphi_{ext}}{4} \\ &- 4E_J \sin\frac{\varphi_a}{2}\sin\frac{\varphi_b}{2}\sin\varphi_c\sin\frac{\varphi_{ext}}{4} \\ &+ \frac{1}{4}E_J^{shunt}(\varphi_a^2+\varphi_b^2+2\varphi_c^2),\end{aligned} \tag{20}$$

where $E_J = \varphi_0 I_0$ is the Josephson energy of a ring junction (red), $E_J^{shunt} = \varphi_0 I_0$ is the Josephson energy of a shunting junction (yellow) and φ_{ext} is the magnetic flux threading the loop. $\varphi_{a,b,c}$ are the normal modes of the JRM, that can be deduced from the ring symmetries and can be written as a function of the reduced fluxes in the nodes of the ring, $\varphi_{1,2,3,4}$, as

$$\begin{cases}\varphi_a &= \varphi_1 - \varphi_3 \\ \varphi_b &= \varphi_2 - \varphi_4 \\ \varphi_c &= \frac{\varphi_1-\varphi_4}{2} + \frac{\varphi_3-\varphi_2}{2}\end{cases} \tag{21}$$

We refer to the modes a and b as differential modes, and to the mode c as the common mode. Note that in the ring Hamiltonian, we have neglected the inductance of the wires in the loop, that are in series with Josephson junctions. To see how to add these inductances in the model, on can refer to the PhD thesis of Emmanuel Flurin [60].

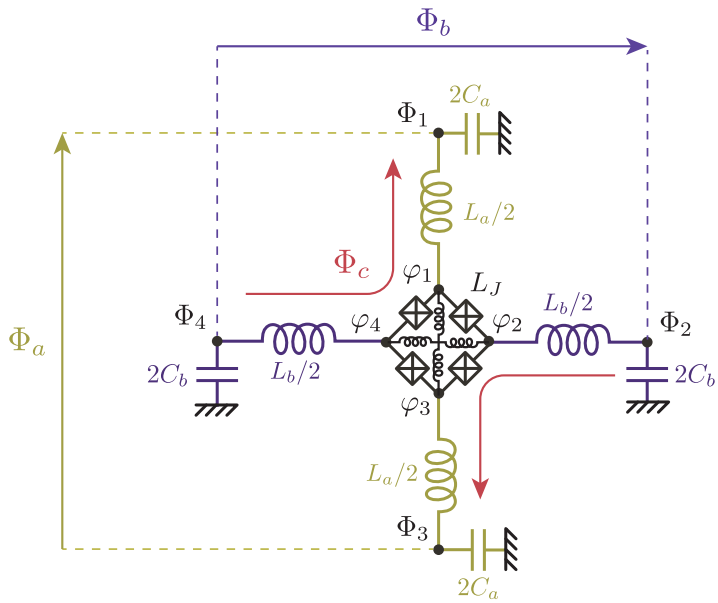

Figure 11: Lumped circuit model of the Josephson Mixer. Φ_a and Φ_b are the two differential $\lambda/2$ modes and Φ_c is the common excitation mode.

The Josephson Mixer is a circuit consisting of the JRM embedded between two microwave resonators a and b. In the lumped circuit model, these resonators can be represented as LC oscillators, with inductances $L_{a,b}$ given by the length of the wire and capacitances $C_{a,b}$, as shown in Fig. 11. Normal modes of the entire circuit, $\Phi_{a,b,c}$, have the same symmetries as the normal modes of the ring and can be related to them through the participation ratios of the ring inductance in the total mode inductance

$$\xi_{a,b,c}(\varphi_{ext}) = \varphi_0 \frac{\varphi_{a,b,c}}{\Phi_{a,b,c}} = \frac{L^{JRM}_{a,b,c}(\varphi_{ext})}{L_{a,b,c} + L^{JRM}_{a,b,c}(\varphi_{ext})}, \tag{22}$$

where $L^{JRM}_{a,b,c}(\varphi_{ext}) = \varphi_0^2 (\frac{\partial^2 H_{JRM}}{\partial \varphi^2_{a,b,c}})^{-1}$ are the inductances of the modes a, b, c of the JRM and $L_{a,b,c}$ are the wire inductances for each mode, such that $L^{JRM}_{a,b,c}(\varphi_{ext}) + L_{a,b,c} = L^{tot}_{a,b,c}(\varphi_{ext})$ are the total inductances of the modes a, b and c of the circuit.

Unshunted Josephson Ring	
Hamiltonian	$\hat{H}_{JRM} = -4E_J[\cos\frac{\varphi_a}{2}\cos\frac{\varphi_b}{2}\cos\varphi_c\cos\left(\frac{\varphi_{ext}+2n\pi}{4}\right)]$ $-4E_J[\sin\frac{\varphi_a}{2}\sin\frac{\varphi_b}{2}\sin\varphi_c\sin\left(\frac{\varphi_{ext}+2n\pi}{4}\right)]$
Hamiltonian for $\varphi_{a,b,c} \ll 1$	$\hat{H}_{JRM} = -E_J\sin\left(\frac{\varphi_{ext}}{4}+n\frac{\pi}{2}\right)\varphi_a\varphi_b\varphi_c$ $+E_J\cos\left(\frac{\varphi_{ext}+2n\pi}{4}\right)[\frac{\varphi_a^2}{2}+\frac{\varphi_b^2}{2}+2\varphi_c^2-4]$
ring modes inductances	$L_{a,b}^{JRM}(\varphi_{ext}) = \frac{\varphi_0^2}{E_J\cos\left(\frac{\varphi_{ext}+2n\pi}{4}\right)}$
stability condition	n such that $L_c^{JRM}(\varphi_{ext}) = \frac{\varphi_0^2}{4E_J\cos\left(\frac{\varphi_{ext}+2n\pi}{4}\right)} > 0$
degeneracy	4 different possible flux configurations indexed by n

Table 2: Summary of useful expressions for an unshunted JRM.

Shunted Josephson Ring	
Hamiltonian	$\hat{H}_{JRM} = -4E_J[\cos\frac{\varphi_a}{2}\cos\frac{\varphi_b}{2}\cos\varphi_c\cos\left(\frac{\varphi_{ext}}{4}\right)]$ $-4E_J[\sin\frac{\varphi_a}{2}\sin\frac{\varphi_b}{2}\sin\varphi_c\sin\left(\frac{\varphi_{ext}}{4}\right)]$ $+\frac{1}{4}E_J^{shunt}[\varphi_a^2+\varphi_b^2+2\varphi_c^2]$
Hamiltonian for $\varphi_{a,b,c} \ll 1$	$\hat{H}_{JRM} = -E_J\sin\left(\frac{\varphi_{ext}}{4}\right)\varphi_a\varphi_b\varphi_c$ $+[E_J\cos\left(\frac{\varphi_{ext}}{4}\right)+\frac{E_J^{shunt}}{2}]\left(\frac{\varphi_a^2}{2}+\frac{\varphi_b^2}{2}\right)$ $+2[E_J\cos\left(\frac{\varphi_{ext}}{4}\right)+\frac{E_J^{shunt}}{4}]\varphi_c^2$ $-4E_J\cos\left(\frac{\varphi_{ext}}{4}\right)$
ring modes inductances	$L_{a,b}^{JRM}(\varphi_{ext}) = \frac{\varphi_0^2}{\frac{E_J^{shunt}}{2}+E_J\cos\left(\frac{\varphi_{ext}}{4}\right)}$
stability condition	n such that $L_c^{JRM}(\varphi_{ext}) = \frac{\varphi_0^2}{E_J^{shunt}+4E_J\cos\left(\frac{\varphi_{ext}}{4}\right)} > 0$
degeneracy	lifted degeneracy

Table 3: Summary of useful expressions for a shunted JRM.

For small phase differences the non-linear Hamiltonian of the ring can be expanded to the third order

$$\begin{aligned}\hat{H}_{JRM} = &- 4E_J \cos\frac{\varphi_{ext}}{4} + E_J \cos\frac{\varphi_{ext}}{4}\left(\frac{\varphi_a^2}{2} + \frac{\varphi_b^2}{2} + 2\varphi_c^2\right) \\ &- E_J\varphi_a\varphi_b\varphi_c \sin\frac{\varphi_{ext}}{4} \\ &+ \frac{1}{4}E_J^{shunt}(\varphi_a^2 + \varphi_b^2 + 2\varphi_c^2) + O(|\varphi|^4).\end{aligned} \tag{23}$$

The first term corresponds to the rest energy of the ring, the second to the inductive energy of the junctions, the last term to the energy of the shunt inductances. The particularity of the Josephson Ring is that the only third order term is the pure three-wave mixing term $\varphi_a\varphi_b\varphi_c$ that is at the origin of the parametric interaction. From here, fields are quantized by introduction of creation and annihilation operators of excitations in modes a, b, and c

$$\begin{cases}\Phi_a = \sqrt{\frac{\hbar Z_a}{2}}(\hat{a} + \hat{a}^\dagger) \\ \Phi_b = \sqrt{\frac{\hbar Z_b}{2}}(\hat{b} + \hat{b}^\dagger) \\ \Phi_c = \sqrt{\frac{\hbar Z_c}{2}}(\hat{c} + \hat{c}^\dagger),\end{cases} \tag{24}$$

where $Z_{a,b,c}$ are the mode impedances. At third order, the Hamiltonian of a Josephson Mixer can thus be written as

$$\frac{1}{\hbar}\hat{H} = \omega_a\hat{a}^\dagger\hat{a} + \omega_b\hat{b}^\dagger\hat{b} + \omega_c\hat{c}^\dagger\hat{c} + \chi(\hat{c}^\dagger + \hat{c})(\hat{a}^\dagger + \hat{a})(\hat{b}^\dagger + \hat{b}), \tag{25}$$

where we have defined the coupling term

$$\chi = \frac{1}{2\varphi_0 L_J}\xi_a\xi_b\xi_c\sqrt{\frac{\hbar}{2}Z_aZ_bZ_c}\sin\frac{\varphi_{ext}}{4} \tag{26}$$

and resonance frequencies $\omega_{a,b,c} = \sqrt{\frac{Z_{a,b,c}}{L^{tot}_{a,b,c}}}$. Natural modes frequencies are renormalized by the presence of ring junctions and the shunting junctions that modify the total inductance of the modes. The most frequently used expressions for shunted and unshunted JRM are summarized in Table 2 and Table 3.

2.2.2 *Amplification mode*

Josephson Mixer is commonly used as a quantum limited amplifer. This is done by applying a time-dependent drive of the amplitude $|p|$

on a common mode c in an off-resonant way. The Hamiltonian then becomes

$$\frac{1}{\hbar}\hat{H} = \omega_a \hat{a}^\dagger \hat{a} + \omega_b \hat{b}^\dagger \hat{b} + \chi(p^* + p)(\hat{a}^\dagger + \hat{a})(\hat{b}^\dagger + \hat{b}). \tag{27}$$

This driving field excites the circuit and provides energy for parametric processes. It is called a pump tone and can be treated classically in the stiff pump regime, which occurs when it is driven far from any resonance frequency.

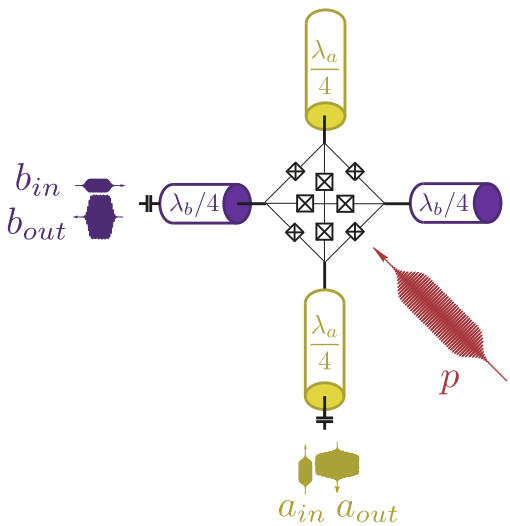

Figure 12: Schematic of the Josephson Mixer. Two $\lambda/2$ resonators a and b are coupled through a shunted JRM. A pump tone of the amplitude p is applied off-resonantly on the common mode c.

If the circuit is pumped at a frequency that is equal to the sum of the frequencies of the two oscillators, $\omega_p = \omega_a + \omega_b$, the rapidly oscillating terms in the interaction Hamiltonian can be neglected, so that it simplifies to the parametric down conversion or amplification Hamiltonian

$$\frac{1}{\hbar}\hat{H}_{amp} = \chi p_B(\hat{a}\hat{b} + \hat{a}^\dagger \hat{b}^\dagger), \tag{28}$$

where p_B is the real amplitude of the so called blue pump (the blue color evoking large frequencies in the visible electromagnetic spectrum). The interaction term $p_B \hat{a}^\dagger \hat{b}^\dagger$ describes the annihilation of one pump photon at frequency ω_p and simultaneous creation of a pair of

photons at frequencies ω_a and ω_b. It is this term that gives rise to parametric amplification and that enables the Josephson Mixer to be used for the readout of superconducting qubits with the measurement efficiency of order 1.

If this interaction is turned on with the two oscillators in the vacuum state, it results in a creation of quantum correlated radiation at frequencies ω_a and ω_b. The two outgoing modes are then prepared in a particular two-mode-squeezed state

$$|EPR\rangle = e^{ra^\dagger b^\dagger - r^* ab} |0,0\rangle = \frac{1}{\cosh(r)} \sum_k \tanh(r)^k |k,k\rangle , \quad (29)$$

where r is a squeezing parameter that satisfies

$$\cosh(r) = \sqrt{G} = \frac{\kappa_a \kappa_b + 4\chi^2 |p_B|^2}{\kappa_a \kappa_b - 4\chi^2 |p_B|^2}, \quad (30)$$

and $\sqrt{G}$ is the direct amplitude gain of the Josephson Mixer. This state was first introduced by Einstein, Podolsky and Rosen (EPR) in their original formulation of the nonlocality paradox [61]. They argued that, if Alice and Bob share this type of two-mode squeezed state, and Alice performs either a position or momentum measurement on her part of the state, she remotely prepares either a state with a certain position or one with a certain momentum at Bob's location, no matter how distant it is. It is what Einstein called "spooky action at a distance".

To quantify the parametric coupling strength between a and b parts, it is convenient to introduce a dimensionless variable such as cooperativity

$$C = \frac{4|\chi p_B|^2}{\kappa_a \kappa_b}. \quad (31)$$

The amplitude gain then reads

$$\sqrt{G} = \frac{1+C}{1-C}. \quad (32)$$

It diverges when $C \to 1$, which corresponds to the limit $\chi|p_B| \to \frac{\sqrt{\kappa_a \kappa_b}}{2}$ where the parametric down conversion rate exactly compensates the total dissipation of the resonator.

In order to characterize a Josephson Mixer, we begin by measuring the complex reflexion coefficient on the mode a

$$r_a[\omega] = \frac{\kappa_a - \kappa_a^{loss} + 2i(\omega - \omega_a)}{\kappa_a + \kappa_a^{loss} - 2i(\omega - \omega_a)} \tag{33}$$

while sweeping the external flux φ_{ext}. This enables us to determine the resonance frequency ω_a at a given flux, as well as the coupling κ_a of the mode a to the transmission line and the total internal losses κ_a^{loss}. We procede in the same way for the mode b. The flux tunability of the frequency is related to the inductance tunability through the participation ratio of the ring inductance in the total mode inductance

$$\omega_{a,b}(\varphi_{ext}) = \frac{1}{\sqrt{L_{a,b}^{tot}(\varphi_{ext})C_{a,b}}} \tag{34}$$

$$= \frac{1}{\sqrt{(L_{a,b} + L_{a,b}^{JRM}(\varphi_{ext}))C_{a,b}}}$$

$$= \frac{1}{\sqrt{(L_{a,b} + \xi_{a,b}L_{a,b}^{tot}(\varphi_{ext}))C_{a,b}}} \tag{35}$$

$$\approx \omega_{a,b}^{max}(1 - \frac{1}{2}\xi_{a,b}(\varphi_{ext}))$$

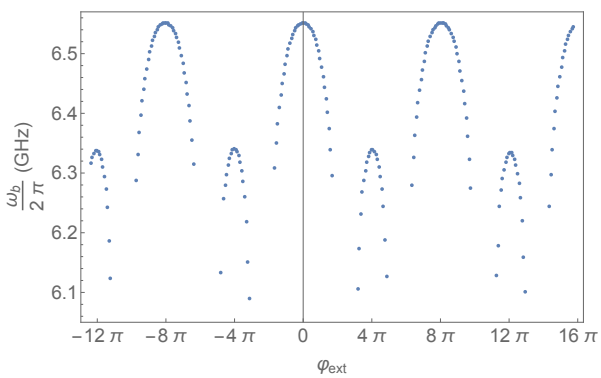

Figure 13: Measured resonance frequency dependence on the external flux for the mode b. The external flux is created by applying voltage V_{coil} on a coil in the proximity of the Josephson Mixer.

Flux dependence of the resonance frequency is shown in Fig. 13. Different arches correspond to different flux distributions between

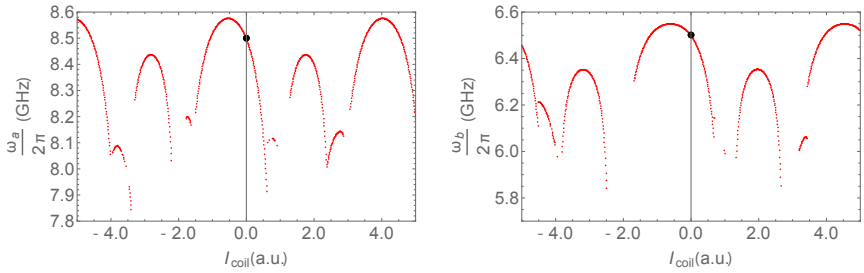

(a) (b)

Figure 14: Measured resonance frequency dependence on the external flux for the two modes a and b during the final cool-down. The third size of arches indicates that there was an asymetry between the subloops of the JRM during this meaurement run. The black point at zero applied voltage corresponds to the external flux at which the USC experiment was done. The resonance frequencies at this flux were $\omega_a = 2\pi \times 8.5$ GHz and $\omega_b = 2\pi \times 6.5$ GHz.

the four subloops. The big arches correspond to the symmetric flux distribution, where the fluxes are equally distributed between the subloops and all flow in the same direction. Smaller arches correspond to different broken symmetries, flux direction, flux amplitude etc. Due to the stability condition $L_c(\varphi_{ext}) > 0$, the symmetric configuration is stable for $-4\frac{E_J}{E_J^{shunt}}\cos\left(\frac{\varphi_{ext}}{4}\right) > 1$. The frequency of the shunted JRM can thus be tuned over a range of fluxes given [62] by

$$\varphi_{ext} \in [0, \varphi_{ext}^{crossover}] \tag{36}$$

where $\varphi_{ext}^{crossover}$ is given by $-4\frac{E_J}{E_J^{shunt}}\cos\left(\frac{\varphi_{ext}}{4}\right) = 1$. To maximize the three-wave mixing Hamiltonian, $-E_J \sin\left(\frac{\varphi_{ext}}{4}\right)\varphi_a\varphi_b\varphi_c$ and minimize the Kerr terms, we would like to set a magnetic field such that $\varphi_{ext} = 2\pi$. However, for the JRM used in this experiment, the ratio E_J/E_J^{shunt} was such that $\varphi_{ext}^{crossover} \simeq 2\pi$ and two flux configurations are metastable at this external flux point (see Fig. 14). Thus, we chose another flux point on the bigger arch that maximizes the gain.

From the phase dependence of the reflected signal we determined the resonance frequencies at this flux to be $\omega_a = 2\pi \times 8.5$ GHz and $\omega_b = 2\pi \times 6.5$ GHz, and the dissipation rates $\kappa_a = 2\pi \times 17.6$ MHz and $\kappa_b = 2\pi \times 21$ MHz. The ring of the Josephson Mixer used in this experiment can be seen in Fig. 15.

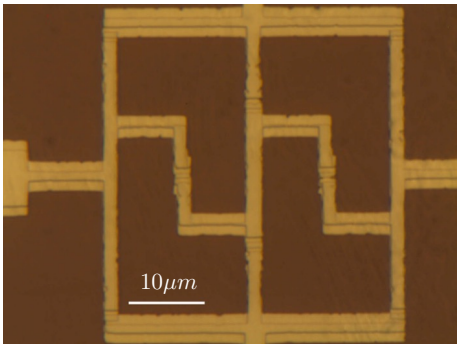

Figure 15: Optical microscope image of the JRM embeded in the Josephson Mixer used in the USC experiment. Four smaller Josephson junctions can be seen in the corners of the ring, and four bigger Josephson junctions are shunting the ring.

We measure the power spectral density of the outgoing mode with the pump tuned on and with the pump turned off. We subtract the later from the former in order to get rid of the noise added by the chain of amplifiers. Then in the added noise spectrum, we see that vacuum fluctuations are amplified at the resonance frequency of the mode ω_a, as shown in Fig. 17. The coupling $g_B = \chi|p_B|$ linearly increases with the pump amplitude until the onset of the parametric oscillation regime where more excitations are produced than the system can dissipate so that it begins to lase. The Josephson Mixer is used in this regime as a quantum limited amplifier of dynamical bandwidth

$$\gamma(G) \sim \frac{2\kappa_a\kappa_b}{\sqrt{G}(\kappa_a+\kappa_b)} = \frac{\gamma_0}{\sqrt{G}} \tag{37}$$

that is inversely proportional to the amplitude gain $\sqrt{G}$, at large gain.

For a given flux, the bandwidth gives the tunability of the amplifier. By detuning the pump frequency, we can amplify the signal within the bandwidth of the amplifier (see Fig. 16). If we further detune the pump, we realize an unexplored regime of off-resonant pumping that will be discussed in the following section, since it will be key to our simulation of USC.

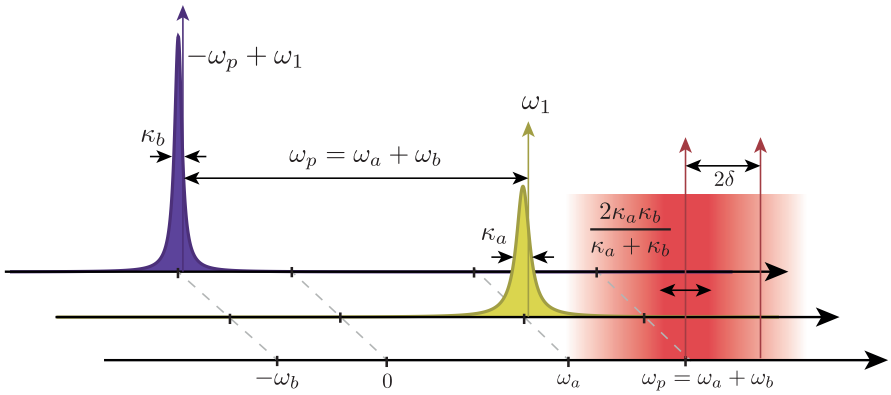

Figure 16: Pumping scheme in amplification mode. The two resonant modes a and b are represented by their Lorentzian response functions. The pump tone applied at the sum of their resonance frequencies provides the energy for the amplification process and determines the amplitude gain. The pump can be applied in the vicinity of $\omega_a + \omega_b$ given by $\gamma_0 = \frac{2\kappa_a\kappa_b}{\kappa_a+\kappa_b} \simeq \kappa_a$. A signal injected on the mode a at the frequency ω_1 will be amplified at that same frequency and converted to the mode b at the frequency $\omega_c - \omega_1$ within the amplifier bandwidth. If the pump is applied with a detuning $2\delta > 2\kappa$, we are in a non standard regime of off-resonant pumping.

2.2.3 *Off-resonant pumping*

Realization of the effective ultrastrong coupling requires a non standard way of pumping a Josephson Mixer, that is at a pump frequency detuned by 2δ, with $\delta > \kappa_a, \kappa_b$. In this section, we are going to study the dynamics of the system in this new regime.

As such a detuned pump tone oscillates at frequency $\omega_p = \omega_a + \omega_b + 2\delta$, when we neglect the rapidly oscillating terms, the Hamiltonian of Eq. (27) simplifies to

$$\frac{1}{\hbar}\hat{H} = \omega_a \hat{a}^\dagger \hat{a} + \omega_b \hat{b}^\dagger \hat{b} + \chi p_B (\hat{a}^\dagger \hat{b}^\dagger e^{-2i\delta t} + \hat{a}\hat{b} e^{2i\delta t}) \tag{38}$$

We can now define new annihilation operators that rotate at frequency δ with respect to $\hat{a}$ and $\hat{b}$

$$\begin{cases} \hat{a} \to \hat{a} e^{-i\delta t} \\ \hat{b} \to \hat{b} e^{-i\delta t} \end{cases}$$

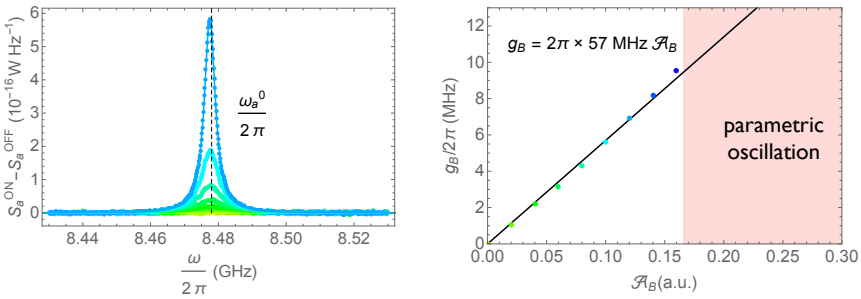

(a) (b)

Figure 17: (a) Added power spectral density of the mode a measured close to the resonance frequency ω_a for several values of the amplitude of the blue pump p_B (dots) and corresponding average emission rate calculated with input-output theory (line). Each color corresponds to an amplitude given in (b). (b) The parametric down conversion rate g_B determined from emission spectra linearly increases with pump amplitude p_B until the threshold of parametric oscillation.

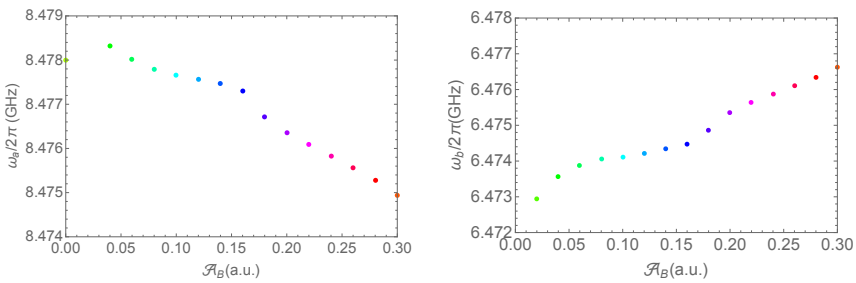

(a) (b)

Figure 18: (a) Resonance frequency of the mode a determined from the measured power spectral density as a function of the pump amplitude decreases owing to the Kerr effect. Red dots are in the parametric oscillation regime. (b) Resonance frequency of the mode b increases with pump amplitude. The color encoding for the pump amplitude is the same as in the Fig. 17.

so that in the reference frame rotating at $\omega_{a,b} + \delta$ the Hamiltonian becomes

$$\frac{1}{\hbar}\hat{H} = -\delta\hat{a}^\dagger\hat{a} - \delta\hat{b}^\dagger\hat{b} + g_B(\hat{a}^\dagger\hat{b}^\dagger + \hat{a}\hat{b}), \tag{39}$$

where we have defined $g_B = \chi p_B$ as the parametric down conversion coupling rate.

2.2.3.1 *Input - Output Theory*

In this section we will use the input-output formalism [63] first introduced by Gardiner and Collett in 1985 [64] to describe the dissipative dynamics of the intracavity fields under the atypical detuned blue pumping described in the previous section, and relate their evolution to the propagating input and output fields. By means of quantum Langevin equations, we take into account the coupling of the intracavity fields to the frequency dependent dissipation baths

$$\begin{cases} \frac{\partial a}{\partial t} = \frac{i}{\hbar}[H, a] - \frac{\kappa_a}{2}a + \sqrt{\kappa_a}a_{in} \\ \frac{\partial b}{\partial t} = \frac{i}{\hbar}[H, b] - \frac{\kappa_b}{2}b + \sqrt{\kappa_b}b_{in}, \end{cases} \tag{40}$$

which for the Hamiltonian 39 gives

$$\begin{cases} \frac{\partial a(t)}{\partial t} = i\delta a(t) - ig_B b(t)^\dagger - \frac{\kappa_a}{2}a(t) + \sqrt{\kappa_a}a_{in}(t) \\ \frac{\partial b(t)}{\partial t} = i\delta b(t) - ig_B a(t)^\dagger - \frac{\kappa_b}{2}b(t) + \sqrt{\kappa_b}b_{in}(t) \end{cases} \tag{41}$$

By the definition of a Fourier transform

$$\frac{1}{\sqrt{2\pi}}\int a(t)e^{-i\omega t}dt = a[\omega], \tag{42}$$

for the Fourier transform of a hermitian conjugate we have

$$\frac{1}{\sqrt{2\pi}}\int a(t)^\dagger e^{-i\omega t}dt = \frac{1}{\sqrt{2\pi}}\Big(\int a(t)e^{i\omega t}dt\Big)^\dagger = a[-\omega]^\dagger. \tag{43}$$

Fourier transforms of the Langevin equations are thus

$$\begin{cases} i\omega a[\omega] = i\delta a[\omega] - ig_B b[-\omega]^\dagger - \frac{\kappa_a}{2}a[\omega] + \sqrt{\kappa_a}a_{in}[\omega] \\ i\omega b[\omega] = i\delta b[\omega] - ig_B a[-\omega]^\dagger - \frac{\kappa_b}{2}b[\omega] + \sqrt{\kappa_b}b_{in}[\omega]. \end{cases} \tag{44}$$

By taking the hermitian conjugate of the second equation and then evaluating it at $-\omega$ we obtain

$$i\omega b[-\omega]^\dagger = -i\delta b[-\omega]^\dagger + ig_B a[\omega] - \frac{\kappa_b}{2}b[-\omega]^\dagger + \sqrt{\kappa_b}b_{in}[-\omega]^\dagger, \tag{45}$$

so that finally

$$b[-\omega]^\dagger = \frac{ig_B}{i(\omega+\delta)+\kappa_b/2}a[\omega] + \frac{\sqrt{\kappa_b}}{i(\omega+\delta)+\kappa_b/2}b_{in}[-\omega]^\dagger. \quad (46)$$

We can now inject this expression in the equation for a

$$a[\omega]\Big[i\omega - i\delta + \kappa_a/2 - \frac{g_B^2}{i\omega + i\delta + \kappa_b/2}\Big] = \frac{-ig_B\sqrt{\kappa_b}}{i\omega + i\delta + \kappa_b/2}b_{in}[-\omega]^\dagger + \sqrt{\kappa_a}a_{in}[\omega], \quad (47)$$

and finally we obtain

$$\begin{aligned} a[\omega] = &\frac{i(\omega+\delta)+\kappa_b/2}{(i(\omega-\delta)+\kappa_a/2)(i(\omega+\delta)+\kappa_b/2)-g_B^2}\sqrt{\kappa_a}a_{in}[\omega] \\ &+\frac{-ig_B\sqrt{\kappa_b}}{(i(\omega-\delta)+\kappa_a/2)(i(\omega+\delta)+\kappa_b/2)-g_B^2}b_{in}[-\omega]^\dagger. \end{aligned}$$

We can put this expression in a more compact form

$$a[\omega] = P[\omega]a_{in}[\omega] + Q[\omega]b_{in}[-\omega]^\dagger, \quad (48)$$

such that the amplitude of the outgoing mode can be written as

$$\begin{aligned} a_{out}[\omega] &= \sqrt{\kappa_a}a[\omega] - a_{in}[\omega] \quad (49) \\ &= (\sqrt{\kappa_a}P[\omega]-1)a_{in}[\omega] + \sqrt{\kappa_a}Q[\omega]b_{in}[-\omega]^\dagger. \quad (50) \end{aligned}$$

Input modes being in vacuum

$$\begin{aligned} &\langle a_{in}[\omega]^\dagger a_{in}[\omega']\rangle = 0 \\ &\langle b_{in}[-\omega]b_{in}[-\omega']^\dagger\rangle = \delta(\omega-\omega') \\ &\langle b_{in}[-\omega]a_{in}[\omega']\rangle = 0 \\ &\langle a_{in}[\omega]^\dagger b_{in}[-\omega']^\dagger\rangle = 0, \end{aligned}$$

we find for the mean number of photons in the outgoing mode

$$\begin{aligned} &\langle \hat{a}_{out}[\omega]^\dagger \hat{a}_{out}[\omega']\rangle = \kappa_a|Q[\omega]|^2\delta(\omega-\omega') \quad (51) \\ &= \frac{g_B^2\kappa_a\kappa_b}{[(\omega+\delta)\frac{\kappa_a}{2}+(\omega-\delta)\frac{\kappa_b}{2}]^2+[\frac{\kappa_a}{2}\frac{\kappa_b}{2}-g_B^2+(\delta^2-\omega^2)]^2}\delta(\omega-\omega') \end{aligned}$$

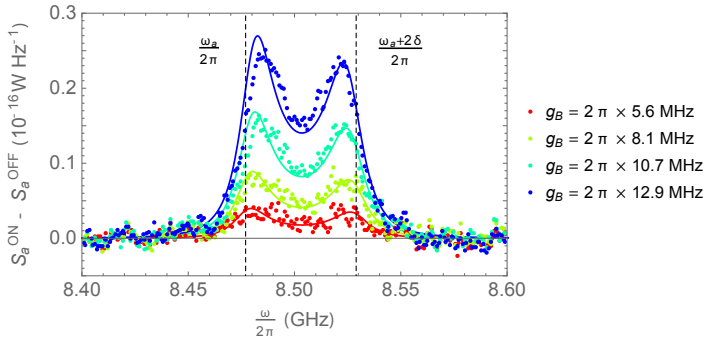

Figure 19: Measured power spectral density for the outgoing mode a for the detuned blue pump (points) and mean number of photons calculated from the Eq. (52) (line), with corresponding coupling g_B. There are two Loretzian peaks at ω_a and $\omega_a + 2\delta$, with $\delta = 2\pi \times 26$ MHz. These frequencies correspond to $-\delta$ and δ in the simulation frame rotating at $\omega_a + \delta$. Note that one peak is higher than the other one because $\kappa_a < \kappa_b$.

Indeed the spectral noise density measured by a spectrum analyzer at room temperature corresponds to the output noise $\mathrm{Var}(a_{out}) = \frac{1}{2}\langle \hat{a}^\dagger_{out}\hat{a}_{out} + \hat{a}_{out}\hat{a}^\dagger_{out}\rangle$ which is linearly amplified by the chain of amplifiers at the output line with a gain G_{chain} and with extra noise S_{chain}. When the pump is turned on, power spectral density reads

$$S^{ON}_{a_{out}}[\omega] = G_{chain}\,\hbar\omega_a \frac{1}{2}\langle \hat{a}^\dagger_{out}\hat{a}_{out} + \hat{a}_{out}\hat{a}^\dagger_{out}\rangle + S_{chain} \tag{52}$$

$$= G_{chain}\,\hbar\omega_a \langle \hat{a}^\dagger_{out}\hat{a}_{out}\rangle + S_{vac} + S_{chain} \tag{53}$$

where S_{vac} is the power spectral density of a vaccum state. When the pump is turned off

$$S^{OFF}_{a_{out}}[\omega] = S_{vac} + S_{chain} \tag{54}$$

so that the added power spectral density gives the emitted number of photons amplified by the gain of the chain of amplifiers

$$S^{ON}_{a_{out}}[\omega] - S^{OFF}_{a_{out}}[\omega] = G_{chain}\,\hbar\omega_a \langle \hat{a}^\dagger_{out}\hat{a}_{out}\rangle. \tag{55}$$

We see from Eq. (52) that the emission spectrum qualitatively changes drastically, compared to the pumping within the bandwidth

(Fig. 17). There are two Lorentzian peaks centered at ω_a and $\omega_a + 2\delta$ effectively corresponding to $\pm\delta$ in a reference frame rotating at $\omega_a + \delta$, as can be seen Fig. 19. We use this expression to determine the parameter g_B from the measured power spectra. The theory agrees with the measured noise raise and enables us to link the pump amplitude p_B and the corresponding parametric down conversion rate g_B.

Furthermore, with a finite detuning of the pump frequency, the self-oscillation threshold is displaced to higher pump powers. This enables us to reach the higher g_B regimes, that is not accessible at zero detuning because they were beyond the onset of the parametric oscillation (see Fig. 20).

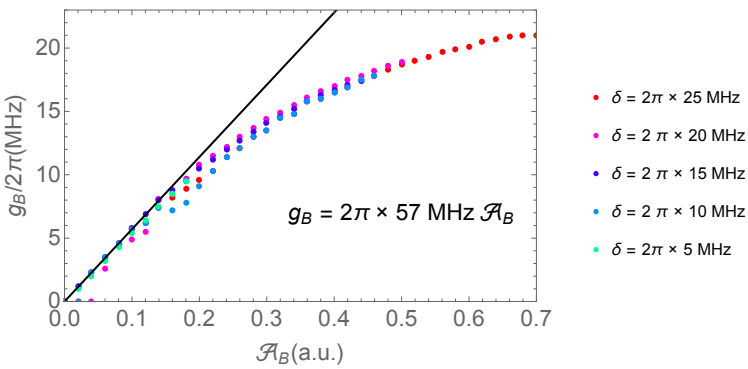

Figure 20: Coupling rate g_B for different pump detunings $\delta/2\pi$ going from 0 to 25 MHz. For high applied pump amplitudes $\mathcal{A}_B$, the coupling diverges from the expected linear dependence in amplitude, though we have checked that the input power is linearly proportional to the square of this requested amplitude.

2.2.4 *Off-resonant amplification*

In the previous section, we have seen how the emission spectrum of the Josephson Mixer changes in the off-resonant pumping regime. There was no signal injected in the circuit, and the energy brought by the pump was used to amplify the vacuum fluctuations. In this section, we are going to see how the amplification and gain characteristcs of the Josephson Mixer change when the pump is detuned, while a finite signal is injected into the mode a.

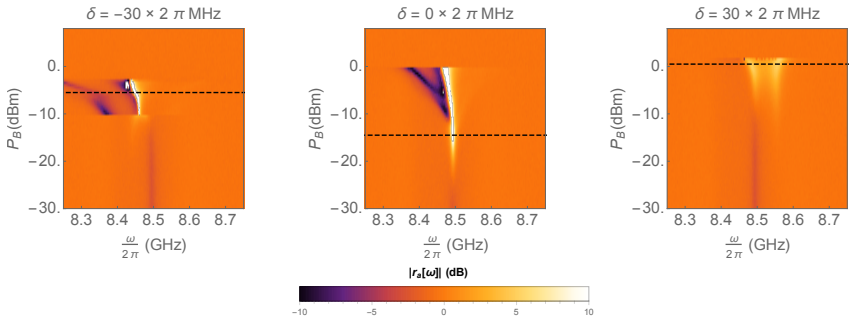

Figure 21: Reflection coefficient $|r_a[\omega]|$ measured with a Vector Network Analyzer (VNA) around the resonance frequency ω_a as a function of the applied pump power P_B, for different detunings δ. For $\delta = 0$, there is one peak at ω_a. The resonance frequency decreases at high powers due to the Kerr effect. For finite detuning δ, there are two peaks at ω_a and $\omega_a + 2\delta$.

From the expression (50) that we found for the outgoing mode $a_{out}[\omega]$ with the input-output theory, we can write the reflection coefficient

$$\begin{aligned} r_a[\omega] &= \frac{a_{out}[\omega]}{a_{in}[\omega]} = \sqrt{\kappa_a} P[\omega] - 1 \\ &= \frac{[i(\omega+\delta) + \frac{\kappa_b}{2}][i(\omega-\delta) + \frac{\kappa_a}{2}] + g_B^2}{[i(\omega+\delta) + \frac{\kappa_b}{2}][-i(\omega-\delta) + \frac{\kappa_a}{2}] - g_B^2} \end{aligned} \tag{56}$$

Note that this expression is valid in the reference frame rotating at $\omega_a + \delta$. To describe the reflection coefficient measured in the laboratory frame, the transformation $\omega \to \omega - \omega_a - \delta$ has to be done such that

$$r_a[\omega] = \frac{[i(\omega-\omega_a) + \frac{\kappa_b}{2}][i(\omega-\omega_a-2\delta) + \frac{\kappa_a}{2}] + g_B^2}{[i(\omega-\omega_a) + \frac{\kappa_b}{2}][-i(\omega-\omega_a-2\delta) + \frac{\kappa_a}{2}] - g_B^2} \tag{57}$$

In Fig. 22c, we see that this gain can be reached for detuning δ going from -50 to 50 MHz which corresponds to a pump frequency in the range of 200 MHz. This result is compared to the gain predicted from the input-output theory in Fig. 22d. The smallest pump power needs to be applied for zero detuning. There is an asymmetry for $\pm\delta$ that is not reproduced by theory (see Fig. 21). The onset of parametric oscillation is at lower powers for negative detunings, wich prevents reaching higher gains at negative detunings. This can be seen in Fig. 23.

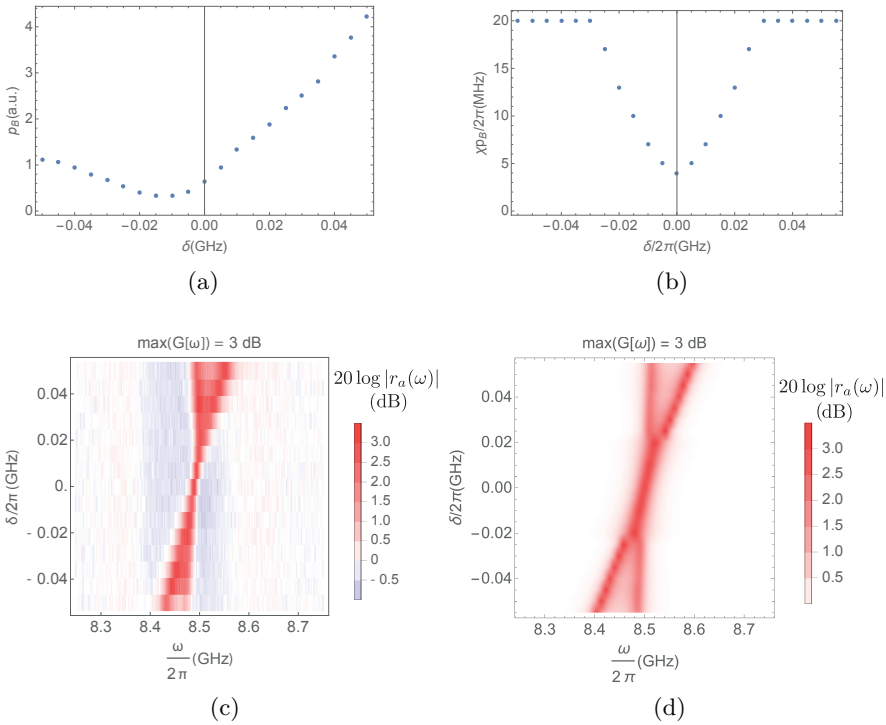

Figure 22: (a) Pump amplitude needed to obtain the gain of 3 dB, as a function of pump frequency. (b) $g_B = \chi p_B$ needed for $\max(G[\omega]) = 3$ dB. (c) Measured gain as a function of signal frequency $f_a = \frac{\omega_a}{2\pi}$ and pump detuning δ. For every detuning, the pump amplitude p_B is tuned so that the maximum gain $\max(G[\omega]) = 3$ dB. For detuning $\delta < \kappa$, there is one peak at $\omega = \omega_a$. For $\delta > \kappa$, there are two discernable peaks at ω_a and $\omega_a + 2\delta$. Detuning δ can take both positive and negative values. (d) Expected gain $G(\omega)$ from the input-output theory, such that the maximum gain for that power is 3 dB.

This function has maxima at ω_a and $\omega_a + 2\delta$. We use a vector network analyzer (VNA) to measure $|r_a[\omega]|$ around ω_a and deduce the gain $G[\omega]$ at frequency ω, given by $\sqrt{G[\omega]} = |r_a[\omega]|^{ON}/|r_a[\omega]|^{OFF}$. The pump frequency is set to $f_B = f_a + f_b + 2\delta$ and detuning $\delta/2\pi$ is varied from -50 MHz to 50 MHz. For each detuning, the applied pump power is swept from -30 dBm to 10 dBm. Gain as a function of the pump power is shown in Fig. 21 for $\delta/2\pi = -30$ MHz, 0 and 30 MHz. The pump power that gives the maximum gain $\max(G[\omega]) = 3$

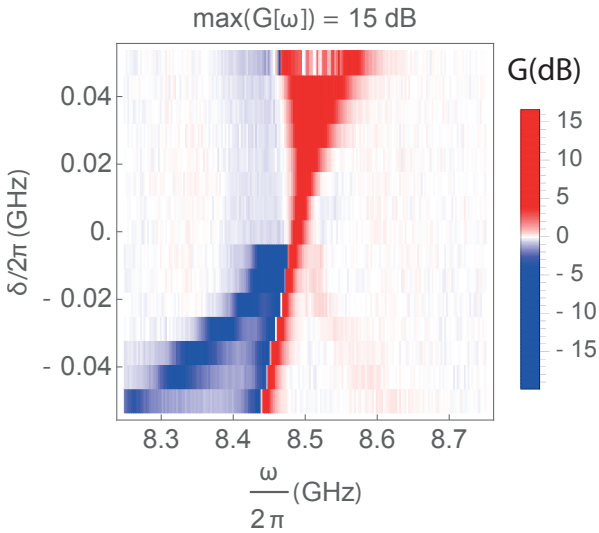

Figure 23: Measured gain in dB as a function of signal frequency $f_a = \frac{\omega_a}{2\pi}$ and pump detuning δ. For every detuning, the pump amplitude p_B is tuned so that the maximum gain $\max(G[\omega]) = 15$ dB. For detuning $\delta < \kappa$, there is one peak at $\omega = \omega_a$. For $\delta > \kappa$, there are two discernable peaks at ω_a and $\omega_a + 2\delta$.

dBm is indicated by a dashed black line. The abrupt gain extinction corresponds to an instable regime that will be discussed in the next chapter.

Furthermore, we can determine the parameter g_B by matching the expectation from Eq. 57 to the measured complex reflection coefficient Fig. 21. Coupling rate g_B for different pump detunings δ is shown in Fig. 24.

2.2.5 *Two tone pumping*

We describe here the main technique we proposed in Ref. [65] to realise an analog simulation of the ultrastrong coupling between two bosonic modes. We simultaneously apply two pumps, a detuned "blue" amplification pump at $\omega_B = \omega_a + \omega_b + 2\delta$ and a "red" conversion pump at $\omega_R = \omega_a - \omega_b$. The Hamiltonian now reads

$$\frac{1}{\hbar}\hat{H} = \omega_a \hat{a}^\dagger \hat{a} + \omega_b \hat{b}^\dagger \hat{b} + \hat{H}_{int}, \tag{58}$$

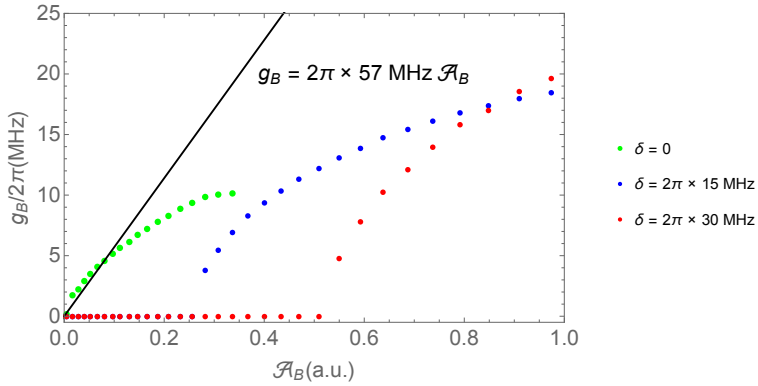

Figure 24: Coupling rate g_B extracted from the reflection coefficient measurements for different pump detunings $\delta/2\pi = 0$, 15 and 30 MHz. For finite detunings, at small applied pump amplitudes there is no gain, so g_B is found to be zero. As in Fig. 20, g_B is linear in pump amplitude until the onset of parametric oscillation.

with

$$\frac{1}{\hbar}\hat{H}_{int} = \chi(p_B^* + p_B)(\hat{a}^\dagger + \hat{a})(\hat{b}^\dagger + \hat{b}) + \chi(p_R^* + p_R)(\hat{a}^\dagger + \hat{a})(\hat{b}^\dagger + \hat{b}). \tag{59}$$

$\hat{H}_{int}$ can be simplified in the RWA by neglecting the fast oscillating terms. We find

$$\frac{1}{\hbar}\hat{H}_{int} = \chi p_B(\hat{a}^\dagger\hat{b}^\dagger e^{-2i\delta} + \hat{a}\hat{b}e^{2i\delta}) + \chi p_R(\hat{a}\hat{b}^\dagger + \hat{a}^\dagger\hat{b}). \tag{60}$$

Now by tuning the coupling of the two pumps to be equal, $\chi p_R = \chi p_B = g$, in a frame rotating at $\omega_{a,b} + \delta$, we obtain the Hamiltonian of two effective modes with resonance frequencies $-\delta$ coupled at a rate g

$$\boxed{\frac{1}{\hbar}\hat{H}_{\text{eff}} = -\delta\hat{a}^\dagger\hat{a} - \delta\hat{b}^\dagger\hat{b} + g(\hat{a}^\dagger + \hat{a})(\hat{b}^\dagger + \hat{b}).} \tag{61}$$

Since δ can be chosen arbitrarily, it is possible to reach a regime where $\kappa < g < \delta$. The two modes are then in the **ultrastrong coupling regime**. Our approach is therefore similar to the analog quantum simulation of ultra strong coupling between a two level system and a resonator [20]. By applying a set of pump tones we create

two effective modes whose frequencies are smaller than the genuine coupling rate g.

Furthermore, this configuration offers the proper level of control on the coupling strength through the pump amplitude, which enables us to study the transition from strong to ultrastrong coupling.

2.2.5.1 *Kerr effect*

The effective USC Hamiltonian Eq. (61) in a rotating frame has been derived from a three wave mixing Hamiltonian in the laboratory frame. However, the fourth order non-linear terms that were neglected in the expansion of the JRM Hamiltonian Eq. (21) give rise to a Kerr effect that shifts the modes resonances. The additional Kerr term reads

$$\begin{aligned}\frac{1}{\hbar}H_{Kerr} &= K_{aa}(a^\dagger)^2a^2 + K_{bb}(b^\dagger)^2b^2 + K_{ab}a^\dagger a b^\dagger b \\ &+ K_{ap}(p_B + p_B^* + p_R + p_R^*)^2(a + a^\dagger)^2 \qquad (62)\\ &+ K_{bp}(p_B + p_B^* + p_R + p_R^*)^2(b + b^\dagger)^2 \qquad (63)\end{aligned}$$

where

$$\begin{aligned}K_{aa} &= -\frac{1}{256}\xi_a^5\omega_a\frac{Z_a}{Z_Q}\frac{L_{JRM}(\varphi_{ext})}{L_J(\varphi_{ext})} \qquad (64)\\ K_{bb} &= -\frac{1}{256}\xi_b^5\omega_b\frac{Z_b}{Z_Q}\frac{L_{JRM}(\varphi_{ext})}{L_J(\varphi_{ext})}\\ K_{ap} &= -\frac{1}{64}\omega_a\xi_a\frac{|\varphi_p|^2}{|p_B|^2}\frac{L_{JRM}(\varphi_{ext})}{L_J(\varphi_{ext})}\\ K_{bp} &= -\frac{1}{64}\omega_b\xi_b\frac{|\varphi_p|^2}{|p_B|^2}\frac{L_{JRM}(\varphi_{ext})}{L_J(\varphi_{ext})}\end{aligned}$$

The complete derivation of these expressions can be found in the thesis of Emmanuel Flurin [60].

If we keep only the non-oscillating terms in the RWA we obtain

$$\begin{aligned}\frac{1}{\hbar}H_{Kerr} &= K_{aa}(a^\dagger)^2a^2 + K_{bb}(b^\dagger)^2b^2 + K_{ab}a^\dagger a b^\dagger b\\ &+ K_{ap}(2|p_B|^2a^\dagger a + 2|p_R|^2a^\dagger a + p_Rp_Ba^\dagger a^\dagger + p_R^*p_B^*aa)\\ &+ K_{bp}(2|p_B|^2b^\dagger b + 2|p_R|^2b^\dagger b + p_Rp_B^*bb + p_R^*p_Bb^\dagger b^\dagger)\end{aligned}$$

In the following section, we will add the Kerr nonlinearity into our input-output theory model in order to take into account the frequency shift that emerges from it at high pump powers.

2.2.5.2 *Input-Output Theory with Kerr terms*

The self-Kerr terms K_{aa} and K_{bb} are much weaker than the cross-Kerr terms and can thus be neglected. The one-color pump terms only renormalize the resonance frequencies of the modes

$$\begin{aligned}\frac{1}{\hbar}H = &[-\delta + 2K_{ap}(|p_B|^2 + |p_R|^2)]a^\dagger a + [-\delta + 2K_{bp}(|p_B|^2 + |p_R|^2)]b^\dagger b \\ &+ g_B(ab + a^\dagger b^\dagger) + g_R(ab^\dagger + a^\dagger b) \\ &+ K_{ap}(p_R p_B a^\dagger a^\dagger + p_R^* p_B^* aa) + K_{bp}(p_R p_B^* bb + p_R^* p_B b^\dagger b^\dagger)\end{aligned} \tag{65}$$

So by defining

$$\begin{cases}\delta(|p_B|, |p_R|) = \delta - 2K_{ap}(|p_B|^2 + |p_R|^2) \to \delta_a \\ \delta(|p_B|, |p_R|) = \delta - 2K_{bp}(|p_B|^2 + |p_R|^2) \to \delta_b\end{cases} \tag{66}$$

we can write

$$\begin{aligned}\frac{1}{\hbar}H = &-\delta_a a^\dagger a - \delta_b b^\dagger b + g_B(ab + a^\dagger b^\dagger) + g_R(ab^\dagger + a^\dagger b) \\ &+ K_{ap}(p_R p_B a^\dagger a^\dagger + p_R^* p_B^* aa) + K_{bp}(p_R p_B^* bb + p_R^* p_B b^\dagger b^\dagger)\end{aligned}$$

We can then write the quantum Langevin equations in frequency domain

$$\begin{cases}(i\omega - i\delta_a + \frac{\kappa_a}{2})a[\omega] = -ig_B b[-\omega]^\dagger - ig_R b[\omega] - iK_{ap}p_R p_B a[-\omega]^\dagger + \sqrt{\kappa_a}a_{in}[\omega] \\ (i\omega - i\delta_b + \frac{\kappa_b}{2})b[\omega] = -ig_B a[-\omega]^\dagger - ig_R a[\omega] - iK_{bp}p_R^* p_B b[-\omega]^\dagger + \sqrt{\kappa_b}b_{in}[\omega]\end{cases} \tag{67}$$

whose hermitian conjugates evaluated at $-\omega$ are

$$\begin{cases}(i\omega + i\delta_a + \frac{\kappa_a}{2})a[-\omega]^\dagger = ig_B b[\omega] + ig_R b[-\omega]^\dagger + iK_{ap}p_R^* p_B^* a[\omega] + \sqrt{\kappa_a}a_{in}[-\omega]^\dagger \\ (i\omega + i\delta_b + \frac{\kappa_b}{2})b[-\omega]^\dagger = ig_B a[\omega] + ig_R a[-\omega]^\dagger + iK_{bp}p_R p_B^* b[\omega] + \sqrt{\kappa_b}b_{in}[-\omega]^\dagger\end{cases} \tag{68}$$

We can write this system in a matrix form

$$M\begin{pmatrix}a[\omega] \\ b[\omega] \\ a[-\omega]^\dagger \\ b[-\omega]^\dagger\end{pmatrix} = D\begin{pmatrix}a_{in}[\omega] \\ b_{in}[\omega] \\ a_{in}[-\omega]^\dagger \\ b_{in}[-\omega]^\dagger\end{pmatrix}$$

with

$$M = \begin{pmatrix} i(\omega-\delta_a)+\frac{\kappa_a}{2} & ig_R & iK_{ap}p_Rp_B & ig_B \\ ig_R & i(\omega-\delta_b)+\frac{\kappa_b}{2} & ig_B & iK_{bp}p_R^*p_B \\ -iK_{ap}p_R^*p_B^* & -ig_B & i(\omega+\delta_a)+\frac{\kappa_a}{2} & -ig_R \\ -ig_B & -iK_{bp}p_Rp_B^* & -ig_R & i(\omega+\delta_b)+\frac{\kappa_b}{2} \end{pmatrix} \tag{69}$$

and

$$D = \begin{pmatrix} \sqrt{\kappa_a} & 0 & 0 & 0 \\ 0 & \sqrt{\kappa_b} & 0 & 0 \\ 0 & 0 & \sqrt{\kappa_a} & 0 \\ 0 & 0 & 0 & \sqrt{\kappa_b} \end{pmatrix} \tag{70}$$

We then use a numerical solver to calculate the inverse of the matrix M so that the solution is given by $F = M^{-1}D$, whose elements $f_{i,j}$ give us the desired expression for a

$$a[\omega] = f_{11}a_{in}[\omega] + f_{12}b_{in}[\omega] + f_{13}a_{in}[-\omega]^\dagger + f_{14}b_{in}[-\omega]^\dagger \tag{71}$$

Finally the average rate of photons emitted from the mode a is

$$\begin{aligned} \langle a_{out}^\dagger[\omega]a_{out}[\omega']\rangle &= \kappa_a\langle a[\omega]^\dagger a[\omega']\rangle \\ &= \kappa_a(|f_{13}|^2\langle a_{in}[-\omega]a_{in}[-\omega']^\dagger\rangle + |f_{14}|^2\langle b_{in}[-\omega]b_{in}[-\omega']^\dagger\rangle) \\ &= \kappa_a(|f_{13}|^2+|f_{14}|^2)\delta(\omega-\omega') \end{aligned} \tag{72}$$

We have checked that these relations satisfy commutation relation $[a_{out}^\dagger[\omega], a_{out}[\omega']] = \delta(\omega-\omega')$.

2.3 GROUND STATE IN USC

In this section we look into different signature properties of the ground state of two ultrastrongly coupled bosonic modes.

2.3.1 *Two mode squeezing*

One of the peculiarities of a pair of ultrastrongly coupled bosonic modes is that its ground state is a two-mode squeezed state. To

demonstrate this, we can rewrite the Hamiltonian of two genuinely ultrastrongly coupled bosonic modes (Eq. (11)) in terms of two collective modes operators $\hat{m} = \frac{1}{\sqrt{2}}(\hat{a} + \hat{b})$ and $\hat{n} = \frac{1}{\sqrt{2}}(\hat{a} - \hat{b})$

$$\frac{1}{\hbar}\hat{H} = (\omega + g)\hat{m}^\dagger\hat{m} + (\omega - g)\hat{n}^\dagger\hat{n} + \frac{g}{2}((\hat{m}^\dagger)^2 + \hat{m}^2) - \frac{g}{2}((\hat{n}^\dagger)^2 + \hat{n}^2), \tag{73}$$

where we have considered the case of two degenerate modes such that $\omega_a = \omega_b = \omega$. The unitary time evolution generated by this interaction Hamiltonian is

$$\hat{U}(t) = e^{-\frac{i}{\hbar}\hat{H}_{int}t} = e^{-i\frac{g}{2}[(\hat{m}^\dagger)^2 + \hat{m}^2 - (\hat{n}^\dagger)^2 - \hat{n}^2]t} \tag{74}$$

Setting $-\frac{igt}{2} = \zeta = re^{i\phi}$, where ζ is the complex squeezing parameter and r and ϕ are real numbers. This evolution is equivalent to the squeezing operator

$$\hat{S}(\zeta) = e^{\zeta\hat{m}^2 - \zeta^*(\hat{m}^\dagger)^2}e^{-\zeta\hat{n}^2 + \zeta^*(\hat{n}^\dagger)^2} \tag{75}$$

In the Heisenberg picture, the time evolution of $\hat{m}$ and $\hat{m}^\dagger$ is given by

$$\begin{cases} \dot{\hat{m}} = \frac{i}{\hbar}[\hat{H}, \hat{m}] = i[\frac{g}{2}(\hat{m}^\dagger)^2, \hat{m}] = ig\hat{m}^\dagger = \zeta\hat{m}^\dagger \\ \dot{\hat{m}}^\dagger = \frac{i}{\hbar}[\hat{H}, \hat{m}^\dagger] = \zeta\hat{m} \end{cases} \tag{76}$$

The evolution of the field quadrature observables $\hat{X}_m = \frac{\hat{m} + \hat{m}^\dagger}{\sqrt{2}}$ and $\hat{P}_m = \frac{\hat{n} - \hat{m}^\dagger}{\sqrt{2}i}$ is thus

$$\begin{cases} \dot{\hat{X}}_m = \zeta\hat{X}_m \\ \dot{\hat{P}}_m = -\zeta\hat{P}_m \end{cases} \tag{77}$$

such that

$$\begin{cases} \hat{X}_m(t) = \hat{X}_m(0)e^{\zeta t} \\ \hat{P}_m(t) = \hat{P}_m(0)e^{-\zeta t} \end{cases} \tag{78}$$

and similarily

$$\begin{cases} \hat{X}_n(t) = \hat{X}_n(0)e^{-\zeta t} \\ \hat{P}_n(t) = \hat{P}_n(0)e^{\zeta t} \end{cases} \tag{79}$$

which finally implies

$$\begin{cases} \langle X_m^2 \rangle = \langle P_n^2 \rangle = \frac{R^2}{2} \\ \langle P_m^2 \rangle = \langle X_n^2 \rangle = \frac{1}{2R^2}, \end{cases} \tag{80}$$

where $R = e^r$. Thus for $R > 1$ the mode m is momentum squeezed and position anti-squeezed, and the opposite for mode n. Indeed, the standard deviations for the two field quadratures obey the Heisenberg uncertainty relation $\langle X^2 \rangle \langle P^2 \rangle = \frac{1}{4}$, while at the same time one of the quadratures' standard deviation is smaller than that of the vacuum, $\langle X^2 \rangle_{vac} = \langle P^2 \rangle_{vac} = \frac{1}{2}$ and the other one necessarily bigger.

As modes m and n are hybrid, $\hat{X}_n = \frac{\hat{X}_a - \hat{X}_b}{\sqrt{2}}$ and $\hat{P}_n = \frac{\hat{P}_a + \hat{P}_b}{\sqrt{2}}$, their squeezing corresponds to a two-mode relative position squeezing and total momentum anti-squeezing in the original basis. In general, the two-mode squeezed vacuum does not imply squeezing in each individual mode. On the contrary

$$\langle X_a^2 \rangle = \frac{\langle X_m^2 + X_n^2 \rangle}{2} = \frac{1}{2}\Big[\frac{1}{2R^2} + \frac{R^2}{2}\Big] = \frac{1 + R^4}{4R^2}, \tag{81}$$

which means that $\langle X_a^2 \rangle > \frac{1}{2}$ for any $R \neq 1$. Indeed, the uncertainty of individual quadratures increases compared to vacuum, while that of the difference of position observables as well as the sum of momentum observables decreases. In the next section, we will see that in the case of USC ground state, the situation is different.

2.3.2 *Single mode squeezing*

Another signature of the ultrastrong coupling is the presence of single mode squeezing in the output radiation fields of both modes. We can see this by identifying the two eigenmodes of the system, which are called polaritons in the case of a genuine light-matter interaction. The annihilation operators $\hat{p}_1$ and $\hat{p}_2$ of the two eigenmodes, defined as $\hat{p}_1 |GS\rangle = \hat{p}_2 |GS\rangle = 0$, can be expressed as linear combinations of the original operators $\hat{a}, \hat{a}^\dagger$ and $\hat{b}, \hat{b}^\dagger$

$$\hat{p}_{1,2} = t_{1,2}\hat{a} + u_{1,2}\hat{b} + v_{1,2}\hat{a}^\dagger + w_{1,2}\hat{b}^\dagger, \tag{82}$$

where the coefficients $t_{1,2}, u_{1,2}, v_{1,2}$ and $w_{1,2}$ are obtained by diagonalizing the Hopfield matrix [66] for the Hamiltonian of Eq.(11). These coefficients are

$$\vec{p}_1 = \frac{1}{\sqrt{N_1}} \begin{pmatrix} \frac{\sqrt{(\delta-2g)\delta}+\delta}{g} - 1 \\ -\frac{\sqrt{(\delta-2g)\delta}+\delta}{g} + 1 \\ -1 \\ 1 \end{pmatrix} \tag{83}$$

and

$$\vec{p}_2 = \frac{1}{\sqrt{N_2}} \begin{pmatrix} \frac{\sqrt{(\delta+2g)\delta}+\delta}{g} + 1 \\ -\frac{\sqrt{(\delta+2g)\delta}+\delta}{g} + 1 \\ 1 \\ 1 \end{pmatrix} \tag{84}$$

with eigenvalues

$$\omega_{1,2} = \sqrt{(\delta \pm g)\delta}. \tag{85}$$

$N_{1,2}$ are the normalization coefficients, such that the condition $|t_{1,2}|^2 + |u_{1,2}|^2 - |v_{1,2}|^2 - |w_{1,2}|^2 = 1$ is satisfied, imposed by the commutation relation for bosonic operators. The expressions of eigenmode operators and eigenvalues determine validity of our model, that treats the nonlinear Hamiltonian up to the third order. As a matter of fact, from Eqs. (83) and (85), it can be seen that for the coupling rate larger than half of the effective mode frequency, $g > \delta/2$, the model is not valid anymore. This limit has also been demonstrated and discussed in the section 2.1.3 in analogy with mechanical resonators.

The Gaussian ground state $|GS\rangle$ is fully caracterized by the covariance matrix $\mathcal{V} = \{\langle x_i x_j + x_j x_i\rangle_{|GS\rangle} - \langle x_i\rangle_{|GS\rangle}\langle x_j\rangle_{|GS\rangle}\}$ in the basis $\{x_1, x_2, x_3, x_4\} = \{\hat{X}_a, \hat{P}_a, \hat{X}_b, \hat{P}_b\}$ and noise properties of the original modes a and b in the ground state are given by the elements of the covariance matrix.

2.3.3 *Revealing the ground state correlations*

Nevertheless, experimentally evidencing the nature of the ground state is not straightforward. While the ground state of an ultra-

strongly coupled system is populated with correlated pairs of photons, these excitations are virtual and cannot escape from the cavity. Indeed, owing to the energy conservation requirements, for an input field in the vacuum state, the output is always in the vacuum state as well and no radiation is emitted [67].

As a matter of fact, for genuine USC, the outgoing fields are related to incoming fields by a symplectic matrix U

$$\begin{pmatrix} a_{out}[\omega] \\ a_{out}[-\omega]^\dagger \\ b_{out}[\omega] \\ b_{out}[-\omega]^\dagger \end{pmatrix} = U \begin{pmatrix} a_{in}[\omega] \\ a_{in}[-\omega]^\dagger \\ b_{in}[\omega] \\ b_{in}[-\omega]^\dagger \end{pmatrix}.$$

As all the real excitations of the considered baths have by definition positive frequency, for $\omega > 0$, the outgoing modes simplify to

$$a_{out}[\omega > 0] = u_{11} a_{in}[\omega] + u_{13} b_{in}[\omega] \tag{86}$$

and

$$b_{out}[\omega > 0] = u_{31} a_{in}[\omega] + u_{33} b_{in}[\omega] \tag{87}$$

If both input states are vacuum, then the output is necessarily vacuum too, because

$$a_{in} |0\rangle = b_{in} |0\rangle = 0. \tag{88}$$

It has been theoretically shown that an ancilla two-level system can be coupled to a bosonic mode ultrastrongly coupled to a bath of two-level systems, such that its Lamb shift can be used to probe the exotic ground state in a non-destructive manner [68]. However, in order to release the bound photons into extra-cavity radiation that can be experimentally observed, one possible solution is to modulate in time the coupling rate g between the two modes in a nonadiabatic way [69]. When the interaction is abruptly switched-off, the energy contained in the virtual excitations of the ground state is released in the form of real excitations, until the system relaxes into its new ground state, the vacuum state. This situation is illustrated in Fig. 25a.

This fast-modulation method is analogous to the dynamical Casimir effect [70], where, if an artificial mirror moves at speed v that is not

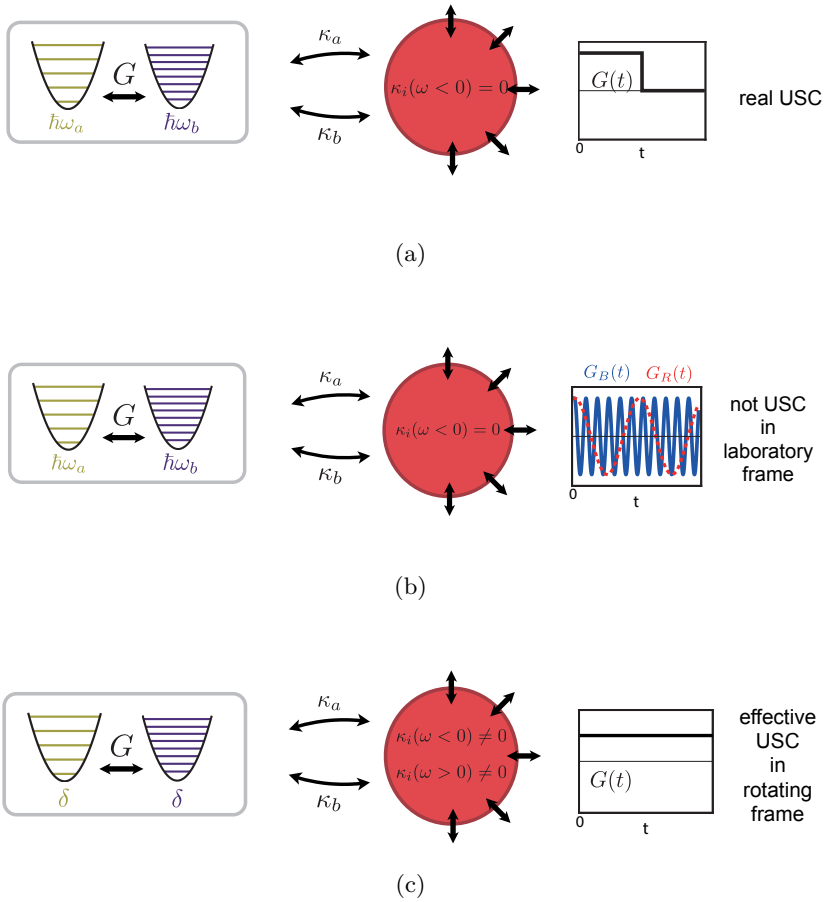

Figure 25: Schemes of three models describing two interacting bosonic modes that are coupled to an environment, in which a squeezed field is emitted. (a) In the case of genuine USC, the coupling needs to be abruptly swiched-off in order to release the ground field virtual excitations. (b) In the laboratory frame, coupling rate is time modulated. (c) In the rotating frame of the simulation, coupling is constant, but the dissipation rate is non-zero even at negative frequencies.

negligible compared to the effective speed of light c, the field cannot adjust smoothly and can be non-adiabatically excited out of the vacuum. Vacuum fluctuations induce screening currents in mirrors that emit electromagnetic radiation consisting of real excitations.

The key is thus in the ultra-fast time modulation which is not easy to realize experimentally. Furthermore, in physical implementations of light-matter coupling, measuring the corresponding correlations between the two output channels of both bosonic modes seems currently out of reach, since matter excitations, such as in an electron gas of quantum wells, decay through a non-radiative channel.

This is why an analog quantum simulation is a good candidate to study the ground state properties of an ultrastrongly coupled system. Whereas in the laboratory frame the coupling rate is time modulated (see Fig. 25b), in the rotating frame of the simulation, the coupling is constant, but due to the shift of the zero frequency in the rotating frame of the simulation, the coupling to the environment is non-zero even at negative frequencies (Fig. 25c). Their contribution to the emitted field thus cannot be neglected as

$$a_{out}[\omega > 0] = u_{11} a_{in}[\omega] + u_{12} b_{in}[\omega] + u_{13} a_{in}[-\omega]^\dagger + u_{14} b_{in}[-\omega]^\dagger \tag{89}$$

and the emitted photon rate is

$$\langle a_{out}[-\omega]^\dagger a_{out}[\omega] \rangle \neq 0. \tag{90}$$

Effective USC in a rotating frame thus allows access to the emitted radiation that carries trace of the intracavity field. In the following chapter, we are going to experimentally characterize both two-mode and single-mode squeezing in the case of such effective USC realized with a Josephson Mixer.

2.4 CONCLUSION

The main results of this chapter are:

- Description of a scheme that maps a three-wave mixing device, such as a Josephson mixer, simultaneously driven with two pump tones, onto a system of two bosonic modes in the ultrastrong coupling regime.
- Characterization of properties of the radiation emitted in the laboratory frame from the ground state of such an effective ultrastrongly coupled system.

3 EXPERIMENTALLY EVIDENCING SIGNATURES OF THE ULTRASTRONG COUPLING

"If you know where it's going it's not worth doing."

Frank Gehry

In Chapter 2 we have shown that starting from a three wave mixing Hamiltonian in the strong coupling regime, we can build an effective ultrastrong coupling between two bosonic modes a and b. When modes a and b are in the vacuum state at the input, the two effective modes are in their ground state and the output ports are in an unusual two-mode state, where each mode is squeezed vacuum, while the two modes are quantum correlated. Moreover, the predicted squeezing occurs between two propagating modes that are separated both in space and frequency. In this chapter, we are going to present an experimental evidence of the predicted ground state properties in the USC regime.

3.1 SPECTRAL EVIDENCE OF MODE HYBRIDIZATION

The USC simulation frame rotates at frequency $\omega_{a,b} + \delta$ with respect to the laboratory frame (Eq. (39)). Thus the positive and negative parts of the frequency spectrum in the rotating frame correspond to measurable noise powers at positive frequencies in the laboratory frame. We first perform a measurement of the power spectral density around the effective frequencies $-\delta$ and δ, i.e. $\omega_{a,b} + \delta \pm \delta$ in the laboratory frame, while tuning the transition from strong to ultrastrong coupling. As the detuning of the blue pump δ defines the resonance frequencies of the effective modes, it has to be small enough so that it is possible to reach the effective ultrastrong coupling $g \lesssim \delta/2$. Despite that, it has to be larger than the dissipation rates of the modes, in order to satisfy the strong coupling condition and be in the band

resolved regime. Dissipation rates being $\kappa_a = 2\pi \times 17.6$ MHz and $\kappa_b = 2\pi \times 21$ MHz, we opt for $\delta = 2\pi \times 26$ MHz.

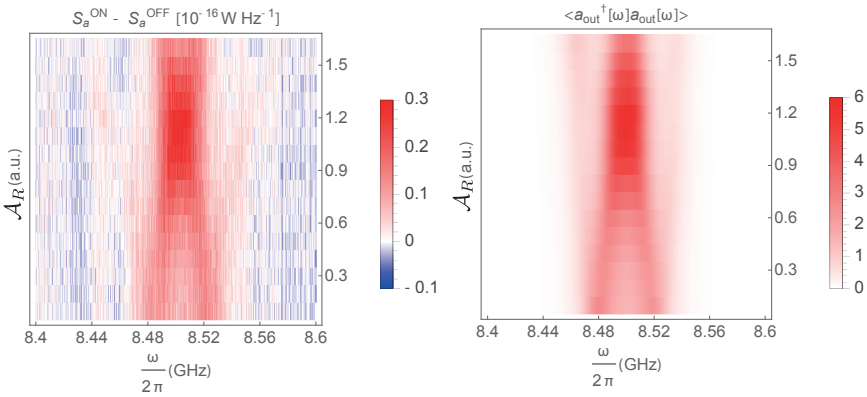

(a) (b)

Figure 26: (a) Measured power spectral density on the output port of mode a as a function of frequency ω and red pump amplitude $\mathcal{A}_R$ in the proximity of the resonance frequency ω_a of the mode a. The coupling of the blue pump is fixed to $g_B = 2\pi \times 12$ MHz. (b) The corresponding mean rate of emitted photons predicted from the input-output model Eq. (72).

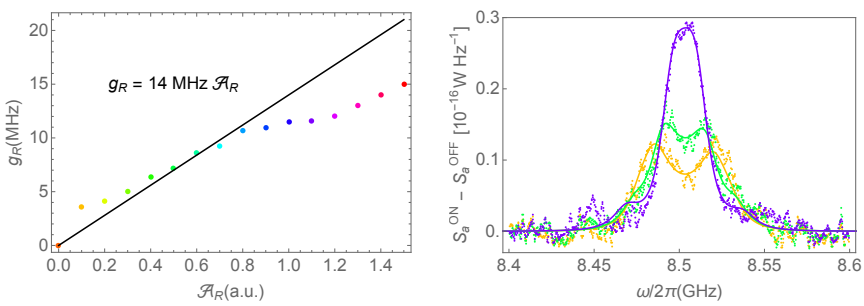

(a) (b)

Figure 27: (a) Coupling rate g_R as a function of the applied pump amplitude $\mathcal{A}_R$ inferred from the mean number of photons emitted from the mode a calculated with the Eq. (72), matched to the measured power spectral density shown in (b). Pump amplitude is color encoded. The deviation from the linear dependence comes in part from the saturation of the amplifier on the input pump line.

We start by setting the coupling rate of the blue pump to $g_B = 2\pi \times 12$ MHz which corresponds to $g_B = 0.46\delta$ for our choice of δ. In this first measurement the red pump is turned off. The spectra then develop a resonance at $\omega = \pm\delta$, symmetrically for positive and negative frequencies in the simulation frame. This resonance occurs at the transition frequency δ of the effectively degenerate modes a and b. As the coupling rate of the red pump g_R is turned on and progressively increased, both the resonance at δ and its image at $-\delta$ split into two, leading to a total of four peaks, as shown in Fig. 27 for mode a and Fig. 33 for mode b. Note that the two central peaks are much more pronounced then the external ones. This splitting is equivalent to the vacuum Rabi splitting in the case of a two level system coupled to a harmonic oscillator, observed in a physically ultrastrongly coupled light-matter systems [49, 50, 15].

As the splitting increases with g_R, two out of four resonance frequencies in the rotating frame shift towards $\omega = 0$. This can be seen as two peaks getting closer to the origin, corresponding to the resonance frequency and its image on the negative part of the spectrum. When the USC simulation condition is reached, $g_R \simeq g_B \sim 0.46\delta$, the two peaks merge at the origin and the resonance occurs at $\omega = 0$. There are no longer four peaks but only three, and the one at the origin is expected to correspond to the largest amount of two-mode squeezing [65].

The limit $g_R = g_B = g = \delta/2$ corresponds to the maximum coupling that can be obtained between two mechanical oscillators coupled through a spring (see Eq. (18)). For this reason, in the following sections we will mainly focus on the physically relevant regime $g_{B,R} < \delta/2$. At larger pump powers, the higher order terms in the Josephson Mixer Hamiltonian change the picture anyway.

This observation of a hybridization of the two modes constitutes a first convincing evidence of the USC regime. The second signature we will be looking for is the single and two mode squeezing of the radiation emitted when the system is in its ground state.

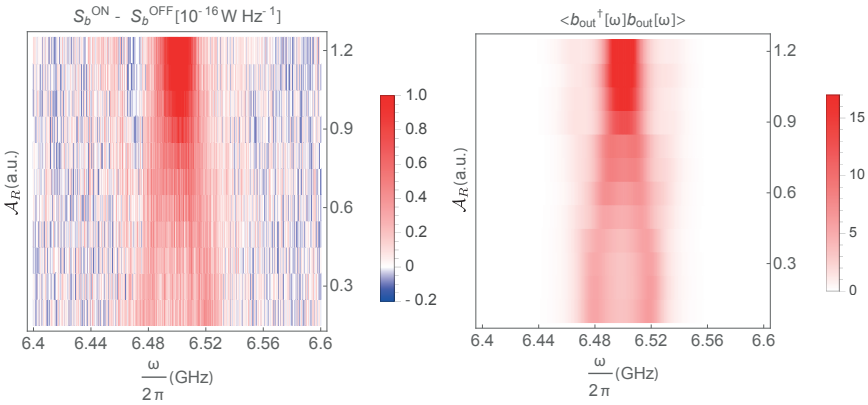

(a) (b)

Figure 28: (a) Measured power spectral density on port b as a function of frequency ω and red pump amplitude $\mathcal{A}_R$ in the proximity of the resonance frequency ω_b of the mode b. (b) Corresponding expectation value of the photon emission rate calculated from the input-output model.

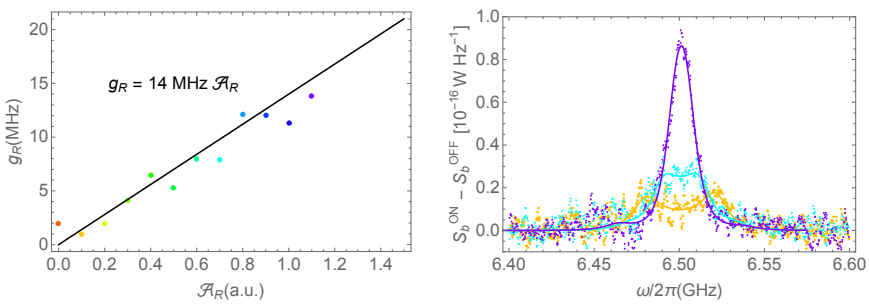

(a) (b)

Figure 29: (a) Coupling rate g_R as a function of the applied pump amplitude $\mathcal{A}_R$ inferred from the mean number of photons emitted from the mode b calculated with the Eq. (72), matched to the measured power spectral density shown in (b). Pump amplitude is color encoded.

3.2 CHARACTERIZATION OF ENTANGLEMENT AND SQUEEZING

One way to demonstrate entanglement is to use an entanglement witness as in ref. [2] where two continuously generated entangled

modes are recombined on a second Josephson mixer. By measuring the decrease of the noise at the output of the witness below what is classically allowed for a separable state, one can infer that the input state presents entanglement [2, 60].

A more direct approach is to use a fast acquisition board to perform a brute-force noise correlation measurement. This strategy consists in recording the distributions of the measurement outcomes of all four quadratures of the two-mode state at room temperature on a large number of realizations. The measured photon field statistics can then be related to generalized quasi-probability distributions and statistical moments. This method has been used to demonstrate entanglement in a number of experiments [71, 72, 73, 74]. Indeed, by performing a full joint tomography of the two-mode state, we can infer the covariance matrix, which contains all the information needed to calculate the amount of single and two-mode squeezing [75]. Two schemes for field quadrature measurement can be used to characterize itinerant microwave fields, the homodyne and the heterodyne detections.

3.2.1 *Homodyne detection*

In the homodyne detection setup, only one generalized field quadrature $\hat{X}_\theta = \frac{1}{2}(\hat{A}_{out}e^{-i\theta} + \hat{A}^\dagger_{out}e^{i\theta})$ of the output field $\hat{A}_{out}$ is measured. The cosine component of the field $\hat{X}_{\theta=0} = \hat{X}$ can be defined as a position variable and the sine component $\hat{X}_{\theta=\frac{\pi}{2}} = \hat{P}$ as a momentum variable. Then the detected signal field $V(t) = X_a \cos(\omega_a t) + P_a \sin(\omega_a t)$ is analogically multiplied by a strong reference tone at the same frequency ω_a using a microwave mixer. The reference tone, $\mathcal{A}_{ref} \cos(\omega_a t + \theta)$ is provided by a local oscillator (LO). Therefore by filtering out the high frequency component and measuring the average value of the output voltage, an outcome proportional to X_θ is obtained. Finally by varying the phase θ of the local oscillator, the angle of the quadrature to measure can be chosen such that the whole phase space is spanned [71]. From the measurement outcomes, the probability density function $P(X_\theta)$ for measuring a particular value of X_θ can be deduced. Note that this technique differs from its counterpart in visible optics where photodiodes are used instead of voltmeters.

The goal of quantum state reconstruction is to estimate the density matrix ρ_{ab} which characterizes the joint state of the propagating field modes a_{out} and b_{out}. This is experimentally achieved by preparing many times the state that we want to characterize and performing a set of measurements on these states, which contain information about diagonal and off-diagonal elements of the joint density matrix ρ_{ab}.

In the particular case where measured observables are field quadratures, measurement results are directly related to the phase space distributions such as the Husimi-Q function $Q_{\rho_a}(\alpha) = \frac{1}{\pi} \langle\alpha| \rho_a |\alpha\rangle$ or Wigner function $W_{\rho_a}(\alpha) = \frac{2}{\pi}\mathrm{Tr}[e^{i\pi\hat{a}^\dagger\hat{a}} D^\dagger(\alpha)\rho_a D(\alpha)]$. In the case of homodyne detection of a single mode, the measured probability density function, $P(X_\theta) = \int dX_{\theta+\pi/2} W(X_\theta, X_{\theta+\pi/2})$, is the marginal of the Wigner function W. Wigner function is a quasi-probability distribution, it is normalized to one, but it is generally non-positive. Measured $P(X_\theta)$ are thus projections of the Wigner function which can be used to reconstruct it by spanning the angle θ. A method such as maximum-likelihood can be used to infer the quantum state from the Wigner function obtained from a homodyne measurement.

3.2.2 *Heterodyne detection*

In our experiment we use the heterodyne detection setup, where the two canonically conjugate field quadratures $\hat{X}$ and $\hat{P}$ are measured simultaneously, so that all the information needed for complete quantum state reconstruction is acquired. The Husimi-Q function naturally emerges from the heterodyne measurement and generates the anti-normally ordered moments

$$\langle a^n (a^\dagger)^m \rangle = \int_\alpha (\alpha^*)^m \alpha^n Q(\alpha). \tag{91}$$

Being the expectation value of an observable, it is a directly measurable quantity. The Q distribution is positive, bounded by $1/\pi$ and normalized, $\int d^2\alpha Q(\alpha) = 1$. For coherent states, the Husimi-Q function is a two-dimensional Gaussian distribution with variance 1 centered around the amplitude of the coherent state. Half of these fluctuations correspond to the intrinsic vacuum fluctuations of the quantum field, while the other half come from the minimal added uncertainty when directly measuring a Q function, which requires

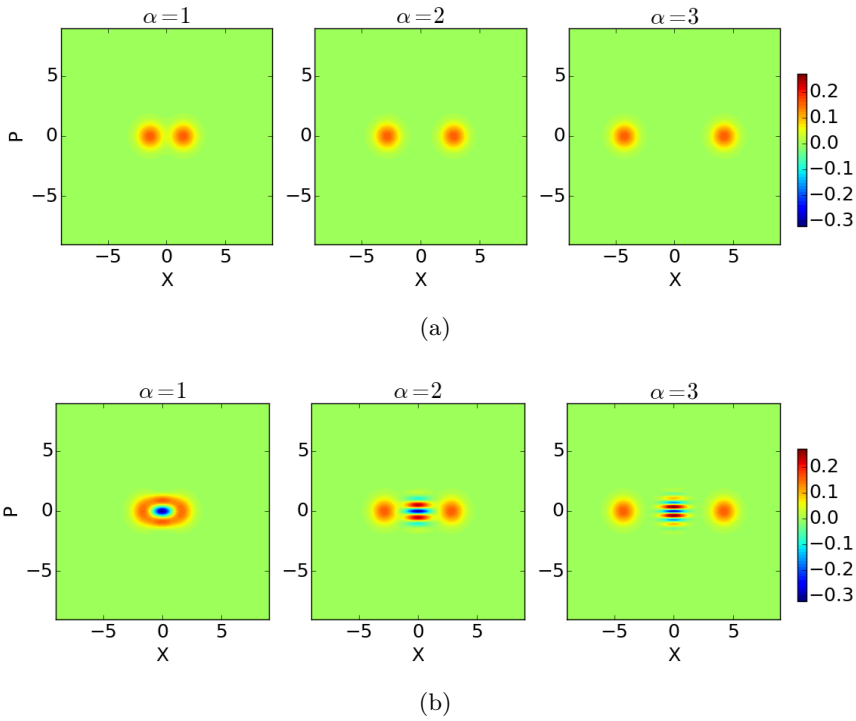

Figure 30: Wigner functions of (a) a statistical mixture state of density matrix $\rho_{mix} = \frac{|\alpha\rangle\langle\alpha| + |-\alpha\rangle\langle-\alpha|}{2}$ and (b) of a coherent superposition cat state $\rho_{cat} = \frac{(|\alpha\rangle + |-\alpha\rangle)(\langle\alpha| + \langle-\alpha|)}{2}$ for $\alpha \in \{1, 2, 3\}$. The interferences around the origin appear as easily distinguishable feature for the cat state.

the simultaneous detection of two non-commuting field quadratures (phase-preserving amplification) [76]. One quadrature can in principle be measured without added noise (phase-sensitive amplification), but not both. Note however that no information is lost on the input state [77].

The state of a single mode of the radiation field belongs to an infinite dimensional Hilbert space. This makes it in principle impossible to exactly reconstruct any state, because an infinite amount of information needs to be acquired. Nevertheless, it is often possible to reduce the relevant state space by measuring a finite set of moments. For instance, coherent, thermal and squeezed states can all be characterized by a finite set of moments. Actually, all of these states are Gaussian [78], thus the statistical moments up to the second order de-

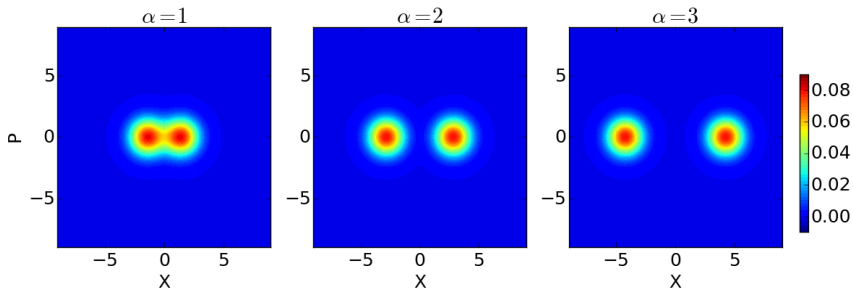

(a)

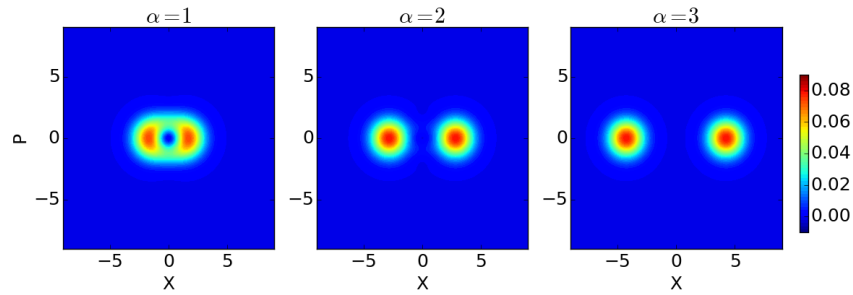

(b)

Figure 31: Husimi functions of (a) a statistical mixture state of density matrix $\rho_{mix} = \frac{|\alpha\rangle\langle\alpha|+|-\alpha\rangle\langle-\alpha|}{2}$ and (b) of a coherent superposition cat state $\rho_{cat} = \frac{(|\alpha\rangle+|-\alpha\rangle)(\langle\alpha|+\langle-\alpha|)}{2}$ for $\alpha \in \{1, 2, 3\}$. Even though Husimi function is bijective to the density matrix just as the Wigner function, the distinguishable features are much less clear. Precision of $1/\sqrt{\alpha}$ is needed to distinguish between the two states.

termine all of their higher order moments. The two-mode phase space distribution is thus fully determined by the 4×4 covariance matrix $\mathcal{V}$, which describes the joint statistics of the amplitude fluctuations of the two modes.

3.2.3 *ON-OFF measurements*

As microwave frequencies oscillate too rapidly to directly measure and process the electric field electronically[1], another purpose of heterodyne mixing is to down shift the signal to a frequency range that can be resolved by commercial acquisition boards. This can be done by mixing the signal with a LO reference tone at a slightly detuned frequency $\omega_a + \omega_h$. The resulting signal on the output of mode a oscillating at frequency ω_h can be recorded using an analog to digital converter (ADC) and numerically demodulated. However, the sensitivity of the ADC is such that it requires large amplitude fields of the order of Volts, which contain a macroscopic number of photons per sampling time, so that a linear amplification stage is needed on the output line. Such an amplification stage necessarily adds some thermal noise which implies that the complex amplitude of the detected field reads

$$\hat{A}_{out} = \sqrt{G_{chain}}\hat{a}_{out} + \sqrt{G_{chain} - 1}\hat{h}^\dagger = \hat{X} + i\hat{P}, \tag{92}$$

where G_{chain} is the gain of the chain of amplifiers and $\hat{h}$ is an additional bosonic mode accounting for the noise added by the chain, dominated by the noise added by a High Electron Mobility Transistors (HEMT) cryogenic amplifier from Caltech university [79], [80]. In order to get rid of this uncorrelated noise and extract the tiny signal corresponding to the quantum microwave field, we are going to use the ON-OFF subtraction technique as illustrated in Fig. 32.

Signal is recorded with pumps turned on and immediately after with pumps turned off and this is repeated to acquire measurement statistics. Finally histogram of values measured with pumps turned off is subtracted from the one with pumps turned on. This technique also allows to compensate residual gain fluctuations that are slower than the measurement repetition rate.

3.2.4 *Calibration of the quadrature measurements*

In order to demonstrate squeezing and entanglement, it is necessary to calibrate the quadrature measurements. By measuring the

1 Although owing to technological developments, this is rapidly changing and could be wrong a few years from now.

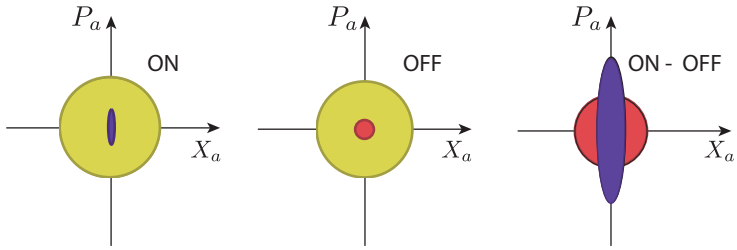

Figure 32: ON-OFF subtraction technique. The detected signal is dominated by added uncorrelated noise (yellow), which hides the squeezed vacuum (purple) when the pumping is turned ON, or the vacuum fluctuations (red), when the pumping is turned OFF.

total noise power at the end of the detection setup as a function of the gain of the Josephson Mixer, the total amplifying chain gain can be estimated, from the Josephson Mixer input to the measurement apparatus. To verify that the amplifying chain gain is constant and doesn't depend on the applied pump amplitudes, we have sent a strong, far detuned reference tone on the input port and measured its refection amplitude as a function of different blue and red pump amplitudes. We found the reflection amplitude to be constant within 0.6 %.

From the Eq. (92), the variance of the detected signal reads [76]

$$\langle \hat{A}_{out}\hat{A}^{\dagger}_{out}\rangle = G_{chain}\langle \hat{a}_{out}\hat{a}^{\dagger}_{out}\rangle + (G_{chain}-1)\langle \hat{h}^{\dagger}\hat{h}\rangle \tag{93}$$

The variance of the noise bosonic mode $\hat{h}$ is taken in a thermal state, whereas the variance of the propagating mode a_{out} depends on the state of the Josephson Mixer. When the amplification pump is turned on, the mean value $\langle \hat{a}_{out}\hat{a}^{\dagger}_{out}\rangle$ is calculated on a squeezed vacuum state, while when the pump is turned off, the output mode is in vacuum. If both input modes are assumed to be in the vacuum, for a given gain of the Josephson Mixer G_{JM}

$$\begin{aligned}\langle \hat{a}_{out}\hat{a}^{\dagger}_{out}\rangle^{ON} &= G_{JM}\langle \hat{a}_{in}\hat{a}^{\dagger}_{in}\rangle + (G_{JM}-1)\langle \hat{b}^{\dagger}_{in}\hat{b}_{in}\rangle \\ &= G_{JM}\end{aligned} \tag{94}$$

so that

$$\langle \hat{A}_{out}\hat{A}^{\dagger}_{out}\rangle^{ON} = G_{chain}G_{JM} + (G_{chain}-1)\langle \hat{h}^{\dagger}\hat{h}\rangle \tag{95}$$

$$= G_{chain}G_{JM} + (G_{chain}-1)\langle \hat{h}^{\dagger}\hat{h}\rangle \tag{96}$$

On the other hand, when the amplifying pump is turned off, the variance of the detected signal becomes

$$\begin{aligned}\langle \hat{A}_{out}\hat{A}^{\dagger}_{out}\rangle^{OFF} &= G_{chain}\langle \hat{a}_{in}\hat{a}^{\dagger}_{in}\rangle + (G_{chain}-1)\langle \hat{h}^{\dagger}\hat{h}\rangle \\ &= G_{chain} + (G_{chain}-1)\langle \hat{h}^{\dagger}\hat{h}\rangle\end{aligned} \tag{97}$$

Finally we can find the gain of the amplification chain

$$\boxed{G_{chain} = \frac{1}{G_{JM}-1}\left[\langle \hat{A}_{out}\hat{A}^{\dagger}_{out}\rangle^{ON} - \langle \hat{A}_{out}\hat{A}^{\dagger}_{out}\rangle^{OFF}\right]} \tag{98}$$

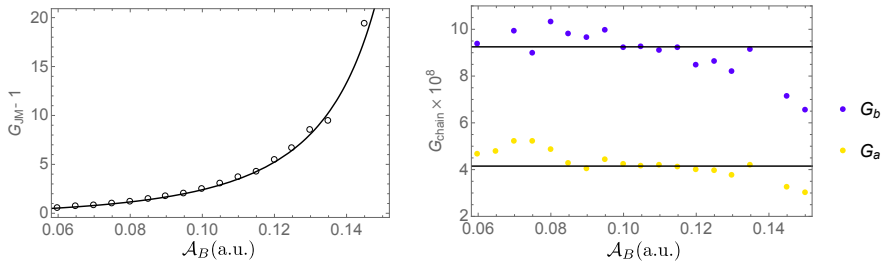

(a) (b)

Figure 33: (a) Measured Josephson Mixer gain G_{JM} as a function of applied pump amplitude $\mathcal{A}_B$. The full line corresponds to expected gain for the Jospehson Mixer Eq. (99). (b) Determination of the amplifying chain gain for different values of the amplifying pump and thus Josephson Mixer gain. We take the mean value of the values corresponding to Josephson Mixer gains up to 10 dB. For higher gains, Kerr effect becomes important and it is harder to estimate the gain properly.

We first measure the gain of the Josephson Mixer G_{JM} using a Vector Network Analizer (VNA) for different pump amplitudes $\mathcal{A}_B$, as shown in Fig. 33a. It is reproduced by

$$G_{JM} = (\frac{1+\rho^2}{1-\rho^2})^2, \tag{99}$$

where $\rho = \frac{\mathcal{A}_B}{\mathcal{A}_{th}}$ and $\mathcal{A}_{th}$ is the threshold amplitude. Then, for those same pump amplitudes, we prepare EPR state and measure the quadratures for the two mode a and b using a fast acquisition card. From the measurement statistics we determine the variance in ON and OFF

state $\langle \hat{A}_{out}\hat{A}^{\dagger}_{out}\rangle = \langle \hat{X}_a\hat{X}^{\dagger}_a\rangle + \langle \hat{P}_a\hat{P}^{\dagger}_a\rangle$. Finally we calculate $G_{chain} = G_a$ for mode a and G_b for mode b. The estimated amplification chain gain for the two modes as a function of blue pump amplitudes is shown in Fig. 33b.

There is an important uncertainty attached to the estimation of G_a and G_b. Although these gains are expected to be independent of the pump amplitudes as shown by the lack of dependance of the amplitude of the reflected tone out of resonance, the calculated values of both G_a and G_b decrease at high pump amplitudes. It can be explained by the saturation of room temperature amplifiers by the strong pump tone. Also, at high gains, close to the parametric oscillation threshold, there is an uncertainty attached to the estimation of the gain as the Kerr effect becomes important. We thus only take into account the values obtained at lower pump amplitudes where amplification is linear. Taking the mean value for Jospehson Mixer gains up to 10 dB, we obtain $G_a = 4.15 \times 10^{-8}$ and $G_b = 9.25 \times 10^{-8}$.

3.2.5 *EPR state*

We first calibrate our technique for squeezing detection by preparing an EPR two-mode squeezed state (Eq.(29)) in the standard resonant amplification pumping scheme [2]. By applying just the blue pump on resonance, the EPR state is created between the propagating modes a_{out} and b_{out}. Indeed, there are few different ways to prepare a two-mode squeezed state that are summarized in Table 4.

By mixing a single mode squeezed state with a vacuum state at the same frequency in a beamsplitter, two spectrally degenerate but spatially separated entangled fields are created. The two mode squeezing is then limited to 3 dB. In the microwave domain, the squeezed state can be produced using a Josephson Parametric Amplifier (JPA) that performs a squeezing operation on the incident vacuum state, $\hat{S}(\xi)\,|0\rangle$, where $\hat{S}(\xi) = e^{\frac{1}{2}\xi^*\hat{a}^2 - \frac{1}{2}\xi(\hat{a}^{\dagger})^2}$ is the single mode squeezing operator. Alternatively, two identical single-mode squeezed states can be recombined on a beamsplitter in order to increase the amount of entanglement. For the optical frequencies, squeezing is created in optical parametric oscillators (OPO) that consist of an optical resonator and a nonlinear crystal that provides a Kerr nonlinearity. Two identi-

two-mode squeezing	spatially degenerate	spatially non degenerate (EPR)
spectrally degenerate	single-mode squeezing 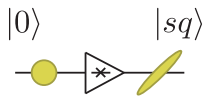	JPA + BS [73, 81, 82] NOPO + BS [83, 84] 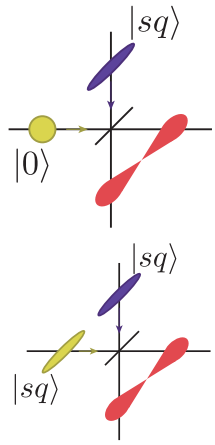
spectrally non-degenerate	JPA [72] 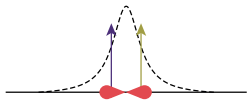	Josephson Mixer [2] 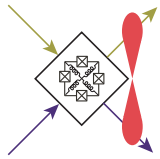

Table 4: Different realizations of two mode squeezing.

cal OPOs can thus be driven by the same LO and their output fields recombined on a beamsplitter in order to create two-mode squeezing.

Moreover, a JPA can be used to create entanglement between two spatially degenerate but spectrally separated modes [72], as illustrated in Table 4. However, the Josephson Mixer is unique in its ability to create both spectrally and spatially non degenerate two-mode squeezing. As a matter of fact, when the amplification pump tone is applied at the sum frequency $\omega_p = \omega_a + \omega_b$, with both modes initially in vacuum state, an EPR pair is generated through spontaneous parametric down-conversion and distributed between modes a and b. As the entangled field continuously leaks out in the propagating modes a_{out} and b_{out}, the two propagating modes are entangled as well.

In order to determine the elements of the covariance matrix, we detect the four quadrature components and store the marginal distributions of their values in two-dimensional histograms for the six possible pairs of components $\{X_a, P_a\}$, $\{X_b, P_b\}$, $\{X_a, P_b\}$, $\{X_b, P_a\}$, $\{X_a, X_b\}$ and $\{P_a, P_b\}$. For each pair we acquire a reference histogram with the pump turned OFF, which characterizes the quadrature distribution of the effective noise mode h (Eq.(92)). This reference histogram is then subtracted from the histogram acquired with the pump turned ON [72]. The pulse sequence used in the experiment can be seen in Fig. 34a.

A square pump pulse is applied at the sum frequency $\omega_p = \omega_a + \omega_b = 2\pi \times 15.0$ GHz for 2.5 μs. The pump amplitude is set to $\mathcal{A}_p = 0.145$ corresponding to the gain of Josephson Mixer $G_{JM} = 16.15$ dB and the coupling rate $g_B = 2\pi \times 8.5$ MHz. Signal from the outgoing mode a_{out} are recorded for 1 μs at $\omega_a = 2\pi \times 8.5$ GHz, and from the mode b_{out} at $\omega_b = 2\pi \times 6.5$ GHz. After 2 μs, the signal is recorded with pumps turned off. The whole sequence lasts 10 μs and is repeated 10^6 times. This enables elimination of the low frequency fluctuations in signal ($\omega < 2\pi \times 100$ kHz).

When the pump tone is turned off, measured noise modes are described by perfectly circular Gaussian distributions of variance σ_{OFF}, as can be seen in Fig. 34b. In the histograms with pumps turned on, there is a tendency that can be recognized between the same quadratures of the two modes a and b, but the signal is however dominated by the added noise.

On the other hand, the subtraction between all the pairs of histograms exhibits clearly distinguishable features. Sub-systems themselves contain no quantum signatures in their self-correlations, but observed cross-quadrature correlations indicate presence of two-mode squeezing. This means that although none of the quadratures $\hat{X}_a$, $\hat{X}_b$, $\hat{P}_a$, $\hat{P}_b$ is squeezed itself, quantum correlations are present in the collective variables, and particularly in the relative position $\hat{X}_a - \hat{X}_b$ and the total momentum $\hat{P}_a + \hat{P}_b$, which are squeezed below the standard vacuum limit of $\sigma_{vac} = \frac{1}{4}$.

Actually, for the single mode histograms $\{X_a, P_a\}$ and $\{X_b, P_b\}$, we observe a phase independent increase in the quadrature fluctuations, implying a higher probability to measure larger quadrature amplitudes. This feature corresponds to the phase-insensitive amplifi-

cation of the vacuum in each of the individual modes a and b. However, for the $\{X_a, X_b\}$ and $\{P_a, P_b\}$ histograms, we find an increase in the fluctuations along the diagonal, indicated by the positive valued regions in the histogram differences and a decrease in the fluctuations in the perpendicular direction. Both of these observed features are characteristic of a two-mode squeezed state.

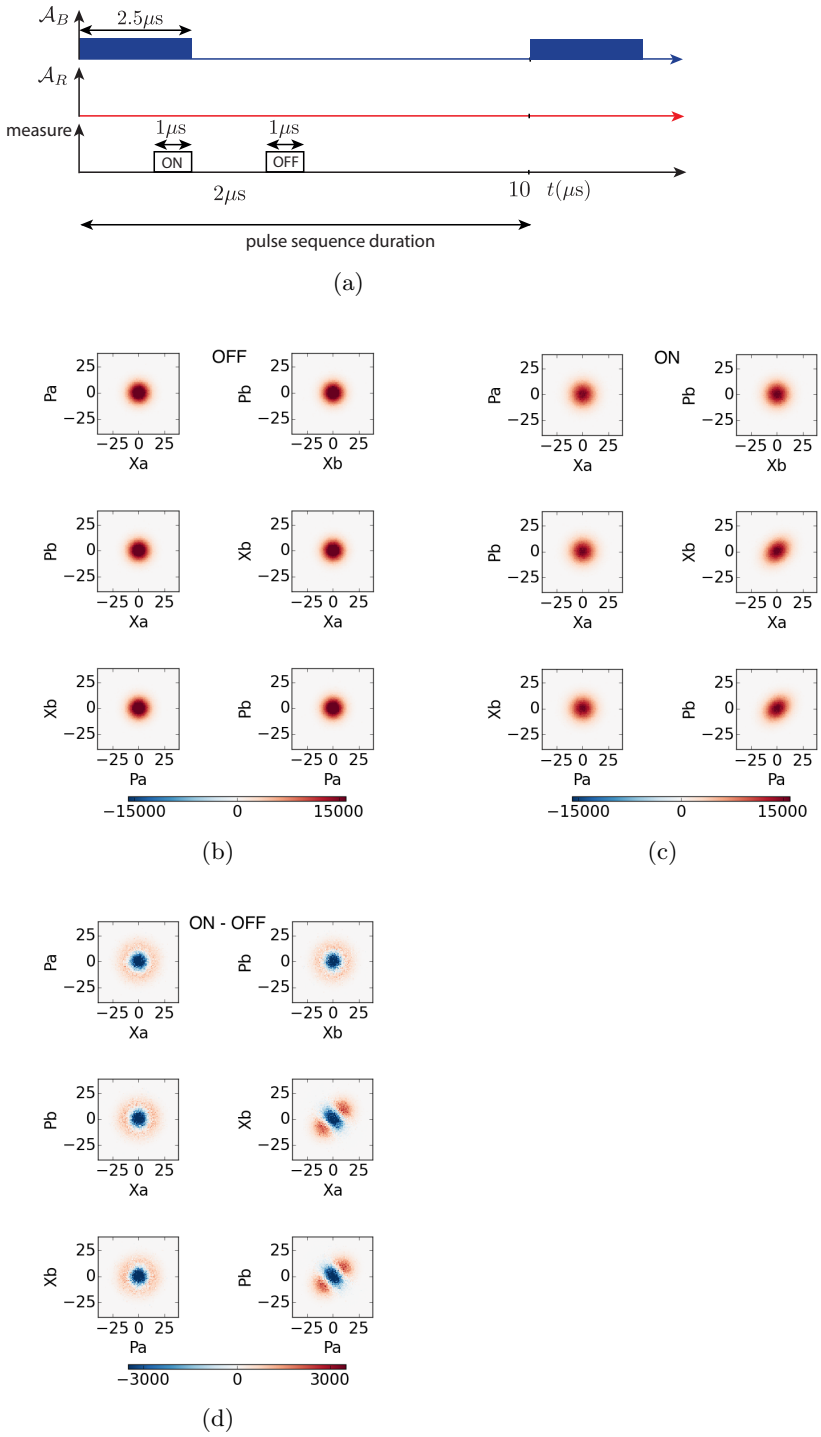

Figure 34: (a) Pulse sequence used in the experiment. Measured quadrature histograms in the EPR state with entangling pump (b) turned OFF, (c) turned ON and (d) subtraction between ON and OFF histograms for 6 different quadrature pairs. Each bin is 1×1 wide and the color bars are expressed in number of counts.

3.2.6 *Pulsed measurement of the USC ground state*

The simulation of the USC requires simultaneous pumping with a detuned blue pump and a resonant red pump. Phases of the RF sources that are used to produce these pump tones can drift in time, and the relative phase acquired over the total duration of a measurement can be non negligible, as a single measurement is repeated 5×10^5 times in order to acquire statistics. A strategy we use to keep the two pump tones well locked in phase is to create them by mixing two RF tones produced by two sources whose frequencies are set to $\omega_a + \Delta + \delta$ and $\omega_b - \Delta + \delta$, such that their sum gives the blue detuned pump $\omega_B = \omega_a + \omega_b + 2\delta$ and their difference is $\omega_a - \omega_b + 2\Delta$. The latter is then mixed with a tone oscillating at 2Δ created by an Arbitrary Wave Generator (AWG), in order to pulse the red pump $\omega_R = \omega_a - \omega_b$, as schematically represented in Fig. 35. The blue pump is pulsed using an RF switch.

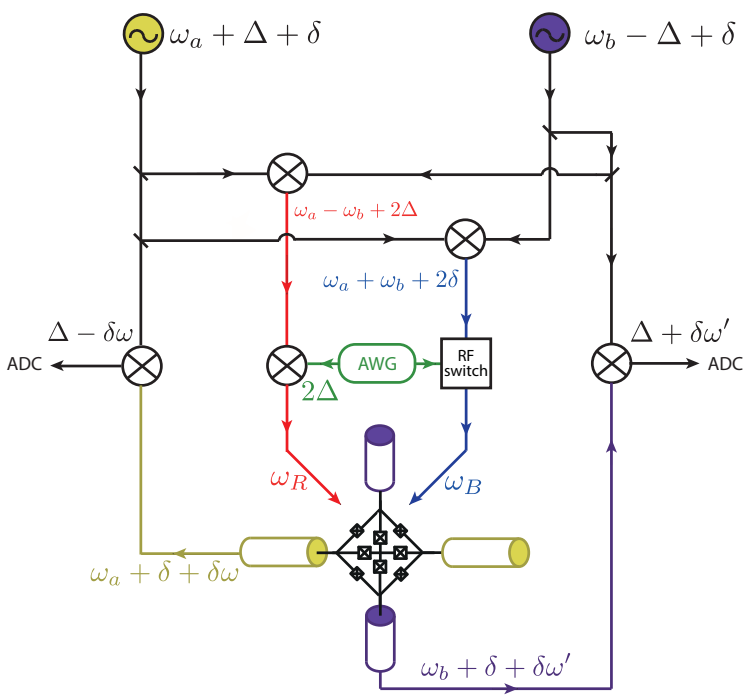

Figure 35: Heterodyne detection setup used for the pulsed off-resonant pumping required for the analog USC simulation.

The purpose of the offset Δ is to avoid a possible leakage of the LO tone at $\omega_{a,b} + \delta$ into the system, because it could interfere with the output field which is at the same frequency as the one at which the field is expected to be squeezed. The offset Δ thus has to be large enough to avoid the risk of interference with the signal, but small enough to be in the bandwidth of the ADC, because as we will see, it will set the heterodyning frequency.

The field is predicted to be maximally squeezed at frequency $\omega_{a,b} + \delta$ in the laboratory frame, corresponding to $\omega = 0$ in the analog simulation frame. For instance, for the mode a, the outgoing signal at frequency $\omega_a + \delta$ is multiplied by a LO tone at $\omega_a + \delta + \Delta$, so that the resulting signal carrier oscillates at $\Delta = 2\pi \times 125$ MHz. Since the observables $\hat{X}_a = \mathrm{Re}[\hat{a}_{out}]$ and $\hat{P}_a = \mathrm{Im}[\hat{a}_{out}]$ associated with these quadratures do not commute, the signal needs to be split in two parts so that the quadratures are detected separately.

3.2.7 *Emission radiation of the USC ground state*

The covariance matrix $\mathcal{V} = \{\langle x_i x_j + x_j x_i \rangle_{|GS\rangle} - \langle x_i \rangle_{|GS\rangle} \langle x_j \rangle_{|GS\rangle}\}$ in the basis $\{x_1, x_2, x_3, x_4\} = \{X_a, P_a, X_b, P_b\}$ can be put in the form

$$\mathcal{V} = \begin{pmatrix} \alpha & \chi \\ \chi^T & \beta \end{pmatrix} \tag{100}$$

where 2×2 matrices α and β are single-mode covariance matrices for modes a and b. They can be independently diagonalized, so that we can determine the amount of squeezing of each of the propagating modes a_{out} and b_{out} from their eigenvalues σ_a^{min}, σ_a^{max}, σ_b^{min} and σ_b^{max}. In order to quantify the squeezing and check that the variance of the squeezed quadrature decreases bellow that of the vacuum fluctuations, we use the measure of squeezing

$$r_{a,b}^{min} = 10 \log_{10} \Big[\frac{\frac{\sigma_{a,b}^{min}}{G_{chain}} - \big(\frac{\sigma_{OFF}}{G_{chain}} - \sigma_{vac} \big)}{\sigma_{vac}} \Big] \tag{101}$$

where $\sigma_{vac} = \frac{1}{4}$ is the variance of the vacuum fluctuations and σ_{OFF} is the variance of the detected signal when the pumps are turned

off. Note that $\frac{\sigma_{OFF}}{G_{chain}} - \sigma_{vac}$ corresponds to the noise added by the amplification chain referred to the input. It is subtracted from the variance of the measured signal in order to recover the variance of the propagating field before the noisy amplifying chain.

Subtracted histograms for the USC interaction turned ON and OFF, shown in Fig. 36b are radically different than in the case of the EPR state, shown in Fig. 34. In the ground state of the effective USC, correlations are present both between the two quadratures of each of the modes a and b, as well as between the two modes.

We can study the transition from strong to ultrastrong coupling regime by measuring single-mode and two-mode squeezing as a function of the applied pump amplitudes.

3.2.7.1 *Single mode squeezing*

We have measured the single-mode squeezing for both modes a and b, for coupling rates of the blue and the red pump going from 0 to $\delta/2$. For each pair of pump amplitudes, 10^6 measurements of the field quadratures were performed, each measurement followed by the reference measurement with pumps turned off. Finally, from measured quadrature distributions, squeezing parameter $r_{a,b}^{min}$ is deduced for each pair of pump amplitudes. It is shown in Fig. 37 as a function of coupling rates of the two pumps.

Since bandwidths of modes given by dissipation rates $\kappa_{a,b}$ are not negligible compared to the detuning δ, when only the blue pump is applied, the process resembles the creation of an EPR state. When the other mode is traced out, the density matrix describing each of the subsystems is that of a thermal state. Their variances are thus increased compared to that of the vacuum, and the squeezing parameter is positive. This corresponds to the red region in each of the plots in Fig. 37.

However, when the amplitude of the red pump is progressively increased, the noise in one field quadrature progressively decreases, reaching the squeezing of -1 dB for the mode a and -2.5 dB (Fig. 37a) for the mode b (Fig. 37a). This asymmetry is due to the difference between the dissipation rates of the two modes, $\kappa_a/2\pi = 17.6$ MHz and $\kappa_b/2\pi = 25$ MHz, and is reproduced by theory (Fig. 37c, 37d).

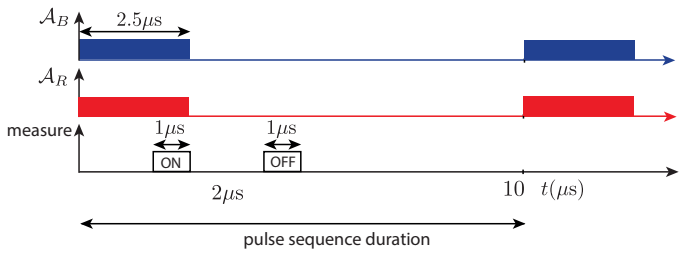

(a)

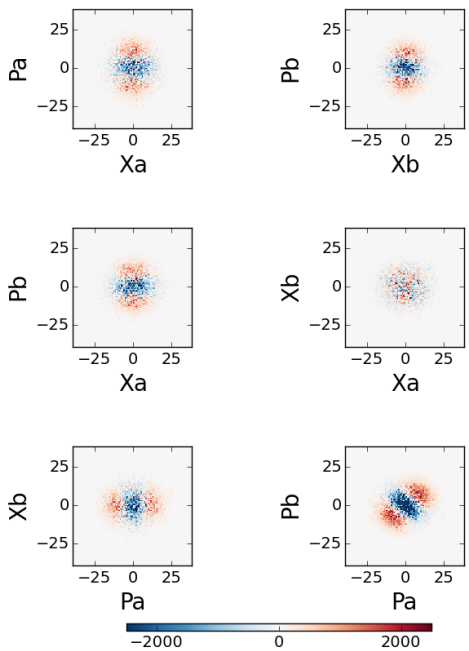

(b)

Figure 36: (a) Pulse sequence used for the ON-OFF subtraction. (b) Subtracted histograms with USC interaction turned ON and OFF for 6 different quadrature pairs in the ground state. Correlations are visible both on the single mode quadratures and between the two delocalized propagating modes. Bins are 1×1 wide and the color bars are expressed in number of counts.

The antisqueezing of the conjugate quadrature in the basis that diagonalizes single-mode covariance matrices α and β reads

$$r_{a,b}^{max} = 10 \log_{10} \left[\frac{\frac{\sigma_{a,b}^{max}}{G_{chain}} - \left(\frac{\sigma_{OFF}}{G_{chain}} - \sigma_{vac} \right)}{\sigma_{vac}} \right]. \tag{102}$$

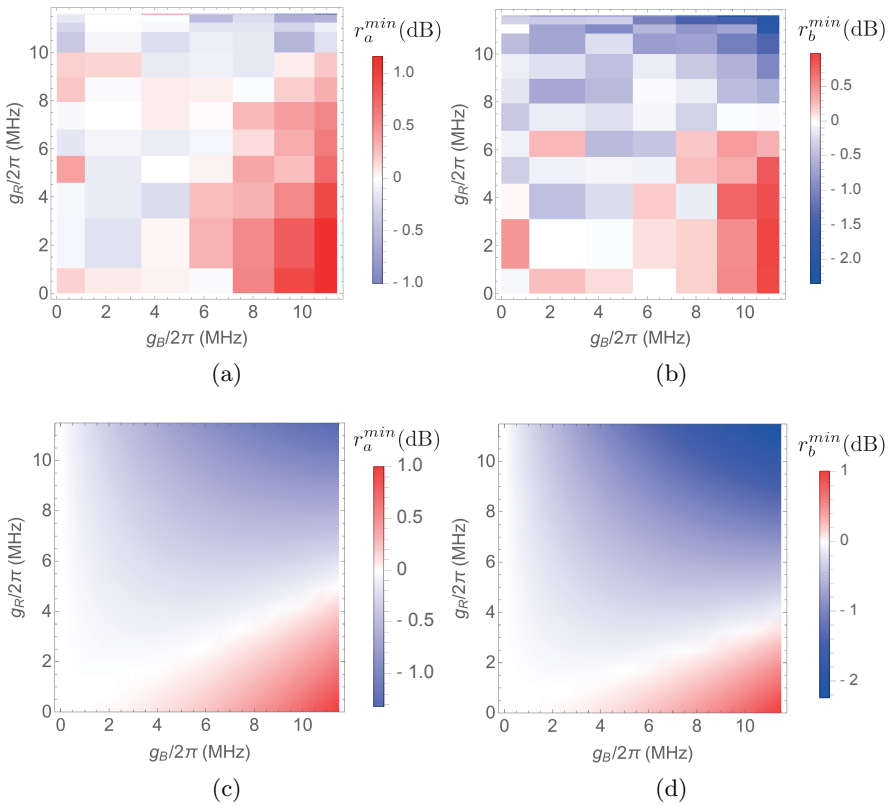

Figure 37: Measured single-mode squeezing on modes a (a) and b (b). Squeezing parameter r^{min} in dB is plotted as a function of pump coupling rates g_B and g_R determined from noise measurements (see Fig. 20 and Fig. 29a). (c) Corresponding predicted single-mode squeezing from input-output theory for the mode a and (d) for the mode b.

It is shown in Fig. 38, as a function of coupling rates g_B and g_R of the two pumps. When only the conversion pump is turned on, the variance remains constant as both modes are in vacuum. When the amplifying pump is turned on, there is more noise added to the mode b than to the mode a, because it is more coupled to the transmission line.

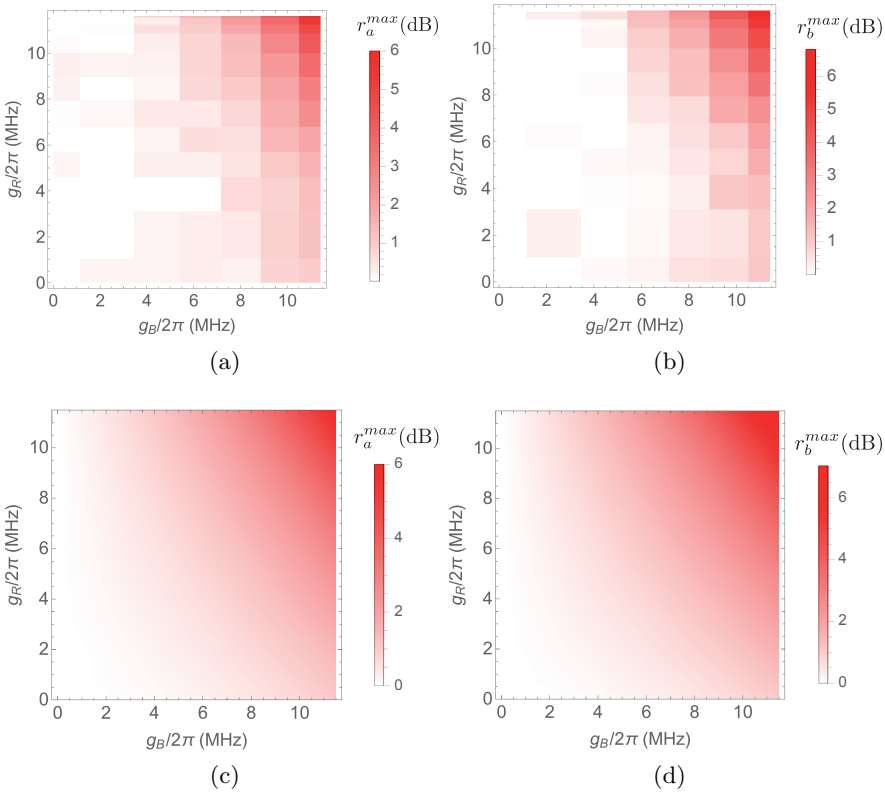

Figure 38: Measured single mode anti-squeezing on modes a (a) and b (b). Antisqueezing parameter $r_{a,b}^{max}$ in dB is plotted as a function of pump coupling rates g_B and g_R determined from noise measurements Fig. 20 and Fig. 29a. (c) Predicted antisqueezing from input-output theory for the mode a and (d) for the mode b.

3.2.7.2 *Two-mode squeezing*

Two-mode squeezing can be characterized by considering the variance of collective variables such as $X_a - X_b$, $X_a + X_b$, $P_a - P_b$ and $P_a + P_b$. Measured variances of the total momentum and relative position are shown in Fig. 39, together with expected variances calculated in the quantum Langevin equation formalism. Similarly, measured variances and their expectations for the complementary antisqueezed collective quadratures, that is relative momentum and total position, are shown in Fig. 40.

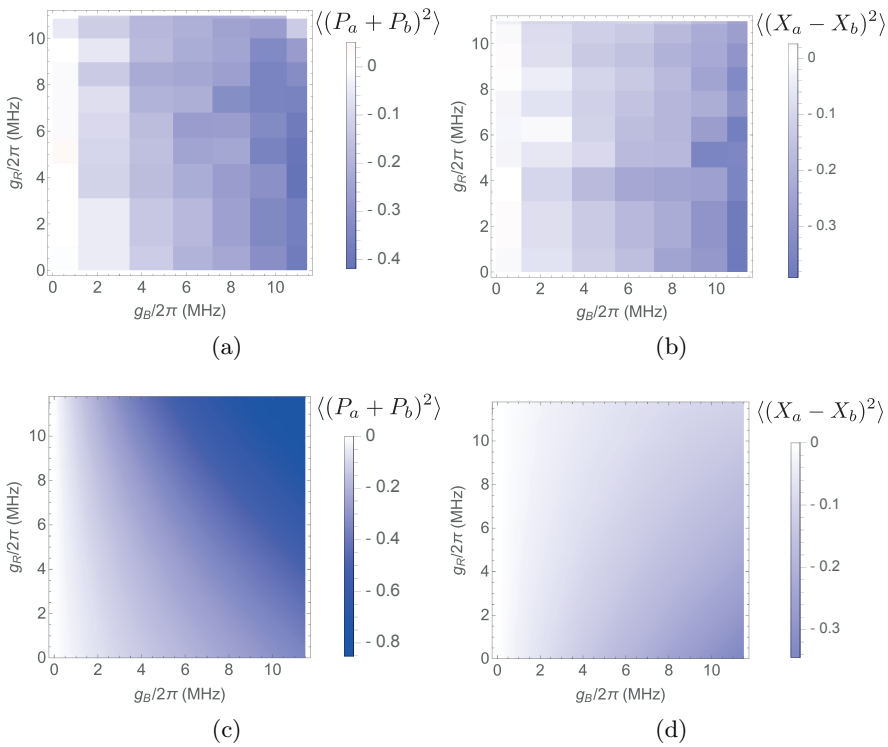

Figure 39: (a) Measured variance of the total momentum and (b) of the relative position. (c) and (d) Expectation values for the variances of the collective squeezed variables calculated using the input-output theory. Note that there is more squeezing in the total momentum than in the relative position.

The determination of a squeezing parameter is highly sensitive to gains G_a and G_b of the amplification setups. The uncertainty on their exact values at high pump amplitudes thus leads to a large

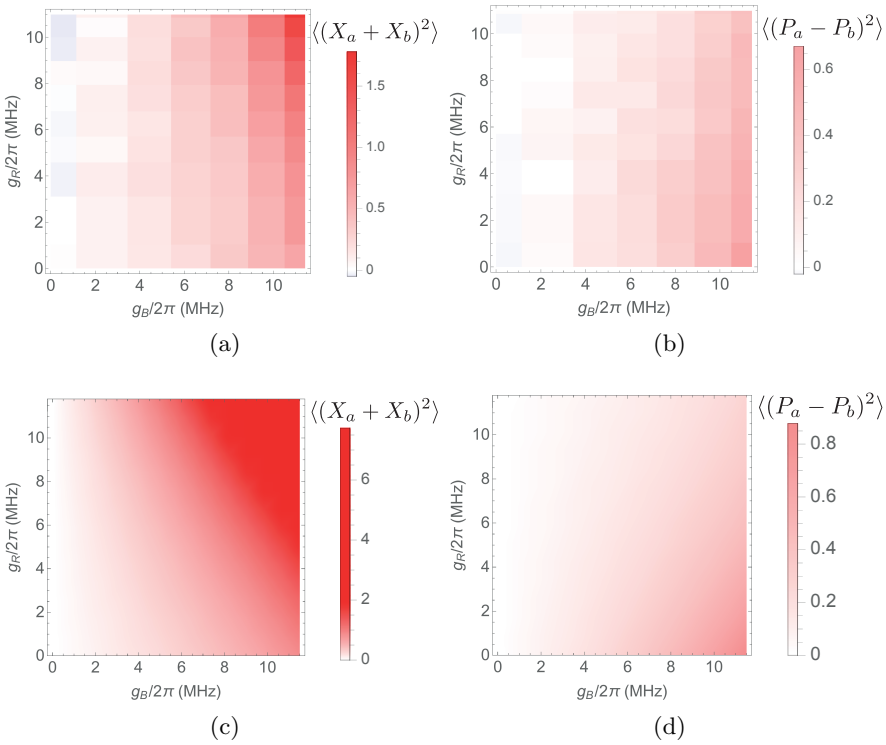

Figure 40: (a) Measured variance of the total position and (b) of the relative momentum. (c) and (d) Expectation values for the variances of the collective antisqueezed variables calculated using the input-output theory.

uncertainty on the squeezing parameter. In practice, the calculated squeezing parameter takes imaginary values for some high values of the pump amplitudes. We have checked however that even with the least favorable values for G_a and G_b, the variance of the squeezed collective variables goes bellow that of the vacuum fluctuations.

In this section we present an improvement on the measured power spectral density as shown in Fig. 29b, where the noise is measured separately for each quadrature of the field as a function of frequency. Characteristic features are predicted for the dependence of the single mode squeezing parameter as a function of frequency, which this measurement aims at demonstrating.

In order to measure the noise on a particular quadrature at a given frequency $\delta\omega$ in the simulation frame ($\omega_a + \delta + \delta\omega$ in the lab frame for port a), we first numerically demodulate the signal on a port at the level of the ADC at frequency $\Delta - \delta\omega$ (see Fig. 35) for two orthogonal quadratures, say x and y. With a varying frequency, the phase reference is ill defined but it is possible to calculate the variance $\sigma(\theta) = \overline{(\cos(\theta)x + \sin(\theta)y)^2}$ for any phase θ. In Fig. 41, we show the maximal and minimal variances $\sigma(\theta)$ as a function of frequency referred to the variance obtained with the pump turned off (0 dB). We have checked that minimal and maximal variances are obtained for orthogonal quadratures as expected for Gaussian states. This procedure is equivalent to calculating the eigenvalues of the full covariance matrix in the measurement basis $x_{a,b}$ and $y_{a,b}$ for a and b modes.

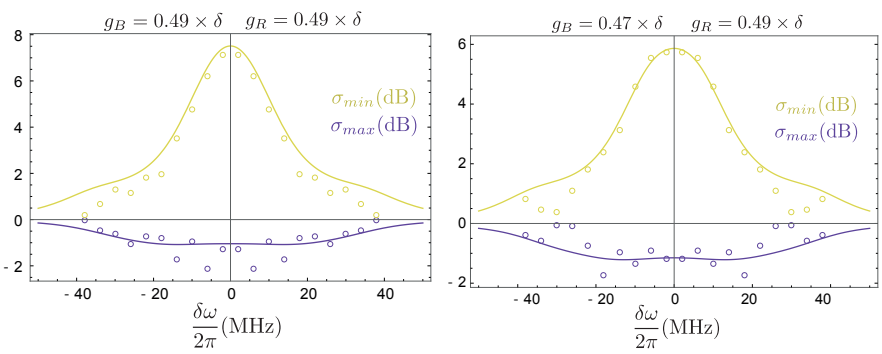

(a) (b)

Figure 41: Measured minimum and maximum variance σ_{min} and σ_{max} as a function of frequency $\delta\omega$ in the proximity of the origin of the rotating frame, corresponding to $\omega_a + \delta$ in the laboratory frame. Figures (a) and (b) correspond to two different values of the coupling rate of the blue pump g_B. Full line corresponds to the expectation values calculated using the input-output theory.

In Fig. 41, we show the measured and predicted variances as a function of frequency for two values of the blue pump amplitude in a regime where $g_B \lesssim \delta/2$. Below vacuum squeezing ($\sigma_{\min} < 1$) can be observed over a range of frequencies comparable to 2δ and a characteristic bump can be observed over the same bandwidth for the antisqueezing component ($\sigma_{\max}$).

3.4 CONCLUSION

The main results of this chapter are:

- Spectroscopic detection of frequency splitting as a function of coupling rate, with demonstrated coupling rates g of the order of the effective frequencies δ.
- Measurement of quadrature statistics for the emitted radiation in the effective ultrastrong coupling regime and detection of both the single mode and the two mode squeezing that go below the variance of the vacuum fluctuations.
- Measurement of single mode quadrature squeezing and antisqueezing as a function of frequency.

Part II

QUANTUM NODE

4

QUANTUM NODE FOR QUANTUM INFORMATION PROCESSING

> "The day science begins to study non-physical phenomena, it will make more progress in one decade than in all the previous centuries of its existence."
>
> *Nikola Tesla*

Building a large scale quantum computer capable of performing fault tolerant quantum information processing requires long coherence lifetime of quantum bits. To extend the lifetimes, the best solution known up to date is the quantum error correction (QEC) [85, 86]. It requires errors to be sparse, below a certain threshold, so that they can be identified and corrected. This threshold and thus the efficiency and complexity of QEC depend on the circuit architectures.

One of the most popular architectures, inspired by that of classical processors, are stabilizer codes. The idea here is to redundantly encode information in a register consisting of many qubits and thus offering a large Hilbert space. A particular stabilizer code, called a surface code, is commonly adopted with superconducting circuits [87, 88]. The main challenge with this architecture consists in building a processor with 100 or even 1000 qubits, which is beyond the current state of the art, as well as monitoring all the decoherence channels brought by every qubit in order to detect the error syndromes.

An alternative is a modular architecture consisting of smaller interconnected registers. Each register should contain a memory qubit that stores the signal and performs local error correction, and communication qubits that interact with other modules [7]. Modular quantum networks are expected to have reduced undesired cross-talk and minimize error propagation [89]. Theoretical work has shown that

relatively high threshold for error rates within each module can be tolerated even with noisy quantum communication channels [90].

A promising implementation of modular architecture for a future quantum network is based on quantum nodes connected through photonic channels [91]. Thanks to their rapid propagation and the ability to be guided through optical fibres with limited loss, optical photons are good candidates for communicating quantum information over long distances. Superconducting qubits on the other hand, have much smaller energy level separations, so that they couple to microwave photons. This qualifies them as a candidate for building a microwave quantum network.

In such quantum network composed of many quantum nodes and channels, quantum interconnects are essential to reversibly convert quantum states from one physical system to another [89]. A microwave quantum node should generate and distribute microwave entangled fields while enabling control of their emission and reception over time [22]. This second functionality is that of a quantum memory.

In this chapter we will first review different existing implementations of a microwave quantum node with various long lived hybrid systems and we will in particular focus on the use of microwave resonators as quantum memories. Then, we will explain how coupling such a memory resonator to a qubit can enable preparation of arbitrary quantum states, as well as their readout. Finally, we will show how a microwave quantum node can be implemented using microwave resonators coupled through a Josephson ring modulator, a device called Josephson Parametric Converter.

4.1 MICROWAVE QUANTUM NODES: STATE OF THE ART

Coupling of microwaves to various systems has been demonstrated over the past few years. By consequence, different hybrid systems have been developed by coupling Josephson circuits to highly coherent systems for quantum state storage. Some examples are summed up in Table 5. We will briefly review the most promising ones.

system	experiment	t_s
NV centers	[35] 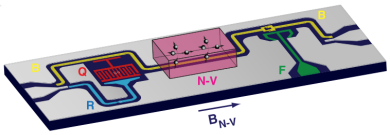	$\sim$ 200 ns
magnons	[92] 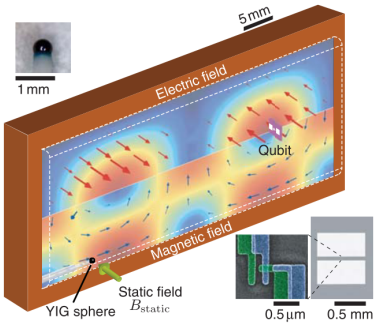	$\sim$ 700 ns
mechanical resonator	[93] 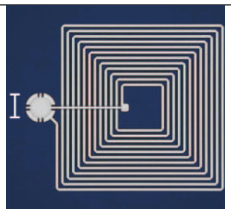	$\sim$ 90 μs
piezoelectric resonator	[94] 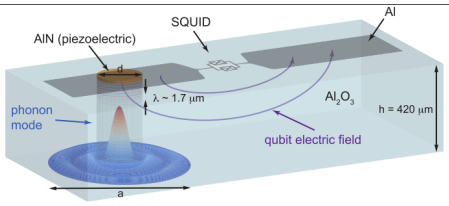	17 μs
coaxial $\lambda/4$ resonator	[95] 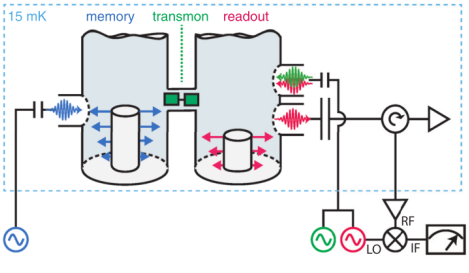	1.33 ms

Table 5: Examples of experimental realizations of a microwave quantum memory with different physical systems.

4.1.1 *Spin ensemble memories*

Spin ensemble based quantum memories for superconducting qubits were built both at CEA Saclay [35] and Atsugi in Japan [36] by coupling a superconducting qubit to a spin ensemble of Nitrogen Vacancy (NV) centers in diamond. Although the coupling rate g of one individual microscopic system, such as a single NV spin, to a superconducting circuit is too weak for quantum information applications [1], ensemble of N such systems is enhanced by collective effects and coupled at a rate $\sqrt{N}g$. In the low excitation limit this collective variable behaves as a harmonic oscillator, which enables coherent exchange of a single quantum of energy between the qubit and the macroscopic ensemble of NV centers. Any arbitrary quantum state of the microwave field can thus be mapped on the coherent state of the spin ensemble. However, the storage time of this memory is limited by two phenomena. On one side the electronic spin of the NV center is coupled through the hyperfine interaction to the nuclear spin of ^{14}N. This hyperfine structure causes an interference effect resulting in short spin dephasing times, ultimately limiting the fidelity of the memory storage-retrieval process. On the other side, each individual spin experiences a different local magnetic environment which results in an inhomogeneous broadening of the spin ensemble resonance. Clever manipulations can however use these effects to realize multimode storage [97].

Finally, although the collective coupling in enhanced with the number of spins N, when this number becomes important, the spin-spin interactions degrade the coherence time. A trade off thus needs to be made on the number of spins between large coupling and long coherence times. An alternative and counterintuitive approach consists in introducing a strong exchange between the neighboring spins and is adopted with ferromagnetic magnons.

4.1.2 *Ferromagnetic magnons memories*

Magnons are quanta of collective excitation modes in ordered spin systems such as a ferromagnets. In ordered systems, the spin dynam-

1 Although works in this direction are very promising [96].

ics is dominated by the strong spin-spin exchange and dipolar interactions. This results in narrow linewidth magnetostatic modes which are thus good candidates for high quality long lived quantum memories. In the Tokyo group, strong coherent coupling has been realized between a single magnon excitation of a yttrium iron garnet (YIG) ferromagnet and a superconducting qubit, mediated by the virtual photon excitation of a microwave cavity [92].

Recently, a big step was made towards encoding the state of a qubit into a superposition of magnon coherent states in a magnetostatic mode, when strong dispersive regime was demonstrated in quantum magnonics [98]. Moreover, bidirectional conversion has been realized between microwave and optical photons in macroscopic YIG sphere [99]. This opened the path towards the transfer of quantum states between superconducting qubits and photons in optical fibers, even tough the maximum achieved photon conversion efficiency was quite small, of the order of 10^{-10}. As a matter of fact, frequency conversion of electromagnetic field requires some nonlinear interaction, such as $\chi^{(2)}$ nonlinearity in ferroelectric crystals like LN and KTP, or Josephson nonlinearity in parametric amplifiers based on Josephson junctions. In the case of the conversion from microwave to optical photons, the difficulty is that the nonlinearity is often small.

The YIG based converter consists of a microwave cavity and a magnetostatic mode called the Kittel mode, that are strongly coupled. An itinerant microwave field mode is then coupled to the converter through the microwave cavity mode, whereas a traveling optical field mode is coupled to the converter through the Kittel mode. The limiting factor for the conversion efficiency is the small magnon-light coupling.

In the following section, we will review the currently most efficient and promising platform for quantum transducers between spectrally distant frequency domains, that is based on optomechanical devices.

4.1.3 *Hybrid Optomechanical Quantum Node*

Since the quantum ground state cooling of mechanical resonators has been demonstrated in 2011 at Boulder [100] and at Pasadena [101], optomechanical systems have entered the scene of possible building blocks for quantum information processing networks.

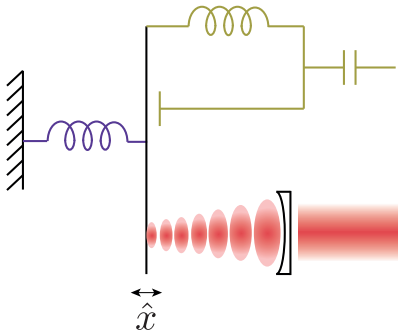

Figure 42: Hybrid optomechanical quantum node is composed of a mechanical oscillator that is simultaneously coupled to an optical and a microwave cavity, thus allowing entanglement distribution and quantum states conversion across the through different ranges of electromagnetic spectrum.

Optomechanical coupling is mediated by the radiation pressure exerted by the light on a mechanical resonator. The interaction is thus proportional to the number of photons in the cavity and to the mechanical displacement, such that the interaction Hamiltonian reads

$$\hat{H}_{int} = \hbar g \hat{a}^\dagger \hat{a}(\hat{b} + \hat{b}^\dagger), \tag{103}$$

where $\hat{a}$ is the annihilation operator for microwave cavity photons and $\hat{b}$ is the annihilation operator for mechanical phonons, such that the position of the mechanical resonator is defined as $\hat{x} = x_{zpf}(\hat{b} + \hat{b}^\dagger)$. The strong coherent field $\hat{a}$ can be split in the average coherent amplitude $\langle \hat{a} \rangle = \alpha$ and the fluctuating term $\delta\hat{a}$

$$\hat{a} = \langle \hat{a} \rangle + \delta\hat{a}, \tag{104}$$

so that the Hamiltonian can be linearized

$$\hat{H}_{int} = \hbar g(\alpha + \delta\hat{a})^\dagger(\alpha + \delta\hat{a})(\hat{b} + \hat{b}^\dagger) \tag{105}$$

and then expended in powers of α. The $|\alpha|^2$ term is an offset coming from the average radiation pressure $\langle F \rangle = \frac{\hbar|\alpha|^2 g}{x_{ZPF}}$. Assuming that $\alpha = \sqrt{N}$ is real and neglecting the second order term in $\delta\hat{a}^\dagger\delta\hat{a}$, the Hamiltonian finally reads

$$\hat{H}_{int} = \hbar g\sqrt{N}(\delta\hat{a}^\dagger + \delta\hat{a})(\hat{b} + \hat{b}^\dagger). \tag{106}$$

The cavity is driven at $\omega_a + \Delta$, where ω_a is the resonance frequency of the optical cavity and Δ is the detuning of the laser to the cavity. If the detuning is set to the frequency of the mechanical mode, $\Delta = \omega_b$, the interaction Hamiltonian simplifies to the parametric down-conversion Hamiltonian

$$\hat{H}_{pdc} = \hbar g\sqrt{N}(\delta\hat{a}^\dagger\hat{b}^\dagger + \delta\hat{a}\hat{b}), \tag{107}$$

equivalent to the parametric amplification Hamiltonian of the Josephson Ring Modulator. Similarly, by setting the detuning to $\Delta = -\omega_b$, the beam-splitter Hamiltonian is obtained

$$\hat{H}_{bs} = \hbar g\sqrt{N}(\delta\hat{a}^\dagger\hat{b} + \delta\hat{a}\hat{b}^\dagger), \tag{108}$$

equivalent to the parametric conversion of the Josephson Ring Modulator.

The two necessary requirements for a quantum node are thus fulfilled and their implementation was experimentally demonstrated, the entanglement distribution [74] and the coherent state transfer between the microwaves and the mechanical resonator [93, 102]. Furthermore, as mechanical oscillators combine high quality factors with low resonance frequencies, they are a promising candidate for long lived quantum memories.

Similarly to magnons, phonons in nanomechanical devices are spatially extended collective excitations that interact coherently both with microwave and optical degrees of freedom. The Boulder group demonstrated record conversion efficiency of 0.1 between microwaves and optical photons on a bandwidth of 30 kHz [103].

Finally, piezoelectric materials can be used to achieve strong coupling between single electrical and mechanical excitations. Recently, the Yale group has demonstrated strong coupling between a superconducting qubit and the phonon modes of an acoustic wave resonator using an aluminum nitride (AlN) piezoelectric transducer [94].

4.1.4 *Microwave cavities*

A straightforward approach for a quantum node design is a full microwave architecture, where a superconducting microwave resonator is used for quantum state storage. Indeed, superconducting resonators

have a very weak Kerr effect nonlinearity and are orders of magnitude more frequency tunable then mechanical resonators. They are also routinely coupled to superconducting qubits and have small intrinsic losses.

There are two broad categories of superconducting microwave resonators, 2D planar on chip resonators and 3D cavities. They will be analyzed in more details in the section 4.2. Quantum memories have been realized with both 2D and 3D microwave resonators. Planar microwave resonator memories were realized at UCSB [104] and at Chalmers [105]. In both cases, tunable coupling was integrated through a superconducting quantum interference device (SQUID), whose inductance can be controlled by an externally applied magnetic flux bias.

The Yale group has recently developed a robust 3D architecture based on a $\lambda/4$ coaxial section [95]. Thanks to a design that does not involve connecting parts with seams, which were identified as the main source of losses and decoherence, it has enabled reaching record storage time of a ms. Note that in another context, microwave cavities reach a fraction of a second lifetime in CQED [106].

4.2 MICROWAVE RESONATORS

4.2.1 *Planar microwave resonators*

In planar resonators, photons are confined in one dimension and travel along a transmission line. The transverse dimension can be much smaller than the wavelength, which enables very strong coupling to mesoscopic objects.

Planar resonators come in several geometries. For the samples used in the experiments described in this thesis we used microstrip and coplanar waveguide (CPW) geometries. Microstrip transmission lines consist of a conductive strip of width w and thickness t and a wider ground plane, separated by a dielectric substrate of height h and relative permittivity ϵ_r, as shown in Fig. 43 (a). When $w < h$, an approximate expression for the characteristic impedance of microstrip transmission line [107] is

$$Z_0^{\mu s} = \frac{60}{\sqrt{\epsilon_{eff}}} \ln\left(8\frac{h}{w} + 0.25\frac{w}{h}\right), \tag{109}$$

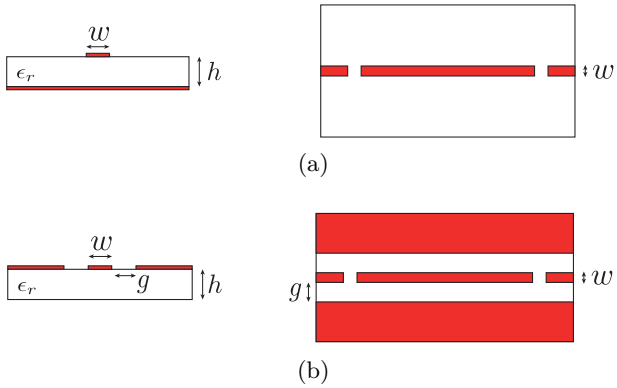

Figure 43: (a) Schematic of the microstrip geometry. Side view is shown on the left and the top view on the right. White area is the substrate and red areas are superconducting films. (b) Schematic of the CPW geometry. These systems are microwave analogs of a Fabry-Perot cavity, where the cuts in the central conductor play the role of mirrors. The size of the cut, that is the value of capacitance, determines the transparence of the mirror.

where the effective dielectric constant is

$$\epsilon_{eff} = \frac{\epsilon_r + 1}{2} + \frac{\epsilon_r - 1}{2}[(1 + 12\frac{h}{w})^{-\frac{1}{2}} + 0.04(1 - \frac{w}{h})^2]. \tag{110}$$

As some of the field lines are in the dielectric region and some are in the air, and $\epsilon_r^{air} = 1$, the effective dielectric constant satisfies

$$1 < \epsilon_{eff} < \epsilon_r. \tag{111}$$

CPW transmission line consists of a conductor separated from a pair of equidistant ground planes on the two sides, all on the same side of the substrate. The substrate should be thick enough so that electromagnetic fields die out before they get out of it.

For both microstrip and CPW, the resonator is created by interrupting the transmission line which creates the impedance discontinuities. This causes microwaves to reflect, like in a Fabry-Perot cavity. The fundamental mode is a $\lambda/2$ mode, corresponding to the length of the resonator equal to half of the wavelength. These are thus distributed resonators, their size is comparable to their wavelength.

By opposition, lumped or compact resonators are much smaller then the resonance wavelength. Typically they consist of a largely

inductive region in parallel with a largely capacitive region. Inductance can take shape of a very thin wire, while compact capacitor can be build of two large plates separated by a dielectric, or by two interdigitated comb structures.

The main limitation of all the planar architectures comes from the fact that they concentrate the electromagnetic energy near the surface of the dielectric substrate which induces losses and limits the coherence times [108, 109, 110, 111]. Various defects in amorphous dielectric material act as macroscopic two-level systems and induce discrete dissipation mechanisms. To increase the quality factor of the resonator, one strategy is to store the energy in the air. This can be done with three dimensional rectangular waveguide resonators.

4.2.2 *Rectangular waveguide microwave resonators*

Alternatively, microwave resonators can be realized as cavities in bulk metal such as copper or aluminum. The electric and magnetic fields are then stored inside of the cavity and coupling is realized through a small aperture in the cavity wall. The resonant modes of a rectangular cavity are transverse electrical TE_{mnl} and transverse magnetic TM_{mnl} modes, where the indices m, n, l refer to the number of variations in the standing wave pattern in directions x, y, z. For a cavity of dimensions $a \times b \times d$, as in the Fig. 44, the resonance frequency for TE_{mnl} mode is

$$f_{mnl} = \frac{c}{2\pi\sqrt{\mu_r \epsilon_r}} \sqrt{(\frac{m\pi}{a})^2 + (\frac{n\pi}{b})^2 + (\frac{l\pi}{d})^2}. \tag{112}$$

If $d < b < a$, the lowest frequency resonant mode will be TE_{110}, which is typically chosen to be the memory mode in our experiments.

The 3D resonators have the advantage of reaching very high quality factors, enabling storage times almost of the order of seconds [106]. However, their coherence was observed to decrease by orders of magnitude when they are coupled to planar superconducting circuits [112, 6], which introduce additional dissipation mechanisms such as substrate loss and mechanical instability. Most importantly, 3D cavities have to be assembled from parts in order to allow for integration of Josephson junction based circuits on chips. This introduces dissipative seams that have been identified as a main source of dissipation

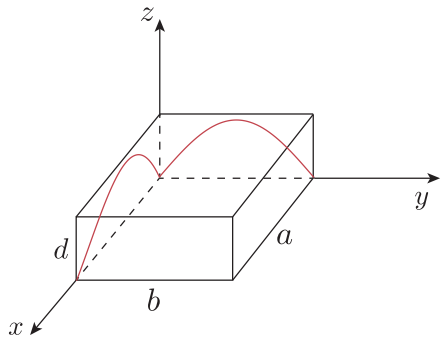

Figure 44: TE_{110} mode of a rectangular waveguide cavity.

[113, 114]. Our experiments have confirmed this, as it will be discussed in Section 5.6.

4.2.3 *Equivalent LC resonator*

Independently of their planar or 3D implementation, the fundamental mode of microwave resonators can be represented by the equivalent LC circuit shown in Fig. 45. The Hamiltonian of the equivalent dissipationless LC circuit reads

$$\hat{H} = \frac{\hat{q}^2}{2C} + \frac{\hat{\phi}^2}{2L}, \tag{113}$$

where flux operator $\hat{\phi}$ and charge operator $\hat{q}$ are conjugate observables and satisfy the commutation relation

$$[\hat{\phi}, \hat{q}] = i\hbar. \tag{114}$$

Thus by defining the annihilation operator

$$\hat{a} = \sqrt{\frac{1}{2\hbar Z_0}}\hat{\phi} + i\sqrt{\frac{Z_0}{2\hbar}}\hat{q}, \tag{115}$$

the Hamiltonian (113) can be quantized into the Hamiltonian of the quantum harmonic oscillator

$$\hat{H} = \hbar\omega_0(\hat{a}^\dagger\hat{a} + \frac{1}{2}), \tag{116}$$

of resonance frequency $\omega_0 = 1/\sqrt{LC}$ and characteristic impedance $Z_0 = \sqrt{\frac{L}{C}}$ as shown in Fig. 45.

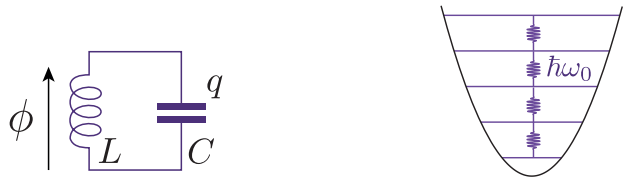

(a) (b)

Figure 45: (a) LC resonator equivalent of the microwave cavity mode. ϕ is the magnetic flux threading the inductor and q is the charge on the electrode of the capacitor. (b) The energy dispersion of this system is that of a quantum harmonic oscillator.

As quantum harmonic oscillator has an infinite dimensional Hilbert state, it can be used for redundant quantum information encoding [24]. Using a microwave cavity mode for a microwave quantum memory, rather then a multiqubit register, presents other advantages as well. Contrary to adding more qubits to a register, the number of decoherence channels does not increase when more photons are added to the cavity.

On the other hand, a linear system such as a harmonic oscillator allows only the preparation of coherent states using classical drives. In the following section, we will explain how resonantly coupling a qubit to a microwave resonator allows to gain controllability over it and prepare arbitrary quantum states. We will also present two models used to describe the system of a qubit coupled to a cavity mode and make predictions of the system parameters relevant for the design of the experiment.

4.3 COUPLING A QUBIT TO A CAVITY

4.3.1 *Transmon qubit*

Superconducting qubits are based on Josephson junctions, made of two superconducting electrodes separated by a thin insulating layer, that allows the Cooper pairs to tunnel through. In our experiments, we use aluminum that is a superconductor at temperatures bellow 1K and whose oxyde, Al_2O_3, is an insulator used for the tunnel barrier. For fabrication details, see section 8. Transmon is a type of super-

conducting qubit that consists of a single small Josephson junction between two capacitive antennas. It is described by the Hamiltonian

$$\hat{H} = 4E_C(\hat{n} - n_g)^2 - E_J \cos\hat{\delta}, \tag{117}$$

where $\hat{\delta} = \frac{\hat{\phi}}{\varphi_0}$ is the dimensionless superconducting phase difference and $\hat{n}$ is the excess number of Cooper pairs on one of the electrodes. The charge energy reads

$$E_C = \frac{e^2}{2C}, \tag{118}$$

where C is the total capacitance between the electrodes and n_g is the offset pair charge. This Hamiltonian can be expanded to

$$\hat{H} = 4E_C(\hat{n} - n_g)^2 + E_J\frac{\hat{\delta}^2}{2} + \hat{H}_1, \tag{119}$$

where $\hat{H}_1$ is the purely nonlinear perturbation that reads to the fourth order

$$\hat{H}_1 = -\frac{E_J}{24}\hat{\delta}^4. \tag{120}$$

Josephson junction is equivalent to a nonlinear inductor of inductance $L_J = \frac{\varphi_0^2}{E_J}$, where E_J is the Josephson energy. Transmon qubit can thus be represented by an equivalent LC circuit shown in Fig. 46. It is the electrical equivalent of the harmonic oscillator, but the nonlinearity of the inductance makes its energy levels anharmonic, i.e. not regularly spaced.

Hamiltonian (117) describes a general Cooper Pair Box (CPB) qubit. Coherence times of qubits are limited by either dissipation T_1 or dephasing T_ϕ. Dissipation sets the limit $T_2 = 2T_1$ on coherence time, but supplementary decoherence channels coming from charge, flux or current fluctuations prevent this limit from being reached, so that in general $\frac{1}{T_2} = \frac{1}{2T_1} + \frac{1}{T_\phi}$. The main source of decoherence for CPB qubits is the charge noise coming from the fluctuations of the charge offset n_g. A transmon is a CPB qubit with a significantly increased ratio of Josephson energy and charging energy $\frac{E_J}{E_C} \sim 40 - 100$, which results in drastically decreased sensitivity to the charge noise and improved coherence time [115, 116], making it one of the favorite qubit flavors for quantum information applications.

(a) (b)

Figure 46: (a) Equivalent LC circuit of a Josephson junction. Transmon qubit is obtained by shunting the junction with a large capacitor formed by two big superconducting antennas. (b) Transmon energy levels in its electromagnetic phase potential.

However, the gain in the charge noise insensitivity is paid by the loss of anharmonicity. The anharmonicity of the qubit, $\alpha = \omega_{ef} - \omega_{ge}$ is essential to reduce the many-level system to a quantum two level system that can be selectively addressed.

It stems from the perturbative treatment of Hamiltonain (117), that the anharmonicity to the leading order is given by the charge energy, $\hbar\alpha \simeq E_C$ and the relative anharmonicity $\alpha_r = \frac{\alpha}{E_{eg}} \simeq (\frac{8E_J}{E_C})^{-\frac{1}{2}}$. The loss in anharmonicity is thus described only by a weak power law in $\frac{E_J}{E_C}$, so that there is an attainable regime where the anharmonicity is much larger then the linewidth given by the dissipation. This is the transmon regime.

4.3.2 *3D transmon*

The integration of a transmon in a 3D resonator was done similarly to the design developed by Paik *et al.* [117]. The so called 3D transmon has become very popular as its coherence time is increased by an order of magnitude compared to a qubit coupled to a planar resonator. This is due to the fact that 3D cavities have larger mode volumes than the planar ones, which results in reduced energy storage in lossy materials such as dielectric substrates. By consequence, the qubit is less sensitive to the poor dielectric quality of the surfaces and material interfaces.

On the other hand, the electric field created by a single photon is reduced compared to the more confined planar architecture, which

makes it more challenging to reach the strong coupling. This is solved by making the electrodes of the qubit significantly larger than in a conventional 2D transmon qubit, so that the dipole moment of the qubit is increased. Usually the qubit is placed in the center of the cavity, at the antinode of the TE_{110} mode, so that their coupling is maximized. This minimizes the coupling to the mode TE_{120} as well, as it has an antinode in the center of the cavity.

4.4 TRANSMON COUPLED TO A CAVITY

Strictly speaking, transmon in a cavity is a weakly nonlinear mode coupled to a continuum of cavity modes. Whereas the CPB Hamiltonian (117) is exactly solvable in terms of Mathieu functions [115], approximations have to be made to find solutions when it is coupled to a discretized environment. Traditionally, the approximation that is made is single mode Jaynes-Cummings method.

4.4.1 *Jaynes-Cummings method in the strong dispersive coupling limit*

Jaynes-Cummings method consists in considering an infinitely anharmonic transmon, such that it can be modeled by a pure two-level system, coupled to a single cavity mode. In other words, a supposition is made that all the other cavity modes are far detuned and can be neglected. The system is then described by the Jaynes-Cummings Hamiltonian (10), that in the dispersive limit [115], $\omega_a - \omega_q \gg g$ simplifies to

$$\hat{H} = \hbar\omega_a \hat{a}^\dagger \hat{a} + \hbar\frac{\omega_q}{2}\hat{\sigma}_z - \hbar\chi\hat{a}^\dagger\hat{a}\,|e\rangle\langle e|\,, \tag{121}$$

where ω_a is the frequency of the fundamental cavity mode, ω_q is the qubit frequency, g is their coupling rate and χ is the dispersive shift or cavity pull. For a true two-level qubit,

$$\chi = \frac{g^2}{\Delta}, \tag{122}$$

where we have introduced the detuning $\Delta = \omega_a - \omega_q$. On the other hand, for the transmon qubit which is only weakly anharmonic [115], the dispersive shift reads

$$\chi = \frac{2g^2}{\Delta}\frac{2\alpha}{\Delta - \alpha}. \tag{123}$$

Qubit and cavity modes are entangled through the cross-Kerr term $-\hbar\chi\hat{a}^\dagger\hat{a}\,|e\rangle\langle e|$ in the Hamiltonian (121), which can be rewritten as

$$\hat{H} = \hbar\hat{a}^\dagger\hat{a}(\omega_a - \chi\,|e\rangle\langle e|) + \hbar\frac{\omega_q}{2}\hat{\sigma}_z, \tag{124}$$

where the first term shows that the cavity frequency depends on the state of the qubit,

$$\begin{cases} \omega_a^g = \omega_a & \text{for qubit in state } |g\rangle \\ \omega_a^e = \omega_a - \chi & \text{for qubit in state } |e\rangle\,, \end{cases} \tag{125}$$

and can be used for the purpose of qubit readout. Furthermore, by putting Hamiltonian (121) in the form

$$\hat{H} = \hbar\omega_a\hat{a}^\dagger\hat{a} + \hbar\frac{\omega_q}{2}\,|g\rangle\langle g| - \hbar(\frac{\omega_q}{2} + \chi\hat{a}^\dagger\hat{a})\,|e\rangle\langle e|\,, \tag{126}$$

we can see that the frequency of the qubit as well depends on the mean number of photons in the cavity $\langle\hat{a}^\dagger\hat{a}\rangle$, which can be used for the photon number counting or cavity state readout. For instance, when the cavity is in the Fock state $|n\rangle$, frequency of the qubit is

$$\omega_q^n = \omega_q - n\chi. \tag{127}$$

The qubit and cavity lifetimes are related as well through the Purcell effect, that corresponds to the relaxation of the qubit by the emission of a photon in the cavity, that is afterwards emitted in the cavity dissipation channels. In the perturbative treatment of Hamiltonian (121), expanding in powers of $\frac{g}{\Delta}$, the Purcell rate for dispersive decay is found to be

$$\gamma_{1,Purcell} = \kappa\frac{g^2}{\Delta^2}, \tag{128}$$

where κ is the average photon loss rate of the cavity. The Purcell rate sets the bound on the relaxation time T_1 of the qubit

$$T_1 = \frac{1}{\gamma_{1,Purcell} + \gamma_{1,non\ radiative}}, \tag{129}$$

where $\gamma_{1,non\ radiative}$ corresponds to other decoherence channels of the qubit. This approximation gives an excellent estimation in the case of a single-mode cavity, but 3D cavity has many independent spatial modes that can couple strongly to the qubit and induce its decay. In particular, the single mode approximation was shown to break down at qubit frequencies larger then the cavity frequency where measured times T_1 deviate considerably from those predicted by Eq. (128) [118].

We can conclude that for strong couplings, the interaction with the higher excited states of the transmon and other cavity modes has to be accounted for.

4.4.2 *Black Box Quantization (BBQ)*

An alternative method, called the Black Box Quantization method (BBQ), was developed at Yale by Nigg *et al.* [119]. Within this approach, the electromagnetic environment of the qubit is treated as a linearized system of harmonic oscillators. The impedance of the linear part of the circuit, including the linear part of the Josephson inductance is

$$Z(\omega) = \sum_{p=1}^{M} \left(j\omega C_p + \frac{1}{j\omega L_p} + \frac{1}{R_p} \right)^{-1}, \tag{130}$$

where M is the number of modes and $j = -i$. Resonance frequencies of the linear circuit are then found as the real parts of the zeros of the admittance $Y(\omega) = Z(\omega)^{-1}$. The Hamiltonian of the total circuit including the Josephson junction is

$$\hat{H} = \sum_p \hbar\omega_p \hat{n}_p + \sum_p \Delta_p \hat{n}_p + \frac{1}{2} \sum_{pp'} \hbar\chi_{pp'} \hat{n}_p \hat{n}_{p'}, \tag{131}$$

where $\hat{n}_p = \hat{a}_p^\dagger \hat{a}_p$ is the number operator for the mode p and Δ_p is the correction to the Lamb shift for the mode frequencies. The oscillators inherit some anharmonicity from the Josephson junction, so that presence of photons in the mode p shifts the frequencies of the modes p' through dispersive shift

$$\chi_{pp'} = 2\sqrt{\chi_{pp}\chi_{p'p'}}, \tag{132}$$

where $\chi_{pp'} = \alpha_p$ is the anharmonicity of the mode p given by

$$\alpha_p = \chi_{pp} = -\frac{L_p}{L_J}\frac{C_J}{C_p} E_C. \tag{133}$$

The qubit frequency can be found as

$$\omega_q = \frac{1}{\hbar}\sqrt{8E_J E_C}. \tag{134}$$

The lifetime of the mode p is given by

$$\kappa_p = \omega_p \frac{Z_p}{R_p}, \tag{135}$$

where the losses R_p and the capacitances C_p of the mode p can be found from the linear environment admittance Y at the frequency of the mode

$$\begin{cases} R_p = \frac{1}{\mathrm{Re}[Y(\omega_p)]} \\ C_p = \frac{1}{2}\,\mathrm{Im}[Y'(\omega_p)]. \end{cases} \tag{136}$$

We can then deduce the relationship between qubit T_1 due to spontaneous emission and admittance of the linear environment is

$$T_1 = \frac{1}{\gamma_1} = \frac{C_J}{\mathrm{Re}[Y(\omega_q)]}. \tag{137}$$

This method is suitable for weakly nonlinear circuits, such as those coupled to a transmon, for which the normal modes of the linearized classical circuit provide a good basis in the quantum case. In section 10.1 we will discuss how both of these methods, the single mode Jaynes-Cummings method and the Black Box Quantization, can be used to predict the relevant parameters of the system, design the experiment and calculate the geometrical constraints.

4.4.3 *Arbitrary quantum state preparation with a coupled cavity-qubit system*

In this section we will explain how a system of two parametrically coupled harmonic oscillators, one of which is also coupled to a qubit, allows preparation of an arbitrary quantum state.

Parametric coupling between the two oscillators, buffer a and memory m, that can be realized using a Josephson ring, allows preparation of an entangled EPR state

$$|EPR\rangle = \sum_k c_k \,|k,k\rangle\,, \tag{138}$$

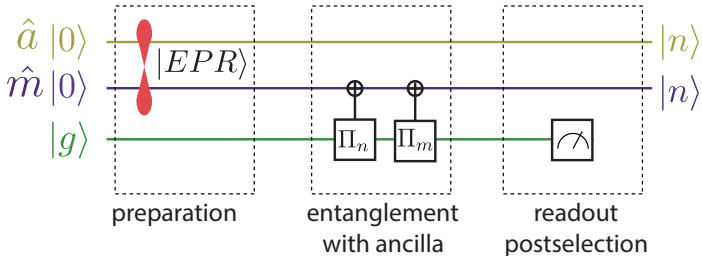

Figure 47: Quantum state preparation protocol.

where $c_k = \tanh(r)^k \cosh(r)^{-1}$ and r is the squeezing parameter. Then using the entanglement between the qubit and the memory field, an arbitrary set of selective π pulses can be performed on the qubit, conditioned on the number of photons in the cavity k, such that the state of the system becomes

$$\sum_k c_k \,|k,k,0\rangle \to \Big[c_n \,|n,n\rangle + c_m \,|m,m\rangle\Big] \otimes |1\rangle + \sum_{k\neq n,m} c_k \,|k,k,0\rangle \tag{139}$$

Finally, by post-selecting on the measurement outcomes where the qubit is found in the excited state $|1\rangle$, the state $c_n \,|n,n\rangle + c_m \,|m,m\rangle$ is prepared with probability $|c_n|^2 + |c_m|^2$.

Interestingly, the buffer mode a can be strongly coupled to a transmission line, so that its field rapidly leaks to the propagating mode. The effective EPR state is then between the stationary memory mode and the mode propagating in the transmission line. By performing local operations on the qubit, the propagating mode can remotely be prepared in an arbitrary quantum state.

A variation on this protocol is entanglement concentration from continuous to discrete variables [120]. The purpose of entanglement distillation is to extract a maximally entangled state from a collection of less entangled states. In the case of continuous variables, it can be for example a conversion from EPR to a Bell state. This protocol can be used as an entanglement resource for repeaters in quantum communication.

4.5 QUANTUM NODE BASED ON JOSEPHSON PARAMETRIC CONVERTER

Two main required functionalities for a quantum node are generation and distribution of entanglement and time control of field reception and emission. Both of them are enabled by the parametric interaction such as the one provided by the Josephson Ring Modulator (JRM). As already discussed in Chapter 2, entanglement distribution can be obtained by applying the amplifying pump on the coupled resonators in the ground state, which results in an EPR state (Eq. 29). If one of the resonators is strongly coupled to a transmission line, the field can continuously leak out to it, such that the final state is an entangled EPR state between the field propagating in the transmission line and the stationary field in the second resonator isolated from the environment.

Time controlled field reception and emission to and from a high quality resonator enables realization of quantum information storage. It requires coherent state conversion of the propagating field to the stationary memory mode. As first demonstrated at Yale [121], such a lossless frequency conversion can be performed by a JRM between its two modes.

We have seen in section 2.2.1 that in a device such as Josephson Mixer or Josephson Parametric Converter (JPC), two planar resonators are coupled through a JRM. The equivalent LC circuit for a JPC is shown in Fig. 48. To realize a quantum memory device, low quality resonator a, of resonance frequency ω_a is strongly coupled to the transmission line, and we refer to it as a buffer resonator. The high quality memory resonator m, of resonance frequency ω_m is decoupled from the environment, such that its losses are decreased and storage time maximized.

The Hamiltonian of this circuit reads

$$\frac{1}{\hbar}\hat{H} = \omega_a \hat{a}^\dagger \hat{a} + \omega_m \hat{m}^\dagger \hat{m} + \chi(p^* + p)(\hat{a}^\dagger + \hat{a})(\hat{m}^\dagger + \hat{m}), \quad (140)$$

where $\hat{a}$ and $\hat{m}$ are annihilation operators for the buffer and memory modes.

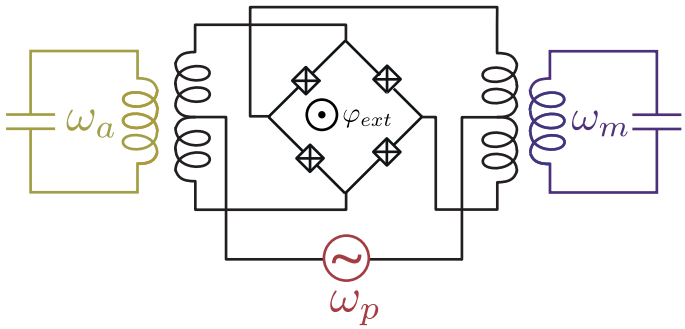

Figure 48: Equivalent LC circuit for a JPC. Buffer mode with a resonance frequency ω_a and memory mode with resonance frequency ω_m are coupled by a ring of four Josephson junction that realizes the three-wave mixing. An external pump tone is applied at frequency ω_p.

When the pump is applied at the difference of the frequencies of the two resonators $\omega_p = \omega_a - \omega_m$, the three wave mixing interaction Hamiltonian simplifies to the parametric conversion Hamiltonian

$$\frac{1}{\hbar}\hat{H}_{conv} = \chi|p|(\hat{a}\hat{m}^\dagger + \hat{a}^\dagger\hat{m}), \tag{141}$$

where $\chi|p|$ corresponds to the conversion rate between modes a and m. This rate can be time controlled through the pump amplitude $|p|$, such that the coupling can be turned on and off on demand. If the buffer mode is strongly coupled to the transmission line, the itinerant field a_{in} can be captured to the memory and retrieved at a later time in the output mode a_{out}.

With coupling and dissipation rates κ_a and κ_a^{loss} for the buffer mode and κ_m and κ_m^{loss} for the memory mode, we can write the Langevin equations

$$\begin{cases} \frac{\partial \hat{a}}{\partial t} = \frac{i}{\hbar}[\hat{H}, \hat{a}] - \frac{\kappa_a + \kappa_a^{loss}}{2}\hat{a} + \sqrt{\kappa_a}\hat{a}_{in} \\ \frac{\partial \hat{m}}{\partial t} = \frac{i}{\hbar}[\hat{H}, \hat{m}] - \frac{\kappa_m + \kappa_m^{loss}}{2}\hat{m} + \sqrt{\kappa_m}\hat{m}_{in}, \end{cases} \tag{142}$$

which for the conversion interaction Hamiltonian Eq. (141) become,

$$\begin{cases} \frac{\partial \hat{a}}{\partial t} = -\frac{i}{\hbar}\omega_a\hat{a} - \frac{i}{\hbar}|\chi p|\hat{m} - \frac{\kappa_a + \kappa_a^{loss}}{2}\hat{a} + \sqrt{\kappa_a}\hat{a}_{in} \\ \frac{\partial \hat{m}}{\partial t} = -\frac{i}{\hbar}\omega_m\hat{m} - \frac{i}{\hbar}|\chi p|\hat{a} - \frac{\kappa_m + \kappa_m^{loss}}{2}\hat{m} + \sqrt{\kappa_m}\hat{m}_{in}. \end{cases} \tag{143}$$

Then using the input/output relation $\sqrt{\kappa_a}\hat{a} = \hat{a}_{in} + \hat{a}_{out}$, the complex reflection coefficient on the buffer mode a can be deduced

$$r_a[\omega] = \frac{\langle \hat{a}_{out}[\omega] \rangle}{\langle \hat{a}_{in}[\omega] \rangle} \tag{144}$$

$$= -\frac{(\omega - \omega_a + i\frac{\kappa_m + \kappa_m^{loss}}{2})(\omega - \omega_a - i\frac{\kappa_a - \kappa_a^{loss}}{2}) - |\chi p|^2}{(\omega - \omega_a + i\frac{\kappa_m + \kappa_m^{loss}}{2})(\omega - \omega_a + i\frac{\kappa_a + \kappa_a^{loss}}{2}) - |\chi p|^2}. \tag{145}$$

The amplitude and phase of the complex reflection coefficient on the buffer resonator bring information on the coupling strength to the memory mode. The coupling between the two resonators can then be parametrized by cooperativity

$$C = \frac{4|\chi p|^2}{\kappa_a^{tot}\kappa_m^{tot}} \tag{146}$$

where $\kappa_{a,m}^{tot} = \kappa_{a,m} + \kappa_{a,m}^{loss}$, which is the ratio between the conversion rate and total environmental decoherence rate. It can be controled through the pump amplitude $|p|$. Using cooperativity as coupling strength parameter, we can distinguish different regimes [60]

- For $C < \frac{\kappa_m}{\kappa_a}$, resonators are effectively decoupled.
- $C = 1$ corresponds to the critical coupling regime, where all the signal that enters in the buffer resonator gets converted to the memory mode.
- For $\frac{\kappa_a}{\kappa_m} < C$, the two resonators are in the strong coupling regime and their fundametal modes are hybridized.

Efficient signal capture to the memory mode, as well as its storage and release back to the transmission line, require the two resonators to be in the strong coupling regime. In the following chapter, I will present few experimental implementations of this system that I have realized during my PhD.

4.6 CONCLUSION

The main points of this chapter are:

- Review of the state of the art in microwave quantum nodes.
- Description of the quantum node with a transmon qubit embedded in the memory mode.

5 BUILDING A QUANTUM NODE

"Another flaw in the human character is that everybody wants to build and nobody wants to do maintenance."

Kurt Vonnegut

In this chapter I will present an implementation of a quantum node based on a Josephson Parametric Converter. For this realization, we have built up on a design for the quantum memory experiment by Flurin *et al.* [6]. In the first part of this chapter I will explain the functioning principle of the quantum memory, discuss the limiting factors for its lifetime and possible solutions to improve it.

As already discussed in section 4.4.1, dispersively coupling a qubit to a cavity offers controllability over the cavity state. Preparation of non-Gaussian states such as Fock states or Schrödinger cat states, that are of interest for quantum computing, requires introducing some quantum non-linearity that can be provided by the Josephson junction of the qubit. In the second part of this chapter, I will explain how we integrated a transmon qubit in the 3D storage resonator and worked towards protected quantum computing with microwave fields [122].

5.1 MICROWAVE QUANTUM MEMORY

5.1.1 *Experimental design*

The quantum memory we have built is based on the Josephson Parametric Converter (JPC), a device consisting of two microwave resonators coupled through an unshunted JRM. JPC is an extremely versatile circuit. It is commonly used as a quantum limited amplifier, typically for the qubit readout in quantum information experiments with superconducting circuits. For this purpose, the circuit is designed

such that the two resonating modes a and b are strongly coupled to the transmission line, so that the product $\sqrt{\text{gain}} \times$ bandwidth of the amplifier is maximized. The couplings κ_a and κ_b of the resonators a and b to their corresponding transmission lines are then of the order of 200 MHz.

For the analog quantum simulation of the USC, presented in Chapter 2 and Chapter 3, a Josephson Mixer, which is a tunable derivative of the JPC with a shunted JRM, was used as the quantum hardware. For this use, the coupling to transmission lines was decreased below the frequencies δ of the effective modes, such that $\kappa_a, \kappa_b < \delta$ in order to have high quality modes.

In the quantum node experiment, the mode a, that we will refer to as buffer mode, is strongly coupled to the transmission line, so that it can efficiently catch the propagating field a_{in}. The memory mode m on the other hand is weakly coupled to a transmission line, in order to limit the dissipation channels to the environment and increase its coherence time (Fig. 49). The coupling and dissipation rates of the buffer mode κ_a and κ_a^{loss} and of the memory mode κ_m and κ_m^{loss} thus satisfy $\kappa_a \gg \kappa_a^{loss}, \kappa_m^{loss} > \kappa_m$.

Figure 49: Schematic of the quantum memory.

In order to further ensure high coherence time for the memory mode, it is realized as the fundamental TE_{110} mode of a 3D superconducting bulk aluminum cavity. The 3D cavity is mounted from three parts, shown in Fig. 50, from left to right, the lid, top and bottom of the cavity. When closed together, the top and the bottom parts form a cavity of dimensions $(27.4 \times 14.2 \times 27)$ mm.

The buffer mode on the other hand is a planar $\lambda/2$ microstrip resonator, shown in Fig. 51. The difficulty thus consists in coupling an on chip mode to a 3D mode through a Josephson ring. Furthermore, the ring requires a magnetic flux bias, so that the chip cannot be

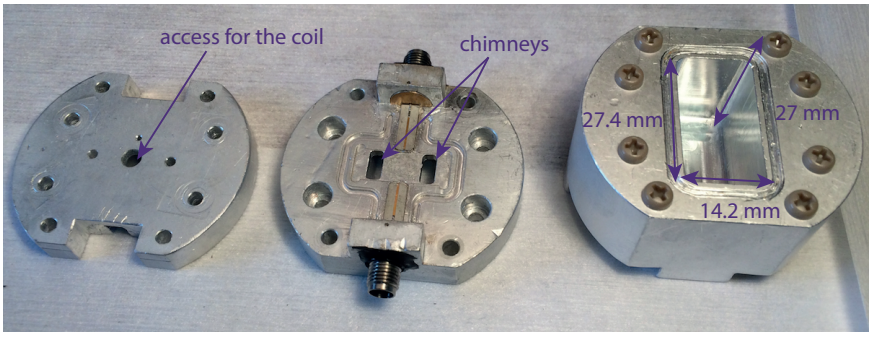

Figure 50: Three parts constituting the 3D memory cavity, from left to right, the lid, the top and the bottom part. The top part contains two chimneys with apertures on the top that allow for the coupling to the buffer resonator. The cylindrical whole that can be seen in the lid allows for insertion of a coil that provides the magnetic flux bias for the Josephson ring.

placed inside of the superconducting aluminum which expels the externally applied magnetic field due to Meissner effect (see Ref. [123] for another design).

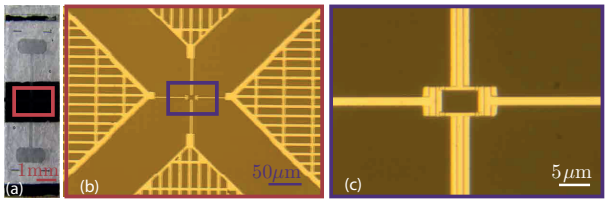

Figure 51: (a) Picture of the sapphire chip hosting the aluminum circuit consisting of the Josephson ring, buffer resonator and the antennas. (b) and (c) Optical microscope images of the Josephson ring coupling the horizontal buffer mode to the vertical antenna.

Buffer resonator and Josephson ring are realized on a sapphire chip that is placed outside of the memory cavity, between the top part and the lid. The 3D cavity is not convex, it has two chimneys with apertures on the top. The coupling is mediated by planar antennas, that are symmetrically aligned on the apertures above the chimneys, as can be seen in the left picture in Fig. 52 and Fig. 53. Field is more strongly confined in the smaller volume of the chimneys, enabling the strong coupling to the antenna mode. To determine the capacitive

coupling κ_c through the antennas, we use Ansys HFSS simulator, as shown in Fig. 53.

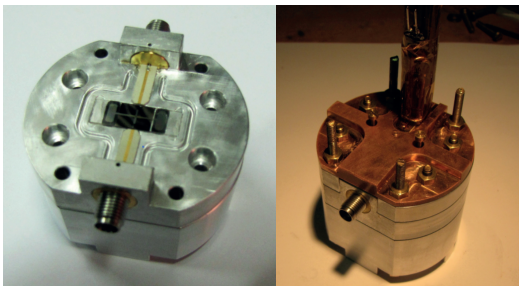

Figure 52: Left : Picture of closed top and bottom parts of the 3D cavity with the sapphire chip inserted on the top. Josephson ring couples the on chip 2D buffer resonator to a 3D memory resonator via symmetric antennas. Right : Picture of the entire device ready to be mounted in the cryostat. A copper lid containing a superconducting coil for magnetic flux bias is placed on the top of the chip with the Josephson ring. It is also used to attach the device to the base temperature stage of the dilution refrigerator.

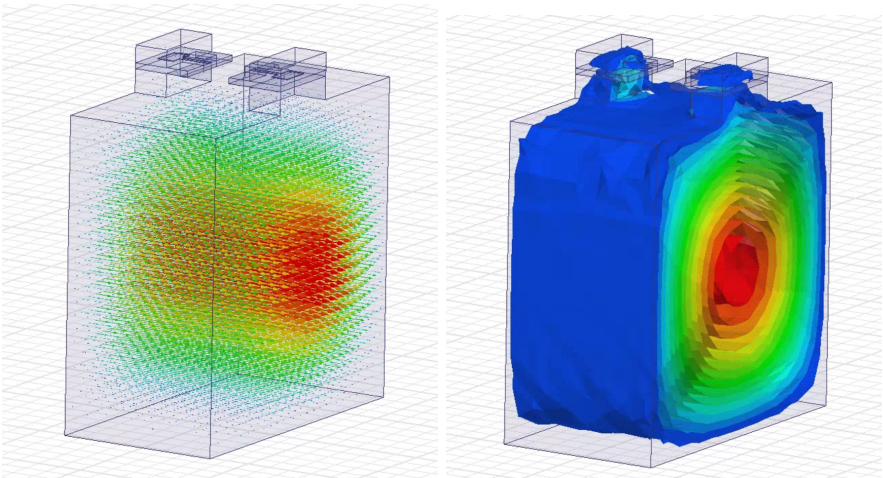

(a) (b)

Figure 53: (a) Vectorial representation and (b) amplitude of the electric field of the TE_{110} mode, used as a memory mode, simulated using Ansys HFSS software. The field is concentrated in the chimneys which enables for the strong coupling to the planar buffer resonator.

The effective input/output coupling rate to the memory then reads [60]

$$\gamma_{io}^{m} = \frac{\kappa_a}{2}\left(1 - \sqrt{1 - \frac{4}{\kappa_a^2(\frac{1}{\kappa_c^2} + \frac{1}{4|\chi p|^2})}}\right). \tag{147}$$

A direct access to the memory mode is realized by drilling a hole in the side wall of the cavity and inserting an SMA connector whose pin dips into the cavity and interacts capacitively with the cavity mode. The length of the pin determines the coupling to the transmission line and it is chosen such that the coupling is smaller than the intrinsic losses, so that the quality factor of the memory mode is not degraded. The memory cavity field can then be probed by measuring the complex reflection coefficient on this direct undercoupled port

$$r_m[\omega] = \frac{\kappa_m - \kappa_m^{loss} + 2i(\omega - \omega_m)}{\kappa_m + \kappa_m^{loss} - 2i(\omega - \omega_m)}. \tag{148}$$

From the amplitude and phase of the measured reflection coefficient we can determine the resonance frequency of the memory mode, as well as coupling and dissipation rates. As we will see in the following section, all of these depend on the surface quality of the cavity walls but also on the presence or not of the transmon and its substrate in the cavity.

5.1.2 *Conversion to the memory mode*

Parametric conversion from buffer to memory mode is characterized by measuring the reflection coefficient on the buffer resonator using a Vector Network Analyzer (VNA), while tuning the amplitude of the conversion pump. From the reflected signal with the pump turned off, we determine the coupling and dissipation rates for the buffer resonator $\kappa_a = 2\pi \times 16.8$ MHz and $\kappa_a^{loss} < 2\pi \times 1$ MHz. Similarly, from the reflection on the memory port, we measure $\kappa_m = 2\pi \times 60$ kHz and $\kappa_m^{loss} = 2\pi \times 170$ kHz. This loss rate is higher then expected for the 3D bulk aluminum cavities. In a later measurement run, after an acid clean of the surface, $\kappa_m^{loss} = 2\pi \times 40$ MHz was measured.

Measured complex reflection coefficient for increasing conversion pump amplitude $|p|$ is shown in quadrature phase space in Fig. 54,

together with the theoretical reflection expected from the Langevin equations.

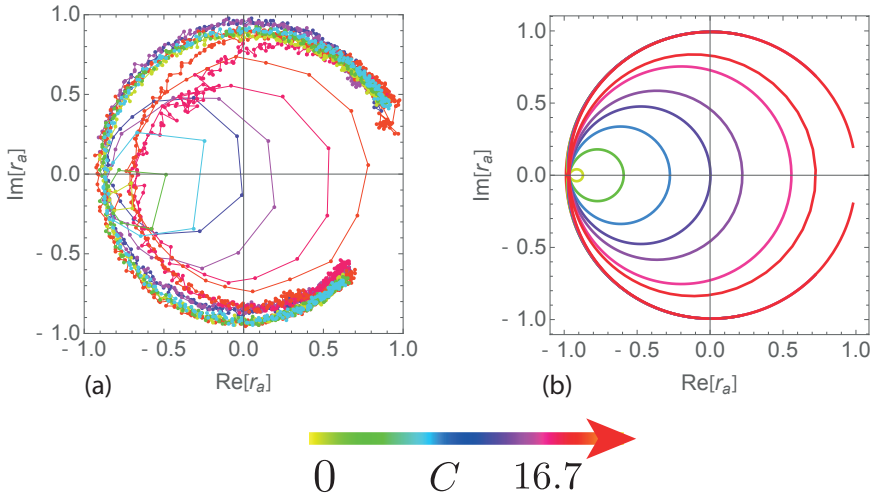

Figure 54: (a) Measured reflection coefficient for increasing pump amplitude that is color encoded. (b) Corresponding reflexion coefficient from input-output model Eq. (145) for cooperativity going from 0 to 16.7. The big loop corresponds to the resonance of the buffer mode and the small loop of increasing size to the resonance of the memory mode.

When the pump is turned off, there is just one big loop in the quadrature phase space, corresponding to 2π phase shift coming from the resonance of the buffer mode. When the pump is turned on, the coupling to the memory resonator is activated and a second loop, corresponding to the memory resonator, appears in the quadrature phase space. The size of the second loop indicates the coupling strength. For instance, the smaller loop that goes through the origin corresponds to the critical coupling $C = 1$. Finally, the strong coupling regime is reached when the size of the smaller loop approaches the size of the bigger one. The maximum cooperativity we reach is $C = 16.7$.

5.1.3 *Mode identification using Kerr shift*

A certain number of other pump frequencies induce conversion to various modes. These modes can be identified by analyzing the cross-Kerr shift between the pump and buffer modes. This procedure is

summarized in Table 6. The pump is applied at frequency ω_p and the reflection coefficient is measured on the buffer mode as a function of frequency, in the proximity of the buffer resonance frequency $\omega_a = 2\pi \times 10.863$ GHz. If the pump tone is applied in the proximity of a conversion frequency to an eigenmode of the system, a cross-Kerr shift is induced on the buffer mode. Then if we increase the pump frequency by $\Delta\omega_p$, the shift of the buffer frequency $\Delta\omega_a$ indicates the relation between the frequencies of the pump ω_p, buffer ω_a and the mode to which the signal is converted ω_c.

$\frac{\omega_p}{2\pi}$ (GHz)	$\frac{\Delta\omega_p}{\Delta\omega_a}$	frequency relation	$\frac{\omega_c}{2\pi}$ (GHz)	mode
6.565	1	$\omega_p = \omega_a - \omega_c$	4.298	antenna
4.09	1	$\omega_p = \omega_a - \omega_c$	6.77	common mode
9.292	-1	$\omega_p = \omega_c - \omega_a$	20.155	3rd cavity mode
1.573	-1	$\omega_p = \omega_c - \omega_a$	12.436	2nd cavity mode
7.5	$-\frac{1}{2}$	$\omega_p = \frac{1}{2}(\omega_c - \omega_a)$	25.86	

Table 6: Mode identification using Kerr shift

Interestingly, this method allows identification of higher oder interactions as well. A frequency shift ratio $\frac{\Delta\omega_p}{\Delta\omega_a} = -\frac{1}{2}$ indicates a process where two pump photons and one buffer photon are invested to create one photon in the conversion mode, i.e. $H_{int} \propto \hat{p}\hat{p}\hat{a}\hat{c}^\dagger$, where $\hat{c}^\dagger$ is the creation operator of the mode in which the signal is converted.

5.2 ADDING A TRANSMON QUBIT TO THE MEMORY

In the previous section, we have shown that strong coupling can be obtained with this unconventional hybrid 2D/3D architecture. The design is thus promising for efficient memory storage. However, the realization of a fully controllable quantum node still requires a qubit. In this section I will explain how we integrated a transmon qubit in the previously described quantum memory device.

Figure 55: Schematic of the 3D architecture for the quantum node experiment. Transmon qubit shown in green is capacitively coupled to the memory resonator.

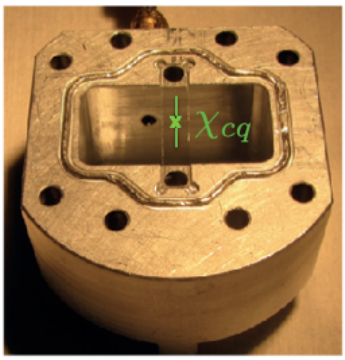

Figure 56: Photo of the bottom part of the 3D aluminum memory cavity with a pocket hosting the transmon qubit on a sapphire chip.

5.2.1 *Aluminum cavity with qubit*

The coupling of the transmon qubit to the memory mode is realized by inserting the sapphire chip hosting the qubit between the top and bottom parts of the 3D cavity. The bottom part has a pocket that can host the chip as shown in Fig. 56. The cavity is cut in the middle, so that the qubit lays in the antinode of the fundamental cavity mode and their coupling is maximized. A bisected cavity is shown in Fig. 52, with a qubit on a sapphire chip laying across the plane of cut. An indium seam used to quench the connection can be seen surrounding the cavity.

We begin by measuring the reflection on the direct port to the memory mode, whose amplitude and phase are shown in Fig. 57. We can first observe that there is not one resonance but three, corresponding to the memory mode dressed by a thermally excited qubit. This is

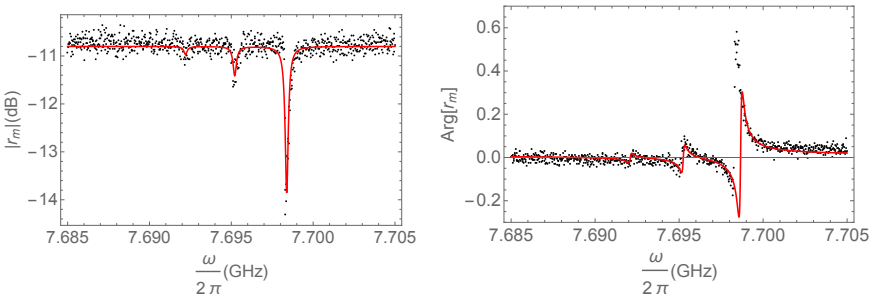

(a) (b)

Figure 57: (a) Amplitude and (b) phase of the reflection coefficient on the aluminum memory cavity. The red line correspond to Eq.(149).

due to the fact that the effective temperature of the qubit's environment is comparable to its transition frequency, so that we find it with finite probabilities in its ground, first and second excited state. These probabilities, $p_g = 1 - p_e - p_f$, p_e and p_f, for the qubit to be respectively in the ground, first and second excited states, are determined by matching the measured reflection coefficient with

$$\begin{aligned} r_m = p_g & \frac{\kappa_m - \kappa_m^{loss} + 2i(\omega - \omega_m)}{\kappa_m + \kappa_m^{loss} - 2i(\omega - \omega_m)} \\ + p_e & \frac{\kappa_m - \kappa_m^{loss} + 2i(\omega - \omega_m + \chi_{mq})}{\kappa_m + \kappa_m^{loss} - 2i(\omega - \omega_m + \chi_{mq})} \\ + p_f & \frac{\kappa_m - \kappa_m^{loss} + 2i(\omega - \omega_m + 2\chi_{mq} - \alpha)}{\kappa_m + \kappa_m^{loss} - 2i(\omega - \omega_m + 2\chi_{mq} - \alpha)}, \end{aligned} \tag{149}$$

where χ_{mq} is the pull between the qubit and the memory mode and α is the anharmonicity of the qubit. We find $p_e = 0.17$ and $p_f = 0.06$. Furthermore, we can determine from this measurement the coupling and dissipation rates of the memory resonator, $\kappa_m = 2\pi \times 76$ kHz and $\kappa_m^{loss} = 2\pi \times 207$ kHz. Similarly, by measuring the reflection on the buffer resonator, we find $\kappa_a = 2\pi\times$ 8 MHz and $\kappa_a^{loss} = 2\pi\times$ 31 MHz.

We can first notice that the losses of the memory resonator have increased compared to the measurement without the qubit. However, there is an important uncertainty attached to this number. Indeed, it was not reproducible from one cooldown to another and even during one measurement run it has been observed to fluctuate up to 20%.

There are few reasons for excessive 3D cavity dissipation. For clarity, they are summarized in Table 7. First, surface can get contaminated during the insertion of the sapphire chip. We have already seen that an acid clean of the surface can improve its dissipation rate by a factor of 4. Second, a mechanical instability due to a large number of components and connects can cause fluctuations both of the cavity frequency and its dissipation rate. Finally, different isolated components are thermalized at the base cryostat temperature using highly thermally conducting copper lines. However, in superconductors such as aluminum, the main mechanism for heat transfer is phonon-phonon scattering. When aluminum is cooled down, its thermal conductivity decreases abruptly when it transits at its critical temperature. As bulk aluminum cavities contain large amounts of superconductor, it takes longer to thermalize them to cryogenic temperatures. Badly thermalized pockets are thus suspected to cause frequency and dissipation fluctuations as well.

memory losses	buffer losses
surface polution	2D/3D connectors
mechanical instability	ground plane continuity
Al thermalization	impedance mismatch

Table 7: Sources of dissipation in the hybrid 2D/3D quantum node with an aluminum 3D memory cavity.

More importantly, the dissipation rate of the buffer resonator is found to exceed its coupling rate to the transmission line. This rate is not reproducible from one cool-down to another and it is found to vary by almost two orders of magnitude. There are few explanations for such excessive losses.

First, the buffer resonator is differentially biased by the microwave launchers at the 3D/2D interface. The outer shell of the SMA connectors that are used to connect the transmission lines to the circuit is made in brass. The connectors are inserted into the brass pockets in the holes made in the aluminum cavity and soldered to insure the ground plane continuity. However, the contact between these two materials appears to be prone to losses and mechanical instability. Second, the ground plane of the microstrip buffer resonator is real-

ized as 500 nm thick layer of silver on the back side of the sapphire substrate. The ground plane continuity can be damaged by a bad metallic contact between the silver and aluminum surfaces. Finally, we suspect that there is an impedance mismatch between the SMA connectors and the base stage circulators that causes a spurious reflection that is manifested as a frequency independent offset in the phase of the reflection coefficient. This would have the same effect to the reflection coefficient as intense losses of the buffer resonator, but we cannot distinguish between these two effects during a single measurement run.

Due to the excessive losses of the buffer resonator, the resonator is undercoupled, which is undermining the realization of an efficient quantum memory. In order to circumvent this problem, we replaced the aluminum cavity by one in copper.

5.2.2 *Lead plated copper cavity with qubit*

The primary motivation for replacing the aluminum cavity by the one in copper was to decrease the losses of the buffer resonator. From the previous experience in our group, soldering brass connectors on copper revealed itself much easier and less prone to losses than in the case of aluminum. Furthermore, we expected the continuity of the ground plane to be better with a copper surface.

Additional motivation comes from the qubit thermalization. One of the consequences of the bad thermalization of superconducting bulk aluminum is that the effective temperature of the qubit environment can be increased. A normal metal such as copper would insure better and faster thermalization of the qubit environment and of the qubit itself.

Although it is advantageous to have a normal metal bulk, the interior of the cavity should be superconducting in order to avoid losses due to the finite conductivity of the metal and maintain the high quality factor of the resonator [124].

This issue is resolved by electrodepositing a thin layer of lead, which becomes superconducting below 7.2 K, on the interior of a bulk copper cavity, as shown in Fig. 58b. The lead plating process that we use is described in Section 8.2.

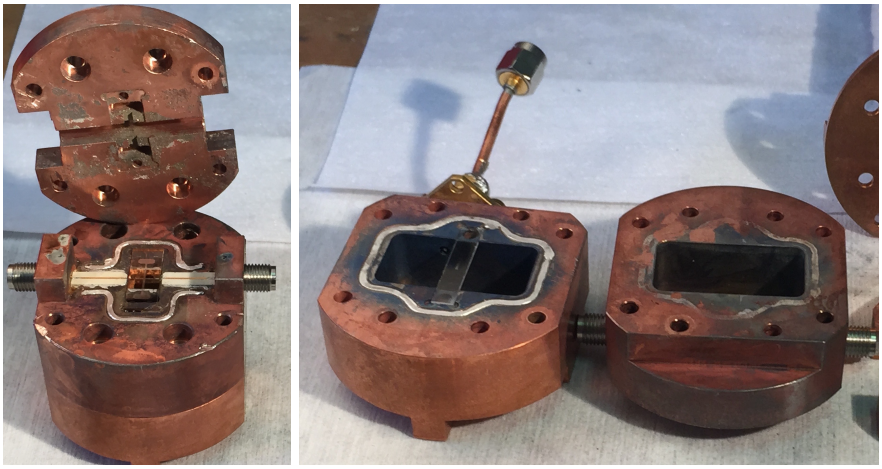

(a) (b)

Figure 58: (a) Photograph of the copper cavity with a JPC on its top. JPC is connected through PCBs on left and right to the SMA connectors that insure its connection to transmission lines and a hybrid coupler. (b) Top and bottom parts of the lead plated copper cavity. Sapphire chip hosting the transmon qubit is inserted between the two cavity parts that are afterwards screwed together and quenched using an Indium seal.

Amplitude and phase of the reflection coefficient measured on the direct access port to the memory cavity are shown in Fig. 59. Contrary to what we expected, the thermal population of the qubit excited states is not negligible. It can be explained by the transmission lines that were not well thermalized between the cryostat stages or by a bad mechanical anchoring of the transmon chip.

Similarly, by measuring the signal reflected on the buffer mode, we find the resonance frequency ω_a, coupling and decoherence rates κ_a and κ_a^{loss} of the buffer resonator. From these measurements, we find the conversion pump frequency $\omega_p = \omega_a - \omega_m = 2\pi \times 1.12$ GHz. System parameters determined from these reflection measurements are summarized in Table 8 in comparison to the same parameters for the aluminum cavity. Both dissipation rates for the buffer and memory modes are improved by an order of magnitude. Thermal population of the excited qubit levels is not improved tough.

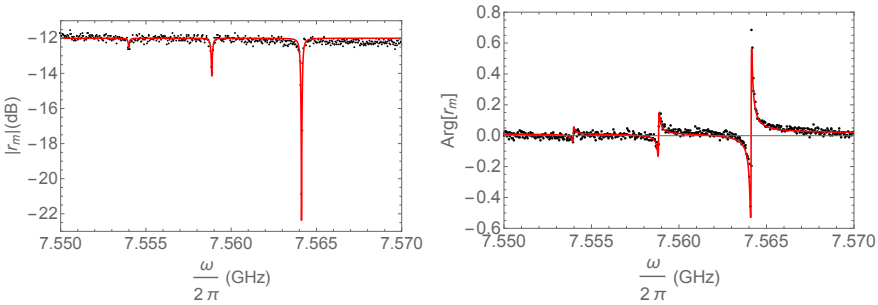

(a) (b)

Figure 59: (a) Amplitude and (b) phase of the reflection coefficient on the lead plated copper memory cavity. The red lines correspond to Eq. 149.

cavity	Al	Cu/Pb
ω_a	$2\pi\times$ 9.401 GHz	$2\pi\times$ 8.68 GHz
κ_a	$2\pi\times$ 8 MHz	$2\pi\times$ 5 MHz
κ_a^{loss}	$2\pi\times$ 31 MHz	$2\pi\times$ 3 MHz
ω_m	$2\pi\times$ 7.69866 GHz	$2\pi\times$ 7.56412 GHz
κ_m	$2\pi\times$ 76 kHz	$2\pi\times$ 59 kHz
κ_m^{loss}	$2\pi\times$ 207 kHz	$2\pi\times$ 70 kHz
p_g	0.77	0.75
p_e	0.17	0.19
p_f	0.06	0.06
χ_{mq}	$2\pi\times$ 3.3 MHz	$2\pi\times$ 5.3 MHz
α	$2\pi\times$ 0.2 MHz	$2\pi\times$ 0.4 MHz

Table 8: Comparison of the system parameters determined from reflection measurements for the aluminum cavity coupled to a qubit and a lead plated copper cavity coupled to a qubit.

We then measure the reflection on buffer resonator with the conversion pump turned on. It is plotted in polar coordinates for the maximum cooperativity C we could reach in Fig. 60c. There are two small loops which correspond to the memory mode dressed by a qubit in the ground state and in the excited state. Qubit being in thermal

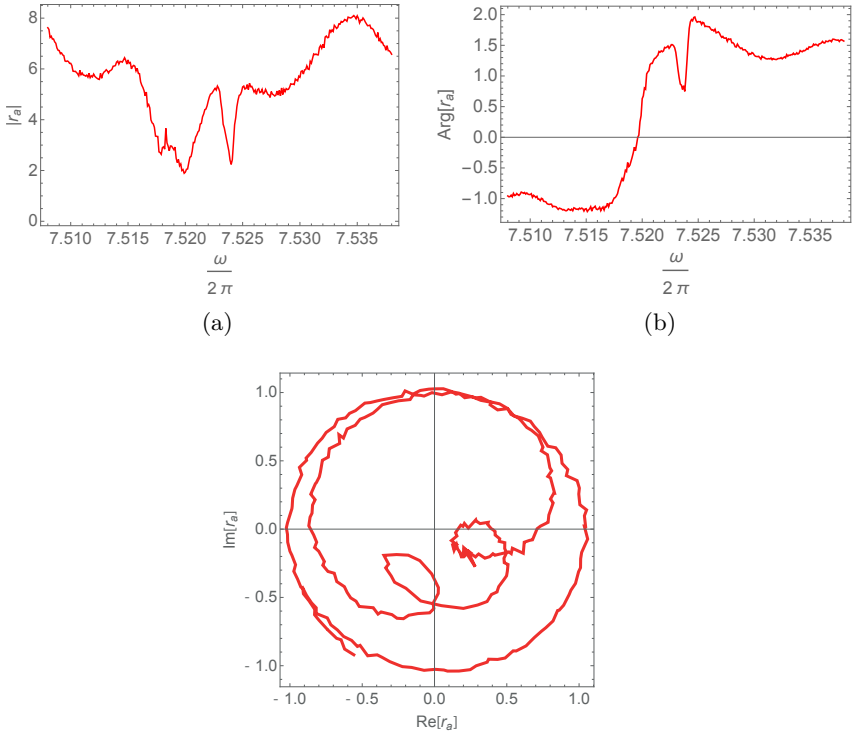

Figure 60: (a) Amplitude, (b) phase and (c) quadratures of the average measured reflection coefficient for the memory containing a qubit. The two small loops correspond to the memory dressed by a qubit either in the ground state or in the excited state. This measurement corresponds to the maximum cooperativity C obtained with the lead plated copper cavity containing a transmon qubit.

state, average conversion is not efficient and we do not reach the strong coupling regime. This is due to the fact that for 30% of realizations, pump, which is applied at frequency $\omega_p = \omega_a - \omega_m^g$, is not resonant with the transition frequency.

Following experiments described in this chapter are done using the lead plated copper memory cavity.

In this section we demonstrate the first task that the quantum node is required to execute, which is the on demand data storage, with time controlled capture and release of the propagating field.

The pulse sequence used for this experiment is shown in Fig. 61a. It consists in sending a 500 ns pulse signal on the buffer mode and applying the conversion pump for 1 μs to let the signal go into the memory mode. The pump is then turned off for the time duration Δt which is the storage time of the signal. Finally the pump is turned on a second time for 1 μs to release the signal out of the memory to the buffer mode and consequently to the transmission line. The output field from the buffer mode a is measured during 1 μs using a fast data acquisition card with sampling time of 2 ns.

Amplitude of the measured signal is shown in Fig. 61b for $\Delta t = 500$ ns. Most of the incoming signal gets reflected on the buffer resonator and only the small exponentially decaying signal measured 500 ns later corresponds to the field that has been stored in the memory and released after 500 ns. This low capture efficiency is due to the fact that the signal pulse in this measurement was square shaped. It can however be improved by temporally shaping the signal [6].

The exponential envelope of the signal released from the memory, shown in Fig. 61d, reveals the access time of 136 ns. The access time determines the duration of writing and reading operations in the memory, that should be as fast as possible compared to the memory lifetime in order to allow a maximum number of operations. Memory lifetime is determined by performing the capture and release pulse sequence for different storage times Δt. We define the capture efficiency as the ratio between the total integrated amplitude of the output field after the storage for time Δt and the total output field without storage

$$\eta = \frac{\int_{t_0+\Delta t}^{t_0+\Delta t+T} |a_{out}|^2 dt}{\int_{t_0}^{t_0+T} |a_{out}|^2_{OFF} dt}, \tag{150}$$

where $|a_{out}|_{OFF}$ is the measured amplitude of the output field with the pump turned off. It is integrated from the time t_0 when the signal from the microwave source arrives to the sample at the base temperature stage of the cryostat, until the time $t_0 + T$, where T = 500 ns is

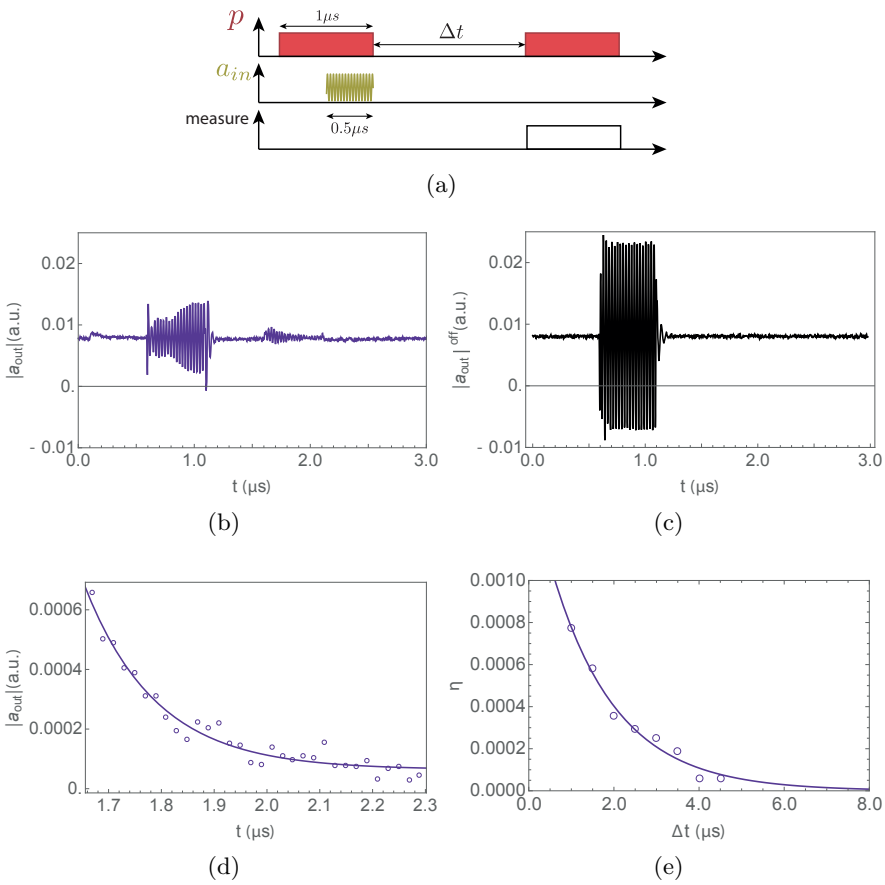

Figure 61: (a) Pulse sequence for the signal capture and release measurement. (b) Time trace of the measured amplitude of the output field for $\Delta t = 1\mu$s. (c) Time trace of the measured amplitude of the output field with the pump turned off. (d) Time envelope of the measured amplitude of the signal released from memory. The full line corresponds to $|a_{out}|(t_0 + \Delta t)e^{-\frac{t-t_0-\Delta t}{\tau}}$ the access time τ =136 ns. (e) Efficiency as a function of the storage time Δt. Full line corresponds to $\eta(\Delta t = 0)e^{-\frac{\Delta t}{\tau_m}}$ with the initial efficiency $\eta(\Delta t = 0) = 0.015$ and the memory lifetime $\tau_m = 1.52$ μs.

the duration of the square pulse that we send. From the exponentially decaying efficiency we find the memory lifetime $\tau_m = 1.52$ μs.

This lifetime is shorter than what can be achieved with superconducting resonators where a 3D cavity coupled to a qubit has been observed to reach the lifetime of 1 ms [95]. As discussed in section 5.6,

it was limited by the non-convex architecture of the 3D cavity and the presence of cuts and apertures for the chip integration.

5.4 CHARACTERIZING THE QUBIT

5.4.1 *Transmission through frequency conversion*

The frequency conversion opens up a new possibility to probe the qubit-cavity system. The signal at frequency ω_c is injected on the memory resonator on a range of frequencies in the proximity of the buffer resonance frequency ω_m. Then by continuously applying the conversion pump $\omega_p = \omega_a - \omega_m$, one can monitor the field transmitted from the memory to the buffer at the buffer output, at frequency $\omega_c + \omega_p$.

The complex transmission coefficient through frequency conversion expected from the Langevin equations Eq. (142) reads

$$\begin{aligned} t[\omega] &= \frac{\langle \hat{a}_{out} \rangle}{\langle \hat{m}_{in} \rangle} \\ &= \frac{i|\chi p|\sqrt{\kappa_a \kappa_m}}{(\omega - \omega_m - i\frac{\kappa_m + \kappa_m^{loss}}{2})(\omega - \omega_a - i\frac{\kappa_a + \kappa_a^{loss}}{2}) - |\chi p|^2}. \end{aligned} \tag{151}$$

The measured amplitude of the transmitted field is shown in Fig. 62b.

To determine the transition frequency of the qubit, we make use of the fact that the cavity transmittance is dependent on the qubit state. We do a continuous wave measurement with Vector Network Analyzer (VNA) as shown in Fig. 63. We measure the signal transmitted from the memory to the buffer mode through frequency conversion just as in Fig. 62b, but we add a supplementary drive at frequency ω_d that we sweep in the range of frequencies around the resonance frequency of the qubit expected from its geometrical characteristics.

For few different drive frequencies we observe hybridization of the dressed cavity resonances. This measurement enables us to deduce the qubit frequency $\omega_q = \omega_{eg} = 2\pi \times 5.204$ GHz.

In order to probe the qubit, we realize a heterodyne setup shown in Fig. 64, that allows the measurement of the field transmitted from the memory to the buffer mode by the parametric frequency conversion. The signal is now injected on the buffer resonator, while the conversion pump is applied on the JPC so that the signal is converted from

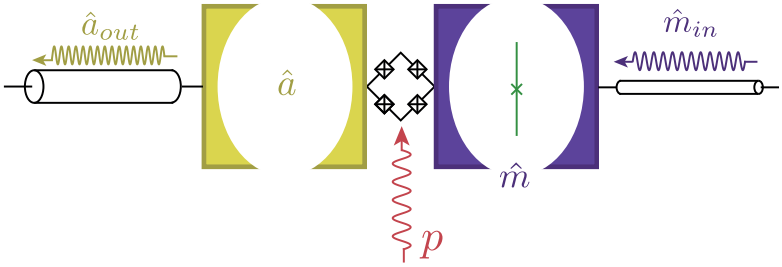

(a)

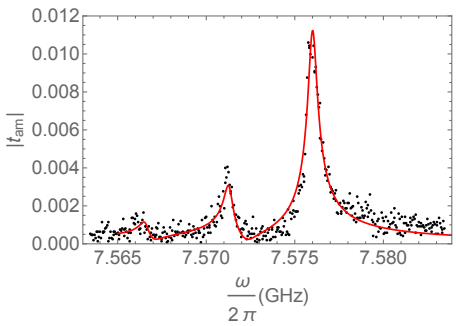

(b)

κ_a	$2\pi \times 5.3$ MHz
κ_a^{loss}	$2\pi \times 3.2$ MHz
κ_m	$2\pi \times 110$ kHz
κ_m^{loss}	$2\pi \times 400$ kHz
p_e	0.19
p_f	0.06
χ_{mq}	$2\pi \times 4.7$ MHz
$\lvert\chi p\rvert$	$2\pi \times 2.5$ MHz

Figure 62: (a) Schematic of transmission through frequency conversion measurement. The signal is sent to the direct memory port at frequency ω_c in the proximity of the memory resonance frequency ω_m and the outgoing field from the buffer mode a is measured at up-converted frequency $\omega_c + \omega_p$. (b) Measured amplitude of the signal transmitted through conversion from memory to buffer resonator as a function of memory probing frequency. Red line corresponds to the Eq. (142) with the fit parameters summarized the table on the right.

the buffer to the memory resonator. Finally the signal outgoing from the memory mode is down-converted and digitized using an analog to digital converter (ADC).

We use the qubit state dependent cavity transmittance to measure the qubit. We apply a tone at the frequency of the cavity dressed by the qubit in its ground state ω_m^g and measure how much of the signal is transmitted. If we get a relatively large transmission, we can infer that the qubit must be in the ground state, while a relatively small signal indicates that the qubit is excited. In order to increase

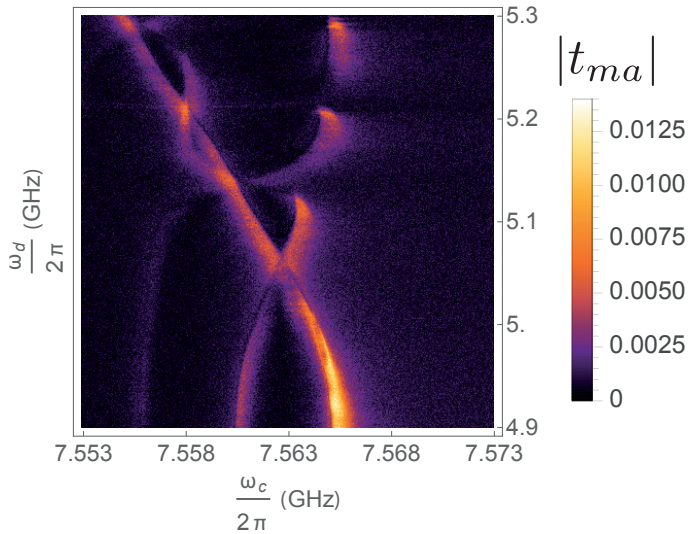

Figure 63: Measured amplitude of the signal transmitted through conversion from memory to buffer resonator as a function of memory probing frequency ω_c and continuous qubit drive frequency ω_d.

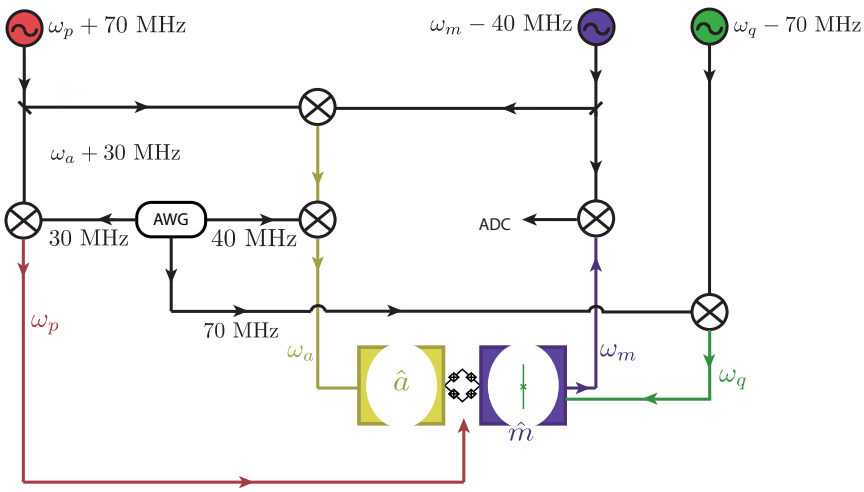

Figure 64: Schematic of the heterodyne measurement of the signal transmitted through frequency conversion from the buffer to the memory mode.

the contrast, we initialize the measurement by forcing the warm qubit from the thermal equilibrium state to the ground state using a reset protocol detailed in section 5.4.2.

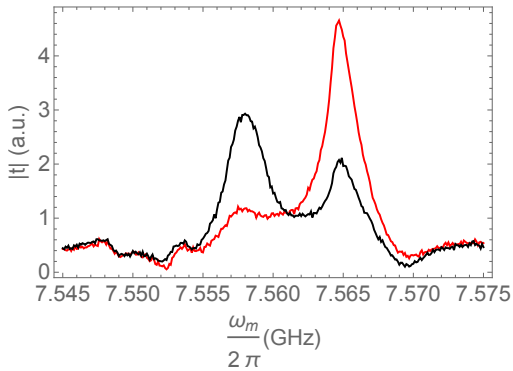

Figure 65: Amplitude of the signal transmitted by conversion from buffer to the memory as a function of frequency, for the qubit initially prepared in the ground state using the cooling protocol (red) and in the excited state (black).

The qubit state measurement using cavity transmission is demonstrated in Fig. 65. Red plot corresponds to the measurement with the qubit cooled into the ground state using the reset protocol. The highest transmission peak is at the frequency ω_m^g, even though there is some residual transmission at the frequency of the cavity dressed by the excited qubit ω_m^e due to the fact that the reset protocol is not absolutely efficient. The black plot on the other hand corresponds to the qubit prepared in the excited state with a $\pi/2$ pulse applied at the end of the cooling sequence. The highest transmission peak is then at ω_m^e, although there is a finite probability for the qubit to decay during the measurement, resulting in an additional peak for the black curve at the ground state cavity frequency ω_m^g.

The qubit lifetime measurement is shown in Fig. 66a. It consists in performing a calibrated π pulse and measuring the qubit state dependant transmission after waiting time Δt. For $\Delta t = 0$, the cavity transmission measured at ω_m^e corresponds to the qubit in its excited state and for $\Delta t \to \infty$ for the qubit in its ground state. From the exponential decay of transmission coefficient with the delay time, we find $T_1 = 10.5\ \mu$s.

The decoherence time T_2 is found from the Ramsey measurement as shown in the Fig. 66b. The pulse sequence consists in a first $\frac{\pi}{2}$ pulse on the qubit, followed by the free evolution during time Δt and

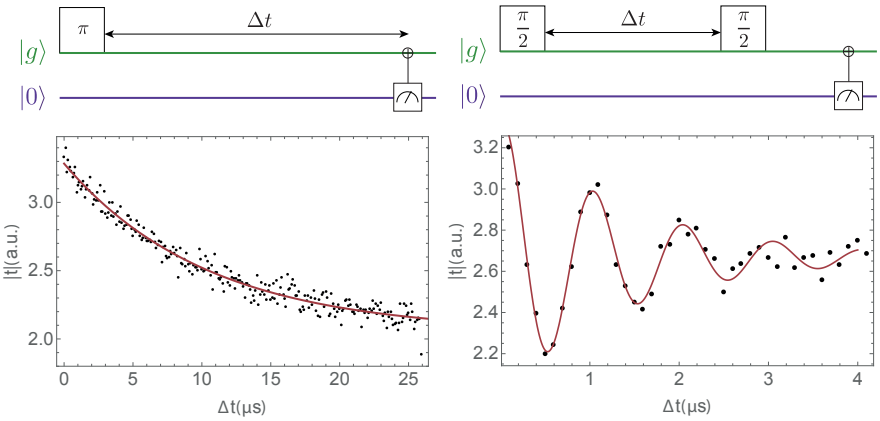

(a) (b)

Figure 66: Transmon qubit characterization measurements. (a) The qubit lifetime T_1 is measured by performing a π pulse and measuring the energy decay. The full red line corresponds to $T_1 = 10.5$ μs. (b) Ramsey pulse sequence and the measured amplitude of the transmission at frequency $\omega_m^e = 7.558$ GHz as a function of time delay between the two $\frac{\pi}{2}$ pulses. The full red line corresponds to $T_2 = 1.4$ μs

a second $\frac{\pi}{2}$ pulse preceding the measurement of the state of the qubit. From the exponential decay of the coherences, we find $T_2 = 1.4$ μs.

5.4.2 *DDROP cooling protocol*

When the thermal environment of the qubit is hot on the scale of the transition frequency of the qubit, it is interesting to use an active reset protocol to force the qubit into a known pure state or a ground state. A protocol called the Double Drive Reset of Population (DDROP) was proposed and demonstrated by the Devoret group in 2013 [125].

DDROP cooling pulse sequence consists in simultaneously applying two microwave drives on the qubit-cavity system for a time of few κ^{-1}. One drive is applied at ω_{eg}^0, that is at the transition frequency of the qubit when there are no photons in the cavity. The second drive is applied with amplitude ϵ_c at ω_m^g, that is at the cavity frequency when the qubit is in the ground state.

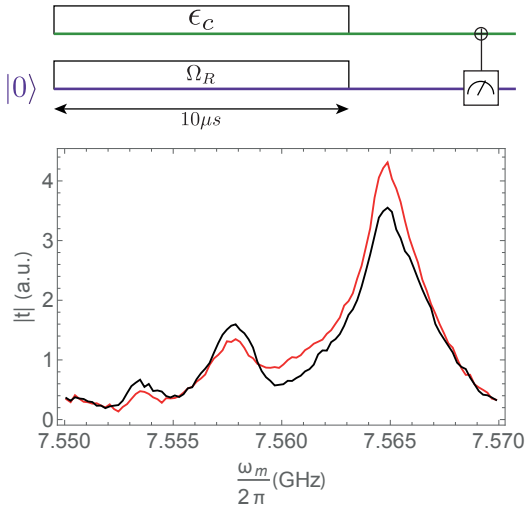

Figure 67: DDROP cooling sequence and the measured cavity transmission with the qubit in thermal equilibrium is shown in black, and with qubit cooled by DDROP procedure in red.

The first tone drives the Rabi oscillations $|0,g\rangle \leftrightarrow |0,e\rangle$ at Ω_R in order to accelerate the dynamics of the qubit. The second drive populates the cavity with photons when the qubit is in the ground state such that $|0,g\rangle \rightarrow |\alpha,g\rangle$. It prepares the state $|\alpha,g\rangle$, that once the drives are turned off relaxes to $|0,g\rangle$ in few κ^{-1}.

Cavity transmission as a function of frequency is shown in Fig. 67 for the qubit in thermal equilibrium in black and for the qubit initialized to the ground state using the DDROP protocol in red. The red plot has higher transmission at ω_m^g and decreased transmission at ω_m^e indicating that the probability to find the qubit in the ground state is increased compared to the thermal equilibrium. We thus initialized all the measurements that we have performed with this protocol in order the contrast in qubit state dependent transmission and increase the readout efficiency.

5.5 QUBIT AS AN ANCILLA FOR THE QUANTUM NODE

In this section we will look into the dispersive coupling of the memory mode and the qubit as a resource for the quantum state control and measurement.

5.5.1 *Dressed qubit spectroscopy*

Let's consider the dispersively coupled system of the memory cavity and transmon qubit, in the presence of driving fields for both the qubit and the memory cavity modes. The Hamiltonian of this system reads

$$\begin{aligned}\hat{H} = \hbar\omega_m \hat{m}^\dagger \hat{m} + \hbar\frac{\omega_q}{2}\hat{\sigma}_z - \hbar\chi_{mq}\hat{m}^\dagger\hat{m}\left|e\right\rangle\left\langle e\right| \\ + \hbar(\epsilon_c e^{-i\omega_c t}\hat{a}^\dagger + \epsilon_c^* e^{i\omega_c t}\hat{a}) + \hbar(\epsilon_d e^{-i\omega_d t}\hat{\sigma}_+ + \epsilon_d^* e^{i\omega_d t}\hat{\sigma}_-),\end{aligned} \tag{152}$$

where ϵ_c and ϵ_d are respectively the amplitudes of the cavity and qubit drives at frequencies ω_c and ω_d.

As the memory cavity-qubit pull is larger than dissipation rates of both the qubit and the memory mode, $\chi_{mq} \gg \gamma_1, \kappa_m$, the system is in the resolved photon number regime, as can be seen in Fig. 68. The measured amplitude of the transmitted signal is shown as a function of the frequency of the continuous wave qubit drive ω_d and the amplitude ϵ_c of the second continuous wave cavity drive at frequency ω_c. The memory cavity is probed at frequency ω_m^g, such that the transmission decreases when the probability for the qubit to be excited increases.

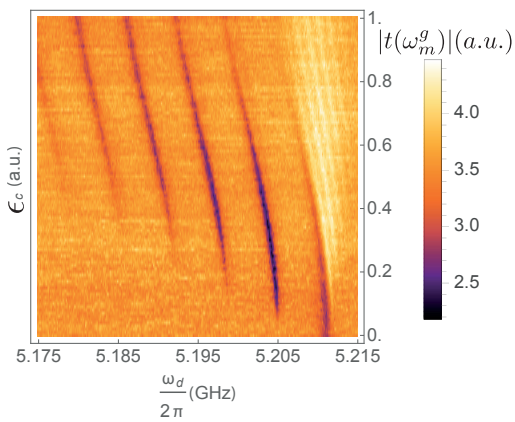

Figure 68: Spectroscopy of a qubit dressed with cavity photons.

The frequency of the qubit drive ω_d, represented in the horizontal axis of the Fig. 68, is swept in the proximity of the bare qubit frequency $\omega_q = 2\pi \times 5.205$ GHz. When there are no photons in the

cavity, for $\epsilon_c = 0$, the qubit is excited only when $\omega_d = \omega_q$. When the amplitude of the cavity drive is increased, such that there is k photons in the memory cavity, the resonances appear for qubit drive frequencies $\omega_d = \omega_q - k\chi_{qm}$. Furthermore, the resonances shift towards the lower frequencies due to a non-linear effect induced by the driving field.

Another interesting feature is the presence of transmission that is even higher than that of the cavity dressed by the qubit in its ground state, measured at $\omega_d = \omega_q$ for large values of the cavity drive amplitude ϵ_c. It corresponds to the increased population of the ground state of the qubit compared to that of the thermal equilibrium in which the measurement is initiated. Indeed, this measurement involves the same drives that are used for the DDROP protocol and they generate cooling of the qubit.

This measurement has shown that as the system is in the sideband resolved regime, by applying the drive at frequency $\omega_d = \omega_q - k\chi_{mq}$, transitions $|g, k\rangle \leftrightarrow |e, k\rangle$, of the qubit dressed by k photons, can be selectively driven. In the next section, we will use this regime to calibrate selective π_k pulses conditioned on the number of photons in the cavity that are a necessary building block for quantum information protocoles such as the remote state preparation protocol described in section 47.

5.5.2 *Fock state occupation probabilities for a coherent state*

Let's suppose that we want to know if there are n photons in the cavity. A way to ask this question using the qubit as an ancilla, is to apply a π pulse on the qubit at frequency $\omega_q - n\chi_{mq}$, which is the frequency of the qubit dressed by n photons. We can then measure the qubit and if we find it in the excited state, we can deduce that the π pulse worked because there were n photons in the cavity. The pulse needs to be long enough to be spectrally selective and not excite the qubit dressed by $n \pm 1$ photons. We can also ask more complicated and less restrictive questions, such as if there are either n or $n + 1$ photons in the cavity and post select on the memory in the state $\rho_m = |n\rangle \langle n| + |n + 1\rangle \langle n + 1|$.

In order to calibrate the conditioned π_n pulses, we first measure the probabilities P_n for the memory field described by density matrix ρ_m to host n photons

$$P_n = Tr(\rho_m |n\rangle \langle n|). \tag{153}$$

In the case of the memory mode in the coherent state of amplitude α, $\rho_m = |\alpha\rangle \langle \alpha|$, these probabilities are

$$P_n(\alpha) = e^{-|\alpha|^2} \frac{|\alpha|^{2n}}{n!}. \tag{154}$$

The pulse sequence used for the measurement is shown in Fig. 69. First, the memory cavity is prepared in the coherent state $|\alpha\rangle$ by applying a 300 ns gaussian displacement pulse $D(\alpha)$ of amplitude ϵ_c at frequency ω_m, on the memory in vacuum state.

Second, a π pulse is applied to the qubit at frequency $\omega_q - n\chi_{mq}$ for $n \in \{0, 5\}$. In order to have the spectral pulse selectivity larger than 90%, the bandwidth of the gaussian envelope is set such that $1 - e^{-\frac{\chi_{mq}^2}{2\sigma^2}} > 0.9$.

Finally, the cavity transmission is measured at readout frequency ω_m to deduce the state of the qubit. As in the previous cavity transmission measurements, we measure the transmission through frequency conversion from the buffer to the memory resonator. We thus turn on the conversion pump 500 ns before we turn on the readout. The average transmission as a function of the amplitude of the displacement field ϵ_c is shown in Fig. 69.

This measurement allows us to calibrate the amplitude of the displacement tone ϵ_c in a number of photons. The amplitude for which the transmission reaches the smallest value is the one for which the probability to excite the qubit with the pulse π_n is the highest, so it corresponds to $n = |\alpha|^2$ photons in the cavity.

The red curve corresponding to no photons in the cavity reaches higher transmission values for large ϵ_c. This is due to the fact that qubit is initially not in the ground state but in a thermal equilibrium, with probability $p_e = 0.17$ to be in the excited state. With probability p_e then the system starts in the state $|e, 0\rangle$ and the displacement tone does not displace the cavity. However the final π_0 pulse brings the system to $|g, 0\rangle$. This is equivalent to DDROP cooling procedure and

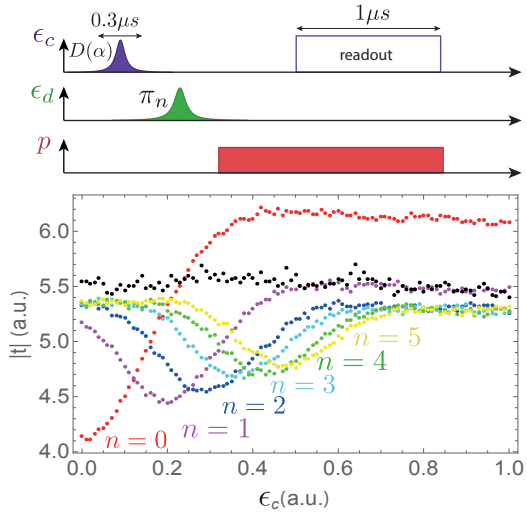

Figure 69: Pulse sequence and measured amplitude of the transmission coefficient at readout frequency ω_m and π pulse applied at $\omega_q - n\chi_{mq}$ for color encoded Fock states $n \in \{0, 5\}$, as a function of the cavity displacement rate ϵ_c. Black reference curve corresponds to the measurement without any qubit pulse drive.

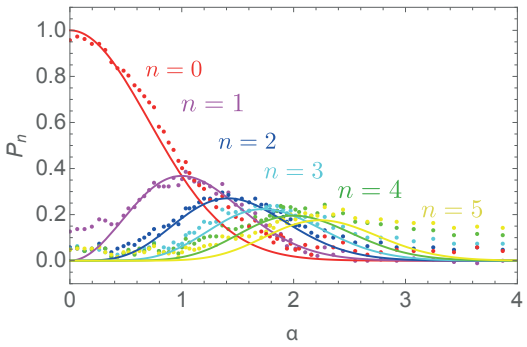

Figure 70: Fock state probabilities deduced from measured transmission, as a function of the amplitude of the coherent displacement α. Full lines correspond to the Poisson distribution $P_n(\alpha) = e^{-|\alpha|^2} \frac{|\alpha|^{2n}}{n!}$.

increases the population of the ground state, so that the transmission is higher.

Fock state probabilities deduced from the transmission measurement with π pulses conditioned on the number of photons in the cavity are shown in Fig. 70, plotted as a function of the amplitude of

the coherent cavity displacement $\alpha = \sqrt{n}$. The full lines correspond to the Poisson distribution Eq. 154.

5.6 LIMITING FACTORS OF THE HYBRID 2D/3D QUANTUM NODE

In this chapter we have presented a hybrid architecture of the quantum node, based on a Josephson Parametric Converter coupling a low quality 2D buffer mode to a high quality 3D memory mode. Although we have successfully coupled a qubit to the memory mode and demonstrated cavity photon number dependent qubit rotations, there are a few limiting factors that make this device not suitable for the quantum node.

First, the qubit readout in this architecture can be done either by qubit state dependent transmission through frequency conversion from buffer to the memory mode, or by qubit state dependent reflection on the direct port to the memory. However, both of these are slow as they are limited by the coupling of the direct memory port. This port is undercoupled in order not to degrade the quality factor of the storage mode, and as the coupling is small, the π pulses have to be long. As we will see in the next chapter, this can be solved by adding a supplementary resonator, strongly coupled to the qubit, whose only purpose is to measure its state and reinitialize it to the ground state.

Second difficulty is obtaining the frequency tunability. The main disadvantage of the 3D architecture is the rigidity of its design. Frequency tunability is most commonly obtained using the flux modulation of a squid or Josephson ring. Magnetic flux is commonly applied either through fast on chip DC lines or using an external magnetic field. In the case of 3D cavities both of these are challenging. Integrating fast flux lines necessarily involves making holes or cuts in the cavity walls, which decreases its quality factor. External magnetic field on the other hand is expelled from the cavity as they are realized in superconducting material. We have opted for the second solution, with the external magnetic field produced by applying a voltage on a NbTi superconducting coil that is fixed above the superconducting cavity and the Josephson ring that was situated outside of the cavity and coupled to it through apertures in the cavity walls.

metal	Al	Al	Al	Al	Cu/Pb
JRM	yes	no	no	yes	yes
qubit	no	no	no	yes	yes
$\frac{\kappa_m^{loss}}{2\pi}$ (kHz)	50-200	30-100	1	50-200	70
Q	4.5×10^4	8×10^4	6×10^6	3.5×10^4	10^5

Table 9: Measured dissipation rates and quality factors for different test 3D cavities coupled or not to superconducting circuits. Ranges of values obtained during different cool-downs are shown for the non-reproducible values. JPC chip is represented in yellow and qubit chip in green.

In order to identify the limiting sources of losses in our device, we have done a series of tests summarized in Table 9. By putting two cavity bottoms together, that do not include any chimneys nor apertures, losses comparable to those of compact convex 3D cavities are obtained. This result points out that the main sources of losses are different cuts and seams needed to integrate the JPC and the transmon, although the presence of sapphire substrate is evidenced to introduce further losses as well.

We can conclude that hybrid 2D/3D architecture is prone to excessive losses. To address this problem and increase the lifetime of the storage mode, we have thus adopted two different strategies, that will be presented in the following chapter.

5.7 CONCLUSION

The main results of this chapter are:

- Demonstration of a qubit in the photon number resolved regime coupled to the memory of a quantum node.
- Characterization of a lead plated copper cavity.
- Population reset protocol for the 3D transmon qubit of the quantum node.
- Characterization of losses in 3D microwave cavities and determination of the limiting factors for the hybrid 2D/3D quantum node architecture.

6 QUANTUM NODE ARCHITECTURES

"One's destination is never a place but rather a new way of looking at things."

Henry Miller

In the previous chapter we have seen that transitions between 2D and 3D resonators in the hybrid architecture engender dissipation and uncontrolled losses. In this chapter we will present two different solutions that bypass the 2D/3D interconnects, first a fully 3D waveguide architecture and then a fully 2D CPW geometry.

6.1 FULLY 3D WAVEGUIDE ARCHITECTURE

3D cavities have been demonstrated in multiple experiments to improve coherence times by orders of magnitude, both of the cavity itself and of the 3D transmon qubits embedded inside of them. This is why the first strategy we adopt consists in a fully 3D architecture.

6.1.1 *Separate photon storage and qubit readout modes*

As discussed in the previous chapter, counting the number of photons in the memory cavity consists in selective, photon number conditioned excitation of the qubit, followed by the qubit readout. However, the qubit measurement requires the cavity to be in an empty state, which necessitates waiting for few lifetimes of the memory mode for the cavity to empty out. It is thus interesting to completely decouple the detection setup from the system by adding a third resonator that is strongly coupled to the qubit and whose unique role is to efficiently measure and reset it [126]. A scheme with separated photon storage and qubit readout modes is represented in Fig. 71.

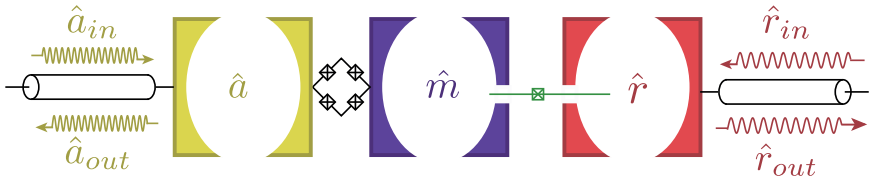

Figure 71: Schematic of the three resonators architecture with buffer resonator a and memory resonator m coupled through a JRM, and a separate cavity r for the qubit readout.

The Hamiltonian of the system reads

$$\begin{aligned}\hat{H} &= \hbar\omega_a \hat{a}^\dagger \hat{a} + \hbar\omega_m \hat{m}^\dagger \hat{m} + \hbar\omega_r \hat{r}^\dagger \hat{r} \\ &+ \hbar\frac{\omega_q}{2}\hat{\sigma}_z - \hbar\chi_{mq}\hat{m}^\dagger\hat{m}\left|e\right\rangle\left\langle e\right| - \hbar\chi_{rq}\hat{r}^\dagger\hat{r}\left|e\right\rangle\left\langle e\right|,\end{aligned} \tag{155}$$

where χ_{mq} is the pull between the memory mode and the qubit and χ_{rq} between the readout mode and the qubit. These parameters have to satisfy a few contraints in order to enable both the dispersive readout and arbitrary state preparation. While the photocounting requires the qubit-memory cavity pull to be large enough such that system is in the photon number resolved regime, $\chi_{mq} > \kappa_m, \kappa_q$, it should still be sufficiently small so that a π pulse spectrally large enough to address the qubit dressed by the first ~10 photon states can be performed. Similarly, qubit-readout cavity pull should be larger than the cavity linewidth $\chi_{rq} \gtrsim \kappa_r$ to optimize the readout strength. In the following section we will see how the system is designed to respect these requirements.

6.1.2 *Fully 3D design*

Both the memory and the readout resonators are implemented as 3D cavities, with a transmon qubit located in the tunnel in the bulk metal between the two, similarly to the architecture developed by the Yale group [112].

For a 3D cavity coupled to a planar JPC, the main source of decoherence are the interconnects that transition between the coaxial microwave environment of the transmission lines, and planar and 3D microwave environments of the resonators. In this full 3D design, the JPC is wirelessly embedded inside of a cavity, similarly to the wire-

less Josephson amplifier implemented by the Yale group [127]. The bottom half of the device is shown in Fig. 72.

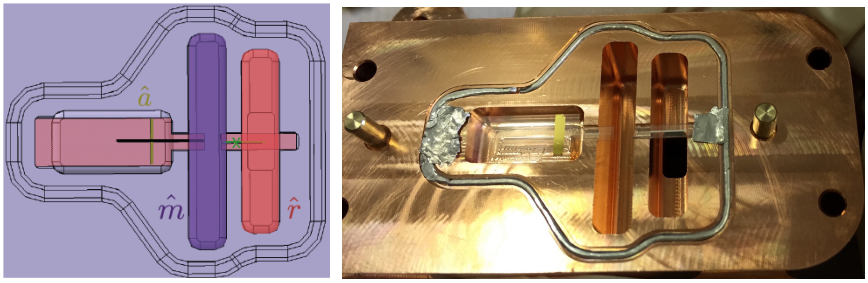

(a) (b)

Figure 72: (a) CATIA drawing and (b) photograph of the bottom half of the three-cavity cQED device with the left cavity hosting the buffer resonator a, the memory cavity m in the middle and the readout cavity r on the right. Two sapphire chips are placed between the top and the bottom parts. The left chip carries a microstrip buffer resonator a with a JRM in the middle, coupling it to a planar antenna that dips through the left tunnel into the memory cavity. The right sapphire chip hosts the transmon that couples to the memory cavity on its left and to the readout cavity on its right. Josephson junction of the qubit is located in the tunnel in the bulk metal.

The three cavities are machined in copper and the plan is to ultimately electroplate the memory cavity with lead in order to get a high Q factor. The left cavity has the dimensions of a rectangular WR62 waveguide and its top part contains an iris whose dimensions were chosen to enable strong coupling of the buffer resonator situated in this cavity to the transmission line. The iris is backed by a waveguide to SMA adapter, that connects the device to the input coaxial transmission line.

Buffer mode a is a planar resonator realized in microstrip architecture on a sapphire chip with a gold ground plane strip on its back. The HFSS simulations that we have done, showed that the microstrip ground plane is necessary because due to the ground plane defined by the walls of the waveguide cavity, the buffer mode impedance would be very large, which would result in the buffer mode resonating at a frequency too high and too detuned from the qubit to obtain the

strong coupling, even if the resonator extends on the whole width of the cavity. Furthermore, as we will see in the next section, the buffer resonance would be too high for the bandwidth of the waveguide cavity. The width of the ground plane is 10 times larger than the width of the buffer antenna, but is chosen small compared to the length of the cavity to avoid spurious reflection of the incoming field a_{in} on it. The buffer mode is coupled directly to the propagating mode of the rectangular waveguide through dipole antennas, which eliminate the need for PCB and wirebonds. This is a great simplification in the impedance perceived by the device compared to the hybrid 2D/3D architecture. The coupling is maximized by setting the distance between the bottom wall of the rectangular waveguide cavity and the sapphire chip to the quarter wavelength of the lowest propagating mode. The bottom wall is an effective shorted termination, such that the buffer resonator is at an electric field antinode of the standing wave.

The signal propagating down the rectangular waveguide cavity excites the differential mode across the buffer resonator which eliminates the need for hybrid couplers used in previous experiments to distribute the field with differential polarization. Hybrid couplers are lossy and cumbersome elements which makes the design where they are not necessary very appealing. In this design however, a hybrid coupler is still used for the pump tone. Full cryostat wiring is shown in Fig. 95. Pump field is applied through two symmetrical pins that dip on the two sides of the rectangular waveguide cavity aligned with the dipole coupling antennas of the buffer resonator. One of the SMA cables for the pump excitation can be seen on the closed device in Fig. 73b.

Josephson Ring Modulator (JRM) is located in the middle of the buffer resonator. As the cavity is made of copper, the JRM can be unobstructedly flux biased with an external magnetic field. JRM couples the buffer mode to an antenna, which extends through a tunnel in the bulk metal to the memory cavity. Memory cavity, in the middle in Fig. 72 has no direct ports to the environment. Before the final cool down, it can be selectively lead plated using the electrodeposition technique developed for the previously studied architecture. As the lead oxydizes quickly and its oxyde is not superconducting, the lead plating is not done for the calibration measurement runs.

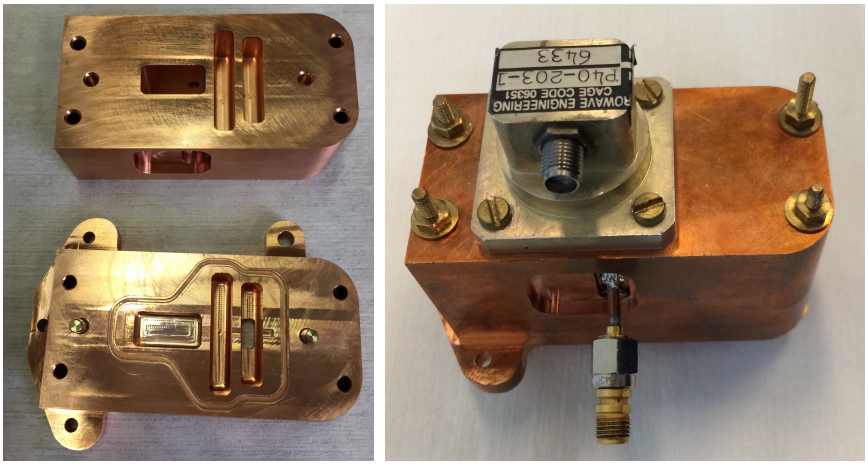

(a) (b)

Figure 73: (a) Top and bottom halves of the three-cavity cQED device. (b) Closed device with waveguide to SMA adapter used to differentially excite the buffer mode. One of the two pump ports is visible on the front side.

The difficulty compared to the previous design is that the coupling between the antenna and the memory mode is done asymmetrically, with only one arm of the antenna coupling to the memory field on one side of the JRM. By consequence, JRM does not perceive the same impedance on both sides. To remedy this, we have made one arm of the antenna longer than the other one. The optimal length difference was simulated using HFSS software by maximizing the quality factor of the memory mode. This issue will be discussed in more details in section 6.1.6.

Finally, the cavity on the right in Fig. 72 is the qubit readout cavity. The junction of the qubit is located in the tunnel between the memory and readout cavities, and couples to them with two antennas whose lengths were determined in electromagnetic HFSS simulations to ensure strong dispersive coupling. An iris in the bottom of the readout cavity connects it to the transmission line through a waveguide to SMA connector. The size of the iris was determined in HFSS simulations to allow for strong coupling.

Both the buffer and readout modes are addressed by waveguide transmission lines. In the following section, we will explain how waveg-

uides can be used as a filtering tool to extend the lifetimes of the qubit and the memory cavity without compromising on the readout efficiency.

6.1.3 *Waveguide filtering*

The 3D architecture has the advantage of being compatible with microwave waveguides. Microwave waveguides are metallic transmission lines used at microwave frequencies. The maximum wavelength a rectangular waveguide can support is given by twice the length of the longer dimension of the cross-section, labeled d in Fig. 74a. Close to that cutoff, they thus act as high-pass filters with a lower cutoff frequency $f_c = \frac{c}{2d}$, where c is the speed of light.

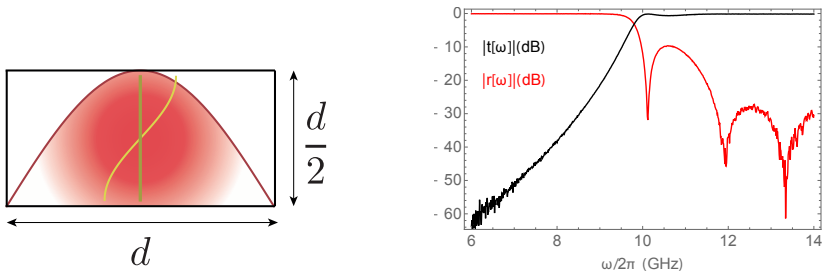

(a) (b)

Figure 74: (a) Cross-section of a waveguide with largest supported wavelength mode TE_{10}. Planar $\frac{\lambda}{2}$ buffer mode is represented in yellow. (b) Measured transmission and reflection coefficients for WR62 waveguide with cutoff frequency $f_c = 9.5$ GHz.

By designing the readout cavity and buffer resonators such that their resonance frequencies satisfy $\omega_r, \omega_a > 2\pi \times f_c$, we ensure that they can propagate in the waveguide without dissipation. On the other hand, waveguides can be used to filter out the qubit and memory modes that are designed to resonate bellow the cutoff frequency $\omega_q, \omega_m < 2\pi \times f_c$. In this experiment we use the WR62 waveguides. Reflection and transmission coefficients for this waveguide measured at room temperature are shown in Fig. 74b, with the cutoff frequency $f_c = 9.5$ GHz.

In fact, rectangular waveguides behave rather like bandpass than high pass filters. The accepted limits of operation, where losses are negligible, are approximately between 125% and 189% of the lower cutoff frequency, that is 12.4 GHz to 18 GHz for WR62 waveguide. This sets an additional constraint for the frequency of the buffer mode, which made it necessary to realize it as a compact, lumped element resonator.

6.1.4 *Lumped buffer resonator*

Planar buffer resonator is oriented in the direction of the shorter dimension of the waveguide cross-section as shown on Fig. 74a. It is thus differentially polarized by the fundamental TE_{10} mode propagating in the rectangular waveguide. The minimum resonance frequency a distributed $\frac{\lambda}{2}$ buffer mode can take is given by the maximum possible length of the resonator, that is $\frac{\lambda_a}{2} = \frac{d}{2}$ (see Fig. 72). The minimum buffer frequency is then twice the lower cutoff frequency

$$f_a^{min} = \frac{c}{\lambda_a} = \frac{c}{d} = 2f_c > 189\% \ f_c, \tag{156}$$

which places it outside of the waveguide bandwidth.

Having the buffer resonance frequency outside of the waveguide bandwidth would attenuate the propagating signal and make strong coupling to the buffer mode unattainable. One possible strategy to reduce the resonance frequency of the buffer mode is to increase the effective length of the distributed resonator by creating meanders. This approach has an important drawback which is the spectral crowding coming from the multiple spurious modes due to the signal reflections at bending points which induce impedance discontinuities in this geometry without an infinite ground plane. An alternative approach is concentrating the inductance and capacitance of the buffer mode in a smaller region by making a compact or lumped resonator. As a clean spectral environment reduces the number of unwanted decoherence channels, we opt for the second approach.

The size of the lumped buffer resonator is reduced to the size of the Josephson ring. Most of the buffer inductance L_a comes from the wires of the ring, which is shunted by four identical capacitors C_s,

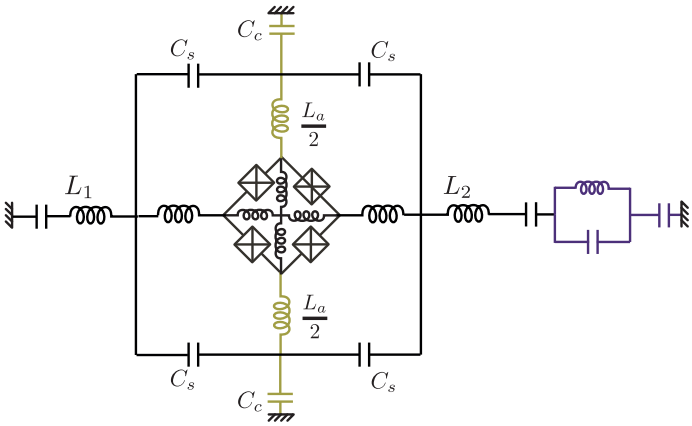

Figure 75: Equivalent circuit of the lumped buffer resonator with four large shunting capacitors C_s. Josephson ring couples the buffer mode to an asymmetric antenna mode, that capacitively couples to the memory resonator. L_1 and L_2 are inductances of the two arms of the antenna. Capacitors C_c couple the compact buffer resonator to the dipole antennas that couple it to the incoming signal field.

as shown in the Fig. 75. The differential eigenmode of this circuit is given by

$$\omega_a = \frac{1}{\sqrt{(L_a + L_{JRM})C_s}}, \tag{157}$$

where L_{JRM} is the effective inductance of the Josephson ring. Coupling capacitors C_c couple the buffer resonator to the antennas, that mediate the coupling to the waveguide. Both the shunting and coupling capacitors are realized in the interdigitated architecture as shown in Fig. 76a.

Unlike the microstrip resonator, the lumped buffer resonator does not have higher harmonic resonances. By consequence, the pump applied at frequency $\omega_a + \omega_m$ can be considered stiff to a good approximation. Furthermore, lumped resonators have higher internal quality factors than the microstrip ones likely due to the absence of the dipole radiation on the edges.

On the other hand, capacitances larger then 0.5 pF are difficult to achieve using the interdigitated configuration, which makes some frequencies unattainable [128]. Furthermore, the interdigitated capacitors present some parasitic capacitances and inductances, which

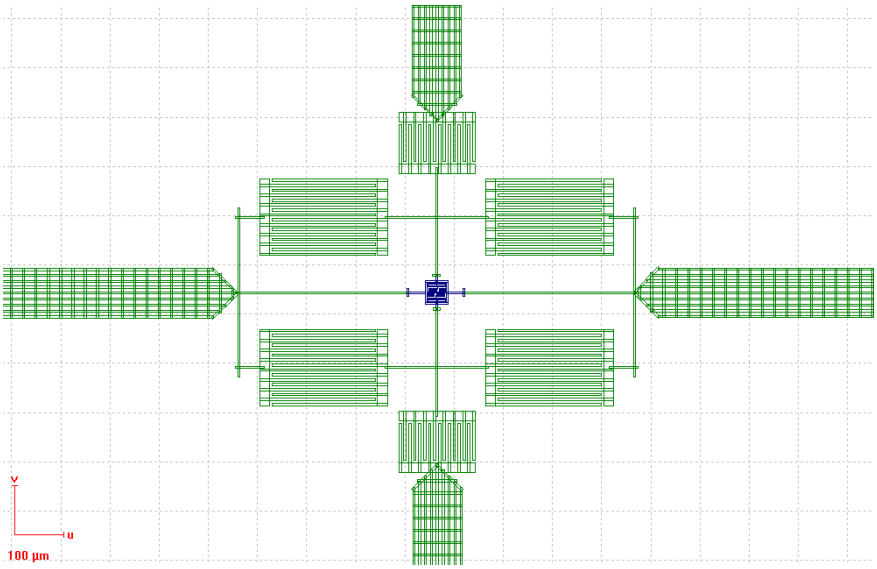

(a)

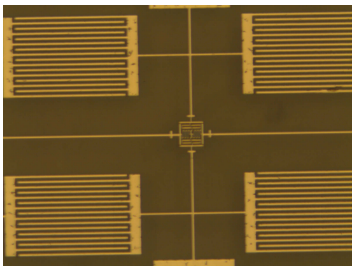

(b)

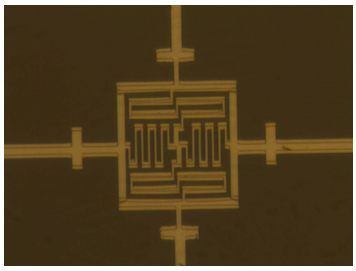

(c)

Figure 76: (a) Electron lithography drawing of the Josephson ring shunted by four large capacitors an coupled through two smaller capacitors to the antennas. (b) Optical microscope image of the lumped buffer resonator with the four shunting capacitors in the corners. (c) Optical microscope image of the Josephson ring shunted by meanders that acts as linear inductors.

makes their scaling to match a given frequency not straightforward. This is why we use a microwave simulation tool called *qucs* [129]. In a simulation explained in more details in section 10.2, we have fixed the buffer resonance frequency to a value of $\omega_a = 2\pi \times 13.1$ GHz within the waveguide bandwidth and for fixed length of wires and thus fixed buffer impedance, we have done a parametric optimization

on the shunting and coupling capacitances C_s and C_c. We determine $C_s = 145$ fF and $C_c = 71.5$ fF.

To a good approximation, the capacitance of an interdigitated capacitor is given by [130]

$$C = \frac{\epsilon}{h} S, \tag{158}$$

where $S = l_x \times l_z$ is the surface of the capacitor, ϵ is the electric permittivity and $h = d + w$ where d is the distance between two neighboring fingers and w is the width of an individual finger, as shown in Fig. 77. This enables us to roughly determine the size and number of fingers for the capacitors.

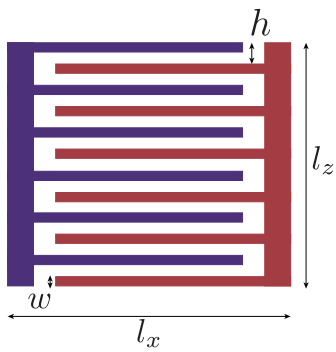

Figure 77: Schematic of an interdigitated capacitor. The total surface $S = l_x \times l_z$, the width of one finger w and the distance between two neighboring fingers $h - w$ to a good approximation determine the total capacitance.

For the sample used in this experiment, there are $N = \frac{l_z}{2h} = 8$ fingers for each plate of both the shunting and the coupling capacitor. Their dimensions are $l_x \times w = (220 \times 5)$ μm for the shunting capacitors and (110×5) μm for the coupling capacitors, as can be seen in Fig. 76.

6.1.5 *Vanishing Kerr shift*

We have created an atypical Josephson mixer, where a Josephson ring couples one lumped resonator to a 3D resonator. We characterize this device by measuring the signal reflected on the buffer resonator while sweeping the current through the magnetic coil I_{coil}. From the

reflected signal dependance in frequency, we determine the buffer resonance frequency as a function of flux bias, see Fig. 78.

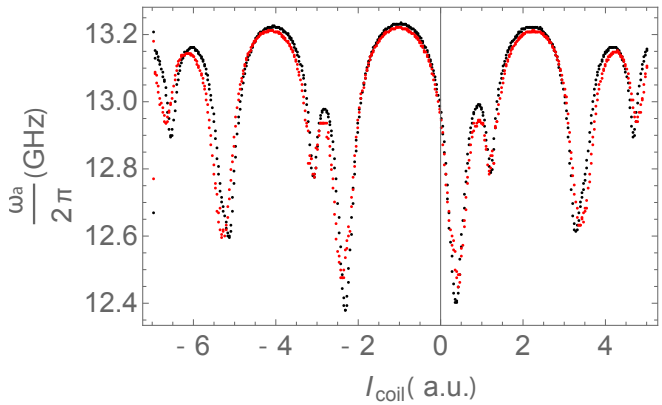

(a)

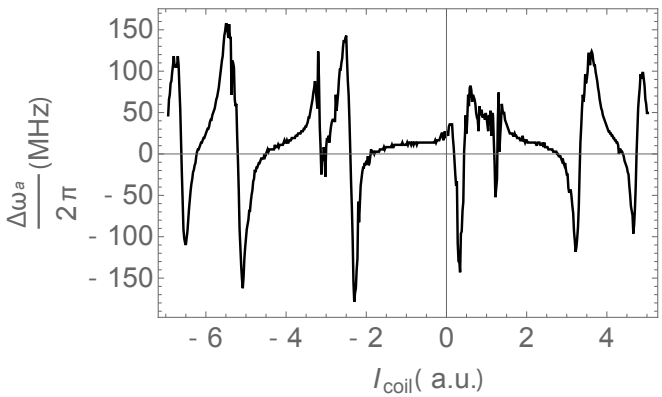

(b)

Figure 78: (a) Measured buffer resonance frequency as a function of the current in the magnetic coil. Red dots correspond to a measurement with high probe power $P = 5$ dBm and black dots to a measurement with low probe power $P = -40$ dBm. They intersect at "sweet flux points" where the cross Kerr shift induced by the pump tone is vanishing. (b) Frequency shift due to the self-Kerr effect as a function of the current in the magnetic coil.

As explained in the section 2.2.2 on the Josephson mixer, there is a critical flux at which a shunted Josephson ring switches from the symmetric to a broken symmetry flux configuration in the ring subloops.

The two flux configurations correspond to two sizes of the arches that are observed in the flux dependance of the eigenfrequencies. The irregularity of the pattern is due to imperfections in the areas of the subloops of the Josephson ring and inequality of the junction sizes [122].

The measurement is done at two different probe powers shown in black and red in Fig. 78a. For no bias current $I_{coil} = 0$, and at probe power $P = -40$ dBm referred to the output of the signal generator, resonance frequency of the buffer mode is found to be $\omega_a = 2\pi \times 13.164$ GHz, the coupling rate is $\kappa_a = 2\pi \times 30.5$ MHz and the dissipation rate is $\kappa_a^{loss} < 2\pi \times 1$ MHz. At high probe power, the resonance frequency shifts due to the self-Kerr effect. For the Josephson ring shunted by inductances though, the Kerr term in Hamiltonian has a cosinusoïdal dependance on the external magnetic flux φ_{ext}, see Table 3. There are thus certain "sweet points", corresponding to $\varphi_{ext} = 2\pi$, at which this term goes to zero and the Kerr shift vanishes, as can be seen in Fig. 78b. This is an important advantage of the Josephson mixer employed for the quantum node, compared to other simpler sources of nonlinear interaction such as a single Josephson junction of a transmon qubit [131], that were used to perform efficient release of multiphoton quantum states, but not yet the signal capture.

Vanishing Kerr shift presents few benefits for quantum node realization. First, operating the quantum node requires fast switching between the amplification and conversion regimes. As the pump tones used in these two regimes are spectrally far from each other, they require powers that can differ by orders of magnitude. By consequence, if the Kerr term is non zero, frequencies of the modes coupled to the nonlinearity shift between the amplification and conversion regimes. Few feedback steps are thus needed to adjust the frequency and the amplitude of the pump tone. Working at the "sweet flux" where the Kerr shift vanishes greatly simplifies this routine.

Furthermore, capture efficiency Eq. (150) of the signal incoming to the memory mode is limited by the Kerr effect. Indeed, when a gaussian shaped signal wavepacket starts entering the cavity, the resonance frequency of the memory mode shifts due to the self-Kerr effect. The pump amplitude and frequency would thus have to be

adapted while the signal is entering in order to match its amplitude and obtain the maximum efficiency $\eta = 1$.

6.1.6 *Asymmetric coupling to the memory mode*

The coupling between the buffer and memory modes is mediated by an asymmetric antenna through a tunnel in the copper bulk between the two cavities. The size of the tunnel is small, so that it doesn't introduce losses to the memory mode. However, buffer and antenna are on the same chip and the chip needs to be wide enough to support the large antennas for the strong coupling κ_a of the buffer to the transmission line. This is why the chip has a nontrivial shape that can be seen in Fig. 79. The chip is laser cut because dicing only allows rectangular shape for samples. Laser cutting is made possible by using a sapphire substrate that is only 150 μm thick. E-beam lithography resists are deposited on the sapphire wafer previous to the laser cutting because the shape of a single chip does not allow for the spin coating. E-beam resists are protected from the contamination during the laser cutting step by a thick UVIII resist that can be selectively removed using the IPA.

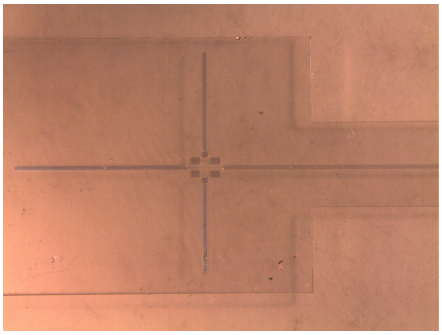

Figure 79: JPC with a lumped buffer resonator on a laser cut sapphire substrate.

Amplitudes of the electric field of the system eigenmodes, simulated with the HFSS software, are shown in Fig. 80. The memory mode shown in Fig. 80b is delocalized on the planar antenna that couples it to the JRM. Simulated frequency of the memory mode is $\omega_m = 2\pi \times 8.14$ GHz.

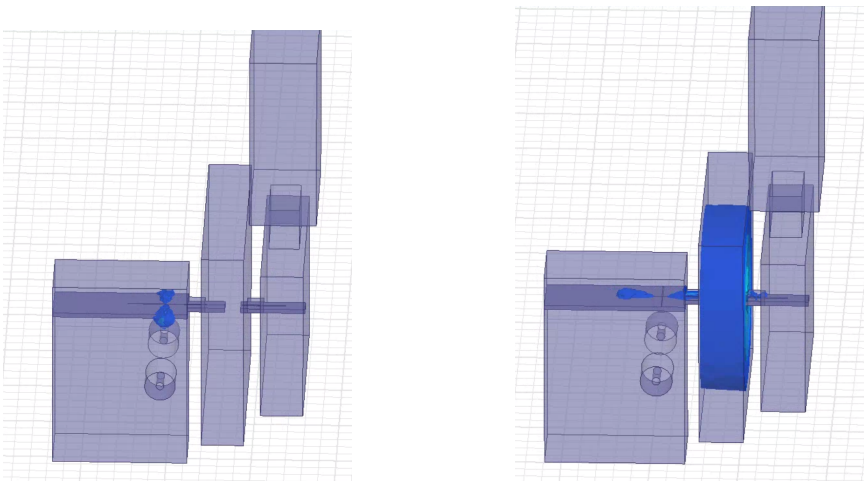

(a) (b)

Figure 80: Amplitude of the electric field simulated using Ansys HFSS software for (a) the buffer $\frac{\lambda}{2}$ mode and (b) the fundamental mode of the memory cavity.

As there is no direct port that allows probing the memory mode, we resort to an indirect probing technique that makes use of the Kerr shift. We measure the reflection coefficient on the buffer resonator while sweeping the frequency of a strong pump tone. When the pump tone is resonant with one of the eignemodes of the system, a cross Kerr shift is induced on the buffer mode, as can be seen in Fig. 81. This measurement is an indirect way to determine the frequencies of the eigenmodes of the system. Guided by the expected value from the electromagnetic simulation, we find the memory mode at $\omega_m = 2\pi \times 8.106$ GHz. These two measurements allow us to determine the pump frequency for the parametric conversion between the buffer and memory modes $\omega_p = \omega_a - \omega_m = 2\pi \times 5.058$ GHz.

6.1.7 *Conversion pump*

The pump tone is applied through symmetrical pins that dip into the waveguide cavity right above the antennas of the lumped buffer resonator in order to excite the common mode of the Josephson mixer. However, the cutoff frequency of this waveguide being 9.5 GHz, the

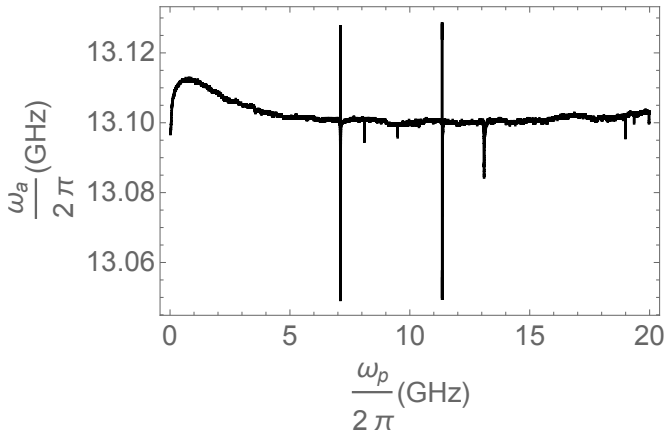

Figure 81: Measured buffer frequency as a function of the frequency of the pump tone. When the pump frequency is resonant with an eigenmode of the system, noticeable Kerr shift is induced on the buffer mode.

conversion pump frequency is well below the waveguide bandwidth and there is a considerable attenuation of the signals propagating at lower frequencies. During the first measurement run, we understood that even at the maximum pump power that we could send using a microwave source backed by a room temperature amplifier, we could not succeed in inducing the conversion to the memory mode. In another measurement run, the pins for the pump tone were made much longer and curved such that they come to the immediate proximity of the buffer resonator. However, in this configuration, the incoming signal gets reflected on the pins resulting in a Fano resonance on the buffer mode.

On the other hand, for a pump tone at frequency $\omega_p = 2\pi \times 7.927$ GHz, a phase roll of 4π at buffer frequency shown in Fig. 82 indicates a conversion to a high frequency mode, $\omega_p = \omega_{mode} - \omega_a$. This is an encouraging result because it means that by changing the dimensions of the memory cavity in order to lower its resonance frequency such that $\omega_a - \omega_m \gtrsim 2\pi \times 7.9$ GHz, the problem of pump tone attenuation would be solved.

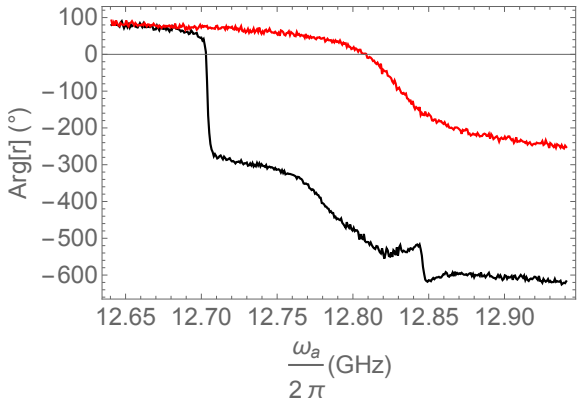

Figure 82: Phase of the measured reflection on the buffer mode with the conversion pump turned on at a frequency corresponding to a conversion from the buffer to a high frequency mode. The phase roll of 4π indicates the strong coupling regime.

6.1.8 *Conclusion on the full 3D geometry*

Most of the building blocks of this complex device were demonstrated to operate as expected. The memory mode has been indirectly observed at the resonance frequency expected from the electromagnetic simulations, but the conversion to memory mode couldn't be attained because the pump tone was filtered out by the waveguide. However, a signature of frequency conversion to a high frequency mode in the strong coupling regime has been observed. This shows that the architecture could be modified to enable quantum node implementation by setting the memory mode at a lower frequency.

In parallel with this design, we have realized another solution which is a full 2D architecture.

6.2 2D COPLANAR WAVEGUIDE ARCHITECTURE

An alternative strategy to disposing of 2D/3D interconnects and the dissipation that comes with them is going full 2D. Even though this approach lacks the clean electromagnetic environment that comes with the 3D cavity, it has a lot of other advantages.

First, nanofabrication recipes are well known and changes in the design can be incorporated much more readily than in the case of 3D cavities that have to be machined in the bulk metal. Second, the devices are much less cumbersome, especially with the new proposals of integrating on chip microwave components such as circulators and microwave switches [5, 132]. Finally, a great progress in the understanding of sources of decoherence has been made, in particular identifying the locations of the TLSs as metal-substrate and substrate-air interfaces [133]. This has lead to emergence of techniques to reduce their impact that enabled achieving quality factors of 10^6.

During the writing of this thesis, the full 2D quantum node project is still in a stage of preliminary measurements. Few considerations concerning the circuit design and simulations prior to the experiment will be detailed here.

6.2.1 *Circuit design*

In the previous experiments described in this thesis, planar resonators were fabricated in a microstrip architecture. This architecture is convenient for the Josephson mixer, however, when it comes to optimizing the resonator lifetime, it is not the most competitive one. Indeed, microstrip resonators have large radiation losses due to the large electric dipole induced between the strip and the ground that is radiating at the extremities of the resonator. In the CPW architecture on the other hand, the dipole moment vanishes due to the ground plane that is surrounding the resonator on both sides.

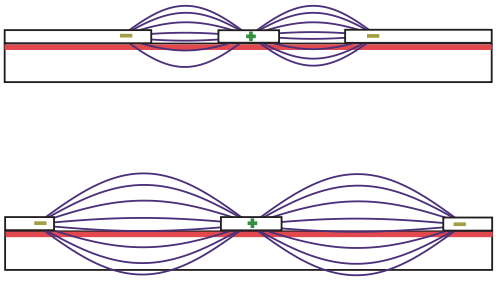

Figure 83: Cross section of CPW resonators with different gap widths. Participation ratio of the surface of the dielectric substrate is more important for smaller gaps.

The quantum node circuit described in this section is realized in CPW architecture. The schematic of the experiment is the same as the one described in Fig. 71. Buffer mode is strongly coupled to the transmission line through the port that can be seen on the top left in Fig. 84. Frequency tunability of the device is ensured by a large participation ratio of the variable inductance of the Josephson ring, controlled by magnetic flux, in the total inductance of the buffer resonator. The tunability can thus be increased by decreasing the geometric inductance of the buffer resonator, which is equivalent to decreasing its impedance as $Z = \sqrt{\frac{L}{C}}$. This can be done by decreasing the size of the gap between the resonator and the surrounding ground plane. The fabrication technique that uses a laser writer sets this gap to the minimum value of 10 μm.

However, small gaps concentrate the electric field lines in the proximity of the lossy metal-substrate and substrate-air interfaces, as illustrated in Fig. 83, which makes them detrimental for the coherence of the resonator [134]. Increasing the gap decreases the participation ratio of the dielectric surface and by consequence increases the quality factor of the resonator. In a recent systematic study at UCSB it was found that quality factor saturates around the gap width of 50 μm where the other loss mechanisms such as radiation become dominant [135]. The gap for the memory resonator, for which the quality factor needs to be maximized, is fixed to 60 μm.

A transmon qubit is capacitively coupled to the memory mode with one antenna and to the readout mode with the other antenna. Geometrical parameters that determine the coupling, such as the antenna dimensions and the distance to the resonators were simulated using the Sonnet software. It is an electromagnetic solver for high frequency RF and microwave analysis. Simulated current distributions for four eigenmodes are shown in Fig. 84.

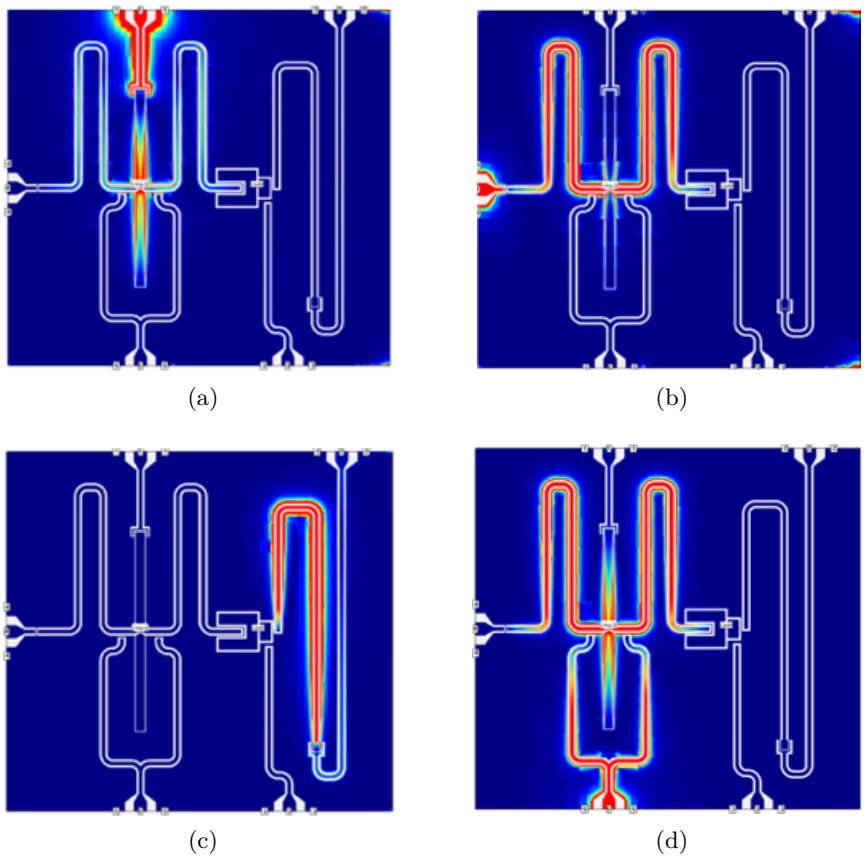

Figure 84: Current amplitude simulated using Sonnet. (a) $\lambda/2$ mode of the buffer resonator, (b) $\lambda/2$ mode of the memory resonator, (c) $\lambda/2$ mode of the readout resonator and (b) common mode of the JPC.

6.3 CONCLUSION

Quantum node based on a Josephson mixer is an ongoing project in our group. Its first experimental realization, where a single cavity was used both for the photon storage and qubit readout gave encouraging preliminary results for the arbitrary state preparation. In this chapter we have presented two upgraded realizations.

The main results of this chapter are:

- Josephson mixer with a JRM shunted by inductances was used instead of a Josephson Parametric Converter, in order to enable cancelling out the Kerr shift and increase the efficiency of the quantum memory. A qubit readout mode separate from the photon storage mode was added.
- Design and realization of a fully 3D waveguide quantum node. A wireless Josephson mixer addressed by microwave waveguides with a lumped buffer mode was integrated in this architecture.
- Design and simulation of a fully 2D CPW quantum node.

Part III

PARAMETRIC OSCILLATION

7

PARAMETRIC OSCILLATION

"There's a crack in everything, that's how the light gets in."

Leonard Cohen

Parametric interaction in a Josephson mixer provides quantum limited parametric amplification, as well as noise squeezing and parametric frequency conversion between modes. All of these applications are in the pumping regime of the linear resonator response. In this regime the stiff pump approximation applies, and the pump tone can be treated as a classical drive connected to a large classical energy reservoir. As such a reservoir cannot be easily depleted, the pump is unaffected by the amplification process.

However, for strong pump powers, a strongly non-linear high-gain amplification regime is attained. This nonlinearity limits the gain and squeezing at the threshold, and also saturates the parametric instability such that above the parametric instability threshold a self-oscillation regime is established. This regime is equivalent to the lasing regime in optics.

This transition occurs when the effective coupling rate, that is the insertion rate of photons in the modes, equals the loss rate of photons from the cavity [136]. In this regime, the amplified signal power becomes a considerable fraction of the pump power, so that the stiff pump approximation breaks down. In the soft pump regime, the interaction between the pump and the signal leads to pump depletion, which gives rise to spontaneous oscillation.

Interestingly, the non linear evolution leading to the parametric oscillation can also be provided by a strong Kerr effect instead of the pump depletion.

In this section we will be interested in the boundary between the parametric amplification and the self-oscillation. We will define the parametric instability threshold above which the linear response of the oscillator tends to diverge at its resonance frequency.

As already seen in Chapter 2, when a Josephson mixer is pumped at frequency $\omega_a + \omega_b + 2\delta$, its Hamiltonian in the frame rotating at $\omega_{a,b} + \delta$ reads

$$\hat{H} = -\hbar\delta\hat{a}^\dagger\hat{a} - \hbar\delta\hat{b}^\dagger\hat{b} + \hbar\chi|p_B|(\hat{a}\hat{b} + \hat{a}^\dagger\hat{b}^\dagger), \tag{159}$$

where p_B is the amplitude of the so called blue detuned pump, and the Langevin equations can be put in the matrix form

$$\frac{\partial}{\partial t}\begin{pmatrix}\hat{a}\\ \hat{b}^\dagger\end{pmatrix} = M\begin{pmatrix}\hat{a}\\ \hat{b}^\dagger\end{pmatrix} + \begin{pmatrix}\sqrt{\kappa_a}\hat{a}_{in}\\ \sqrt{\kappa_b}\hat{b}^\dagger_{in}\end{pmatrix}, \tag{160}$$

with

$$M = \begin{pmatrix} i\delta - \frac{\kappa_a}{2} & -i\chi|p_B| \\ i\chi|p_B| & -i\delta - \frac{\kappa_b}{2}\end{pmatrix}. \tag{161}$$

For zero mean input fields $\langle a_{in}\rangle = \langle b_{in}\rangle = 0$, a trivial solution to this system is the empty cavity state $\langle a\rangle = \langle b\rangle = 0$. In the linear amplification regime this solution is stable, as the cavity quickly dissipates the amplified input vacuum fluctuations. When the system is pumped so strongly that amplification of the vacuum fluctuations creates more excitations than the system can dissipate, new stationary solutions emerge. The instability threshold can thus be found by studying the stability of the empty cavity state. The stability condition can be found by diagonalizing the matrix M

$$\mathrm{Det}(M + i\Delta) = 0, \tag{162}$$

which gives

$$[\delta + i\frac{\kappa_a}{2} + \Delta][\delta - i\frac{\kappa_b}{2} - \Delta] = |\chi p_B|^2. \tag{163}$$

Stability condition reads $\mathrm{Im}\Delta < 0$ [137], so that the parametric instability threshold is given by $\mathrm{Im}\Delta = 0$. At threshold, Eq. (163) can be solved independently for the real and imaginary parts, giving

$$\begin{cases} \Delta = \frac{\kappa_a - \kappa_b}{\kappa_a + \kappa_b}\delta \\ |\chi p_B^{th}|^2 = \frac{\kappa_a \kappa_b}{4} + \delta^2[1 - (\frac{\kappa_a - \kappa_b}{\kappa_a + \kappa_b})^2]. \end{cases} \tag{164}$$

The second equation defines the threshold pump amplitude $|p_B^{th}|$. At zero pump detuning, $\delta = 0$, we find the minimum threshold $|\chi p_B^{th}|^2 = 4\kappa_a\kappa_b$ corresponding to the cooperativity $C = 1$. Beyond this threshold, an empty cavity state still exists as an instable solution, whereas self-sustained parametric oscillation emerges as a new stable solution, with complex amplitudes given by a non-linear solution to Eq. 160

$$\begin{cases} a = a_0 e^{i\theta_a} \\ b = b_0 e^{i\theta_b}, \end{cases} \tag{165}$$

where amplitudes a_0 and b_0 are well defined whereas phases θ_a and θ_b present a continuous degeneracy.

Using the same device as in part i, we first measure the power spectral density of the emitted field from the mode a as a function of the pump power for different pump detunings δ. We then determine the self-oscillation threshold as a function of the detuning, as shown in Fig. 85. There is an asymmetry for positive and negative values of δ which comes from the Kerr effect. In fact, the effective detunings renormalized by self Kerr K_{aa} and cross-Kerr K_{ab} for the two modes are

$$\begin{cases} \delta_a = \delta + K_{aa}|a|^2 + K_{ab}|b|^2 \\ \delta_b = \delta + K_{bb}|b|^2 + K_{ab}|a|^2. \end{cases} \tag{166}$$

Indeed, Kerr effect stabilizes negative detunings such that there is a region of bistability for the empty cavity and self-oscillating solutions [137].

In the following, we measure the emitted quadrature statistics as shown in Fig. 86 below the instability threshold and in Fig. 87 in the parametric self-oscillation regime. The Josephson mixer, with zero

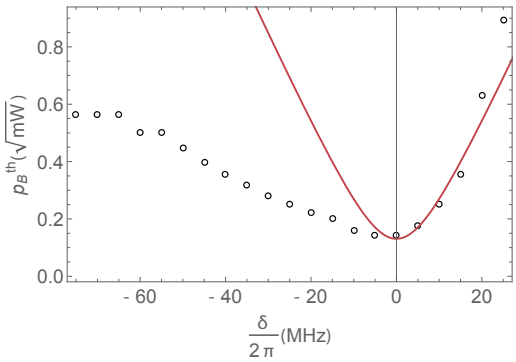

Figure 85: Measured parametric oscillation threshold pump amplitude as a function of the pump detuning δ. Full red line corresponds to Eq. (164) up to an attenuation factor. The pump amplitude is measured at the output of the signal generator, which far exceeds the one at the input of the Josephson mixer.

mean fields at the input, is pumped with zero pump detuning $\delta = 0$, at $\omega_p = \omega_a + \omega_b$. The signal emitted from each of the modes a and b is mixed with an external local oscillator and the resulting quadrature components are digitized with a fast acquisition board. In the parametric amplification regime, the output field is described by a Gaussian distribution centered around the origin. The variance of a single mode a or b is that of the vacuum fluctuations amplified by the Josephson mixer and with the thermal noise added by the chain of amplifiers, as shown in Fig. 86. In the cross-quadrature planes, signature of two-mode squeezing can be seen [72, 73, 6]. Here we have chosen a pump phase such that the correlations are only visible in the $X_a - X_b$ and $P_a - P_b$ planes. However this choice is arbitrary and with another phase correlations would be visible in all the cross-quadrature planes.

In the parametric oscillation regime, the emission amplitude abruptly increases, as can be seen in Fig. 87. The amplitude is constant and reveals the square root of the mean number of photons in the intra-resonator mode, $a_0 = \sqrt{N_a}$. On the other hand, only the sum of the two phases $\Theta = \theta_a + \theta_b$ is constant, but each of the phases θ_a and θ_b can take a continuum of values. As we will see in the following section, the phase of the emitted field can be locked by injecting a small resonant signal.

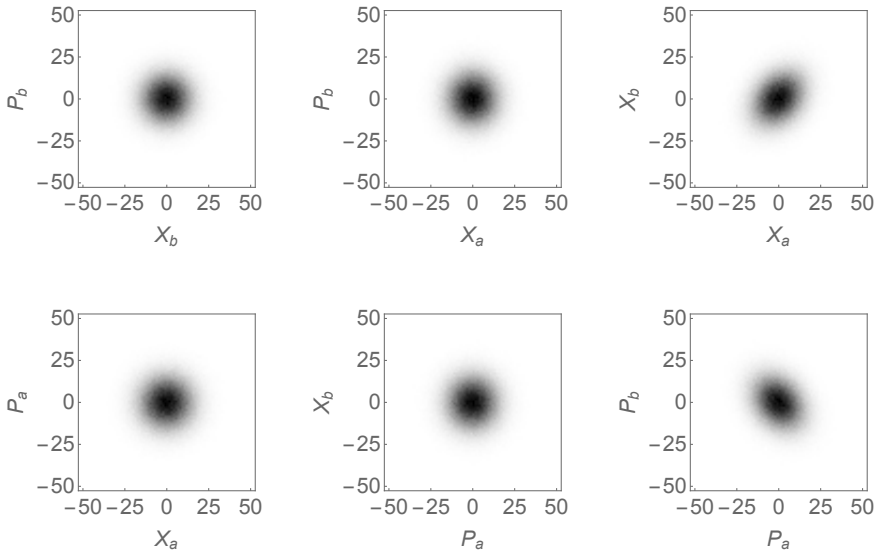

Figure 86: Field quadrature histograms of the output fields measured in the linear amplification regime. They correspond to a stable empty cavity state with a signature of two-mode squeezing that can be seen in the cross-quadrature histograms.

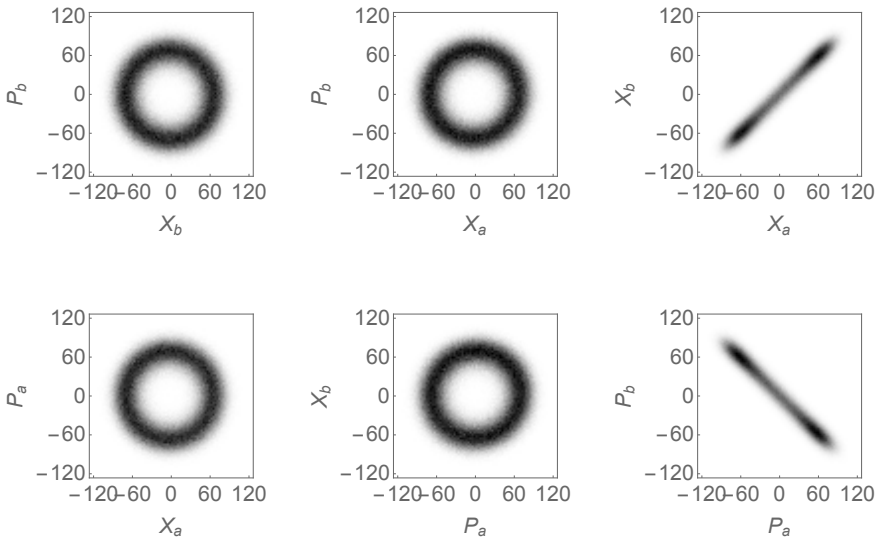

Figure 87: Field quadrature histograms of the output fields measured in the parametric self-oscillation regime. Pump phase was chosen such that the correlations are only visible in the $X_a - X_b$ and $P_a - P_b$ planes.

7.2 INJECTION LOCKING

Injection locking is one of the techniques commonly used with optical laser diodes to obtain narrow linewidths and increase frequency resolution and stability [138]. This technique relies on the injection of a tone at frequency ω_{in}, which stimulates the emission of the atom, natural or artificial, at this injected frequency. This results in the narrowing of the emission spectrum.

Competition between spontaneous and stimulated emission sets a lower limit on the laser linewidth, first calculated by Schawlow and Townes (ST) [139]. In solid-state and semiconducting lasers, charge noise fluctuations induce broadening of the emission peak such that natural linewidths are 10-100 times larger than the ST limit.

Recently injection locking has been demonstrated with semiconductor double quantum dot micromaser [27], as well as with an ac Josephson junction laser [28] and trapped-ion phonon laser [29].

7.2.1 *Injection locking theory*

Time dependent complex amplitude of the cavity output field is

$$\alpha(t) = X(t) + iP(t) = |\alpha| e^{i\omega_{in} t + i\phi(t)}, \tag{167}$$

where $\phi(t) = \phi_e(t) - \phi_{in}$ is the relative phase of the emitted field ϕ_e and injected field ϕ_{in}, as shown in Fig. 88a. The time evolution of the relative phase is described by the Adler equation

$$\frac{d\phi}{dt} + (\omega_{in} - \omega_e) = -\frac{\Delta\omega_{in}}{2} \sin\phi, \tag{168}$$

where ω_e is the natural emission frequency and $\Delta\omega_{in}$ is the range of injection frequencies on which the emission field can get locked. When $|\omega_{in} - \omega_e| < \frac{\Delta\omega_{in}}{2}$, there is a static solution to this equation, that reads

$$\phi = \arcsin\left[\frac{2(\omega_e - \omega_{in})}{\Delta\omega_{in}}\right], \tag{169}$$

so that the phase of the emitted field gets locked to the phase of the injected field, as shown in Fig. 88b.

When the injection tone at frequency ω_{in} is detuned by few linewidths from the natural emission frequency ω_e, this last one is pulled and

locked to the injection tone if its amplitude is large enough. The frequency range $\Delta\omega_{in}$ over which the emission can be injection locked increases with the power of the injected tone

$$\Delta\omega_{in} \propto \sqrt{P_{in}}, \tag{170}$$

as was first predicted by Adler [140]. At low injection tone powers, mean number of photons in the cavity is smaller than 1 and the emission is not affected by the injection.

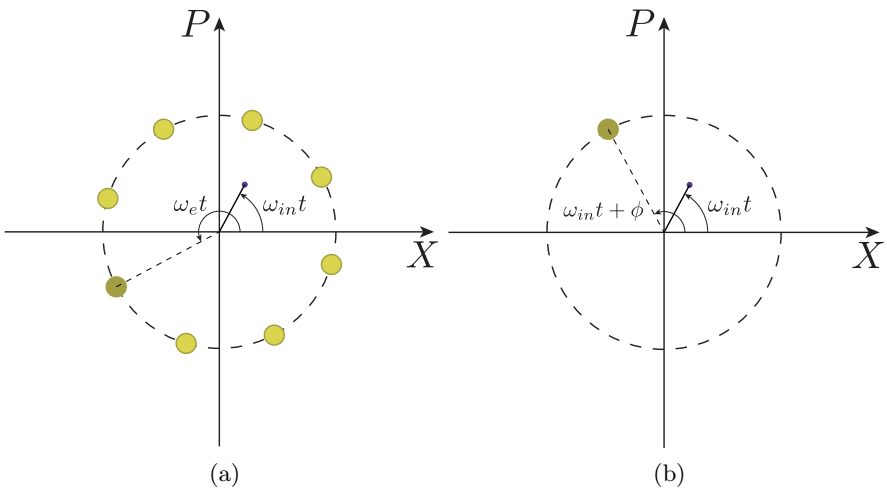

Figure 88: (a) In the unlocked regime, the phase of the natural emission field at frequency ω_e is fluctuating with respect to the phase of the injection tone at frequency ω_{in}. (b) In the injection locked regime, the relative phase ϕ between the emission and injection is fixed.

Outside of the injection locking range, i.e. for $|\omega_{in} - \omega_e| > \frac{\Delta\omega_{in}}{2}$, solution of the Adler equation Eq. (168) is given by

$$\tan\frac{\phi(t)}{2} = -\frac{\omega_b}{\omega_e - \omega_{in}}\tan\frac{\omega_b t}{2} - \frac{\Delta\omega_{in}}{2(\omega_e - \omega_{in})}, \tag{171}$$

where ω_b is the beating frequency and it reads

$$\omega_b = (\omega_e - \omega_{in})\sqrt{1 - \left(\frac{\frac{\Delta\omega_{in}}{2}}{\omega_e - \omega_{in}}\right)^2}. \tag{172}$$

In the transient regime, the emission frequency is pulled towards the injection frequency

$$\omega_e = \omega_{in} + \omega_b. \tag{173}$$

General solution for the complex cavity field amplitude in the transient regime is

$$\alpha = |\alpha| e^{i(\omega_{in}+\omega_b)t} \sum_{n=-\infty}^{\infty} a_n e^{in\omega_b t}, \tag{174}$$

where a_n are the expansion coefficients that can be analytically calculated [141]. There is thus a set of emission frequencies ω_e^n given by

$$\omega_e^n = \omega_{in} + (n+1)\omega_b, \tag{175}$$

where $n = 0$ corresponds to the pulled emission frequency and $n = \pm 1, \pm 2$ etc. correspond to higher order distortion sidebands. Note that $n = -1$ corresponds to the injection tone.

7.2.2 *Standard injection locking of a Josephson mixer*

The Josephson mixer is pumped above self-oscillation threshold at the blue pump amplification frequency $\omega_B = 2\pi \times 14.92$ GHz and power $P_B = -16$ dBm. A weak injection tone at frequency ω_{in} is applied on resonance on the mode a and its power is swept from -83 to -53 dBm referred to the output of the signal generator. Measured quadrature statistics for four powers of injected signal are shown in Fig. 89 which puts in evidence the transition from the phase unlocked to the phase locked regime. Note that there is approximately 50 dB of attenuation on the amplification pump line between the signal generator and the device, and 70 dB on the signal line (see Fig. 93).

In the following measurement, the power of the injected signal is fixed to $P_{in} = -35$ dBm and its frequency is swept in the range of 50 MHz in proximity of the resonance frequency ω_a. Measured power spectral density of the field propagating from the mode a is shown in Fig. 90c. Dashed red line corresponds to Eq. (175) with the injection locking range $\Delta\omega_{in} = 4.8$ MHz. This range however is predicted by the Adler theory to depend on the injected power. To experimentally verify this dependence, we repeat the power spectral density measurement as a function of the frequency of the injection tone for increasing injected powers and for four different amplification frequencies. Injection locking range determined by matching Eq. (175)

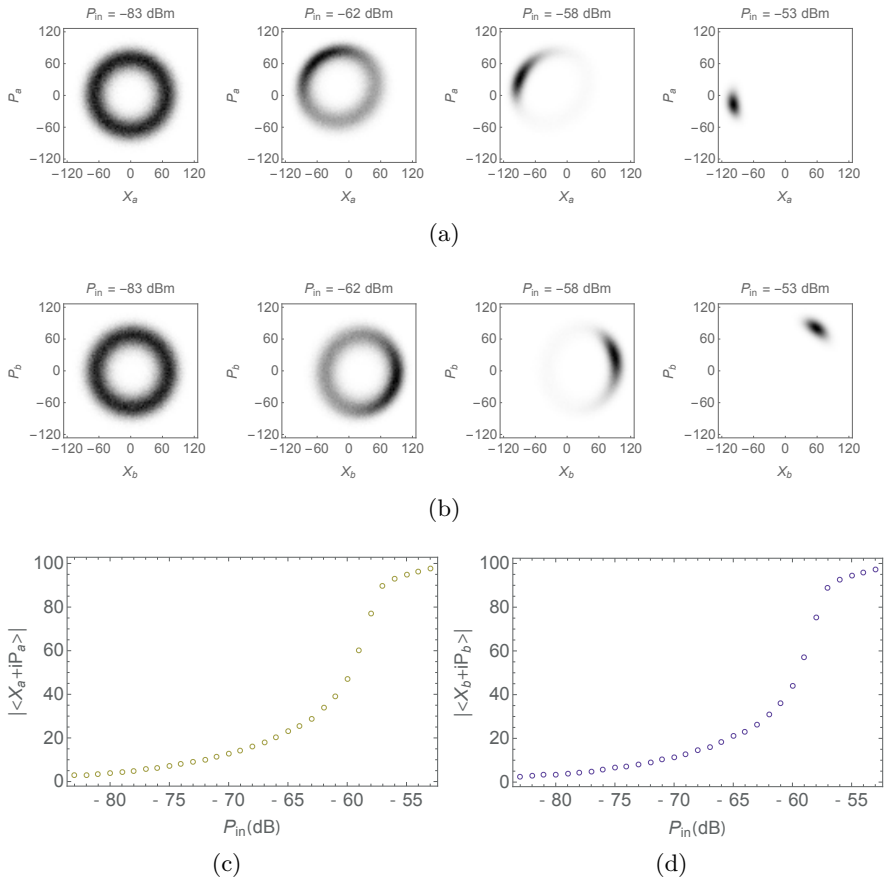

Figure 89: Measured quadrature statistics for modes (a) a and (b) b for the pump power fixed in the self-oscillation regime and for four different powers of the small signal injected on resonance on the mode a. Field quadrature axes are calibrated in number of photons. (c) and (d) Average of the complex amplitudes of the field emitted from modes a and b as a function of the injected signal power.

to these measurements is shown in Fig. 91. Full line corresponds to power dependence Eq. (170).

Interstingly, JPC being a non-degenerate amplifier, emission of the mode a can be locked by a signal injected on the mode b, as shown in Fig. 90d. The slope of the emission peak in the injection locking range is -1 as opposed to 1 in the case of locking with a signal injected on the mode a. The effective injection locking frequency is then

$$\widetilde{\omega}_{in} = \omega_B - \omega_{in}. \tag{176}$$

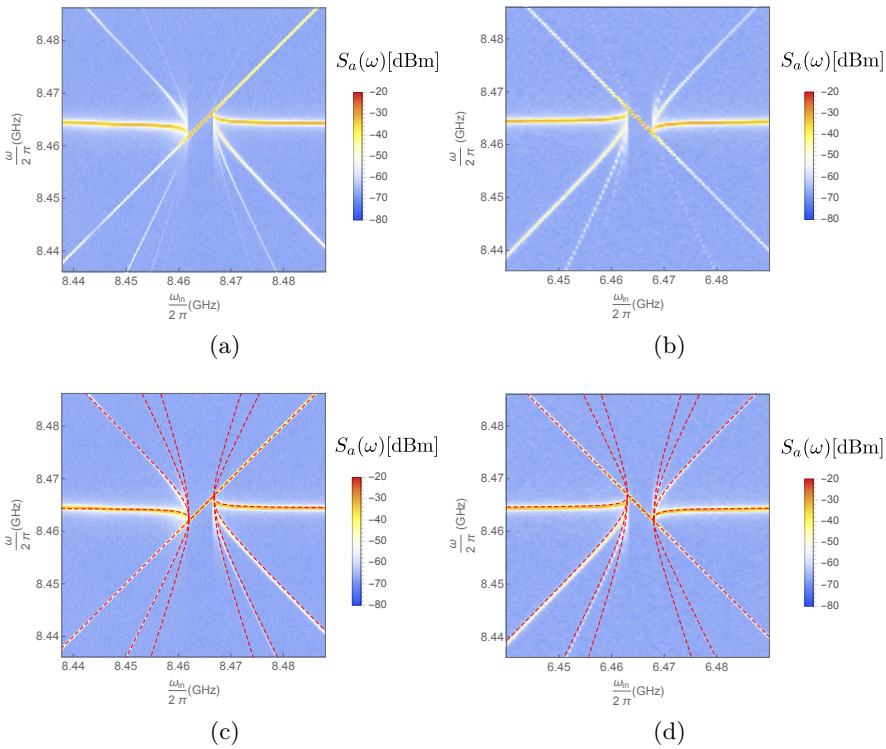

Figure 90: Measured power spectral density $S_a(\omega)$ of the radiation emitted from the mode a, plotted as a function of the frequency ω and frequency ω_{in} of the locking tone injected on (a) mode a and (b) mode b. The power and frequency of the amplification pump are fixed, $P_B = 16$ dBm and $\omega_B = 2\pi \times 14.93$ GHz. Injection tone power is $P_{in} = -35$ dBm. Red line corresponds to Eq. (175) for (a) and Eq. (177) for (b).

and frequencies of the emission peaks read

$$\omega_e^n = \widetilde{\omega}_{in} + n(\omega_a - \widetilde{\omega}_{in})\sqrt{1 - \left(\frac{\frac{\Delta\omega_{in}}{2}}{\omega_a - \widetilde{\omega}_{in}}\right)^2}. \tag{177}$$

Note that there is no conversion pump applied in this measurement. The two intracavity fields of the resonators a and b interact only through the downconversion of the amplification pump tone, which results in phase locking of the cavity field of the resonator a to the field of the resonator b.

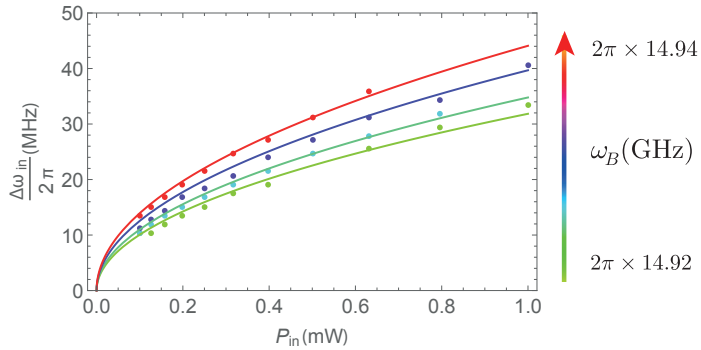

Figure 91: Injection locking range determined by matching Eq. (175) to the measured power spectral density of the emitted radiation, as a function of the injected power. Different colors correspond to different amplification pump frequencies $\omega_B = 2\pi \times 14.925, 14.93, 14.935, 14.94$ GHz. Full line corresponds to Eq. (170).

7.2.3 *Injection locking in conversion*

In this section, we present an atypical injection locking scheme, which makes use of four-wave mixing in a Josephson mixer.

As already seen in Eq. (63), when two pumps are simultaneously applied at frequencies $\omega_a + \omega_b$ and $\omega_a - \omega_b$, two additional terms do not vanish in RWA and contribute to the interaction Hamiltonian

$$\hat{H}_{two\ pumps} = \hbar K_{ap} \hat{p}_B \hat{p}_R \hat{a}^\dagger \hat{a}^\dagger + \hbar K_{bp} \hat{p}_B \hat{p}_R^\dagger \hat{b}^\dagger \hat{b}^\dagger, \tag{178}$$

where $\hat{p}_B$ and $\hat{p}_R$ and annihilation operators for the blue parametric amplification and red conversion pumps. The first process of Eq. (178) corresponds to a coherent conversion of one pump photon at $\omega_B = \omega_a + \omega_b$ and one injected photon at $\omega_{in} = \omega_a - \omega_b$ to two photons in the resonator a at ω_a. Frequency of the effective injection locking tone is then given by

$$\widetilde{\omega}_{in} = \frac{\omega_{in} + \omega_B}{2}, \tag{179}$$

and frequencies of the emission peaks read

$$\omega_e^n = \widetilde{\omega}_{in} + n(\omega_a - \widetilde{\omega}_{in}) \sqrt{1 - \left(\frac{\frac{\Delta\omega_{in}}{4}}{\omega_a - \widetilde{\omega}_{in}} \right)^2}. \tag{180}$$

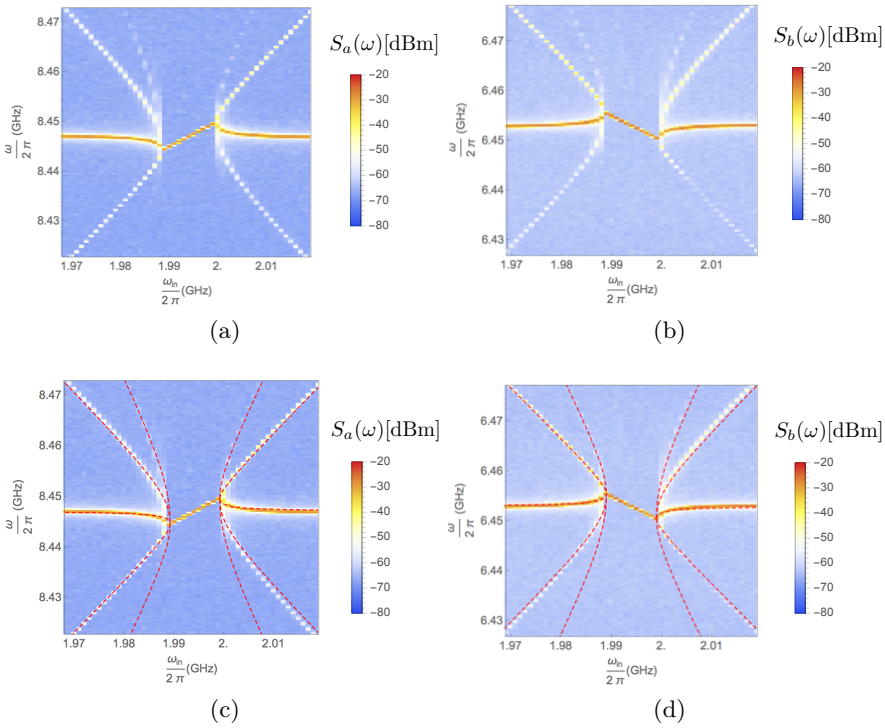

Figure 92: Measured power spectral density (a) $S_a(\omega)$ of radiation emitted from the mode a and (b) $S_b(\omega)$ from the mode b, as a function of frequency ω and frequency of the locking tone ω_{in} injected on the pump port in the proximity of the conversion pump frequency. Red dashed line corresponds to Eq. (180) with effective injection frequency given by Eq. (179) for (c) and (181) for (d). The power and frequency of the amplification pump are fixed, $P_B = 16$ dBm and $\omega_B = 2\pi \times 14.9$ GHz. Injection tone power is $P_{in} = -28$ dBm.

Similarly, the second process of Eq. 178 corresponds to a coherent conversion of one pump photon at $\omega_B = \omega_a + \omega_b$ to one photon at the injection frequency $\omega_{in} = \omega_a - \omega_b$ and to two photons in the resonator b at ω_b. For the field emitted from the mode b, the effective injection frequency is thus given by

$$\widetilde{\omega}_{in} = \frac{-\omega_{in} + \omega_B}{2}. \tag{181}$$

Measured power spectral densities of the fields emitted from modes a and b as a function of frequency and frequency of the injection tone

are shown in Fig. 92. Spectra similar to those for the standard injection locking scheme develop with few differences. As locking in conversion requires two pump photons to create one signal photon, the slope of the $n = 0$ harmonic is $\frac{1}{2}$ for the mode a and $-\frac{1}{2}$ for the mode b. Moreover, the injection locking range $\Delta\omega_e = \frac{\Delta\omega_{in}}{2}$. With these two considerations taken into account, the positions of sidebands given by Eq. (180) reproduce well the measured ones.

7.3 CONCLUSION

The main results of this chapter are:

- Determination of the parametric self-oscillation threshold for a Josephson mixer as a function of pump detuning.
- Demonstration of phase locking of the radiation of both non-degenerate modes of the Josephson mixer, by signal injection on one of the modes.
- Demonstration of the injection locking of the emission of the two modes of the Josephson mixer through a four-wave mixing Kerr effect.
- Description of the emission spectra in the injection locking regime and in its proximity using the Adler theory for lasers.

Part IV

EXPERIMENTAL TECHNIQUES

8 DEVICE FABRICATION

"What is the shape of this problem?"

Louise Bourgeois

8.1 NANOFABRICATION

All the samples discussed in this thesis contained Josephson junctions made using the Dolan bridge technique, as we have used a 30 keV Raith e-beam writer for e-beam lithography. Note that with a 100 keV e-beam writer, a bridge free technique could be used [142]. Depending on the experiment, samples were realized on sapphire or silicon substrate. Thermal conductivity of sapphire being 5 times smaller than that of silicon, baking time on a hot plate for the e-beam lithography resist was longer for sapphire substrates, as indicated in Table 12. Samples are summarized in Table 10. All the steps involving metal evaporation, including the angle evaporation for the Dolan bridge shadow technique, are performed in a Plassys e-beam evaporator in the clean room of University Paris Diderot.

	experiment	substrate	R_t
JM	USC	Si	300 - 400 Ω
transmon	quantum node	sapphire	5 - 10 kΩ
microstrip JPC	hybrid quantum node	sapphire	300 - 400 Ω
lumped JPC	full 3D quantum node	sapphire	300 - 400 Ω
CPW JM	CPW quantum node	Si	300 - 400 Ω

Table 10: Samples, substrates and room temperature resistances R_t of the Josephson junctions.

Most of the fabrication steps were the same for all types of samples, with some additional steps for CPW samples compared to microstrip ones. In order to avoid redundancy, processes for each type of sample are summarized in Table 11, and then detailed one by one further in the text.

Josephson mixer, microstrip JPC, lumped JPC	transmon	CPW JM
substrate cleaning	substrate cleaning	substrate cleaning
ground plane deposition		Nb sputtering
		positive resist deposition
		laser writer lithography
		development
		etching
positive resist deposition	positive resist deposition	positive resist deposition
electron beam lithography	electron beam lithography	electron beam lithography
development	development	development
e-beam evaporation Al/AlO_x/Al	e-beam evaporation Al/AlO_x/Al	e-beam evaporation Al/AlO_x/Al
lift-off in hot acetone	lift-off in hot acetone	lift-off in hot acetone

Table 11: Fabrication steps for different samples.

Substrate cleaning

- 10 min sonicator in acetone
- IPA rinse
- 10 min oxygen plasma cleaning using reactive ion etching (RIE)

Ground plane deposition

- **for microstrip samples**: ground plane consists of 500 nm of gold, evaporated on the back side of the substrate using an e-beam evaporator. Before this step, a thick layer of PMMA resist is deposited on the front side to protect it from dirt.
- **for CPW samples**: 150 nm of Nb are deposited on the entire front side of the substrate using sputtering.

The next three fabrication steps, i.e. optical lithography, development and etching are only performed for CPW samples in order to etch the gaps for the resonators in Nb. The first two steps are performed at College de France clean room facility. Development is done after the transport between different facilities in order to avoid surface contamination and in particular dirt deposition in the narrow gaps.

Optical lithography resist deposition

- 1 drop of S1813, spin for 10 s at 1000 rpm, then spin for 30s at 2000 rpm
- bake for 1 min on a hot plate at 115°C

Laser writer lithography

- performed using *microtech* LW405-B+ laser writer in the clean room facility at Collège de France
- 490 mJ/cm^2

Development

- AZ726 for 90 s
- H2O rinse

Etching

- dry etching with CF_4 for 60s using RIE
- remove the remaining resist using acetone and IPA

Positive electron sensitive resist deposition

Amplifiers, both shunted and unshunted, require junctions that are weakly nonlinear compared to those of a transmon qubit. Josephson inductance being inversely proportional to the surface of the junction A, $L_J \propto \frac{1}{A}$, junctions need to be large ($\simeq$ few μm^2). This is obtained by suspending the Dolan bridge over a larger height than for smaller junctions, so that a larger area is in its shadow during the angle evaporation. For amplifiers, two layers of MAA are deposited, followed by one layer of PMMA so that the total polymer height is $\sim$1200 nm. For transmon fabrication, one layer of MAA is deposited prior to one layer of PMMA giving the total polymer height of $\sim$ 700 nm. Baking time is the same for MAA and PMMA and is given for different substrates in Table 12.

substrate	bake time
Si	3 min
sapphire	4 min

Table 12: Baking time for different substrates.

- dry for 2 min on a hot plate at 185°C
- 1 min cooling
- 3 drops of MAA, spin for 60s, speed 4000 rpm, acceleration 4000 rpm/s
- bake on a hot plate at 185°C
- 1 min cooling
- 3 drops of MAA, spin for 60s, speed 4000 rpm, acceleration 4000 rpm/s
- bake on a hot plate at 185°C
- 1 min cooling

- 3 drops of PMMA, spin for 60s, speed 4000 rpm, acceleration 4000 rpm/s
- bake on a hot plate at 185°C

Electron beam lithography

E-beam lithography is performed on a Raith e-beam writer. The whole pattern is done in a single lithography step. Current is measured in the Faraday cage immediately prior to the lithography.

	device	aperture	dose	current
JRM	amplifiers	7.5 μm	283 μC/cm^2	$\sim$ 25 pA
junction	transmon	7.5 μm	283 μC/cm^2	$\sim$ 25 pA
resonators	amplifiers	120 μm	283 μC/cm^2	$\sim$ 6 nA
antennas	transmon	120 μm	283 μC/cm^2	$\sim$ 6 nA

Table 13: Angle evaporation parameters for different samples.

Development

- 35 s in a MIBK 1:3 IPA
- IPA rinse

Aluminum deposition

Josephson junctions are formed in two aluminum deposition steps at two different angles, separated by an oxidation step. Evaporation angles and heights of the layers depend on the sample and are summarized in Table 14. The main steps of the process are

- pumping for 45 min until pressure $p < 3 \times 10^{-6}$ mbar is reached in the evaporation chamber
- Al evaporation of thickness h_1 at angle θ_1, at a rate 1 nm/s
- static oxidation for 7 min at 20 mbar in a O_2 1:4 Ar atmosphere
- Al evaporation of thickness h_2 at angle θ_2, at a rate 1 nm/s

JJ size	resist	θ_1	θ_2	h_1	h_2
small	MAA/PMMA	-30°	30°	35 nm	100 nm
large	MAA/MAA/PMMA	-35°	35°	100 nm	130 nm

Table 14: Angle evaporation parameters for different samples.

Lift off

- 15 minutes in acetone heated to 40 °C
- IPA rinse

8.2 LEAD PLATING THE CAVITY

Coating copper cavities in thin layers of superconducting materials has already proven to give exceptionally coherent resonators. In the Haroche group in Paris, coherence time $\tau_c = 130$ ms at resonance frequency $\omega_c = 2\pi \times 51$ GHz was obtained by sputtering a thin layer of Niobium on copper mirrors of a Fabry-Perrot cavity, giving record quality factor $Q = 4.2 \times 10^{10}$ at the single photon level [106].

However, due to their aspect ratio, sputtering technique cannot be used on rectangular microwave waveguide cavities. Electrodeposition on the other side can be used independently of the geometry of the cavity and appears thus as a good solution for microwave cavities with strong geometrical constraints. Lead has already been demonstrated to give quality factors of $Q = 3.7 \times 10^{10}$ when electrodeposited on copper cavities [124]. What is more, electroplating enables deposition of thicker layers of superconductor, whereas thicknesses that can be obtained by evaporation are limited to few hundreds of nanometers. In this section we describe the protocol used for the cavity for the quantum node experiment.

Surface preparation

- solvent cleaning: 10 min sonication in acetone followed by IPA rinse and N_2 dry.
- acid cleaning: 10 min in nitric acid at 2 mol.l^{-1} at 40°C followed by a water rinse.

Solution

- 10g of PbO powder
- 100 ml of distilled water
- 28.6 g of methanesulfonic acid
- 70 ml of distilled water
- agitate the solution
- 0.5 g of polyethylene glycol
- 0.5 g of gelatine previously dissolved in 2 ml of distilled water at 50°C.

A DC source is mounted in series with a 10 Ω resistance, lead cathode and copper cavity anode. Cavity is placed in the solution and lead cathode is placed inside of the cavity. A magnetic stirrer is used to improve the convective transport of lead in the solution. The whole process takes few minutes.

After being taken out of the solution, the cavity is rinsed with water and dried using nitrogen flow. As lead oxidizes very quickly, the cavity needs to be either immediately mounted in the cryostat or kept in the vacuum chamber.

9 LOW TEMPERATURE MEASUREMENTS

"It's not just music, it's techno."

Laurent Garnier

9.1 CRYOGENICS AND WIRING

Typical resonance frequencies of superconducting qubits and resonators range between 5 and 10 GHz. In order to witness non-classical behavior, and detect and process single microwave photons, the energy of thermal excitations of the environment has to be much smaller than the energy of one photon. This condition reads

$$k_B T \ll \hbar\omega_r, \tag{182}$$

where k_B is the Boltzmann constant and ω_r is the typical resonance frequency. Reaching quantum regime with microwave photons thus requires environment temperature $T \ll 200$ mK. These temperatures can be obtained using dilution refrigerators.

All of the experiments described in this thesis were realized in a *Cryoconcept* dry dilution refrigerator with base temperature of 37 mK. Full cryostat wiring for the ultrastrong coupling and injection locking experiments is shown in Fig. 93, for the hybrid 2D/3D quantum node experiment in Fig. 94 and for the full 3D quantum node experiment in Fig. 95. Most of the wiring at higher temperature stages is identical. Input lines are attenuated using XMA attenuators to reduce the thermal noise. For the input lines, cupronickel (CuNi) and stainless steel coaxial cables with low thermal conductivity are used between different temperature stages of the cryostat in order to minimize the heat exchange. At the base temperature stage of the cryostat, copper coaxial cables are used between different microwave elements. All the microwave components are thermalized one by one using highly

conductive copper wires. For the output lines, between the base temperature stage and the HEMT amplifier, superconducting NbTi coaxial cables were used to minimize both the signal dissipation and the temperature exchange between the cryostat stages. Above the HEMT amplifier stainless steel cables were used up to the room temperature stage.

A superconducting coil used for the external magnetic flux was biased through a twisted pair strongly filtered using a homemade Ecosorb filter.

At the base temperature stage, 180°-hybrid couplers are used to distribute the signal with either differential symmetry from the port Δ or common symmetry from the port Σ. The former one is used to address the two resonators and the later one to off resonantly address the common mode at the pump frequency.

Finally, a cryoperm magnetic shield is used to isolate the sample from residual magnetic fields. For the optimum performance, a superconducting aluminum foil is used to cover the cryoperm box both from the outside and the inside.

9.2 ROOM TEMPERATURE MEASUREMENTS AND WAVEGUIDE FILTERING

Microwave pulses are generated by mixing a continuous local oscillator (LO) tone with a square shaped or gaussian shaped pulse generated by the Arbitrary Wave Generator *Tektronix* AWG5014B.

Squeezing measurements being very sensitive to the leaking LO signal, we use few stages of filtering after the mixer. Commercial *Mini-Circuits* filters are followed by micromachined cavity filters and rectangular waveguide filters. Cavity filters consist of a cylindrical cavity machined on purpose to be resonant with the signal and are used in transmission to attenuate the high frequency leaking tones. Rectangular waveguides are used as high pass filters.

The output signal is down converted by mixing with the LO tone and then digitized using a 2 channel ATS9351 waveform digitizer by *Alazar*.

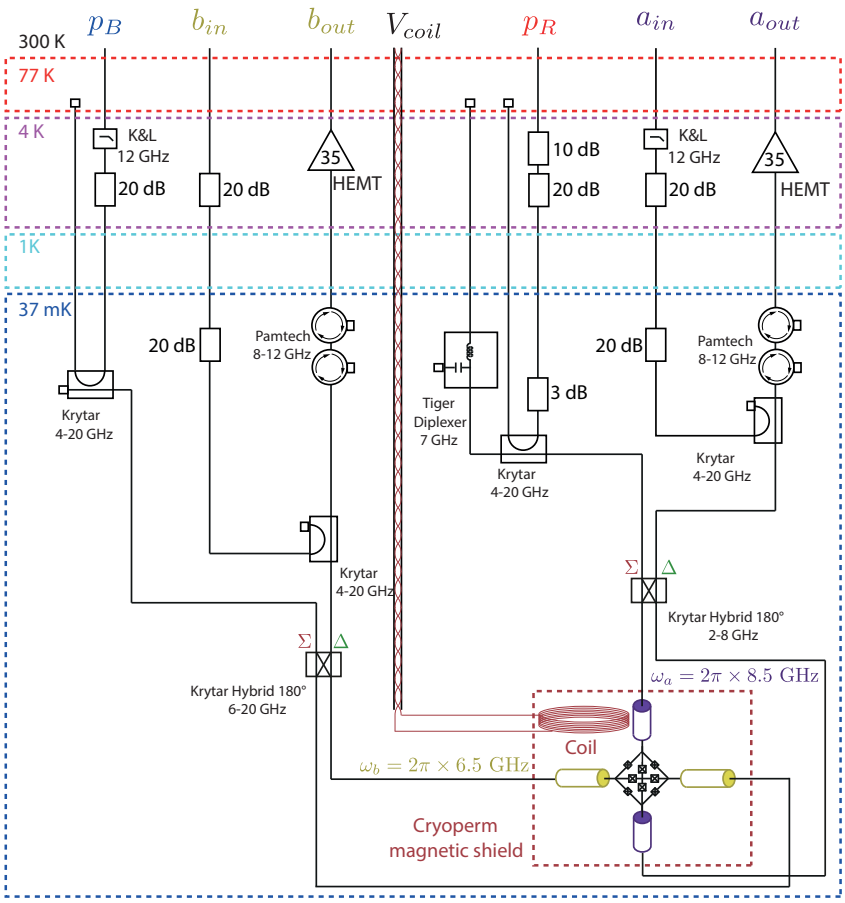

Figure 93: Cryostat wiring used for the ultrastrong coupling and injection locking experiments. Microwave signals a_{in} and b_{in} are sent to the sample through input lines attenuated with XMA attenuators. Reflected signals a_{out} and b_{out} are amplified by HEMT cryogenic amplifiers from Caltech. Isolation is provided by two Pamtech 8-12 GHz circulators in series.

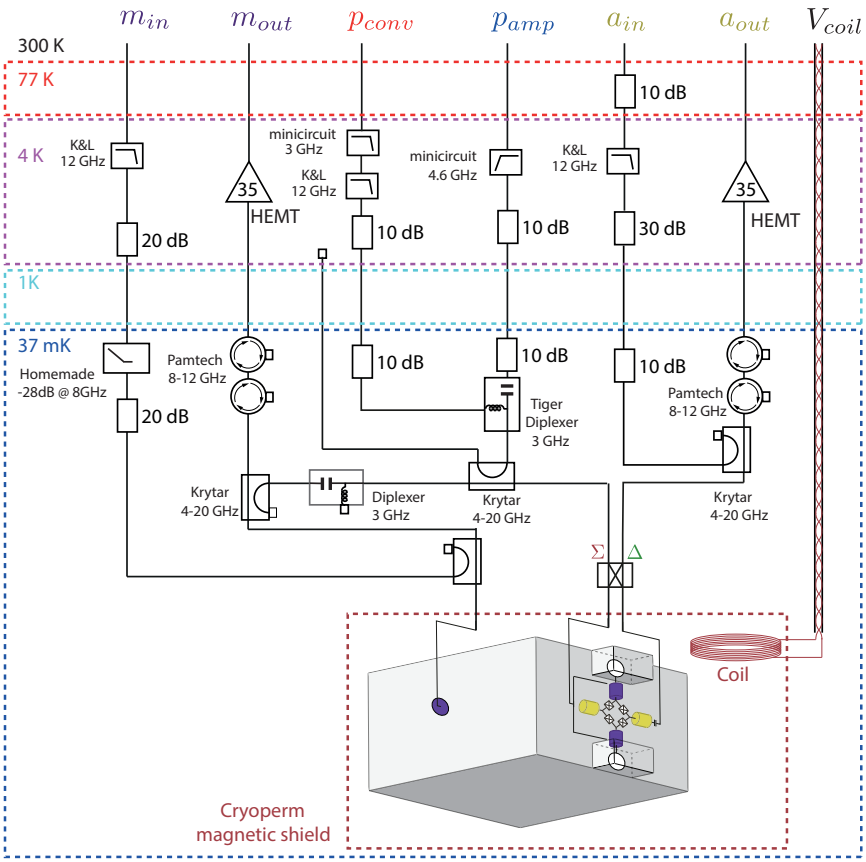

Figure 94: Cryostat wiring used for the hybrid 2D/3D quantum node experiment.

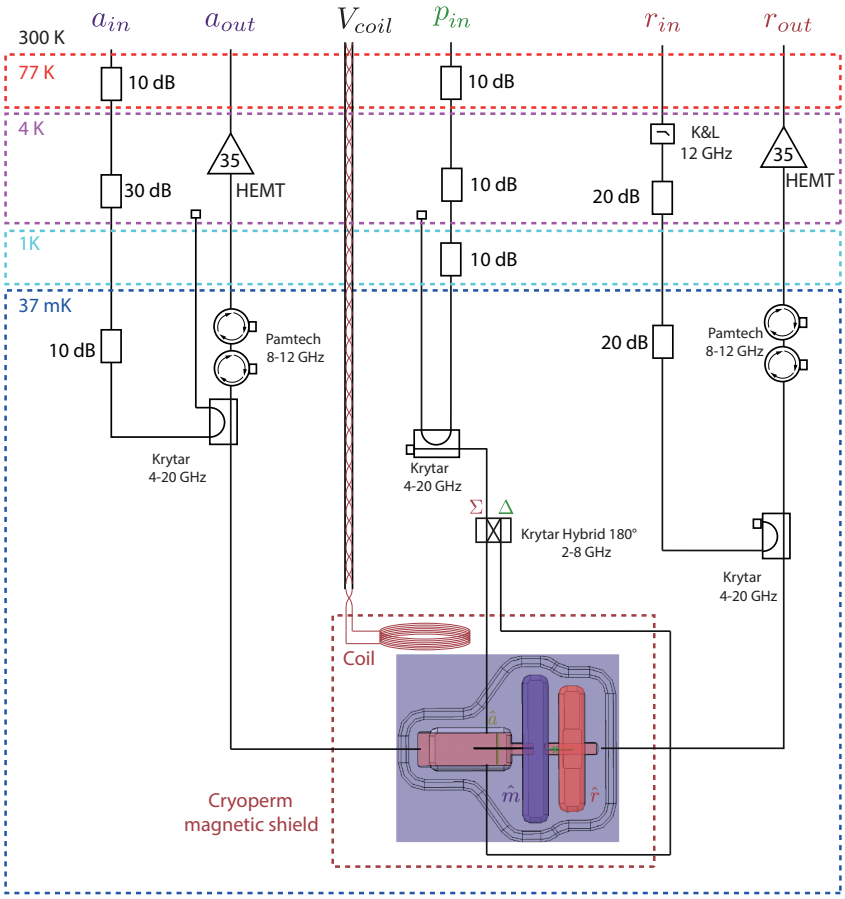

Figure 95: Cryostat wiring used for the full 3D quantum node experiment with separate storage and readout cavities.

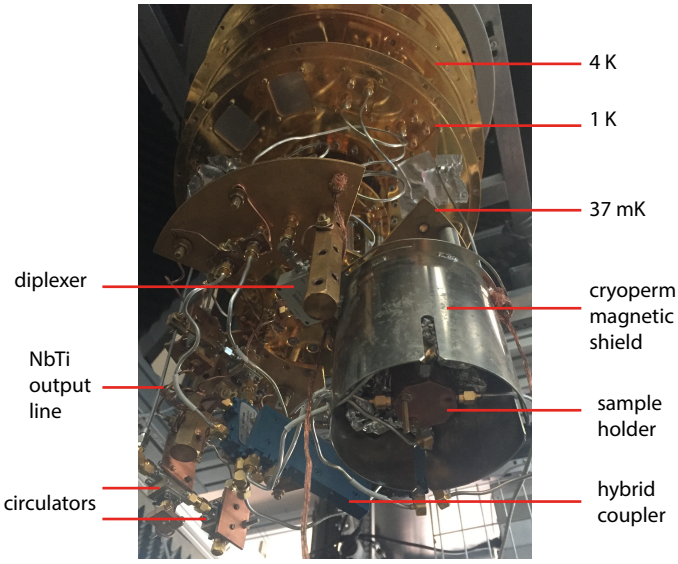

Figure 96: Picture of the base temperature stage of the *Cryoconcept* dilution refrigerator. The bottom of the cryoperm shield is unmounted so that the sample holder for the Josephson mixer used in the ultrastrong coupling experiment is visible.

10 ELECTROMAGNETIC SIMULATIONS

"Consistency is the playground of the dull minds."

Yuval Noah Harari

Few different electromagnetic simulation tools were used to design the experiments performed during this PhD thesis. In this chapter we will focus on *Ansys HFSS* software, used for 3D structures and *qucs* software, used for planar samples.

10.1 HFSS

High Frequency Structure Simulator (HFSS) is a software from *Ansys* that uses finite elements method to perform 3D electromagnetic simulations. It can be used in two modes, the *eigenmodal* and the *driven modal* regime.

The *eigenmodal* regime calculates the resonance frequencies of the whole system and allows the visualization of the vector fields corresponding to each resonance. All the metallic surfaces are defined as perfectly conducting boundaries and the Josephson junction is approximated by a pure linear inductor.

The *driven modal* regime enables simulation of a reflection measurement on a surface defined as a waveport or a transmission measurement between two waveports. It can be used to calculate the coupling of a resonator to a transmission line by fitting the phase roll of the reflected signal.

10.1.1 *Single mode Jaynes-Cummings method*

One method that we used to predict the coupling between the cavity and the qubit relies on the single mode Jaynes-Cummings ap-

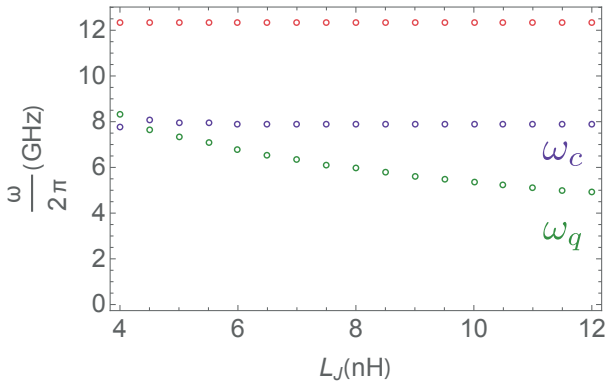

Figure 97: Frequencies of the first three eigenmodes of the system simulated using *HFSS*, as a function of the Josephson inductance L_J. The nonlinear qubit mode at frequency ω_q presents an anticrossing with the fundamental cavity mode at frequency ω_c.

proximation. Even though computationally it is not the most efficient method, it gives good predictions for a simple system of a transmon coupled to a single cavity. Transmon is simulated by a purely inductive lumped element, galvanically connected to two planar antennas that are defined as perfect conductors. It is placed on a sapphire substrate with a corresponding tangent loss, which enables including the dielectric dissipation in the model. Finally the chip is placed in the middle of a perfectly conducting box with the dimensions of the 3D cavity. The *eigenmodal* regime is used to simulate the eigenfrequencies of the qubit-cavity system for different values of the Josephson inductance assigned to the lumped element. The first three levels are shown in Fig. 97. Fundamental cavity mode is constant at $\omega_c = 2\pi \times 7.9$ GHz and the second cavity mode at 12.3 GHz. The frequency of the qubit is $\omega_q \propto \frac{1}{\sqrt{L_J}}$. For a given Josephson inductance L_J, the dispersive detuning between the cavity and the qubit is

$$\Delta(L_J) = \omega_c - \omega_q(L_J). \tag{183}$$

For a cavity-qubit system described by a Jaynes-Cummings Hamiltonian

$$\hat{H} = \hbar\omega_c \hat{c}^\dagger \hat{c} + \hbar\omega_q \hat{d}^\dagger \hat{d} + \hbar g(\hat{c}^\dagger \hat{d} + \hat{c}\hat{d}^\dagger), \tag{184}$$

where c and d are respectively cavity and qubit annihilation operators, at resonance $\omega_c \simeq \omega_q$, eigenvalues read $\widetilde{\omega}_c \simeq \omega_c + g$ for the cavity-like

mode and $\widetilde{\omega}_q = \omega_q - g$ for the qubit like mode. The coupling is thus given by half of the minimum detuning at the anticrossing

$$g = \frac{1}{2}\min[\omega_m(L_J) - \omega_q(L_J)]. \tag{185}$$

Finally we can find the qubit-cavity pull

$$\chi_{cq}(L_J) = 2E_C \frac{g^2}{\Delta(L_J)^2}. \tag{186}$$

This method requires finding the eigenmodes for ~ 10 values of L_J, which makes is not efficient in terms of computation time. Furthermore, the validity of the Jaynes-Cummings approximations breaks down when more cavity modes come into play, for instance when qubit is strongly coupled to separate storage and readout modes.

We have also used another simulation method, based on the work by Minev, Leghtas *et al, in prep.*, that will not be described here. It relies on the calculation of the participation ratio of the electromagnetic energy stored in the Josephson junction and the total energy of the mode. We found a good agreement with the predictions of the Jaynes-Cummings method, while it is much more computationally efficient because it requires performing the eigenmode simulation only for one value of the Josephson inductance L_J.

10.1.2 *Full 3D device design*

Designing a complex device such as the full 3D quantum node requires few simulation steps in different regimes. They are briefly explained in this section.

1. Buffer resonance frequency is simulated as a function of the shunting lumped element capacitors in the eigenmodal regime.

2. Iris size between the waveguide cavity and the waveguide-to-SMA adapter is simulated in the driven modal regime to obtain the buffer coupling rate $\kappa_a \simeq 2\pi \times 100$ MHz. The reflection is simulated with the waveport on the SMA connector. The coupling also depends on the size of the antennas.

3. Coupling of the buffer to the memory cavity is simulated as a function of the antenna length in the driven modal regime.

4. Quality factor of the memory cavity is simulated as a function of the opposite antenna length in the eigenmodal regime.

5. Couplings between the qubit and the memory and readout cavities are simulated in the eigenmodal regime in Jaynes-Cummings approximation and using the participation ratio of the Josephson junction in the memory and readout modes.

6. Iris size between the waveguide and the readout cavity is simulated in the driven modal regime to obtain the coupling rate of the readout mode to the transmission line $\kappa_r \simeq 2\pi \times 1.5$ MHz. The reflection is simulated with the waveport on the top of the waveguide.

10.2 QUCS

For electromagnetic simulations of the 2D circuits and in particular the lumped element buffer resonator, we have used *qucs* software. *Quite Universal Circuit Simulator (qucs)* is an opensource electronic circuit simulator. Among different analysis types that it supports, there is the S parameter simulation as a function of frequency, that can be used to determine the resonance frequencies of the circuit, as well as the coupling rates to the transmission line.

We input in the simulator the equivalent circuit for the lumped buffer resonator coupled to a Josephson ring shunted by central inductances, as shown in Fig. 98.

Ring junctions are approximated to the first order by pure inductors $L_J = 0.12$ nH. The ring is shunted by meander inductances $L = 30$ pH. The inductances of the wires are estimated from the length of the wire $L = l \times 1$ nH.mm^{-1}. In order to obtain the response function, the circuit is differentially excited by a 180°-hybrid coupler. Phase of the S parameter is shown in Fig. 99. From this simulation, we were able to estimate the capacitances for the lumped buffer resonator needed for its resonance frequency to be in the desired range for the experiment.

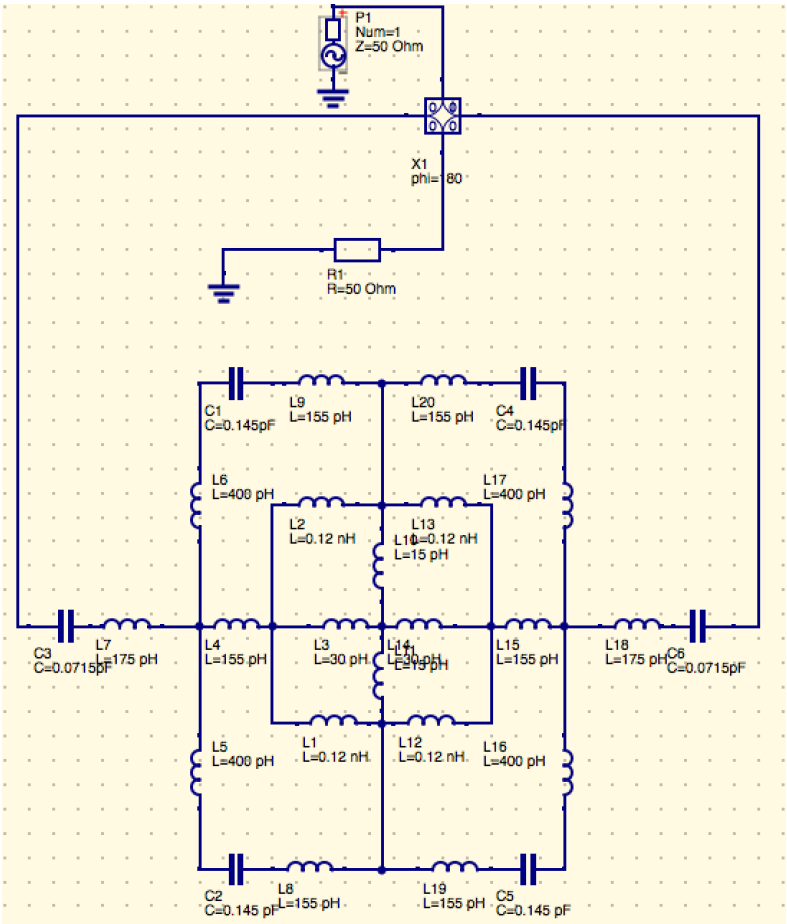

Figure 98: The equivalent circuit used for the simulation of the lumped buffer resonator coupled to a Josephson ring shunted by inductances.

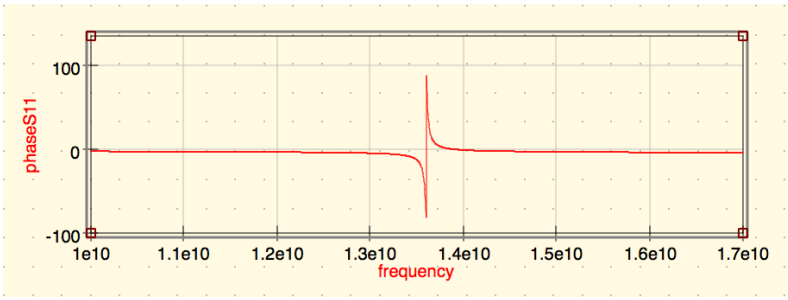

Figure 99: Simulated reflection on the lumped buffer resonator coupled to a Josephson ring shunted by inductances.

11 SUMMARY AND CONCLUSIONS

"Last words are for fools who haven't said enough."

Karl Marx

The potential of superconducting circuits for Hamiltonians built by design, due to their high degree of control, has been recognized for more than a decade now and is being actively exploited for quantum information applications. During my thesis, I have used a particular superconducting circuit called the Josephson mixer for few different applications.

In the first part of my thesis I presented a scheme that maps a three-wave mixing device, such as a Josephson mixer, simultaneously driven with two pump tones, onto a system of two bosonic modes in the ultrastrong coupling regime. We have theoretically demonstrated that radiation emitted in the laboratory frame from the ground state of such an effective ultrastrongly coupled system is characterized by single-mode and two-mode squeezing. We have implemented this scheme with a Josephson mixer which enabled us to experimentally characterize the ground state of an effective system of ultrastrongly coupled harmonic oscillators. By measuring the emitted radiation, we have performed a spectroscopic detection of frequency splitting as a function of coupling rate, with demonstrated coupling rates of the order of the effective frequencies. Furthermore, we have measured the quadrature statistics for the emitted radiation and detected both the single mode and the two mode squeezing that go below the variance of the vacuum fluctuations.

In the second part of this thesis, we have emphasized the possibility to use the Josephson mixer for a quantum node of a potential future modular microwave quantum network. We first compared the Josephson mixer to the other existing quantum microwave nodes based on various mesoscopic systems and then showed that a Josephson mixer coupled to a transmon can perform any set of operations required

from such a quantum node. We have experimentally realized such a device in three different architectures, that we have characterized and compared. In particular, we have presented an analysis of different sources of losses in 3D microwave cavities and determination of the limiting factors for the hybrid 2D/3D quantum node architecture.

Finally in the last part of this thesis, we have investigated the regime of parametric oscillation for a non-degenerate parametric amplifier such as a Josephson mixer. We have studied the onset of this regime as a function of pump detuning and compared it to recent theoretical predictions. In this regime, we have demonstrated phase locking of the radiation of both non-degenerate modes of the Josephson mixer, by signal injection on one of the modes. Finally, we have demonstrated a novel injection locking technique, characteristic for a non-degenerate amplifier that relies on the four-wave mixing in such a device.

In conclusion, although it is mostly used as a parametric amplifier and frequency converter, the Josephson mixer is a highly versatile tool that can be used as a quantum simulation platform as well as a building block for a microwave quantum network. As illustrated by the injection locking through four-wave mixing experiment, the physics behind this device is extremely rich, and the higher order mixing terms that it provides can be explored and used as ressources for quantum information and simulation.

Part V

BIBLIOGRAPHY

BIBLIOGRAPHY

[1] N. Roch, E. Flurin, F. Nguyen, P. Morfin, P. Campagne-Ibarcq, M. H. Devoret, and B. Huard, "Widely tunable, nondegenerate three-wave mixing microwave device operating near the quantum limit.," *Physical review letters*, vol. 108, p. 147701, April 2012. (Cited on pages 1 and 25.)

[2] E. Flurin, N. Roch, F. Mallet, M. H. Devoret, and B. Huard, "Generating entangled microwave radiation over two transmission lines," *Physical review letters*, vol. 109, p. 183901, October 2012. (Cited on pages 1, 25, 58, 59, 66, and 67.)

[3] A. Kamal, A. Roy, J. Clarke, and M. H. Devoret, "Asymmetric frequency conversion in nonlinear systems driven by a biharmonic pump," *Physical review letters*, vol. 113, p. 247003, December 2014. (Cited on pages 1 and 25.)

[4] B. Abdo, K. Sliwa, S. Shankar, M. Hatridge, L. Frunzio, R. Schoelkopf, and M. Devoret, "Josephson directional amplifier for quantum measurement of superconducting circuits," *Physical review letters*, vol. 112, p. 167701, April 2014. (Cited on pages 1 and 25.)

[5] K. M. Sliwa, M. Hatridge, A. Narla, S. Shankar, L. Frunzio, R. J. Schoelkopf, and M. H. Devoret, "Reconfigurable josephson circulator/directional amplifier," *Physical Review X*, vol. 5, p. 041020, November 2015. (Cited on pages 1, 25, and 153.)

[6] E. Flurin, N. Roch, J. D. Pillet, F. Mallet and B. Huard, "Superconducting quantum node for entanglement and storage of microwave radiation," *Physical review letters*, vol. 090503, pp. 1–5, March 2015. (Cited on pages 1, 8, 25, 92, 107, 121, and 162.)

[7] M. H. Devoret and R. J. Schoelkopf, "Superconducting circuits for quantum information: an outlook.," *Science*, vol. 339, pp. 1169–1174, March 2013. (Cited on pages 2, 7, and 83.)

[8] N. Bergeal, F. Schackert, M. Metcalfe, R. Vijay, V. E. Manucharyan, L. Frunzio, D. E. Prober, R. J. Schoelkopf, S. M. Girvin, and M. H. Devoret, "Phase-preserving amplification near the quantum limit with a Josephson ring modulator," *Nature*, vol. 465, no. 7294, pp. 64–68, 2010. (Cited on pages 2 and 25.)

[9] N. Bergeal, R. Vijay, V. E. Manucharyan, I. Siddiqi, R. J. Schoelkopf, S. M. Girvin, and M. H. Devoret, "Analog information processing at the quantum limit with a Josephson ring modulator," *Nature Physics*, vol. 1516, 2010. (Cited on pages 2 and 25.)

[10] C. Weisbuch, M. Nishioka, A. Ishikawa, and Y. Arakawa, "Observation of the coupled exciton-photon mode splitting in a semiconductor quantum microcavity," *Physical review letters*, vol. 69, no. 23, pp. 3314–3317, 1992. (Cited on page 3.)

[11] A. Wallraff, D. Schuster, A. Blais, L. Frunzio, R. Huang, J. Majer, S. Kumar, S. Girvin, and R. Schoelkopf, "Strong coupling of a single photon to a superconducting qubit using circuit quantum electrodynamics," *Nature*, vol. 431, no. 7005, pp. 162–167, 2004. (Cited on pages 3 and 16.)

[12] E. Peter, P. Senellart, D. Martrou, A. Lemaître, J. Hours, J. M. Gérard, and J. Bloch, "Exciton-photon strong-coupling regime for a single quantum dot embedded in a microcavity," *Physical review letters*, vol. 95, p. 067401, August 2005. (Cited on page 3.)

[13] K. Hennessy, A. Badolato, M. Winger, D. Gerace, M. Atatüre, S. Gulde, S. Fält, E. L. Hu, and A. Imamoglu, "Quantum nature of a strongly coupled single quantum dot cavity system," *Nature*, vol. 445, pp. 896–899, February 2007. (Cited on page 3.)

[14] C. Ciuti, G. Bastard, and I. Carusotto, "Quantum vacuum properties of the intersubband cavity polariton field," *Physical Review B*, vol. 72, p. 115303, September 2005. (Cited on pages 4 and 16.)

[15] G. Günter, A. A. Anappara, J. Hees, A. Sell, G. Biasiol, L. Sorba, S. D. Liberato, C. Ciuti, A. Tredicucci, A. Leitenstorfer, and R. Huber, "Sub-cycle switch-on of ultrastrong light-matter interaction," *Nature*, vol. 458, pp. 10–13, March 2009. (Cited on pages 4, 16, 19, and 57.)

[16] F. Yoshihara, T. Fuse, S. Ashhab, K. Kakuyanagi, S. Saito, and K. Semba, "Superconducting qubit-oscillator circuit beyond the ultrastrong-coupling regime," *Nature Physics*, vol. 13, pp. 44–47, January 2017. (Cited on pages 4, 19, and 20.)

[17] M. Goryachev, W. G. Farr, D. L. Creedon, Y. Fan, M. Kostylev, and M. E. Tobar, "High-cooperativity cavity QED with magnons at microwave frequencies," *Physical Review Applied*, vol. 2, p. 054002, 2014. (Cited on pages 4, 19, and 20.)

[18] Q. Zhang, M. Lou, X. Li, J. L. Reno, W. Pan, J. D. Watson, M. J. Manfra, and J. Kono, "Collective non-perturbative coupling of 2D electrons with high-quality-factor terahertz cavity photons," *Nature Physics*, vol. 1, pp. 1–8, August 2016. (Cited on pages 4 and 23.)

[19] C. Maissen, G. Scalari, F. Valmorra, M. Beck, J. Faist, S. Cibella, R. Leoni, C. Reichl, C. Charpentier, and W. Wegscheider, "Ultrastrong coupling in the near field of complementary split-ring resonators," *Physical Review B*, vol. 90, p. 205309, 2014. (Cited on pages 4 and 23.)

[20] J. Jochen Braumüller, M. Marthaler, A. Schneider, A. Stehli, H. Rotzinger, M. Weides, and A. V. Ustinov, "Analog quantum simulation of the Rabi model in the ultra-strong coupling regime," 2016. (Cited on pages 4, 21, and 44.)

[21] N. K. Langford, R. Sagastizabal, M. Kounalakis, C. Dickel, A. Bruno, F. Luthi, D. J. Thoen, A. Endo, and L. Dicarlo, "Experimentally simulating the dynamics of quantum light and matter at ultrastrong coupling," pp. 1–26, 2016. (Cited on pages 4 and 21.)

[22] J. I. Cirac, P. Zoller, H. J. Kimble, and H. Mabuchi, "Quantum state transfer and entanglement distribution among distant

nodes in a quantum network," *Physical review letters*, vol. 78, no. 16, pp. 3221–3224, 1997. (Cited on pages 6 and 84.)

[23] A. G. Fowler, M. Mariantoni, J. M. Martinis, and A. N. Cleland, "Surface codes: Towards practical large-scale quantum computation," *Physical Review A*, vol. 86, p. 032324, September 2012. (Cited on page 7.)

[24] Z. Leghtas, G. Kirchmair, B. Vlastakis, R. J. Schoelkopf, M. H. Devoret, and M. Mirrahimi, "Hardware-efficient autonomous quantum memory protection," *Physical review letters*, vol. 111, p. 120501, September 2013. (Cited on pages 7 and 94.)

[25] H. L. Stover and W. H. Steier, "Locking of laser oscillators by light injection," *Applied Physics Letters*, vol. 8, no. 4, pp. 91–93, 1966. (Cited on page 8.)

[26] U. Schünemann, H. Engler, M. Zielonkowski, M. Weidemuller, and R. Grimm, "Magneto-optic trapping of lithium using semiconductor lasers," *Optics Communications*, vol. 158, pp. 263–272, December 1998. (Cited on page 8.)

[27] Y. Liu, J. Stehlik, M. J. Gullans, J. M. Taylor, and J. R. Petta, "Injection locking of a semiconductor double-quantum-dot micromaser," *Physical Review A*, vol. 92, p. 053802, 2015. (Cited on pages 8 and 164.)

[28] M. C. Cassidy, A. Bruno, S. Rubbert, M. Irfan, J. Kammhuber, R. N. Schouten, A. R. Akhmerov, and L. P. Kouwenhoven, "Demonstration of an ac Josephson junction laser," *Science*, vol. 355, pp. 939–942, 2017. (Cited on pages 8 and 164.)

[29] S. Knünz, M. Herrmann, V. Batteiger, G. Saathoff, T. Hänsch, K. Vahala, and T. Udem, "Injection locking of a trapped-ion phonon laser," *Physical review letters*, vol. 105, p. 013004, July 2010. (Cited on pages 8 and 164.)

[30] C. J. Hood, M. S. Chapman, T. W. Lynn, and H. J. Kimble, "Real-time cavity qed with single atoms," *Physical review letters*, vol. 80, pp. 4157–4160, May 1998. (Cited on page 15.)

[31] S. Gleyzes, S. Kuhr, C. Guerlin, J. Bernu, S. Deleglise, U. B. Hoff, M. Brune, J.-M. Raimond, and S. Haroche, "Quantum jumps of light recording the birth and death of a photon in a cavity," *Nature*, vol. 446, pp. 297–300, March 2007. (Cited on page 15.)

[32] C. Guerlin, J. Bernu, S. Deleglise, C. Sayrin, S. Gleyzes, S. Kuhr, M. Brune, J.-M. Raimond, and S. Haroche, "Progressive field-state collapse and quantum non-demolition photon counting," *Nature*, vol. 448, pp. 889–893, August 2007. (Cited on page 15.)

[33] G. Gabrielse, H. Dehmelt, and U. Washington, "Observation of inhibited spontaneous emission," *Physical review letters*, vol. 55, no. 1, 1985. (Cited on page 15.)

[34] D. Leibfried and C. Monroe, "Quantum dynamics of single trapped ions," *Reviews of Modern Physics*, vol. 75, pp. 281–324, January 2003. (Cited on page 15.)

[35] Y. Kubo, C. Grezes, A. Dewes, T. Umeda, J. Isoya, H. Sumiya, N. Morishita, H. Abe, S. Onoda, T. Ohshima, V. Jacques, A. Dréau, J.-F. Roch, I. Diniz, A. Auffeves, D. Vion, D. Esteve, and P. Bertet, "Hybrid quantum circuit with a superconducting qubit coupled to a spin ensemble," *Physical review letters*, vol. 107, p. 220501, November 2011. (Cited on pages 15, 85, and 86.)

[36] X. Zhu, S. Saito, A. Kemp, K. Kakuyanagi, S.-i. Karimoto, H. Nakano, W. J. Munro, Y. Tokura, M. S. Everitt, K. Nemoto, M. Kasu, N. Mizuochi, and K. Semba, "Coherent coupling of a superconducting flux qubit to an electron spin ensemble in diamond," *Nature*, vol. 478, pp. 221–224, October 2011. (Cited on pages 15 and 86.)

[37] K. Hammerer, M. R. Vanner, and M. Aspelmeyer, "Observation of strong coupling between a micromechanical resonator and an optical cavity field," *Nature*, vol. 460, pp. 724–727, August 2009. (Cited on page 15.)

[38] E. Peter, P. Senellart, D. Martrou, A. Lemaître, J. Hours, J. M. Gérard, and J. Bloch, "Exciton-photon strong-coupling regime for a single quantum dot embedded in a microcavity," *Physical review letters*, vol. 95, p. 067401, August 2005. (Cited on page 15.)

[39] D. Braak, "Integrability of the Rabi model," *Physical review letters*, vol. 107, no. 10, pp. 2–5, 2011. (Cited on page 18.)

[40] V. E. Manucharyan, A. Baksic, and C. Ciuti, "Resilience of the quantum Rabi model in circuit QED," *Journal of Physics A: Mathematical and Theoretical*, vol. 50, p. 294001, 2017. (Cited on page 19.)

[41] L. Garziano, V. Macrì, R. Stassi, O. D. Stefano, F. Nori, and S. Savasta, "One photon can simultaneously excite two or more atoms," *Physical review letters*, vol. 117, p. 043601, July 2016. (Cited on page 19.)

[42] A. F. Kockum, V. Macri, L. Garziano, S. Savasta, and F. Nori, "Frequency conversion in ultrastrong cavity QED," *arXiv:1701.07973*, pp. 1–16, 2017. (Cited on page 19.)

[43] G. Romero, D. Ballester, Y. M. Wang, V. Scarani, and E. Solano, "Ultrafast quantum gates in circuit QED," *Physical review letters*, vol. 108, p. 120501, March 2012. (Cited on page 19.)

[44] P. Nataf and C. Ciuti, "Protected quantum computation with multiple resonators in ultrastrong coupling circuit QED," *Physical review letters*, vol. 107, p. 190402, November 2011. (Cited on page 19.)

[45] T. H. Kyaw, S. Felicetti, G. Romero, E. Solano, and L. Kwek, "Scalable quantum memory in the ultrastrong coupling regime," *Scientific Reports*, vol. 5, no. 1, p. 8621, 2015. (Cited on page 19.)

[46] T. Schwartz, J. A. Hutchison, C. Genet, T. W. Ebbesen, and G. Monge, "Reversible switching of ultrastrong light-molecule coupling," *Physical review letters*, vol. 106, p. 196405, May 2011. (Cited on pages 19 and 20.)

[47] M. Geiser, F. Castellano, G. Scalari, M. Beck, and L. Nevou, "Ultrastrong coupling regime and plasmon polaritons in parabolic semiconductor quantum wells," *Physical review letters*, vol. 108, p. 106402, March 2012. (Cited on pages 19 and 20.)

[48] Y. Todorov, A. M. Andrews, R. Colombelli, S. D. Liberato, C. Ciuti, P. Klang, G. Strasser, and C. Sirtori, "Ultrastrong light-matter coupling regime with polariton dots," *Physical review letters*, vol. 105, p. 196402, November 2010. (Cited on page 19.)

[49] T. Niemczyk, F. Deppe, H. Huebl, E. P. Menzel, F. Hocke, M. J. Schwarz, D. Zueco, T. Hümmer, E. Solano, A. Marx, and R. Gross, "Circuit quantum electrodynamics in the ultrastrong-coupling regime," *Nature Physics*, vol. 6, no. 8, pp. 1–5, 2010. (Cited on pages 19 and 57.)

[50] P. Forn-Diaz, J. J. Garcia-Ripoll, B. Peropadre, J.-L. Orgiazzi, M. A. Yurtalan, R. Belyansky, C. M. Wilson, and A. Lupascu, "Ultrastrong coupling of a single artificial atom to an electromagnetic continuum in the nonperturbative regime," *Nature Physics*, vol. 13, pp. 39–43, jan 2017. (Cited on pages 19 and 57.)

[51] S. J. Bosman, M. F. Gely, V. Singh, A. Bruno, D. Bothner, and G. A. Steele, "Multi-mode ultra-strong coupling in circuit quantum electrodynamics," *arXiv:1704.06208*. (Cited on page 19.)

[52] R. P. Feynman, "Simulating physics with computers," *International Journal of Theoretical Physics*, vol. 21, pp. 467–488, 1982. (Cited on page 19.)

[53] S. J. Bosman, M. F. Gely, V. Singh, D. Bothner, A. Castellanos-gomez, and G. A. Steele, "Approaching ultrastrong coupling in transmon circuit QED using a high-impedance resonator," *Physical Review B*, vol. 95, p. 224515, 2017. (Cited on page 23.)

[54] S. D. Liberato, C. Ciuti, and I. Carusotto, "Quantum vacuum radiation spectra from a semiconductor microcavity with

a time-modulated vacuum rabi frequency," *Physical review letters*, vol. 98, p. 103602, March 2007. (Cited on page 23.)

[55] A. Bayer, M. Pozimski, S. Schambeck, D. Schuh, R. Huber, D. Bougeard, and C. Lange, "Terahertz light-matter interaction beyond unity coupling strength," *Nano Letters*, vol. 17, pp. 6340–6344, 2017. (Cited on page 23.)

[56] B. Yurke, P. Kaminsky, R. Miller, E. Whittaker, A. Smith, A. Silver, and R. Simon, "Observation of 4.2-K equilibrium-noise squeezing via a Josephson-Parametric Amplifier," *Physical review letters*, vol. 60, no. 9, pp. 764–767, 1988. (Cited on page 25.)

[57] I. Siddiqi, R. Vijay, F. Pierre, C. M. Wilson, M. Metcalfe, C. Rigetti, L. Frunzio, and M. H. Devoret, "RF-Driven Josephson bifurcation amplifier for quantum measurement," *Physical review letters*, vol. 93, pp. 1–4, November 2004. (Cited on page 25.)

[58] M. Hatridge, R. Vijay, D. H. Slichter, J. Clarke, and I. Siddiqi, "Dispersive magnetometry with a quantum limited SQUID parametric amplifier," *Physical Review B*, vol. 83, p. 134501, 2011. (Cited on page 25.)

[59] I. M. Pop, I. Protopopov, F. Lecocq, Z. Peng, B. Pannetier, O. Buisson, and W. Guichard, "Measurement of the effect of quantum phase slips in a Josephson junction chain," *Nature Physics*, vol. 6, no. 8, pp. 589–592, 2010. (Cited on page 25.)

[60] E. Flurin, *The Josephson mixer: A Swiss army knife for microwave optics*. Phd thesis, Ecole Normale Supérieure, 2014. (Cited on pages 26, 45, 59, 104, and 111.)

[61] A. Einstein, B. Podolsky, and N. Rosen, "Can quantum-mechanical description of physical reality be considered complete?," *Physical Review*, vol. 47, pp. 777–780, May 1935. (Cited on page 31.)

[62] F. D. O. Schackert, "A practical quantum-limited parametric amplifier based on the Josephson Ring Modulator," *Thesis*, 2013. (Cited on page 33.)

[63] D. A. Steck, *Quantum and atom optics*. available online at http://steck.us/teaching (revision 0.12.0, 16 May 2017), 2007. (Cited on page 37.)

[64] C. W. Gardiner and M. J. Collett, "Input and output in damped quantum systems: Quantum stochastic differential equations and the master equation," *Physical Review A*, vol. 31, no. 6, pp. 3761–3774, 1985. (Cited on page 37.)

[65] S. Fedortchenko, S. Felicetti, D. Marković, S. Jezouin, A. Keller, T. Coudreau, B. Huard, and P. Milman, "Quantum simulation of ultrastrongly coupled bosonic modes using superconducting circuits," *Physical Review A*, vol. 95, p. 042313, April 2017. (Cited on pages 43 and 57.)

[66] J. J. Hopfield, "Theory of the contribution of excitons to the complex dielectric constant of crystals," *Physical Review*, vol. 112, no. 5, pp. 1555–1567, 1958. (Cited on page 50.)

[67] C. Ciuti and I. Carusotto, "Input-output theory of cavities in the ultrastrong coupling regime: The case of time-independent cavity parameters," *Physical Review A*, vol. 74, p. 033811, 2006. (Cited on page 51.)

[68] J. Lolli, A. Baksic, D. Nagy, V. E. Manucharyan, and C. Ciuti, "Ancillary qubit spectroscopy of vacua in cavity and circuit quantum electrodynamics," *Physical review letters*, vol. 114, p. 183601, May 2015. (Cited on page 51.)

[69] S. De Liberato, C. Ciuti, and I. Carusotto, "Quantum vacuum radiation spectra from a semiconductor microcavity with a time-modulated vacuum Rabi frequency," *Physical review letters*, vol. 98, no. 10, pp. 1–4, 2007. (Cited on page 51.)

[70] C. M. Wilson, G. Johansson, A. Pourkabirian, J. R. Johansson, T. Duty, F. Nori, and P. Delsing, "Observation of the dynamical Casimir effect in a superconducting circuit," *Nature*, vol. 479, no. 7373, pp. 376–379, 2011. (Cited on page 51.)

[71] F. Mallet, M. A. Castellanos-Beltran, H. S. Ku, S. Glancy, E. Knill, K. D. Irwin, G. C. Hilton, L. R. Vale, and K. W.

Lehnert, "Quantum state tomography of an itinerant squeezed microwave field," *Physical review letters*, vol. 106, p. 220502, June 2011. (Cited on page 59.)

[72] C. Eichler, D. Bozyigit, C. Lang, M. Baur, L. Steffen, J. M. Fink, S. Filipp, and A. Wallraff, "Observation of two-mode squeezing in the microwave frequency domain," *Physical review letters*, vol. 107, no. 11, pp. 1–5, 2011. (Cited on pages 59, 67, 68, and 162.)

[73] E. P. Menzel, R. D. Candia, F. Deppe, P. Eder, L. Zhong, M. Ihmig, M. Haeberlein, A. Baust, E. Hoffmann, D. Ballester, K. Inomata, T. Yamamoto, Y. Nakamura, E. Solano, A. Marx, R. Gross, B. A. D. Wissenschaften, and D. Garching, "Path entanglement of continuous-variable quantum microwaves," *Physical review letters*, vol. 109, p. 250502, December 2012. (Cited on pages 59, 67, and 162.)

[74] T. A. Palomaki, J. D. Teufel, R. W. Simmonds, and K. W. Lehnert, "Entangling mechanical motion with microwave fields," *Science*, vol. 342, pp. 710–3, November 2013. (Cited on pages 59 and 89.)

[75] C. Eichler, D. Bozyigit, and A. Wallraff, "Characterizing quantum microwave radiation and its entanglement with superconducting qubits using linear detectors," *Physical Review A*, vol. 86, p. 032106, September 2012. (Cited on page 59.)

[76] C. M. Caves, J. Combes, Z. Jiang, and S. Pandey, "Quantum limits on phase-preserving linear amplifiers," *Physical Review A*, vol. 86, p. 063802, 2012. (Cited on pages 61 and 64.)

[77] B. Huard, *Quantum information with superconducting circuits*. Mémoire d'habilitation à diriger des recherches, Ecole Normale Supérieure de Paris, 2014. (Cited on page 61.)

[78] C. Weedbrook, R. Garcia-Patron, C. Weedbrook, and T. C. Ralph, "Gaussian quantum information," *Review of Modern Physics*, vol. 84, October 2011. (Cited on page 61.)

[79] S. Weinreb, J. Bardin, H. Mani, and G. Jones, "Matched wide-band low-noise amplifiers for radio astronomy," *Review of Scientific Instruments*, vol. 80, p. 044702, March 2009. (Cited on page 63.)

[80] A. H. Akgiray, S. Weinreb, R. Leblanc, M. Renvoise, P. Frijlink, R. Lai, and S. Sarkozy, "Noise measurements of discrete HEMT transistors and application to wideband very low-noise amplifiers," *IEEE Transactions on microwave theory and techniques*, pp. 1–13, 2013. (Cited on page 63.)

[81] H. S. Ku, W. F. Kindel, F. Mallet, S. Glancy, K. D. Irwin, G. C. Hilton, L. R. Vale, and K. W. Lehnert, "Generating and verifying entangled itinerant microwave fields with efficient and independent measurements," *Physical Review A*, vol. 91, no. 4, p. 042305, 2015. (Cited on page 67.)

[82] K. G. Fedorov, S. Pogorzalek, U. L. Heras, M. Sanz, P. Yard, P. Eder, M. Fischer, J. Goetz, E. Xie, K. Inomata, Y. Nakamura, R. D. Candia, E. Solano, A. Marx, F. Deppe, and R. Gross, "Finite-time quantum entanglement in propagating squeezed microwaves," vol. 25, pp. 1–5. (Cited on page 67.)

[83] A. Furusawa, J. L. Sørensen, S. L. Braunstein, C. A. Fuchs, H. J. Kimble, and E. S. Polzik, "Unconditional quantum teleportation," *Science*, vol. 282, pp. 706–710, October 1998. (Cited on page 67.)

[84] C. Silberhorn, P. K. Lam, O. Weiß, F. König, N. Korolkova, and G. Leuchs, "Generation of continuous variable Einstein-Podolsky-Rosen entanglement via the Kerr nonlinearity in an optical fiber," *Physical review letters*, vol. 86, pp. 4267–4270, 2001. (Cited on page 67.)

[85] P. W. Shor, "Scheme for reducing decoherence in quantum computer memory," *Physical Review A*, vol. 52, no. 4, pp. 2493–2496, 1995. (Cited on page 83.)

[86] A. M. Steane, "Error correcting codes in quantum theory," *Physical review letters*, vol. 77, pp. 793–797, July 1996. (Cited on page 83.)

[87] J. Kelly, R. Barends, A. G. Fowler, A. Megrant, E. Jeffrey, T. C. White, D. Sank, J. Y. Mutus, B. Campbell, Y. Chen, Z. Chen, B. Chiaro, A. Dunsworth, I. Hoi, C. Neill, P. J. J. O. Malley, C. Quintana, P. Roushan, A. Vainsencher, J. Wenner, A. N. Cleland, and J. M. Martinis, "State preservation by repetitive error detection in a superconducting quantum circuit," *Nature*, vol. 519, no. 7541, pp. 66–69, 2015. (Cited on page 83.)

[88] D. Riste, S. Poletto, A. Bruno, V. Vesterinen, L. Dicarlo, and D. Riste, "Detecting bit-flip errors in a logical qubit using stabilizer measurements," *Nature Communications*, no. 7983, 2015. (Cited on page 83.)

[89] H. J. Kimble, "The quantum internet," *Nature*, vol. 453, pp. 1023–1030, June 2008. (Cited on pages 83 and 84.)

[90] N. H. Nickerson, Y. Li, and S. C. Benjamin, "Topological quantum computing with a very noisy network and local error rates approaching one percent," *Nature Communications*, vol. 4, pp. 1755–1756, 2013. (Cited on page 84.)

[91] R. J. Schoelkopf and S. M. Girvin, "Wiring up quantum systems," *Nature*, vol. 451, pp. 664–669, February 2008. (Cited on page 84.)

[92] Y. Tabuchi, S. Ishino, A. Noguchi, T. Ishikawa, R. Yamazaki, K. Usami, and Y. Nakamura, "Coherent coupling between a ferromagnetic magnon and a superconducting qubit," *Science*, vol. 349, no. 6246, pp. 405–408, 2015. (Cited on pages 85 and 87.)

[93] T. A. Palomaki, J. W. Harlow, J. D. Teufel, R. W. Simmonds, and K. W. Lehnert, "Coherent state transfer between itinerant microwave fields and a mechanical oscillator.," *Nature*, vol. 495, pp. 210–4, March 2013. (Cited on pages 85 and 89.)

[94] Y. Chu, P. Kharel, W. H. Renninger, L. D. Burkhart, L. Frunzio, T. Rakich, and R. J. Schoelkopf, "Quantum acoustics with superconducting qubits," *arXiv preprint 1703.00342v1*, 2017. (Cited on pages 85 and 89.)

[95] M. Reagor, W. Pfaff, C. Axline, R. W. Heeres, N. Ofek, K. Sliwa, E. Holland, C. Wang, J. Blumoff, K. Chou, M. J. Hatridge, L. Frunzio, M. H. Devoret, L. Jiang, and R. J. Schoelkopf, "Quantum memory with millisecond coherence in circuit QED," *Physical Review B*, vol. 94, p. 014506, 2016. (Cited on pages 85, 90, and 122.)

[96] S. Probst, A. Bienfait, J. J. Pla, B. Albanese, J. F. D. S. Barbosa, T. Schenkel, D. Vion, D. Esteve, K. Mølmer, J. J. L. Morton, R. Heeres, and P. Bertet, "Inductive-detection electron-spin resonance spectroscopy with 65spins/ $\sqrt{\mathrm{hz}}$ sensitivity," pp. 1–6. (Cited on page 86.)

[97] P. Haikka, Y. Kubo, A. Bienfait, P. Bertet, and K. Mølmer, "Proposal for detecting a single electron spin in a microwave resonator," *Physical Review A*, vol. 95, p. 022306, 2017. (Cited on page 86.)

[98] D. Lachance-Quirion, Y. Tabuchi, S. Ishino, A. Noguchi, T. Ishikawa, R. Yamazaki, and Y. Nakamura, "Resolving quanta of collective spin excitations in a millimeter-sized ferromagnet," *Science Advaces*, vol. 3, July 2017. (Cited on page 87.)

[99] R. Hisatomi, A. Osada, Y. Tabuchi, T. Ishikawa, A. Noguchi, R. Yamazaki, K. Usami, and Y. Nakamura, "Bidirectional conversion between microwave and light via ferromagnetic magnons," *Physical Review B*, vol. 93, p. 174427, 2016. (Cited on page 87.)

[100] J. D. Teufel, T. Donner, D. Li, J. W. Harlow, M. S. Allman, K. Cicak, A. J. Sirois, J. D. Whittaker, K. W. Lehnert, and R. W. Simmonds, "Sideband cooling of micromechanical motion to the quantum ground state," *Nature*, vol. 475, no. 7356, pp. 359–363, 2011. (Cited on page 87.)

[101] J. Chan, T. P. M. Alegre, A. H. Safavi-naeini, J. T. Hill, A. Krause, S. Groblacher, M. Aspelmeyer, and O. Painter, "Laser cooling of a nanomechanical oscillator into its quantum ground state," *Nature*, vol. 478, pp. 89–92, 2011. (Cited on page 87.)

[102] E. Verhagen, S. Deléglise, S. Weis, A. Schliesser, and T. J. Kippenberg, "Quantum-coherent coupling of a mechanical oscillator to an optical cavity mode," *Nature*, vol. 482, pp. 63–67, 2012. (Cited on page 89.)

[103] R. W. Andrews, R. W. Peterson, T. P. Purdy, K. Cicak, R. W. Simmonds, C. A. Regal, and K. W. Lehnert, "Bidirectional and efficient conversion between microwave and optical light," *Nature Physics*, vol. 10, pp. 321–326, April 2014. (Cited on page 89.)

[104] J. Wenner, Y. Yin, Y. Chen, R. Barends, B. Chiaro, E. Jeffrey, J. Kelly, A. Megrant, J. Y. Mutus, C. Neill, P. J. J. O. Malley, P. Roushan, D. Sank, A. Vainsencher, T. C. White, A. N. Korotkov, A. N. Cleland, and J. M. Martinis, "Catching Time-Reversed Microwave Coherent State Photons with 99 . 4 % Absorption Efficiency," *Physical review letters*, vol. 112, p. 210501, May 2014. (Cited on page 90.)

[105] M. Pierre, I.-m. Svensson, S. R. Sathyamoorthy, G. Johansson, and P. Delsing, "Storage and on-demand release of microwaves using superconducting resonators with tunable coupling," *Applied Physics Letters*, vol. 104, no. 2014, p. 232604, 2014. (Cited on page 90.)

[106] S. Kuhr, S. Gleyzes, C. Guerlin, J. Bernu, U. B. Hoff, S. Deléglise, S. Osnaghi, M. Brune, J. Raimond, E. Jacques, P. Bosland, B. Visentin, S. Kuhr, S. Gleyzes, C. Guerlin, J. Bernu, U. B. Hoff, S. Deléglise, and S. Osnaghi, "Ultrahigh finesse Fabry-Pérot superconducting resonator," *Applied Physics Letters*, vol. 90, no. 2007, p. 164101, 2015. (Cited on pages 90, 92, and 180.)

[107] D. M. Pozar, *Microwave Engineering*. John Wiley & Sons, 2009. (Cited on page 90.)

[108] I. Martin, Y. Makhlin, A. Shnirman, and G. Scho, "Low- and high-frequency noise from coherent two-level systems," *Physical review letters*, vol. 127002, pp. 1–4, April 2005. (Cited on page 92.)

[109] A. D. O. Connell, M. Ansmann, R. C. Bialczak, M. Hofheinz, N. Katz, E. Lucero, C. Mckenney, M. Neeley, H. Wang, E. M. Weig, A. N. Cleland, J. M. Martinis, A. D. O. Connell, M. Ansmann, R. C. Bialczak, M. Hofheinz, N. Katz, and E. Lucero, "Microwave dielectric loss at single photon energies and millikelvin temperatures," *Applied Physics Letters*, vol. 92, p. 112903, 2008. (Cited on page 92.)

[110] J. M. Martinis, K. B. Cooper, R. Mcdermott, M. Steffen, M. Ansmann, K. D. Osborn, K. Cicak, S. Oh, D. P. Pappas, R. W. Simmonds, and C. C. Yu, "Decoherence in Josephson qubits from dielectric loss," *Physical review letters*, vol. 95, p. 210503, November 2005. (Cited on page 92.)

[111] C. Wang, C. Axline, Y. Y. Gao, T. Brecht, Y. Chu, L. Frunzio, M. H. Devoret, R. J. Schoelkopf, C. Wang, C. Axline, Y. Y. Gao, T. Brecht, Y. Chu, L. Frunzio, and M. H. Devoret, "Surface participation and dielectric loss in superconducting qubits," *Applied Physics Letters*, vol. 107, p. 162601, 2015. (Cited on page 92.)

[112] G. Kirchmair, B. Vlastakis, Z. Leghtas, S. E. Nigg, H. Paik, E. Ginossar, M. Mirrahimi, L. Frunzio, S. M. Girvin, and R. J. Schoelkopf, "Observation of quantum state collapse and revival due to the single-photon Kerr effect.," *Nature*, vol. 495, no. 7440, pp. 205–9, 2013. (Cited on pages 92 and 138.)

[113] M. Reagor, H. Paik, G. Catelani, L. Sun, C. Axline, E. Holland, I. M. Pop, N. A. Masluk, T. Brecht, L. Frunzio, M. H. Devoret, L. Glazman, R. J. Schoelkopf, M. Reagor, H. Paik, G. Catelani, L. Sun, C. Axline, M. H. Devoret, L. Glazman, and R. J. Schoelkopf, "Reaching 10 ms single photon lifetimes for superconducting aluminum cavities," *Applied Physics Letters*, vol. 102, no. 2013, p. 192604, 2016. (Cited on page 93.)

[114] T. Brecht, M. Reagor, Y. Chu, W. Pfaff, C. Wang, L. Frunzio, M. H. Devoret, R. J. Schoelkopf, T. Brecht, M. Reagor, Y. Chu, W. Pfaff, C. Wang, L. Frunzio, and M. H. Devoret, "Demonstration of superconducting micromachined cavities," *Applied*

Physics Letters, vol. 107, no. 2015, p. 192603, 2016. (Cited on page 93.)

[115] J. Koch, T. M. Yu, J. Gambetta, A. A. Houck, D. I. Schuster, J. Majer, A. Blais, M. H. Devoret, S. M. Girvin, and R. J. Schoelkopf, "Charge-insensitive qubit design derived from the Cooper pair box," *Physical Review A*, vol. 76, p. 042319, 2007. (Cited on pages 95, 97, and 98.)

[116] J. A. Schreier, A. A. Houck, J. Koch, D. I. Schuster, B. R. Johnson, J. M. Chow, J. M. Gambetta, J. Majer, L. Frunzio, M. H. Devoret, S. M. Girvin, and R. J. Schoelkopf, "Suppressing charge noise decoherence in superconducting charge qubits," *Physical Review B*, vol. 77, p. 180502, 2008. (Cited on page 95.)

[117] H. Paik, D. I. Schuster, L. S. Bishop, G. Kirchmair, G. Catelani, A. P. Sears, B. R. Johnson, M. J. Reagor, L. Frunzio, L. I. Glazman, S. M. Girvin, M. H. Devoret, and R. J. Schoelkopf, "Observation of high coherence in Josephson junction qubits measured in a three-dimensional circuit QED architecture," *Physical review letters*, vol. 107, p. 240501, December 2011. (Cited on page 96.)

[118] A. A. Houck, J. A. Schreier, B. R. Johnson, J. M. Chow, J. Koch, J. M. Gambetta, D. I. Schuster, L. Frunzio, M. H. Devoret, S. M. Girvin, and R. J. Schoelkopf, "Controlling the spontaneous emission of a superconducting transmon qubit," *Physical review letters*, vol. 101, p. 080502, August 2008. (Cited on page 99.)

[119] S. E. Nigg, H. Paik, B. Vlastakis, G. Kirchmair, S. Shankar, L. Frunzio, M. Devoret, R. Schoelkopf, and S. Girvin, "Black-box superconducting circuit quantization," *Physical review letters*, vol. 108, p. 240502, 2012. (Cited on page 99.)

[120] S. L. Braunstein and P. van Loock, "Quantum information with continuous variables," *Reviews of Modern Physics*, vol. 77, pp. 513–577, April 2005. (Cited on page 101.)

[121] B. Abdo, K. Sliwa, F. Schackert, N. Bergeal, M. Hatridge, L. Frunzio, A. D. Stone, and M. Devoret, "Full coherent fre-

quency conversion between two propagating microwave modes," *Physical review letters*, vol. 110, p. 173902, April 2013. (Cited on page 102.)

[122] M. Mirrahimi, Z. Leghtas, V. V. Albert, S. Touzard, R. J. Schoelkopf, L. Jiang, and M. H. Devoret, "Dynamically protected cat-qubits : a new paradigm for universal quantum computation," *New Journal of Physics*, vol. 16, p. 045014, 2014. (Cited on pages 107 and 148.)

[123] K. Juliusson, S. Bernon, X. Zhou, V. Schmitt, H. le Sueur, P. Bertet, D. Vion, M. Mirrahimi, P. Rouchon, and D. Esteve, "Manipulating fock states of a harmonic oscillator while preserving its linearity," *Physical Review A*, vol. 94, p. 063861, December 2016. (Cited on page 109.)

[124] J. M. Pierce, "Residual microwave surface resistance of superconducting lead," *Journal of Applied Physics*, vol. 44, pp. 1342–1347, mar 1973. (Cited on pages 117 and 180.)

[125] K. Geerlings, Z. Leghtas, I. M. Pop, S. Shankar, L. Frunzio, R. J. Schoelkopf, M. Mirrahimi, and M. H. Devoret, "Demonstrating a driven reset protocol for a superconducting qubit," *Physical review letters*, vol. 110, pp. 1–5, March 2013. (Cited on page 127.)

[126] P. J. Leek, M. Baur, J. M. Fink, R. Bianchetti, L. Steffen, S. Filipp, and A. Wallraff, "Cavity quantum electrodynamics with separate photon storage and qubit readout modes," *Physical review letters*, vol. 104, p. 100504, 2010. (Cited on page 137.)

[127] A. Narla, K. M. Sliwa, M. Hatridge, S. Shankar, L. Frunzio, R. J. Schoelkopf, and M. H. Devoret, "Wireless Josephson amplifier," *Applied Physics Letters*, vol. 104, no. 23, p. 232605, 2014. (Cited on page 139.)

[128] B. Abdo, A. Kamal, and M. Devoret, "Nondegenerate three-wave mixing with the Josephson ring modulator," *Physical Review B*, vol. 87, p. 014508, 2013. (Cited on page 144.)

[129] http://qucs.sourceforge.net. Accessed: 2017-10-01. (Cited on page 145.)

[130] K. W. Mak and J. Hao, "Advance in the analysis models for characterizing multi-layered interdigitatal capacitors," *International Journal of Advanced Applied Physics Research*, vol. 1, pp. 1–8, 2014. (Cited on page 146.)

[131] W. Pfaff, C. J. Axline, L. D. Burkhart, U. Vool, P. Reinhold, L. Frunzio, L. Jiang, M. H. Devoret, and R. J. Schoelkopf, "Controlled release of multiphoton quantum states from a microwave cavity memory," *Nature Physics*, vol. 13, June 2017. (Cited on page 148.)

[132] M. Pechal, J. Besse, M. Mondal, M. Oppliger, S. Gasparinetti, and A. Wallraff, "Superconducting switch for fast on-chip routing of quantum microwave fields," vol. 6, p. 024009, July 2016. (Cited on page 153.)

[133] J. Wenner, R. Barends, R. C. Bialczak, Y. Chen, J. Kelly, E. Lucero, M. Mariantoni, A. Megrant, O. Malley, D. Sank, A. Vainsencher, H. Wang, T. C. White, Y. Yin, J. Zhao, A. N. Cleland, J. M. Martinis, J. Wenner, R. Barends, R. C. Bialczak, Y. Chen, J. Kelly, E. Lucero, M. Mariantoni, A. Megrant, P. J. J. O. Malley, D. Sank, A. Vainsencher, and H. Wang, "Surface loss simulations of superconducting coplanar waveguide resonators," *Applied Physics Letters*, vol. 99, p. 113513, 2011. (Cited on page 153.)

[134] K. L. Geerlings, *Improving coherence of superconducting qubits and resonators*. PhD thesis, 2013. (Cited on page 154.)

[135] J. M. Martinis and A. Megrant, "UCSB final report for the CSQ program: Review of decoherence and materials physics for superconducting qubits," *arXiv preprint*, October 2014. (Cited on page 154.)

[136] A. Kamal, A. Marblestone, and M. Devoret, "Signal-to-pump back action and self-oscillation in double-pump Josephson parametric amplifier," *Physical Review B*, vol. 79, p. 184301, May 2009. (Cited on page 159.)

[137] W. Wustmann and V. Shumeiko, "Nondegenerate parametric resonance in a tunable superconducting cavity," *Physical Review Applied*, vol. 8, p. 024018, 2017. (Cited on page 161.)

[138] H. Engler, M. Zielonkowski, M. Weidemuller, and R. Grimm, "Magneto-optic trapping of lithium using semiconductor lasers," *Optics Communications*, vol. 158, pp. 263–272, December 1998. (Cited on page 164.)

[139] A. L. Schawlow and C. H. Townes, "Infrared and optical masers," *Physical Review*, vol. 112, pp. 1940–1949, 1958. (Cited on page 164.)

[140] R. Adler, "A study of locking phenomena in oscillators," *Proceedings of the IEEE*, vol. 61, pp. 1380–1385, October 1973. (Cited on page 165.)

[141] M. Armand, "On the output spectrum of unlocked driven oscillators," *Proceedings of the IEEE*, vol. 57, pp. 798–799, May 1969. (Cited on page 166.)

[142] F. Lecocq, I. M. Pop, Z. Peng, I. Matei, T. Crozes, T. Fournier, C. Naud, W. Guichard, and O. Buisson, "Junction fabrication by shadow evaporation without a suspended bridge," *Nanotechnology*, vol. 22, August 2011. (Cited on page 175.)

Résumé

Les circuits supraconducteurs sont parmi les technologies de l'information quantique les plus avancées. Ils ont aujourd'hui atteint la maturité qui offre un grand degré de contrôle et une large gamme d'interactions qui peuvent être précisément réalisées sur mesure. Le mixeur Josephson est un exemple de circuit supraconducteur qui effectue le mixage à trois ondes aux fréquences micro-ondes.

Dans cette thèse, trois expériences, où le mixeur Josephson est utilisé pour trois applications différentes sont décrites. D'abord, nous avons réalisé le couplage ultrafort effectif entre deux modes bosoniques afin d'étudier les propriétés de l'état fondamental de ce système, tels que le *squeezing* à un mode et à deux modes du champ radié. Ensuite, nous avons construit un nœud quantique, capable de créer et distribuer de l'intrication sur un réseau quantique micro-onde, alors que de stocker et relâcher de l'information quantique à la demande. Nous avons intégré un qubit de mesure dans ce dispositif pour augmenter le degré de contrôle sur son état quantique.
Finalement, nous avons poussé le mixeur Josephson au delà du seuil de l'oscillation paramétrique, où nous avons démontré une technique inhabituelle de verrouillage par injection en conversion de fréquence dans ce dispositif non-dégénéré.

Abstract

Superconducting circuits stand among the most advanced quantum information processing platforms. They have nowadays reached a maturity that offers a high level of controllability and a large variety of interactions that can be precisely designed on demand. The Josephson mixer is one such superconducting device that performs three-wave mixing at microwave frequencies.

In this thesis, we describe three experiments in which the Josephson mixer was used for different applications. First, we have realized an effective ultrastrong coupling of two bosonic modes that allowed us to study the ground state properties of this system, such as the single mode and the two mode squeezing of the emitted radiation. Second, we have built a quantum node, able to generate and distribute entanglement over a microwave quantum network, as well as to store and release quantum information on demand. We have integrated an ancilla qubit to this device in order to increase the degree of control over the quantum state of the system. Finally, we have pushed the Josephson mixer beyond the parametric oscillation threshold, where we have demonstrated an atypical injection locking technique that relies on coherent frequency conversion in this non-degenerate device.